IMPROVED POWER CONVERTER FOR DISTRIBUTED PHOTOVOLTAIC GENERATION SYSTEM

Ph.D. THESIS

by

AUROBINDA PANDA

DEPARTMENT OF ELECTRICAL ENGINEERING
INDIAN INSTITUTE OF TECHNOLOGY ROORKEE
ROORKEE – 247667 (INDIA)

JULY, 2015

IMPROVED POWER CONVERTER FOR DISTRIBUTED PHOTOVOLTAIC GENERATION SYSTEM

A THESIS

Submitted in partial fulfilment of the requirements for the award of the degree

of

DOCTOR OF PHILOSOPHY

in

ELECTRICAL ENGINEERING

by

AUROBINDA PANDA

DEPARTMENT OF ELECTRICAL ENGINEERING
INDIAN INSTITUTE OF TECHNOLOGY ROORKEE
ROORKEE – 247667 (INDIA)

JULY, 2015

INDIAN INSTITUTE OF TECHNOLOGY ROORKEE
ROORKEE

CANDIDATE'S DECLARATION

I hereby certify that the work which is being presented in this thesis entitled **"IMPROVED POWER CONVERTER FOR DISTRIBUTED PHOTOVOLTAIC GENERATION SYSTEM"** in partial fulfilment of the requirements for the award of the Degree of Doctor of Philosophy and submitted in the Department of Electrical Engineering of the Indian Institute of Technology Roorkee is an authentic record of my own work carried out during a period from December, 2009 to July, 2015 under the supervision of Dr. Mukesh Kumar Pathak, Associate Professor and Dr. Satya Prakash Srivastava, Professor, Department of Electrical Engineering, Indian Institute of Technology Roorkee, Roorkee.

The matter presented in this thesis has not been submitted by me for the award of any other degree of this or any other Institute.

(**AUROBINDA PANDA**)

This is to certify that the above statement made by the candidate is correct to the best of our knowledge.

(MUKESH KUMAR PATHAK)
Supervisor

(SATYA PRAKASH SRIVASTAVA)
Supervisor

Date: _____

ABSTRACT

Solar power is one of the most popular form of renewable energy which can be easily used in the distributed generation (DG) system through the use of photovoltaic (PV) module. A Photovoltaic Distributed Generation (PVDG) system is well suited for clean power generation. However, the power generated by the PV module is still considered to be expensive and the spread of the PVDG system is subject to pace of its cost reduction. A lot of research work has been carried out to obtain an efficient and cheaper PV module based on new cell materials and manufacturing technologies. Moreover, an alternative way to reduce the overall cost of PVDG system is by increasing the effectiveness of the whole system using an improved power conditioning system and also by introducing an improved power quality features in its control system. The primary goal of a power conditioning unit in PVDG system is to increase the energy injection to the grid by optimizing the energy extraction process from the PV module by keeping track of maximum power point (MPP), by operating at a lower switching frequency thereby reducing the switching losses. In addition to that the price of the power converter also plays a vital role in developing a cost effective PVDG system. The main focus of this research is to optimally control the power conditioning unit to improve the overall performance of the single phase PVDG system. These power conditioning units are used to regulate the voltage and current for the power flow during grid-connected operation, and also for the maximum power extraction. In order to analyze the power converters for PVDG system, it is essential to model a PV module attached to the converter. PV module presents a nonlinear $I-V$ characteristic with several parameters to be adjusted according to experimental data obtained from the datasheet of a practical device. For the dynamic analysis of the converters, and maximum power point tracking (MPPT) algorithms mathematical modelling of the PV module is useful. The first part of this research work presents the modelling and simulation of PV module. However, the major challenges in the modelling a PV module is that, all the parameters which are required for the modelling purpose are not available on the manufacturer's datasheet. Here the determination of parameters of the PV module is performed by using Gauss Seidel iteration Method and the modelling is carried out using all the known and the determined parameters..

At present the most commonly used converter topology for PVDG system is the two level multistring inverter. This inverter consists of several PV strings that are connected with DC-DC converters to form a common DC-bus. This topology has advantages of independent tracking of the MPP of each string. However, the major challenges in such type of system are, low efficiency of PV module and high implementation cost, thus it becomes necessary to use these systems more optimally. For this, a fuzzy-logic based MPPT controller is proposed.

Fuzzy-logic based MPPT technique offers fast and accurate converging to the MPP during steady-state and varying weather conditions compared to the conventional perturb and observe based MPPT method. The synchronization of PV inverter with the grid is made with the help of a phase locked loop (PLL). The main task of the PLL is to provide a unity power factor operation which includes synchronization of the inverter output current with the grid voltage. There has been an increasing interest in PLL topologies for DG system. It is a grid voltage phase detection structure which requires an orthogonal voltage system. In the single-phase PLL, accurate and fast phase estimation can be obtained by processing a signal in phase with the grid voltage (original signal) and another one which is 90^0 phase shifted from it. The PLL that generates the orthogonal signal by delaying the original signal is called a transport-delay based PLL(TDPLL). This type of PLL is simple and its transient response is fast and smooth among all available PLL methods. The other methods for generating orthogonal voltage are Hilbert transformation, Park transformation, etc. All these methods have some shortcoming such as high complexity, nonlinearity and have slower response than TDPLL. The main drawback of a conventional TDPLL is its sensitivity to the grid frequency changes, since the delay is determined assuming constant frequency. Here, a modified TDPLL is presented which uses two delay blocks to make TDPLL robust against frequency variation.

In a PVDG system, the demand of local load is fulfilled by the combined action of PV inverter and grid, based on the atmospheric and load conditions. During favourable atmospheric condition (or light load condition), the local load demand is supplied by the PV inverter and surplus power is fed to the grid. Similarly, during the unfavourable atmospheric condition or overload condition, both PV inverter and the grid jointly meet the local load demand. Thus, in both the aforementioned conditions the quality of the grid current is decided by the load. In present day distribution systems, major power consumption has been in reactive/non-linear loads, such as motor drives, fans, pumps, and power electronic converters. These types of loads draw non-sinusoidal currents from the generation system. The non-sinusoidal current is comprised of reactive and harmonic components in addition to the active component. Excessive reactive component of current results into low power factor, poor voltage regulation and reduction in active power capability of the distribution system. Therefore, the electric power quality (PQ) has become an issue of concern and extensive research is being done to improve the power quality. On the other hand, the PV distributed system produces an amount of active power and injects it into the distribution system. This active power is influenced by atmospheric condition, which causes voltage fluctuations at PCC, because it changes independently of load power demand. This makes voltage regulation in the distribution lines more difficult. On the other hand, harmonic regulations or guidelines such as IEEE 1547 and IEC 61727 are applied to limit the current and voltage harmonic levels. To meet these requirements, these harmonics must be mitigated by using

harmonic filters. Active and passive filters are used either together to form hybrid filters or separately to mitigate harmonics. Recently, many researchers have devoted efforts to develop a PV inverter with real power injection with improved PQ features such as compensation of reactive power and local load current harmonics. One of the possible ways of the PQ enhancement scheme in a DG system is by interfacing an external shunt active power filter (APF) at the PCC. Here the PV inverter is only used for the active power flow in PVDG system and shunt APF is responsible for the PQ enhancement in PVDG system. However, the main drawback of such PVDG system is the high cost and underutilization of hardware circuits. Therefore, to eliminate the complexity and underutilization of the above mentioned topology of PVDG system, an enhanced power quality based PVDG system with an integrated shunt APF mechanism is presented. The main advantage of this topology is that it doesn't need any additional hardware circuit for reactive power and load current harmonic compensation. With this approach, the PV inverter regulates the active power flow between the PV module and the grid. In addition to this, the system also carries out the compensation of reactive power and load current harmonics thereby making the grid current sinusoidal. Moreover, one of the major drawbacks of the conventional grid-tie PV inverter is that, it generates real power only during the daytime, with completely in idle state during night-time. This leads to further underutilization of such an expensive system in the night-time. To address the issue of underutilization in PVDG system, the PV inverter is utilized as a shunt APF during night time. The main goal of this research work is to formulate and implement the 1-ϕ instantaneous reactive power theory in the PVDG system for the enhancement of PQ to obtain the following objectives,

- To transmit the maximum possible real power from the PV module by using the MPPT controller
- To meet the real power demanded by the local load
- To compensate the reactive and harmonic components of load current at PCC
- To utilize the PV inverter as a shunt APF during night time.

Thus, with an adequate control of PV inverter, all the above-mentioned objectives have been achieved either separately or simultaneously. Hence, in this research work the PQ requirements as per the utility standards at the PCC are accomplished without requiring any additional hardware circuits. For the further improvement of PQ and also to increase the overall power transmission capacity of the two-stage PVDG system a multilevel inverter topology is introduced in place of the two-level inverter. In recent years multilevel inverter topologies have become more attractive for researchers as they offer improved output waveform as compared to the conventional two level inverter. With the improvement in the output waveform, the harmonic content and hence the size of the filter can be reduced. Among all these available MLI topologies, the cascaded H-bridge MLI (CHBMLI) requires separate DC sources and hence constitutes a promising alternative, providing a modular

design that can be extended to allow a transformer less operation in grid connected PV system. The power flow control in such type of PVDG system requires two control loops. The inner current control loop is used to modulate the output current of the PV CHBMLI to meet magnitude and phases of waveform whereas the outer voltage control loop regulates the output power of the PV inverter according to the MPP of PV modules. These two control loops are realized by two stages of power conversion. One is a DC to DC converter with MPPT control and the other is a DC to AC inverter. But two stage operation may lead to more power loss than that of a single-stage conversion. In a single stage PVDG system, both the control loops are realized simultaneously in one power conversion stage, thus simplifying the system topology and hence decreases the overall power loss in the system. However, there is always a chance of imbalance in the input DC-link voltages of CHBMLI when fed from PV module. This is due to the non-ideal conditions in PV modules. The most common non-ideal conditions of a PV module include partial shading, dust collection and PV ageing. Hence the balancing of the DC voltages is one of the important issues in the control of CHBMLI when used in PV application. If this voltage balance is not perfectly accomplished, the modulation methods create errors in the modulated output voltage. This leads to the distortion in the output voltages and currents of the CHBMLI. To overcome the DC-link voltage error of CHBMLI, a single phase space vector modulation (SVM) scheme for the CHBMLI is proposed and implemented.

In order to verify the proposed control approach for CHBMLI based two-stage and single stage enhanced PQ based PVDG system an extensive simulation is carried out using MATLAB/Simulink environment. Both two-stage and single-stage PVDG system is actively controlled to achieve sinusoidal grid current at unity displacement factor in spite of highly non-linear load connected at PCC under varying atmospheric and load conditions. The MPPT control of the two-stage PVDG system is accomplished by DC-DC converter, whereas in single-stage PVDG system, it is achieved by each H-bridge cell of CHBMLI. Finally, for the power flow control in PVDG system, the reference compensating current is derived from the DC-link voltage controller and the PQ enhancement controller. A non-linear load consisting of an uncontrolled rectifier and a RL element on the DC-side, have been taken for the analysis of the system. The system is validated for different modes of controller action, varying atmospheric and load conditions. Finally, based on the simulation results a comparative analysis is made between two-level and five level CHBMLI based PVDG system with single-stage CHBMLI based topology. In single-stage topology, the need of DC-DC converter for MPPT is eliminated. This leads to more power injection to the grid as compared to two-stage system.

To verify the simulations of 1-ϕ, 230 V, two-stage and single stage PVDG system, the following prototypes have been developed in the laboratory:

(i) Enhanced PQ based Single-phase two-stage 2-level inverter in PVDG System

(ii) Enhanced PQ based Single-phase two-stage 5-level CHBMLI in PVDG System

(iii) Enhanced PQ based Single-phase single-stage CHBMLI in PVDG System

For the hardware development, two 128 W PV modules manufactured by Maharishi Solar, India are used. A 1-ϕ downscaled topologies has been designed and constructed to realize the above mentioned PVDG topologies. In case of two-stage topology, the outputs of two DC-DC converters are connected in a cascaded manner to have a single DC-link for the two-level inverter. However, in case of 5-level CHBMLI, each DC-DC converter output is directly connected across two individual H-bridge cells. Finally, the developed PV inverter output is connected to the PCC with a series connected coupling inductor. A 35.8V (50 V peak), 50 Hz grid is developed in the laboratory by using a step down transformer and is interfaced with the PV inverter through an isolation transformer. All the rquired controllers for the PVDG system are implemented in dSPACE. The performance of the above mentioned single phase two stage enhanced PQ based PVDG system is investigated for following modes of operations (i) under different modes of power quality enhancement controller (PQEC) (ii) under different modes of MPPT Controller (iii) under varying load condition. With the integrated PQ enhancement scheme, in PV inverter, the grid current has been observed to be sinusoidal and its corresponding THDs have also been found to be well within the limits of IEEE 1547 and IEC 61727 recommended value of 5%. A smooth control of DC voltages ensures the effectiveness of the DC voltage controller. Further, the experimental results of the capacitor voltage balancing of the H-bridge cells in CHBMLI have been studied. The experimental results have been found to be in good agreement with the simulation results.To verify the viability and effectiveness of the enhanced PQ based single stage PVDG system for power flow operation, harmonic elimination and reactive compensation, experimental investigations have been conducted with non-linear loads. Here, the maximum power extraction from each PV module is accomplished by PV CHBMLI itself. As in case of single-stage CHBMLI based PVDG system, with the PV module directly connected across the H-bridge cell, there is always a possibility of an input DC-link unbalancing in CHBMLI. This voltage unbalance in CHBMLI leads to distortion in the output voltage and current of the multilevel inverter. Therefore, to obtain an optimal output from CHBMLI fed from PV module, the single stage PVDG system is operated with SVM controller. The experimental validation of single stage CHBMLI based PVDG system is divided into two stages. In section-1, the 1-ϕ SVM scheme for the CHBMLI under both balanced and unbalanced DC-link voltage conditions are experimentally validated and in section-2, the experimental results of enhanced PQ based single stage CHBMLI based PVDG system with SVM scheme under varying load conditions is presented.

ACKNOWLEDGEMENTS

Apart from personal efforts and steadfastness to work, constant inspiration and encouragement given by a number of individuals acted as the driving force in attaining this day in my life. To quote them all may be an onerous task, but direct and indirect assistance and guidance received is gratefully acknowledged. I would like to express my feelings of gratefulness and submit my acknowledgement for them further in the following lines.

I take this opportunity to express my sincere gratitude towards my guides Dr. Mukesh Kumar Pathak, Associate Professor and Dr. Satya Prakash Srivastava, Professor, Electrical Engineering Department (EED), Indian Institute of Technology Roorkee (IITR) for their proficient and enthusiastic guidance, valuable suggestions, discussions, continuous encouragement and constant inspiration throughout the course of this study and critically examining the thesis write-up.

I also express my sincere gratitude towards my research committee members, namely Prof. S.P. Gupta (EED), Prof. Promod Agrawal (EED), Dr. B. Anand (ECED) and Chairman, Department Research Committee (DRC) for their valuable suggestions and cooperation.

My thanks are to the Head of the Electrical Engineering Department and all faculty members of the department for their help, moral support, and providing the excellent infrastructure, laboratory and computing facilities for the research work.

I acknowledge my sincere gratitude to the Ministry of Human Resources Development (MHRD), Government of India for its financial support to carry out this research.

I thankfully appreciate and acknowledge my indebtedness to my friends and research scholars for their instant help, cooperation, advice, suggestion, and moral support during my stay. The list may go long, but some of them I would like to mention are Mr. Prabhash Mishra, Dr. H.K.Narang, Dr. Rakesh Mourya, Dr. G. Durga Sukumar, Mr. Sukanta Haldar, Mr. Sanjeev Saxena, Mr. Manmohan Garg, Mr. Y Srennevas, Mr. Dogg Ravendra, Mr. N. Venkataramana Naik, Mr. Pradeep Synodiya, Mr. Rahul Patil, Mr. Anil Gambhir, Mr. Arpit Agrawal, Mr. Vipul Kumar, Mr. Kishore Pedapenki, Mr. Anubhav Agrawal, Mr.D. Suresh and Janardhana Rao.

Finally, I wish to express my deepest gratitude to my parents Late Bhagirathi Panda and Sradhanjali Panda, sisters, Niharika, Sagarika and Smaranika, brother-in-laws, Sharad, Devraj and Chintamani, nephew, Prajwal, nieces, Nancy, Shivansi, Krishnansi and Nyasa for their endless support, encouragement and patience.

May all praise be to the Almighty, the most beneficent, and the most merciful.

(**Aurobinda Panda**)

CONTENTS

LIST OF FIGURES

LIST OF TABLES

LIST OF ACRONYMS

1P2W	Single-phase, two-wire
ac, AC	Alternating Current
APF	Active Power Filter
ASD	Adjustable Speed Drive
CHB	Cascaded H-bridge
CSD	Custom Power Device
CSI	Current Source Inverter
dc, DC	Direct Current
DCMLI	Diode Clamped Multilevel Inverter
DPF	Displacement Power Factor
DSO	Digital Storage Oscilloscope
DSP	Digital Signal Processor
DG	Distributed Generation
EMI	Electro Magnetic Interference
FCMLI	Flying Capacitor Multilevel Inverter
$GtCO_2$	Giga tonnes of carbon dioxide
Gtoe	Giga tonnes of oil equivalent
IEA	International Energy Agency
IEC	International Electrotechnical Commission
IEEE	Institute of Electrical & Electronics Engineers
LSPWM	Level-shifted Pulse width Modulation
MLI	Multilevel Inverter
MOSFET	Metal Oxide Semiconductor Field-effect Transistor
PCC	Point of Common Coupling
pf, PF	Power Factor
PI	Proportional and Integral
PQEC	Power Quality Enhancement Controller
PV	Photovoltaic
PLL	Phase Locked Loop
PWM	Pulse width Modulation
rms, RMS	Root Mean Square
SMPS	Switch Mode Power Supply
SVM	Space Vector Modulation
THD	Total Harmonic Distortion

LIST OF SYMBOLS

v_g	Single-phase grid voltage
i_g	Single-phase grid current
i_L	Single-phase load current
i_{inv}	Single-phase 2-level inverter current
i_{CHBMLI}	Single-phase CHBMLI current
V_{PV}	PV Module output voltage
I_{PV}	PV Module output current
m	Number of levels in inverter
N	Cascade number
f_{cr}	Carrier signal frequency
f_m	Modulating signal frequency
m_a	Amplitude modulation index
m_f	Frequency modulation index
L_{inv}	Filter inductor of PV inverter
L_g	Grid-side inductor
L_1	Inductor of boost converter
L_{ac}	Commutation inductance
p, q	Instantaneous real and reactive powers
$V_{ref,c}$	Cluster reference voltage
$V_{ref,i}$	Reference DC voltage for each H-bridge cell
K_P, K_I	Proportional and integral gains

[This chapter describes introduction to the research work. It starts with a brief background on distributed photovoltaic generation system and the challenges associated with it. Then, the solutions to the problems have been discussed. Next, scope of work, author's contribution, and thesis outlines are explained]

1.1 Overview

As the energy demand is increasing day by day due to the worldwide economic growth and development, the global total primary energy supply (TPES) is found to be more than doubled between 1971 and 2011 (Fig.1.1(a)). Most of these energy demand in today's world are supplied by the hydrocarbon based fossil fuels[1]. Combustion of these fuels produces energy which is converted into electrical energy. As a by-product of combustion, they give rise to pollutant like CO_2, which is the major cause of global warming. Since the industrial revolution, annual CO_2 emission from fuel combustion is dramatically increased from zero to 31 $GtCO_2$ in 2010[1]. This increase in trend of carbon emission is shown in Fig.1.1(b). Moreover, there is only a limited amount of fossil fuels available for the future consumption. This limited availability of conventional energy sources and the concern of global warming, has given a new impetus to renewable energy sources[1, 2]. These sources, known as green energy are environment friendly with a minimum impact on the environment. Renewable energy resources exist over wide geographical areas, in contrast to other energy sources, which are concentrated in a limited number of countries. Rapid deployment of renewable energy and energy efficiency is resulting in significant energy security, climate change mitigation, and economic benefits [2,[3]].

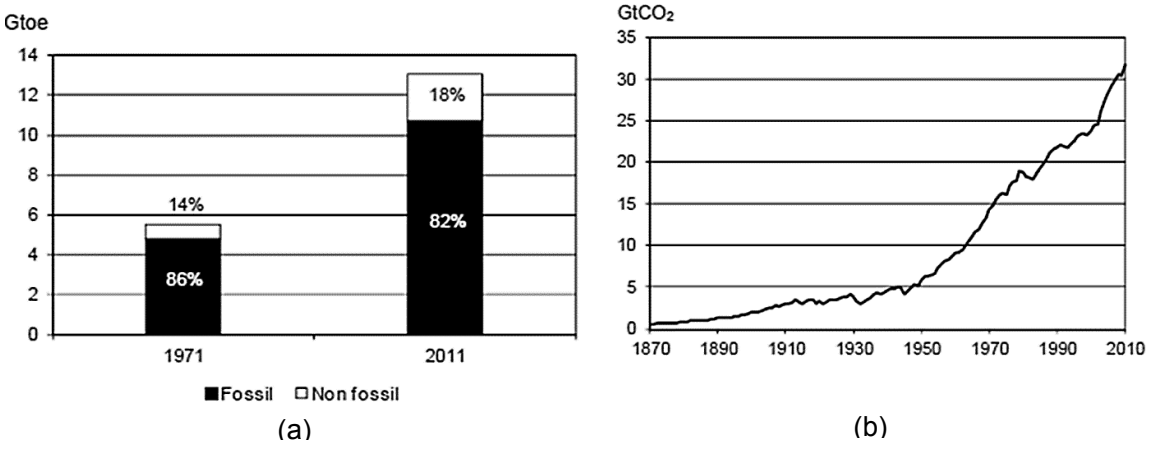

Fig.1.1 (a) World Primary energy supply (b)Trend in CO_2 Emissions from fossil fuel consumption[1]

Conventionally, energy is produced in a large scale of hundreds or thousands of megawatts in power plants fuelled from hydrocarbons or nuclear fuels. The produced energy needs to be transmitted to the consumers through intricate transmission and distribution systems. However, the energy of the future is being proposed to be generated at the site of the consumer in small scale[4]. Alternate sources of energy/renewable energy sources are to be used to generate this power. These sources will be used to generate electrical power in kilowatt ranges to meet the needs of localized demand. They can be installed in residential or commercial complexes to meet partial, entire and even excess of demand of that particular area. This generation scheme as opposed to large scale generation is known as distributed generation (DG). The most prevalent forms of renewable energy are solar, wind, biomass, hydro power, geothermal and biofuels. Among all, solar power is one of the fastest growing renewable energy sources, which can be easily used in the DG system through the use of photovoltaic (PV) arrays and power electronic converters. Panels or modules are available commercially which are rated to generate power depending on environmental conditions. With the government subsidies the installation of PV has become economically viable with a worldwide growth rate at 40%. With this growth rate, PV is poised to be the energy of the future.

1.2 History of the Distributed Photovoltaic Generation System and Motivation

The concept of DG has existed from the very beginning of the commercial supply of electric power. It was known by various names at different times, for example, embedded generation, on-site power systems or backup generation [2]. Some of the components of distributed generation like internal combustion engine or gas turbines have existed for quite sometimes for different applications. With the demand of new age technology, other components like the fuel cells and PV have also been incorporated [2]. With concerns for the need of environment friendly technology and reliability of fuel, new interests have risen towards a modern version of distributed generation. Ideas have been proposed to revolutionize the way electricity is produced today by making distributed generation as ubiquitous as large power plants are today [2[5]. PV energy is an attractive form of renewable energy, as the requirement of fuel to generate power is eliminated and hence making the running cost negligible. With most of the countries set up a target for the amount of PV power in their generation system [3] and PV generation having a worldwide growth of 40% [4], the effect of increased penetration of PV in power systems has to be researched. The government has taken an important role in encouraging the use of PVs through grants, incentives and tax exemptions [5]. The advantage of PV power is: once installed it requires minimum maintenance and has a high lifetime [6]. PV effect, the process of conversion of solar energy into electrical energy was first discovered by Becquerel in 1839 [7]. Over the years, the PV effect has been observed among many materials including semiconductors. Photoelectric properties of p-n junction

have been studied from 1941 [8]. Today, almost all PV devices use p-n junction and are known as solar cells [7]. The PV technology was out of bounds of commercial use because of the costs involved. But there have been continued research in this area.

Power generated by PV modules and injected into the grid is gaining more and more visibility in the area of PV applications[4]. This is mainly because the global energy demand is steadily increasing. The PV module was in the past the major contributor to the cost of the overall system. Earlier, not many PV systems have been put in to the grid (Fig.1.2)[2], due to relatively high cost, compared to more traditional energy sources, such as oil, gas, nuclear, hydro, wind, etc. However, a downward tendency is now been seen in the price of the modules due to a massive increase in its production capacity which increased its share in DG system. The cost of the power converters is for the same reason becoming more visible in the total cost of PVDG system.

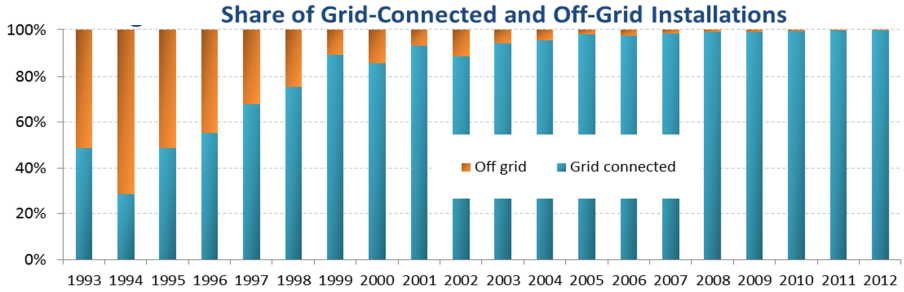

Fig.1.2:Percentage of PV Power by application as per IEA[2]

1.3 Literature Review

PVDG system has been a topic of interest for decades and large amount of work has been reported in the literature. The literature review has been classified into broad groups as follows:

1.3.1 Distributed Generation System

A general structure for distributed systems is illustrated in Fig.1.3. The electricity produced can be delivered to the local loads or to the utility grid, which depends on, where the generation system is connected. All the possible modes of power flow in the DG system are marked in the diagram. One of the important parts of the distributed system is its control. The control tasks can be divided into two major parts,

1. Input side controller, with the main property to extract the maximum power from the input source.

2. Grid side controller, which can have the following tasks:

(i) Control of active power generated to the grid.

(ii) Control of reactive power transfer between the PV module and the grid

(iii) Control of DC-link voltage

(iv) Ensure high quality of the injected power

(v) Grid synchronization

The items listed above for the grid-tie inverter are the basic features this inverter should have. Additionally, ancillary services like local voltage and frequency regulations, voltage harmonic compensation, or active filtering might be requested by the grid operator.

In distributed generation, electric power is produced in comparatively small quantities in areas distributed at various locations as opposed to centralized large scale generation[6]. Different definitions and names are used for distributed generation in different countries. Some define as generation ranging from a few kilowatts to 25 MW or 50 MW or 100 MW, while many other definitions are provided based on location, rating, power delivery area, technology, environmental impact, mode of operation etc.[7]. However, there is no consensus about the definition of DG system[8]. The types of DG system based on the sources of energy are discussed in details in[9], which include micro turbine, wind power, PV and fuel cells. The benefits of using DG system have been enumerated in[7, 9-11]. Parametric cost benefit analysis of various sources of energy used in DG system has been given in[8, 12].

The benefits of DG system are as follows[9, 10]:

1. Standby capacity: They are flexible in terms of their expandability, size and operation
2. Reliability and power quality: some industries might deem the reliability of the grid to be low and might want to have their own distributed generation to have reliable and good quality power.
3. Alternative to the expansion and use of local network: The cost related to the expansion of transmission or distribution can be avoided by using distributed generation.
4. Grid Support: DG may support the grid at times when there are contingencies in the grid. For example, there is a sudden shut down of a unit of the grid, which might result in a decrease in frequency. Distributed generation may be able to supply the demand for a period of time.
5. DG can be easily installed at any location in a very short period of time.
6. DG can decrease the price of power by supplying the grid and decreasing the power demand.
7. The need of types of fuels is diversified and the dependence on one particular fuel is reduced.
8. The DG can reduce the power losses by avoiding the transfer of power over long distances.
9. The use of renewable energy reduces the pollution level
10. They increase the lifetime of system equipment.
11. As they produce power locally, they can act as an emergency supply of power during system outages.

The study of PVDG system has been reported in literature extensively [13]. Research show that distributed generation having PV as a source is able to reduce the losses associated with transmission and is able to reduce the summer peak load demand[14]. PV connected lighting system; inverters and a combination of solar PV and solar thermal system have been discussed in[14]. The impact of distributed PV in rural areas have been discussed in[15] with the effect of PV in voltage regulation. A comparison is made with other methods of voltage regulation and a comparative study of economic viability of PV is made. In [16, 17], a hybrid distributed generation is studied consisting of PV and fuel cells. It discusses how PV and fuel cells jointly are able to improve the voltage quality of the system. A comparative study of distributed PV in rural and urban areas has been presented in[18]. It also discusses the possible drawback that the PV penetration might have on the power systems.

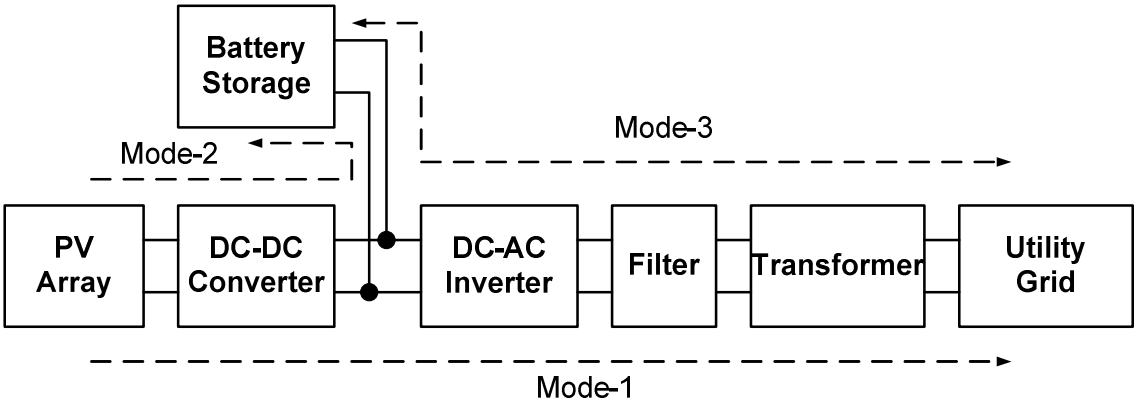

Fig. 1.3: General structure of distributed generation system

1.3.2 PV Sources: Characteristics, Advantages and disadvantages

PV cells, the smallest unit of the PV module are devices which convert energy in electromagnetic radiation in the form of light directly into electrical energy. When irradiated with light, a potential difference appears across its terminals. The current vs. volage characteristic of the PV cells is non-linear with a point on it is called maximum power point (MPP) at which maximum power is delivered by PV[19]. Commercially, PVs are available in the form of modules where a number of cells are connected in series. A number of modules are then connected to form a strings are and then connected in parallel to increase the current rating of the PV source to form an array. The array has an identical characteristic as that of module with a magnified voltage and current as explained in[20]. The PV may also operate in the reverse bias region when there is a partial shading in the array. In[21], the entire $I-V$ characteristics, both forward and reverse bias region have been discussed. The power-voltage characteristics of the PV array with a bypass diodes under partial shading are discussed in[17, 22], where it is shown that there might be multiple local maxima. In[23], the $I-V$ characteristics of the PV under changing irradiance and cell temperature have been

presented. The advantage of using PV power has been presented in[24], as it needs no fuel to produce power which saves billions of dollars of money needed to generate that energy and since it does not produce any greenhouse gas, it will reduce its emissions by 1.7 billion tons a year. It also mentions that the drawback of installing PV farms is that it needs huge ground area and that presently PV system is still too expensive to be economically viable.

1.3.3 PV Module Modelling and Control

To study the effect of PV module, both in stand-alone and grid connected system is very important. With the penetration of PV systems in the power systems as it becomes affordable, a mathematical model of PV are needed, which is able to replicate its VI characteristics under changing irradiance and temperature conditions. The control objectives of a PV source is to extract maximum power available from the PV at the given operating conditions which essentially turns out to be maximum power point tracking (MPPT). Extensive work has been reported in the literature about both modelling and MPPT of PV.

Single diode model of PV has been reported and its simulation methods have been presented in[25]. In[23], a mathematical detail in the determination of the five parameters of PV from datasheet information has been provided. Modellingthe effect of ripple voltage due to high frequency switching of converters associate with PV has been presented in [26]. A comparative study of single diode and double diode models is presented in[19]along with the presentation of analytical details of the estimation of parameters of double diode and single diode array models are presented in [20]. In[27], a procedure of simplifying the diode based models of the PV by piece wise linearization has been reported. Modelling of the PV based on artificial neural network has also been studied and has been presented in [28]. Different models for the study of partial shading of PV have been discussed in [22, 29, 30].

The most important control of PV has been MPPT. A detailed comparative study of MPPT is reported in[31] with pros and cons of perturb and observe (P&O),incremental conductance, ripple correlation control etc. have been presented. Artificial neural network has also been a very popular method for MPPT which is being adopted and presented in [32]. The traditional MPPT methods of P&O control has been proposed to be optimized in [33]. RCC control has been discussed in detail in[34, 35]. While in [36], sliding mode control based MPPT has been used. Novel techniques like biological swarm chasing has also been utilized for MPPT as given in[37]. The application of fuzzy control has also been reported in several papers including [38-40]. MPPT during partial shadow conditions is complicated since that gives rise to more than one local maximum. Various techniques under partial shadow conditions have been presented in [29, 41, 42].

1.3.4 Control of PVDG system

The study of PVDG system has been reported widely in literature. Research work in [43-47]describe the modelling of PV based DG system. In[46], modelling of grid connected PV system has been proposed and stability analysis is performed. It has been shown that the dynamic performance of the PVDG system is dominated by the MPP tracker. In[48], a MATLAB based model of a single phase low voltage PVDG system has been proposed. The model accuracy has been proposed. The model accuracy has been demonstrated by experimental results. Research work on operation and modelling of PV array inverter assembly in island mode has been presented in[47], which shows that the system is able to maintain the power quality in terms of voltage and frequency[49, 50]. In[43, 44], a three phase PV inverter has been investigated with the system is connected to the utility. A computer model has been proposed which is able to be used for the transient stability studies. In[5, 45], the economic effect and effect of small rooftop PVs on load frequency control has been researched and presented. The model has been presented with the meteorological data of Tokyo. In[51], a simulation package has been proposed which is able to optimize the size, economics, operation and performance of grid connected PV. Parameters like capacity credit cost and PV penetration can be determined from the package. Design and analysis of grid connected PV system has been presented in[52] where a DC-DC boost converter has been used to boost the low voltage level of the PV to make it suitable for connection to the grid. A full bridge bidirectional inverter is used to stabilize the DC voltage and to shape the output current. A steady state model of the system has been presented and verified experimentally. In[53, 54], an inverter topology has been proposed which is able to boost the low PV voltage to the level of the grid without using a boost converter. The inverter is able to boost the voltage, perform MPPT and produce good quality power with low total harmonic distortion (THD). The analytical, simulation and experimental results have been presented. In[55], a model of grid connected PV has been developed which is able to simulate the effect of passing clouds on the voltage profile of the distribution feeder and the effect it has on the voltage regulating system. In[52, 56], power factor correction of a PV system in parallel with the grid used to supply a DC load has been presented. Experimental results have been produced to verify the effectiveness of the proposed topology. In[57], a single phase grid connected PV system is shown to be able to be controlled to provide voltage support to the grid and to compensate for the harmonics distortion. The simulation result has been validated with experimental results.

1.3.5 Grid-tie PV Inverter

The power electronic interface for the PVDG systems has two main tasks [11, 13, 58-61]:

- To amplify and invert the generated DC power into a suitable AC current for the grid. A standard PV module generates approximately 100 W to 150 W at a voltage around 23 V to 38 V, whereas the grid mostly requires 110 V at 60 Hz or 230 V at 50 Hz.
- To control the PV module so as to track the MPP for maximizing the power extraction.

It is generally expected that the VSI performs the following functions in DGS [7], [17]–[19]: 1) Load voltage stabilization (±5% voltage regulation) in both parallel processing and stand-alone modes;

2) Uninterruptible power supply (UPS);

3) Reactive power support—grid power conditioning including power factor correction (>0.9) and harmonics mitigation (THD<5%) (Only in grid connected mode) as per IEEE standard 1159 [17];

4) Active power support—load power conditioning including demand side management (DSM). In this mode of operation, a bi-directional VSI is responsible for controlling the active power flow between the DC bus and the AC grid.

Fig.1.4 (a) shows centralized topology which interfaces a large number of modules to the grid [ref].The PV modules were divided into series connections (string), each generating a sufficiently high voltage to avoid further amplification. These series connected strings are then connected in parallel through string diodes, in order to reach high power levels. However, the major drawbacks of such topology are,

(i) High voltage DC cables are required between the PV modules and the inverter
(ii) Power losses due to centralized MPPT
(iii) Mismatch losses between the modules
(iv) Losses in the string diodes
(v) Risk of hotspots in the PV modules during partial shadow
(vi) Individual design for each installation

Fig.1.4 (b) shows a reduced version of the centralized inverter topology, where a single string of PV modules is connected to the inverter.Here the input voltage is high enough to avoid voltage amplification. In this topology, there are no losses associated with string diodes and a separate MPPT can be applied for each string and hence increases the overall efficiency when compared to the centralized inverter. However, the major drawback of such topology is that there is a voltage derating of the semiconductor.

Fig.1.4 (c) shows a multi-string inverter topology which is a further development of the string inverter, where several strings are interfaced with their own DC-DC converter to a common DC-AC inverter [62]. This is beneficial, compared to a centralized system, since every string

can be controlled in an individual manner. Thus the operator may start their own PV power plant with a few modules. Further enlargements are easily done because a new string can be plugged into the existing platform. A flexible design with high efficiency is hereby achieved.
The converter module in Fig.1.4 (d) is a reduction of the string inverter, where each PV module has its own integrated power electronics interface to the utility. The power loss of the system is reduced due to removing the mismatch between the modules, but the constant losses in the inverter may be the same as for the string inverter. Also the AC module concept supports optimal operation of each module which leads to an overall performance.

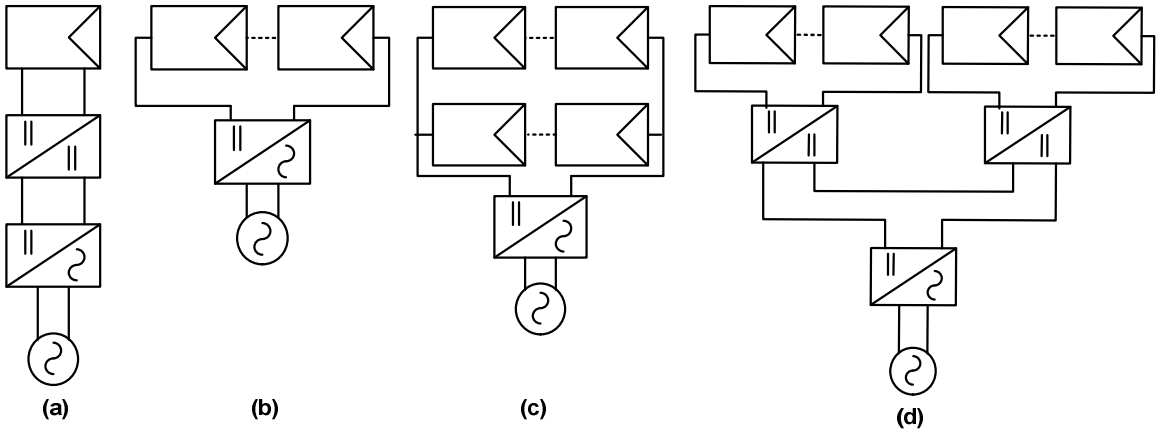

Fig.1.4:PVDG system topologies (a) Two-stage Centralized topology (b) Single-stage (c) Multi string topology (d) Latest AC module

1.3.6 Power Flow Control in DG System

In PVDG system, the PV inverter can further be classified as voltage controlled voltage source inverter (VCVSI) and current controlled voltage source inverter (CCVSI), depending on their control mechanism [63]. VCVSIs use the amplitude and phase of an inverter output voltage relative to the grid voltage to control the power flow[58, 64]. In VCVSIs, the desired current flow is generated by controlling the voltage across a decoupled inductor. The CCVSI uses switching instants to generate the desired current flow in the VSI's inductor, using instantaneous current feedback [58, 65, 66]. There are advantages and limitations associated with each control mechanism. For instance, VCVSIs provide voltage support to the load (the VSI operating as a voltage source), while CCVSIs provide current support (the VSI operating as a current source). The CCVSI is faster in response compared to the VCVSI, as its power flow is controlled by the switching instant, whereas in the VCVSI, the power flow is controlled by adjusting the voltage across the decoupled inductor. Active and reactive powers are controlled independently in the CCVSI, but are coupled in the VCVSI. A brief description on VCVSI and CCVSI is given individually in the following section,

1.3.6.1 Voltage-Controlled VSIs in DGS

- The decoupled inductor (X_L) is an essential part of any VCVSI as it makes the power flow control possible.
- In a VCVSI, the power flow of the DGS is controlled by adjusting the amplitude and the phase [power angle (δ)] of the inverter output voltage with respect to the grid voltage. Hence, it is important to consider the proper sizing of the decoupled inductor and the maximum power angle to provide the required power flow when designing VCVSIs.
- Assuming that the voltage of the inverter has to be kept constant ($V_{inv1} = V_{inv2} = V_{inv}$, load voltage stabilization), for any changes in the grid voltage to control the desired power flow, the power angle has to change in proportion. The power angle could be both lagging or leading, providing either the active power flow from the grid to the VCVSI or vice versa.
- The higher voltage source has to supply all the reactive power demanded by the decoupled inductor as well as the load. In weak grid applications, when the grid voltage drops considerably, the VCVSI has to supply both the rated active power and full reactive power, resulting in over sizing of the inverter (>100% of the rated power).
- Unity power factor operation depends on the size of the decoupled inductor, the load and maximum permissible power angle. Therefore, power factor correction is not possible using VCVSIs in DGS. This is one of the main drawbacks of VCVSI-based DGS.
- As addressed above, since the load voltage must remain constant (load voltage stabilization), the only controllable parameter in the VCVSI is the power angle (δ).
- In PVDG system, it is important to extract the maximum power from PV and supply this power to the load or grid. Assuming that both PV and the grid are supplying the demanded active power by the load, where P_L and P_{PV} are the load and PV active power, respectively. Equation (1.1) explains that as the available PV energy is increased, the power angle is reduced. This means that the PV penetration will increase.

$$\delta = \sin^{-1}\left[\frac{(P_L - P_{PV})X_m}{V_g V_{Inv}}\right] \qquad (1.1)$$

1.3.6.2 Current-Controlled VSIs in DGS

- As CCVSI controls the current flow using the VSI switching instants, it can be modelled as a current source and there is no need for a decoupling inductor.
- As the current generated from the CCVSI can be controlled independently from the AC voltage, the active and reactive power controls are decoupled. Hence, unity power factor operation is possible for the whole range of the load. This is one of the main advantages of CCVSIs.
- As the CCVSI connects in parallel to the DGS, it follows the grid voltage.
- The CCVSI cannot maintain the load voltage in the presence of a DGS without utilizing extra hardware and control mechanisms. This limitation on load voltage stabilization is one of the main drawbacks of CCVSI-based DGS.
- In PVDG system, it is desirable to supply the active power from the PV module, where excess energy from the PV module is injected into the grid. The remaining load reactive power will be supplied by the CCVSI.
- In the worst case, the CCVSI has to supply both the active and reactive powers demanded by the load. This means that the CCVSI sizing can be rated at full load without the need to oversize. This is an advantage of CCVSI-based DGS compared to the VCVSI.

1.4 Power quality requirement in PVDG system

The quality of the power provided by the PV system for the local load and for the power delivered to the grid is governed by practices and standards on voltage, frequency, harmonics and power factor[67, 68]. Deviation from these standards represents out-of-bounds conditions and may require disconnection of the PV system from the grid. A detail description on these issues is given separately in the following sections.

1.5 Harmonic Distortion

Harmonic distortion is caused by the operation of non-linear loads in the power system. Nonlinear loads change the sinusoidal nature of the ac power current, thereby resulting in the flow of harmonic currents in the ac power system that can cause interference with communication circuits and other types of electrical and electronic equipment[69-71]. The prime sources of harmonics in the power system are given in Table 1.1. Harmonics are basically the additional frequency components present in the mains voltage or current which are integral multiples of the mains (fundamental) frequency [54]. Interharmonics are a special category of harmonics which are non-integer multiples of the fundamental frequency. Sub-harmonics are a special category of interharmonics, which have frequency values less than the fundamental frequency. Most equipment only produces odd harmonics but some devices have a fluctuating power consumption, over a duration of half cycle period or less, which may

generate even, inter-harmonic, or sub-harmonics currents [54]. The harmonic distortion of each device depends on its consumption of active power, background voltage distortion and source impedance.Phase controlled rectifiers are major source for harmonics and reactive power burden. They have a wide range of applications, from small rectifiers to large High Voltage Direct Current (HVDC) transmission systems. They are used for electro-chemical process, motor drives, traction equipment, controlled power supplies, and many other applications.

Table 1.1:Prime sources of harmonics.

Sources of harmonics			
High-voltage converters	Low-voltage power electronic devices	Conventional sources	Modern electronic equipment
Adjustable speed drives	Uncontrolled rectifiers	Electrical machines	Personal computers
HVDC converters	Controlled rectifiers	Transformers	Printers
Traction	AC regulators	Inductors	Photocopiers
Arc furnaces	Inverters		Air conditioners
SVCs	Cycloconverters		Televisions
			UPS
			Microwave ovens
			Fluorescent lamps

1.5.1 Effects of Harmonics

Harmonics can lead to mal-operation of power system components. Some of the ways that harmonics may affect the equipment negatively are listed below [69, 70, 72]:

1. Communication interference: Magnetic (or electrostatic) coupling between electrical power circuits and communication circuits can cause communication interference [72]. Current flowing in the power circuit produces a magnetic (or electrostatic) field which, in turn, induces a current (or voltage) in the nearby conductors of the communication circuit. The amount of interference depends upon the magnitude of the induced current (or voltage), frequency, and the magnetic (or electrostatic) coupling. Other types of communication interference are:
    - Induced line noise
    - Interference with power line carrier systems
    - Relay malfunctions.
2. Heating: Harmonic currents can cause excessive losses in motors, capacitors and transformers connected to the system. This in turn, may cause excessive heat in the winding, thus leading to the failure of insulation and danger of a fire hazard [69].

3. Malfunction of solid-state devices: Harmonics can cause solid-state devices to malfunction if the equipment is sensitive to zero crossings or operates in response to the peak values of utility voltage. The typical malfunctions are [69, 70, 73]:
    - Errors in measurement equipment
    - Nuisance tripping of relays and breakers
    - Unstable operation of zero-voltage crossing firing circuit
    - Interference with motor controllers.
4. Damage to capacitors: The presence of capacitors, such as those used for power factor correction, can result in local system resonances, which, in turn, can lead to excessive currents and possible subsequent damage to the capacitors [70].
5. Malfunction of utility Meters: May record measurements incorrectly, result in higher billings to consumers [71].
6. Failure of sophisticated electronic equipment: Failure of sophisticated electronic equipment such as computers, remote monitoring systems, air conditioning systems and premature failure of switched-mode power supplies (SMPS) and uninterrupted power supplies (UPSs) [70].
7. Flickering of lights: Due to the operation of arcing devices such as arc furnaces, arc welders, and discharge type lightning with magnetic ballasts, flickering of lights may take place [70].

1.5.2 Harmonic Standards

There are various organizations on the national and international levels working closely with engineers, equipment manufactures, and research organizations to come up with standards governing guide lines, recommended practices, and harmonic limits [69]. The primary objective of the standards is to provide a common ground for all involved parties to work together to ensure compatibility between the end-user equipment and the system equipment. The most commonly used harmonic standards for PVDG systems are IEEE 1547[68] and International electro technical Commission standard IEC 61727[67][65][65][65][70]. This international standard limits the amount of current harmonics injected by a DG system at the Point of Common Coupling (PCC). For example, the IEEE 1547 and IEC 61727 standard recommends a limit of 5% Total Harmonic Distortion (THD) in the current at the PCC. The THD in the current is the ratio of the rms value of its distortion components to the rms value of its fundamental-frequency component. It is given as,

$$\%THD = \frac{\sqrt{\left(\sum_{h=2}^{\infty} I_h^2\right)}}{I_1} \times 100\% \tag{1.2}$$

Where, I_h = rms value of the current at harmonic order *h*, and I_1 = rms value of the fundamental-frequency current component.

As per these standards, the restrictions on different current harmonic components are given one by one in the following sections.

1.5.3 DC current Injection

A DC current injection in the utility can saturate the distribution transformers, leading to overheating and trips. For the conventional PV systems with galvanic isolation, this problem is minimized, but with the new generation of transformer less PV inverters increased attention is required in this matter. The limit of injected DC current as per IEEE 1547[68] and IEC 61727[67] is given in Table 1.2.

Table 1.2: DC current injection limitation

IEEE 1547	IEC 61727
$I_{dc} < 0.5\%$ of the rated RMS current	$I_{dc} < 1\%$ of the rated RMS current

1.5.4 Current Harmonics

The PV system output should have low current distortion levels to ensure that no adverse effects are caused to other equipment connected to the utility system. The levels given in Table 1.3 are accepted.

Table 1.3: Maximum current harmonics

IEEE 1547 and IEC 61727						
Individual harmonic order (odd) (%)	h<11	11<h<17	17<h<23	23<h<35	35<h	Total THD (%)
	4	2	1.5	0.6	0.3	5

1.6 Average Power Factor and Reactive Power Burden

Only in IEC 61727[67], it is stated that the PV inverter shall have an average lagging power factor greater than 0.9 when the output is greater than 50%. Reactive power burden on distribution systems is due to the operation of loads that draw high reactive power from the system[74]. Reactive power is a concept used by engineers to describe the background energy movement in an ac system arising from the production of electric and magnetic fields [75]. These fields store energy which exchanges through each ac cycle. Devices which store energy by virtue of a magnetic field produced by a flow of current are said to absorb reactive power; while those which store energy by virtue of electric fields are said to generate reactive power. Volt-ampere reactive (var) is a unit used to measure reactive power in an ac electric power system [75].

Reactive power (vars) is required to maintain the voltage to deliver active power (watts) to the utility grid. Motor loads and other loads require reactive power for their successful operation. When enough reactive power is not available, the voltage sags and it is not possible to push the real power demanded by the loads through the lines [75-78].

For better understating, a simple power system model indicating the coupling between source and load is shown in Fig.1.5.

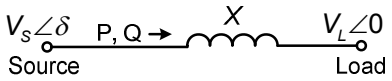

Fig.1.5: A small power system model.

In general the flow of active and reactive powers in a power system is governed by the following equations [75, 76].

The transmitted active power (P) is given by,

$$P = \frac{V_S V_L}{X} \sin\delta \tag{1.3}$$

For small value of δ, the reactive power (Q) transferred to the load is given as,

$$Q = \frac{V_L\left(V_S - V_L\right)}{X} \tag{1.4}$$

The load voltage (V_L) is given by,

$$V_L = V_S - \frac{QX}{V_S} \tag{1.5}$$

Equation (1.2) shows that the active power flow depends on the amplitudes of source voltage and load voltage and it flows from the leading voltage bus to lagging voltage bus. On the other hand, the reactive power depends mainly on the difference of voltage amplitudes across a feeder and it flows from higher voltage side to lower voltage side as given by equation(1.4). It can be observed from an equation (1.5) that to keep the V_L fixed for a given value of V_S, the drop $\left(\frac{QX}{V_S}\right)$ must remain constant. In this expression the only variable quantity is Q, which must be locally adjusted to keep V_L fixed. In other words, let Q be the value of reactive power which keeps V_L to a specified value, and any deviation in Q at load end must be locally adjusted. If Q is made zero (i.e. the load reactive power is supplied locally), the source and load voltages will be the same. The local generation of reactive power can be accomplished by any of the reactive power compensating devices. This is the fundamental mechanism for controlling the reactive power in electric power system [75, 76].

1.6.1 Sources of Reactive Power

The major sources that draw reactive power from distribution systems are [73, 75, 79, 80]:

1. Phase-controlled rectifiers
2. Motors
3. Transformers, tap-changing transformers
4. Choke inductors.

1.6.2 Problems due to High Reactive Power

The highly reactive power burden leads to the underutilization power system capacity due to [73, 75, 76]:

- Increased losses in the transmission and distribution systems.
- Overrated equipment within the AC system: due to large current drawn for a given real power demand, and low efficiency owing to more losses.
- Low power factor and poor voltage regulation.

1.7 Solutions to Power Quality Problem in PVDG System

The low quality power affects electricity customers in many ways. The lack of quality power can cause loss of production, damage of equipment or appliances or can even be detrimental to human health. Therefore, it is very important to maintain a high standard of power quality. Utilities and researchers all over the world have for decades worked on the improvement of what is now known as power quality[81]. There are sets of conventional solutions to the power quality problems, which have existed for a long time. However, these conventional solutions use passive elements and do not always respond correctly as the nature of the power system conditions change. The increased power capabilities, ease of control, and reduced costs of modern semiconductor devices have made power electronic converters affordable in a large number of applications. New flexible solutions to many power quality problems have become possible [82]with the aid of these power electronic converters.

1.7.1 Harmonic Compensation

To deal with harmonics, there are three basic choices: (a) to reinforce the distribution system to withstand the harmonics by derating the transformers and oversizing the conductors[83], (b) to incorporate current waveshaping circuits within the equipment so that they draw sinusoidal currents[84, 85], and (c) to install devices to attenuate or remove the harmonics[86-89].

The first two choices are not cost-effective solutions and the only option is to incorporate filters to remove the harmonics[87]. For reducing the harmonics, passive and/or active filters are used[90, 91]. These filters are either used separately or used in a combined fashion to form a hybrid filter[86-89].

1.7.1.1 Passive Power Filters

Passive filters can be connected either in parallel with the load (shunt passive filter) or in series with load (series passive filter). Shunt passive filters have traditionally been used to absorb current harmonics in power systems [92]. Shunt passive filters provide low-impedance paths to divert harmonics to ground and discourage the flow of harmonics into the power system. There are several types of shunt passive filters: single-tuned, double-tuned, automatically tuned, damped, and band-pass filters [69, 92]. Among these shunt

passive filter topologies, single-tuned, double-tuned and high-pass damped filtersare most commonly used. The tuned filters are designed to exhibit low impedance at one or more harmonic frequencies, while the high-pass damped filters provide low impedance for a wide spectrum of harmonics. The single-phase circuits of single-tuned, double-tuned and second order high-pass damped shunt passive filters are depicted in Fig.1.6.

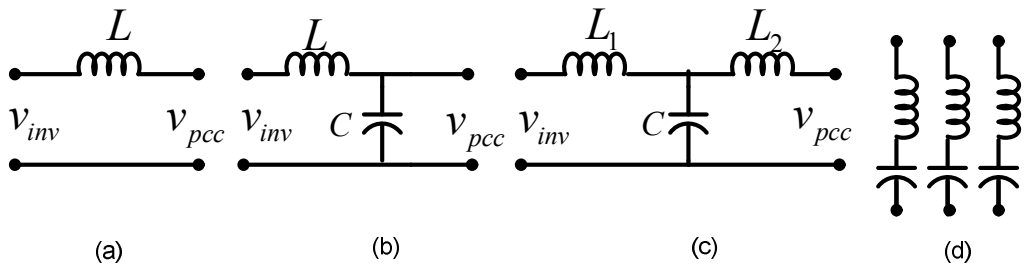

Fig.1.6:Shunt passive filters:(a) Single-tuned; (b)Double-tuned; (c) Second-order high-pass damped.

Passive filtershave hitherto been used in powersystem because of their advantages which are [92]:

1. Simple implementation, high efficiency and almost maintenance-free operation.
2. A single installation can serve many purposes, i.e., reactive power compensation, voltage support on critical buses, and reducing the impact and voltage drop due to the starting of a large motor [92].
3. Implementation at medium power level is possible.

However, passive filters have many problems to discourage their applications and are given below [92, 93]:

1. Passive filters are not suitable for changing system conditions. Once installed, neither the tuned frequency nor the size of the filter can be changed so easily.
2. The filters can either be switched “on” or “off.” Thus, a stepless control of reactive power with enhancement or reduction of load demand is not possible.
3. The source impedance, which is not accurately known and varies with the system configuration, strongly influences the filtering characteristics.
4. The change in the system operating conditions, addition of new compensating devices, aging, deterioration, and temperature effects may increase the designed tolerances thereby causing detuning of the filter.
5. The parallel resonance between the system and the filter may cause an amplification of the current at characteristic and non characteristic harmonics.
6. Single-tuned or double-tuned filters are not possible to employ for certain loads like cycloconverters or when the power system has interharmonics.
7. The Outage of a parallel branch can totally alter the resonant frequency, resulting in overstressing of the filter components and increased harmonic distortion.

The design complexity and high cost of losses of the conventional passive filters, as well as their restricted capability to eliminate inter-harmonics and non-characteristic harmonics have encouraged the development of harmonic compensation technique by means of power electronic devices, commonly referred to as active power filters (APF) [86-89, 94-97].

1.7.1.2 Harmonic Compensation using PI Controller

Since PI controllers typically are associated with dq control structure, the possibilities for harmonic compensation are based on low-pass and high-pass filters [ref].If the current controller has to immune to the grid voltage harmonic distortion(mainly fifth and seventh in three phase systems), harmonic compensator for each harmonic order should be designed.Fig.shows the dq control structure having a harmonic compensator for the +ve sequence of the 5^{th} harmonic. In addition, under unbalanced conditions, harmonic compensators for both +ve and –ve sequences of each harmonic order necessary. As a consequence, four compensator like are necessary to compensate for the 5^{th} and 7^{th} harmonics. The complexity of the control algorithm is noticeable in this case.

1.7.1.3 Harmonic Compensation using PR Controller

In this case harmonic compensation can be achieved by cascading several generalized integrators tuned to resonate at the desired frequency. In this way, selective harmonic compensation at different frequencies is obtained. In this case, it is easy to extend the capabilities of the scheme by adding harmonic compensation features simply with more resonant controllers in parallel to the main controller as shown in Fig.1.7. The main advantage in this situation is given by the fact the harmonic compensator works on both positive and negative sequences of the selected harmonic; thus only one HC is necessary for a harmonic order. An interesting feature of the HC is that it does not affect the dynamic of the PR controller, as it only reacts to the frequencies very close to the resonance frequency. This characteristic makes the PR controller a successful solution in applications where high dynamics and harmonic compensation, especially low-order harmonics are required, as in the case of a PVDG system.

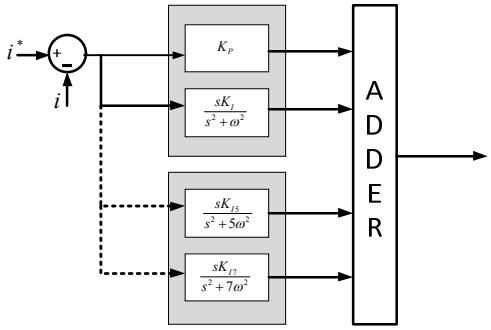

Fig.1.7: Structure of the harmonic compensator attached to the resonant controller of the fundamental current

1.7.1.4 Harmonic Compensation using non-linear Controller

Since both hysteresis and dead-beat controller have fast dynamics, there is no concern about the low-order harmonics when the implemented control structure uses such controllers. In any case, it should be noticed that the current waveform will contain harmonics at switching and sampling frequency order. Another issue is the necessity of fast sampling capabilities of the hardware used.

1.7.1.5 Active Power Filters

In the last two decades, considerable progress has been made in active power filters (APFs). Similar to the STATCOM, APFs are inverter circuits, comprising of active devices, i.e. semiconductor switches that can be controlled such that the APF can be made to act as harmonic current or voltage generators[98]. Different topologies of APFs have been proposed, including shunt, series, and the combination of these two [86-88, 95, 96, 99]. However, only the shunt APFs are considered in the present work.

The shunt active power filter acts as a current source and compensates load current harmonics by injecting equal-but opposite harmonic compensating current at the PCC[100] .Fig.1.8shows the connection of a shunt active power filter[86, 96].

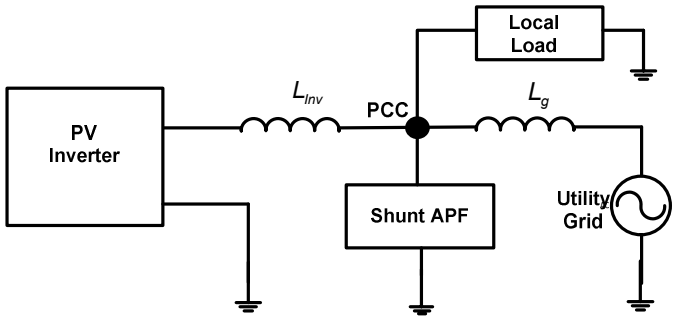

Fig.1.8: A voltage source inverter based shunt active power filter.

The main advantages of APFs are [86-88, 95, 96]:

1. APFs are superior to passive filters in terms of filtering characteristics.
2. A single installation can serve many purposes, i.e. reactive power compensation, flicker mitigation, and imbalance compensation.
3. They are compact in size.
4. Non-susceptibility to resonance problem.
5. Step-less control characteristic

However, high initial cost of active power filters has discouraged their applications in high power systems. To overcome this, the hybrid power filters have been proposed [86, 88, 96, 99] and installed in recent years.

1.8 Scope of Work and Author's Contribution

Although the term "power quality" encompasses all disturbances encountered in a power system, it has been found that reactive power burden and harmonic currents are the most dominant types of power quality problems in modern distribution systems. This thesis exploits this fact in case of PVDG system and evaluating the solutions for improving the power quality of the PVDG system. In this thesis, an attempt has been made for improving power quality in the single phase PVDG system.The main contributions of the author can be summarized as follows:

1. To begin with, a literature survey of different topologies of inverter in PVDGsystem is studied.

2. In order to analyze the power converters for PVDG systems, it is essential to model the PV module attached to the converter. PV module presents a nonlinear current vs. voltage characteristic with several prerequisite parameters to be adjusted according to experimental data obtained from the datasheet of a practical device. For the dynamic analysis of the converters, and maximum power point tracking (MPPT) algorithms, mathematical modelling of the PV module is useful. The first part of this research work presents the modelling and simulation of PV module. However, the major challenges in modelling a PV module is that, all the parameters which are required for the modelling purpose is not available on the manufacturer's datasheet. Here the determination of parameters of the PV module is performed by using Gauss Seidel iteration Method and the modelling is carried out with the adjustment of the parameters with irradiance and temperature. The same model is extended for arrays and is used for the simulation of PVDG system.

3. The main goal of this research work is to formulate and implement the 1-ϕ IRP theory in the PVDG system for the enhancement of power quality to obtain the following objectives,

(i) To transmit the maximum possible real power from the PV module by using the MPPT controller

(ii) To meet the real power demanded by the local load

(iii) To compensate the reactive and harmonic components of load current at PCC

(iv) To utilize the PV inverter as a shunt APF during night time.

Thus, with an adequate control of PV inverter, all the above-mentioned objectives have been achieved either separately or simultaneously. Hence, in this research work the power quality requirements as per the utility standards at the PCC are accomplished without requiring any additional hardware circuits.

4. For the further improvement of power quality and also to increase the efficiency of the two-stage PVDG system a multilevel inverter topology is introduced in place of the two-level inverter. In recent years multilevel inverter topologies have become more attractive for researchers as they offer improved output waveform as compared to the conventional two level inverter. With the improvement in the output waveform, the harmonic content and hence the size of the filter can be reduced. The three basic topologies of multilevel inverter (MLI) are: diode clamped MLI, flying-capacitor MLIs and cascaded H-bridge MLI (CHBMLI). Among all these available MLI topologies, the CHBMLI requires separate DC sources and hence constitutes a promising alternative, providing a modular design that can be extended to allow a transformer less operation in grid connected PV system.

5. The power flow control in such type of PVDG system requires two control loops. The inner current control loop is used to modulate the output current of the PV CHBMLI to meet magnitude and phases of waveform whereas the outer voltage control loop regulates the output power of the PV inverter according to the MPP of PV modules. These two control loops are realized by two stages of power conversion. One is a DC to DC converter with MPPT control and the other is a DC to AC inverter. But two stage operation may lead to more power loss than that of a single-stage conversion. In a single stage PVDG system, both the control loops are realized simultaneously in one power conversion stage, thus simplifying the system topology and hence increases the overall efficiency of the system.

6. There is always a chance of unbalancing in the input DC-link voltages of CHBMLI when fed from PV module. This is due to the non-ideal conditions in PV modules. The most common non-ideal conditions of a PV module include partial shading, dust collection and PV ageing. Hence the balance of the DC voltages is one of the important issues in the control of CHBMLI when used in PV application. If this voltage balance is not perfectly accomplished, the modulation methods create errors in the modulated output voltage. This leads to the distortion in the output voltages and currents of the CHBMLI. To overcome the unbalance in DC-link voltage of CHBMLI during isolated grid operation a single phase SVM for the modulation of the inverter is proposed and implemented in this thesis.

7. In order to verify the simulation studies of the proposed schemes, a downscaled two-level PV inverter and five-level CHBMLI based PVDG system rated at 100 V, 1000 VA has been designed, developed, and tested to verify the viability and effectiveness of the enhanced power quality based PVDG system, 230 V, 15-kVA 1P2W PVDG system. By using real-time workshop (RTW) of MATLAB and real-time interface (RTI) feature of dSPACE, the real-time simulation of the SIMULINK models of the controllers of the PVDG system has been implemented. MOSFET has

been selected as the switching device. The experimental results have been found to be in good agreement with the simulation results.

1.9 Organization of the Thesis

Apart from this chapter, the thesis contains five more chapters and the works included in each chapter are briefly outlined as follows:

CHAPTER 2 starts with a brief introduction of the behaviour and functioning of a PV module. It also presents a numerical method for the estimation of PV module parameters which are not available at the manufacturer's datasheet. Finally, by using the available datasheet parameters and the estimated parameters, a PV panel is modelled in MATLAB Simulink software, to predict the panel behaviour in different temperature and` irradiance conditions. This chapter also includes the modelling of DC-DC boost converter for MPPT control.

CHAPTER 3 presents a single-phase two-stage two-level enhanced power quality based PV distributed generation system.The controller for the proposed power quality enhancement scheme is discussed in detail. Simulation results are provided to verify the steady-state and dynamic performance of the compensators under varying load and varying atmospheric conditions.

A proposed 1-ϕ CHBMLI based two-stage and single stage PVDG system with an improved power quality features is presented in chapter.4. Exhaustive simulation results are presented to investigate the performance of adopted CHBMLI based PVDG system during varying atmospheric, varying load and also with different modes of controller conditions. The system has also validated for night mode operation. This chapter further made a comparative analysis of 1-ϕ single stage CHBMLI based PVDG system with two-stage two-level and CHBMLI based topology.

The detailed discussions for the experimental setups have been given in CHAPTER 5. This includes the discussion on the power circuit, dSPACE based controllers, the measuring system and the generation of gating signals for the inverter. The chapter concludes with experimental results and the corresponding discussion.

The main conclusions of the presented work and possible future research have been summarized in this CHAPTER 6.

At the end of the thesis, the list of references are provided.

Chapter 2: PHOTOVOLTAIC MODULE WITH MPPT CONTROL

[This chapter describes the modelling and parameter determination of photovoltaic module. Single-diode model of PV cell is used for modelling of Photovoltaic module. Modelling of PV module is followed by the design procedure of an efficient MPPT controller. A boost type converter is used for this purpose. To improve the dynamic performance of the whole system a transfer function for an input controlled boost converter is developed]

2.1 Introduction

A PV system directly converts sunlight into electricity. The elementary device of a PV system is the PV cell. Cells are assembled to form modules or arrays. The voltage and current available at the terminals of a PV module may directly feed small loads such as lighting systems or DC motors. However, high power applications require power electronic converters to process PV module power for getting a suitable voltage and power levels. During grid-connected operation, these converters are used to synthesize voltage and current waveforms to regulate the flow of power as well as maximum power extraction. In order to analyze the power converters for PV systems, it is essential to model the PV module attached to the converter. PV module presents a nonlinear current vs. voltage characteristic with several parameters to be adjusted according to experimental data obtained from the datasheet of a PV module. For the dynamic analysis of the converters, and maximum power point tracking (MPPT) algorithms, mathematical modelling of the PV module is useful. The main aim of this chapter is to present a brief introduction of the behaviour of PV module and determination of unknown parameters of a PV module while using a manufacturer's datasheet parameter. This is followed by the modelling and simulation of PV module. In order to obtain large output voltages from the PV panel, cells are generally connected in series. Panels with large output currents are realized by increasing the cell's surface area or by connecting cells in parallel. A PV array may be either a panel or a set of panels connected in series or parallel to form large PV systems.

For maximum power point tracking DC-DC converter is used. This converter uses an algorithm to continuously extract maximum power from the PV array. Here, an improved fuzzy logic based MPPT controller is presented. The drawbacks of the conventional MPPT method are also investigated. The proposed fuzzy logic controller is capable of exploiting the advantages of the P&O method. In the second part of this chapter a design procedure for MPPT control along with input controlled DC-DC boost converter is presented.

2.2 Working Principle of PV cell

A PV cell is basically a semiconductor diode whose p–n junction is exposed to light [1], [2]. Commercially available PV cells are generally monocrystalline and polycrystalline silicon cells. A thin layer of bulk Si or a thin Si film constitutes silicon PV cells, which are connected

to electric terminals. One side of the Si layer is doped to form the p–n junction. A thin metallic grid is positioned in the Sun-facing surface of the semiconductor. Fig.2.1 gives the physical structure of a PV cell. The incident solar radiations produce charge carriers, which generate an electric current if the cell is short-circuited [2]. Charges are generated when the energy of the incident photon is adequate to detach the covalent electrons of the semiconductor; this phenomenon depends on the semiconductor material and on the wavelength of the incident light[101]. Basically, the PV phenomenon may be defined as the absorption of incident solar radiation, generation and transport of free carriers at the p–n junction, and collection of these electric charges at the terminals of the PV device [3], [4]. The rate of generations of charges depends on incident light as well as absorption capacity of semiconductor materials. The absorption capacity of semiconductor material in turn depends on the reflectance of the cell surface, band gap, intrinsic concentration of carriers, recombination rate, electronic mobility and temperature.

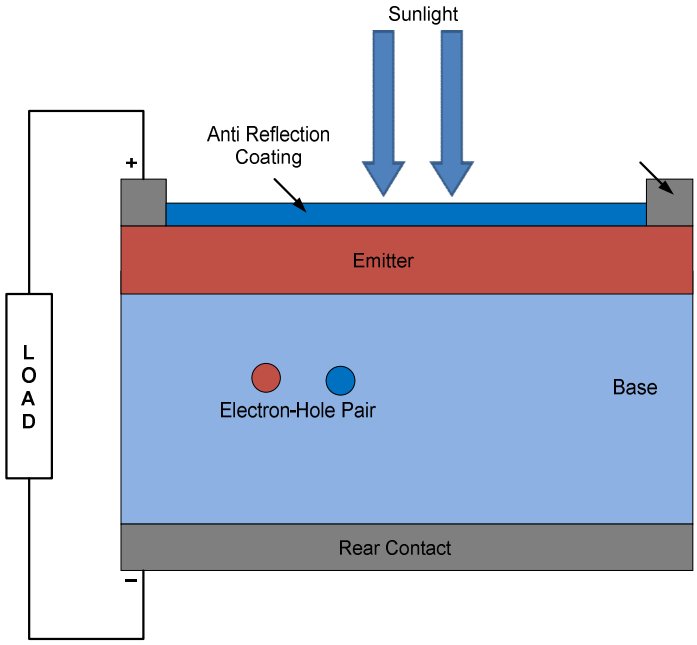

Fig.2.1: Physical Structure of a PV Cell

Solar radiation is composed of photons of different energies. Photons with energies lower than the band gap of the PV cell are unable to generate voltage or electric current. Photons with energy superior to the band gap generate electricity, but only the energy corresponding to the band gap is used. Semiconductors with lower band gaps may take advantage of a larger radiation spectrum, but the generated voltages are lower [5]. Even though Si is not the best semiconductor material for PV cells in terms of energy conversion, its fabrication process is more economical[102]. Other materials can achieve better conversion efficiency, but at much higher cost. For the purpose of evaluating power converters for PV systems, the electrical characteristics of the PV device (cell, panel, and array) are sufficient. The manufacturers of PV devices always provide a set of empirical data that may be used to

obtain the mathematical equation of the device's Current vs. Voltage $(I-V)$ characteristic. Some manufacturers also provide $I-V$ curves obtained experimentally for different operating conditions. The mathematical model is developed from manufacturer data sheet and validated with experimental curves, which is discussed in the following sections.

2.3 Modelling of PV Module

The equivalent circuit of a PV cell is shown in Fig.2.2. From semiconductor theory [13], the basic equation that mathematically describes the $I-V$ characteristic of an ideal PV cell is given by,

$$I = I_{PV,cell} - I_d \tag{2.1}$$

With $I_d = I_{0,Cell}\left[\exp\left(\frac{qV}{AkT}\right)-1\right]$

Where $I_{PV,Cell}$ is the current generated by the incident solar radiation

I_d : Shockley diode equation

$I_{0,cell}$: reverse saturation or leakage current of the diode

q : electron charge (1.60217646 × 10^{-19} C)

k : Boltzmann constant (1.3806503 × 10^{-23} J/ K)

T : Temperature of the p–n junction (in Kelvin)

A : diode ideality constant

However, the basic equation (2.1) of the fundamental PV cell does not represent the $I-V$ characteristic of a practical PV module. Fig.2.3 shows the $I-V$ curve obtained from the equation(2.1). Practical PV modules are composed of several connected PV cells and the derivation of terminal characteristics of the PV module requires the inclusion of additional parameters to the basic equation [13], which can be expressed as,

$$I = I_{PV} - I_0\left[\exp\left(\frac{V+R_SI}{V_T}\right)-1\right]-\frac{V+R_SI}{R_{Sh}} \tag{2.2}$$

Where $I_{PV} = I_{PV,Cell}N_P$: Photovoltaic (PV) current of the module

$I_0 = I_{0,Cell}N_P$: Saturation current of the module

N_p = Number of cells connected in parallel

$V_T = \frac{N_s kTA}{q}$: Thermal voltage of the module with N_S number of cells are connected in series

R_S : Equivalent series resistance of PV module, which is the sum of several structural resistances of the device

R_{Sh} : Equivalent shunt resistance of PV module which exist mainly due to the leakage current of the p-n junction and depends on the fabrication process

Cells connected in parallel increase the current and cells connected in series produce greater output voltages.

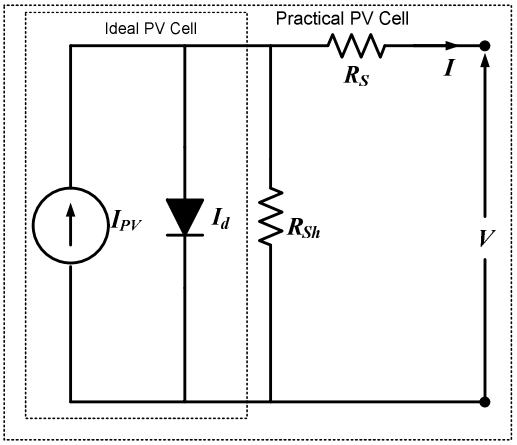

Fig.2.2: Equivalent circuit of an ideal and practical PV Cell

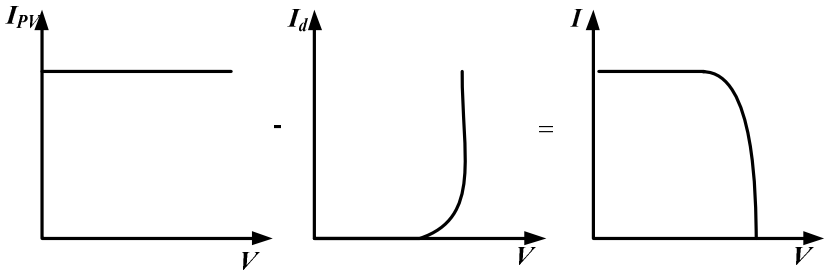

Fig.2.3: $I-V$ curve of the PV cell

[*The net cell current* I *is composed of the light-generated current* I_{PV} *and the diode current* I_d]

Equation(2.2), leads to a $I-V$ curve which is shown in Fig.2.4, where three significant operating points are highlighted as: short circuit point $\left(0, I_{SC}\right)$, maximum power point $\left(V_{MPP}, I_{MPP}\right)$ and open circuit point $\left(V_{OC}, 0\right)$. Equation (2.2) describes the single-diode model presented in Fig.2.2. Some authors have proposed more sophisticated models that present better accuracy. For example, in [14] –[18] an extra diode is used to represent the effect of the recombination of carriers. A three-diode model is proposed in [19] to include the influence of partial shadow effects that are not considered by the previous models. For simplicity, the single diode model of Fig.2.2 is used in this work. This model offers a good compromise between simplicity and accuracy [20]. This chapter presents a simplified approach for the

determination of the parameters of the single-diode model which are given in following subsection.

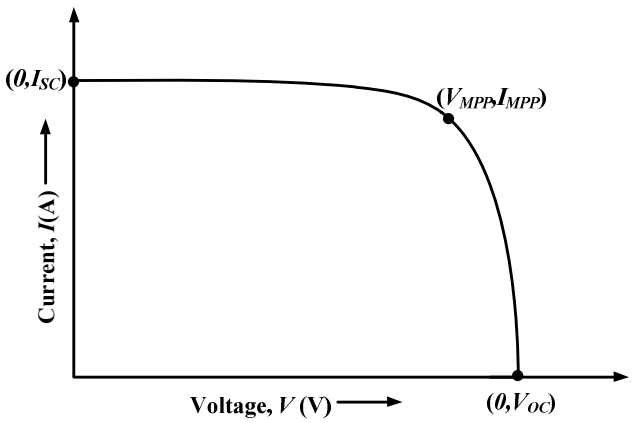

Fig.2.4: $I-V$ Characteristics of PV module

2.3.1 Parameter Determination from Datasheet Values

PV module datasheet generally carries the following information:

1. Nominal open-circuit voltage (V_{OC})
2. Nominal short-circuit current (I_{SC})
3. Voltage at the MPP (V_{MPP})
4. Current at the MPP (I_{MPP})
5. Open-circuit voltage/temperature coefficient (K_V)
6. Short circuit current/temperature coefficient (K_I)
7. Maximum output power (P_{MPP})

These quantities are at nominal condition or standard test conditions (STCs) of temperature (25 ^{0}C) and solar irradiation (1000 W/m^2). However, the following parameters required for the modelling of PV module are not available in the manufacturer's data sheet

1. Light-generated or PV current (I_{PV})
2. Series resistance (R_S)
3. Shunt resistance (R_{Sh})
4. Thermal voltage (V_T)
5. Diodes reverse saturation current (I_0)

From the expression of thermal voltage (V_T), it can be observed that except diode ideality constant (A) all the other quantities are constant. Therefore, in the parameter determination

process, we have to calculate diode ideality constant to determine the thermal voltage of PV module.

In this work, these unknown parameters are found out without physical measurement, using only data-sheet values and a step by step procedure is given below.

Neglecting the term of -1 in the equation(2.2) because the exponential term is much greater than 1, equation(2.2), can be re-written as,

$$I = I_{PV} - I_0\left[\exp\left(\frac{V + IR_S}{N_s V_T}\right)\right] - \frac{V + IR_S}{R_{Sh}} \tag{2.3}$$

Substituting three significant-points of the $I-V$ characteristic into the equation (2.3) we get.

At short circuit point $(0, I_{SC})$,

$$I_{SC} = I_{PV} - I_0\left[\exp\left(\frac{I_{SC}R_S}{N_s V_T}\right)\right] - \frac{0 + I_{SC}R_S}{R_{Sh}} \tag{2.4}$$

At maximum power point $(V_{MPP,}\ I_{MPP})$,

$$I_{MPP} = I_{PV} - I_0\left[\exp\left(\frac{V_{MPP} + I_{MPP}R_S}{N_s V_T}\right)\right] - \frac{V_{MPP} + I_{MPP}R_S}{R_{Sh}} \tag{2.5}$$

At open circuit point $\left(V_{OC}, 0\right)$

$$0 = I_{PV} - I_0\left[\exp\left(\frac{V_{OC}}{N_s V_T}\right)\right] - \frac{V_{OC}}{R_{Sh}} \tag{2.6}$$

An additional equation can be derived using the fact that the derivative of power with respect to voltage (on $P-V$ curve) is zero at the MPP. Thus,

$$\left.\frac{dP}{dV}\right|_{MPP} = 0 \tag{2.7}$$

So far we have four equations, but five unknown parameters, therefore another equation has to be found out. For this, the derivative of the current w.r.t voltage at short-circuit condition is carried out, which is determined by the shunt resistance R_{Sh} [2],

$$\left.\frac{dI}{dV}\right|_{I=I_{SC}} = -\frac{1}{R_{Sh}} \tag{2.8}$$

From the expression of the current at open circuit and short-circuit conditions, the photo-generated current I_{PV} and the dark saturation current I_0 can be expressed as:

From equation (2.6), $I_{PV} = I_0 \exp\left(\frac{V_{oc}}{N_s V_T}\right) + \frac{V_{OC}}{R_{Sh}}$ (2.9)

Substituting equation (2.9) in (2.4),

$$I_{SC} = I_0\left[\exp\left(\frac{V_{OC} - I_{SC}R_S}{N_s V_T}\right)\right] + \frac{V_{OC} - I_{SC}R_S}{R_{Sh}}$$

As $V_{OC} >> I_{SC}R_S$, $I_{SC}R_S$ can be neglected and the above equation written as,

$$I_{SC} = I_0\left[\exp\left(\frac{V_{OC}}{N_sV_T}\right)\right] + \frac{V_{OC} - I_{SC}R_S}{R_{Sh}} \tag{2.10}$$

From the equation (2.10), the dark saturation current can be expressed as,

$$I_0 = \left(I_{SC} - \frac{V_{OC} - I_{SC}R_S}{R_{Sh}}\right)\exp\left(\frac{-V_{OC}}{N_sV_T}\right) \tag{2.11}$$

Substituting I_0 from equation(2.11) into equation(2.9),

$$I_{PV} = \left(I_{SC} - \frac{V_{OC} - I_{SC}R_S}{R_{Sh}}\right) + \frac{V_{OC}}{R_{Sh}}$$

$$\Rightarrow I_{PV} = I_{SC} + I_{SC}\frac{R_S}{R_{Sh}} \tag{2.12}$$

Substituting I_0 from equation(2.11) and I_{PV} from equation(2.12) into equation(2.5),

$$I_{MPP} = \left[I_{SC} - \frac{V_{MPP} + I_{MPP}R_S - I_{SC}R_S}{R_{Sh}}\right] - \left[\left(I_{SC} - \frac{V_{OC} - I_{SC}R_S}{R_{Sh}}\right)e^{\left(\frac{V_{MPP}+I_{MPP}R_S - V_{OC}}{N_sV_T}\right)}\right] \tag{2.13}$$

The above equation has three unknown parameters: R_S, R_{Sh}, V_t. Therefore, for the determination of all these parameters additional equations are required which are derived as follows,

The rate of change of power with respect to voltage at MPP can be written as:

$$\left.\frac{dP}{dV}\right|_{MPP} = \frac{d(IV)}{dV} = I + V\frac{dI}{dV} \tag{2.14}$$

To obtain the derivative of the power w.r.t voltage at maximum power point, the derivative of the equation (2.13), with respect to voltage should be found. However, equation (2.13) is a transcendental equation, i.e $I=f(V, I)$

For f be a function of two real variables such that f has continuous first partial derivatives in a domain D. Therefore, by differentiating the equation $I=f(V, I)$ we have,

$$dI = \frac{\partial f(V,I)}{\partial V}dV + \frac{\partial f(V,I)}{\partial I}dI$$

$$\Rightarrow \frac{dI}{dV} = \frac{\frac{\partial f(V,I)}{\partial V}}{1 - \frac{\partial f(V,I)}{\partial I}} \tag{2.15}$$

Thus, equation (2.14) can also be written as,

$$\left.\frac{dP}{dV}\right|_{MPP} = I_{MPP} + V_{MPP}\frac{\frac{\partial}{\partial V_{MPP}}f(V,I)}{1-\frac{\partial}{\partial I_{MPP}}f(V,I)} \tag{2.16}$$

To determine the partial derivative of the function $f(I,V)$ with respect to V_{MPP} and I_{MPP}, equation (2.13) is differentiated w.r.t V_{MPP} and I_{MPP} and the expressions are given in equation (2.17) and equation (2.18) respectively

$$\frac{\partial f(V,I)}{\partial V_{MPP}} = \frac{\left(V_{OC} - I_{SC}\left(R_S + R_{Sh}\right)\right)\exp\left(\frac{V_{MPP} + I_{MPP}R_S - V_{OC}}{N_s V_T}\right)}{N_s V_T R_{SH}} - \frac{1}{R_{Sh}} \tag{2.17}$$

$$\frac{\partial f(V,I)}{\partial I_{MPP}} = \frac{\left(V_{OC} - I_{SC}\left(R_S + R_{Sh}\right)\right)\exp\left(\frac{V_{MPP} + I_{MPP}R_S - V_{OC}}{N_s V_T}\right)}{N_s V_T R_{Sh}} R_S - \frac{R_S}{R_{Sh}} \tag{2.18}$$

Now, substituting equation (2.17) and equation(2.18) in equation(2.16), we have,

$$\left.\frac{dP}{dV}\right|_{MPP} = I_{MPP} + V_{MPP}\frac{\frac{\left(V_{OC} - I_{SC}\left(R_S + R_{Sh}\right)\right)\exp\left(\frac{V_{MPP} + I_{MPP}R_S - V_{OC}}{N_s V_T}\right)}{N_s V_T R_{Sh}} - \frac{1}{R_{Sh}}}{1 + \frac{R_S\left(I_{SC}\left(R_S + R_{Sh}\right) - V_{OC}\right)\exp\left(\frac{V_{MPP} + I_{MPP}R_S - V_{OC}}{N_s V_t}\right)}{N_s V_T R_{Sh}} + \frac{R_S}{R_{Sh}}} = 0 \tag{2.19}$$

While using equation (2.15) and substituting equation(2.17) and equation (2.18) in equation(2.8), we have,

$$\left.\frac{dI}{dV}\right|_{(0,I_{SC})} = -\frac{1}{R_{Sh}} = \frac{\frac{\left(V_{OC} - I_{SC}\left(R_S + R_{Sh}\right)\right)\exp\left(\frac{I_{SC}R_S - V_{OC}}{N_s V_T}\right)}{N_s V_T R_{SH}} - \frac{1}{R_{sh}}}{1 + \frac{\left(I_{SC}\left(R_S + R_{Sh}\right) - V_{OC}\right)\exp\left(\frac{I_{SC}R_S - V_{OC}}{N_s V_T}\right)}{N_s V_T R_{Sh}} + \frac{R_S}{R_{Sh}}} \tag{2.20}$$

Finally, five equations, (2.6), (2.11), (2.13), (2.19) and (2.20) are obtained to compute the five unknown parameters. It is seen that (2.13), (2.19) and (2.20) are transcendental in nature, necessitating use of numerical methods for solution. Further, these three equations are completely independent of I_{PV} and I_0 hence, the numerical method problem reduces to the determination of three unknowns : V_T, R_S and R_{Sh}, from three equations which can be solved by using Gauss-Seidel method. The flowchart for determining these variables is shown in

Fig.2.6 and then these values are used to compute I_0 and then I_{PV} from equations (2.11) and (2.12) respectively.

2.3.2 Gauss Seidel Method for determination of unknown parameters

The transcendental equations can be solved by an iterative method like the Gauss-Seidel method by which the equations can be expressed in the following form,

$$x^{k+1} = f\left(x^k\right) \tag{2.21}$$

Where x the unknown variable whose value is to be determined at k^{th} iteration. A new value of x^{k+1} is obtained using the old value of x^k on the the right hand side of the equation (2.21). The process is repeated until the absolute difference between the old and the new values is below acceptable limits. To employ the Gauss-Seidel method to determine the values of V_T, R_S, and R_{Sh}, equations (2.13), (2.19) and (2.20) are rearranged to get the form shown in (2.22) through (2.24), respectively,

$$V_T = \frac{\left[I_{MPP}R_s + V_{MPP} - V_{OC}\right]\left[I_{SC}\left(R_S + R_{Sh}\right) - V_{OC}\right]}{N_S \ln\left[\left(R_S + R_{Sh}\right)\left(I_{SC} - I_{MPP}\right) - V_{MPP}\right]} \tag{2.22}$$

$$R_S = \frac{\left(V_{OC} - V_{MPP}\right) + N_S V_T \ln \dfrac{\left[N_S V_t \left\{I_{MPP}\left(R_S + R_{Sh}\right) - V_{MPP}\right\}\right]}{\left[\left(V_{MPP} - I_{MPP}R_S\right) I_{SC}\left(R_S + R_{Sh}\right)\right] - \left[V_{OC}\left(V_{MPP} - I_{MPP}R_S\right)\right]}}{I_{MPP}} \tag{2.23}$$

$$R_{Sh} = \frac{N_S V_T\left(R_S + R_{Sh}\right) + R_S \exp\left[\dfrac{I_{Sc}R_S - V_{OC}}{N_S V_T}\right].\left(I_{SC}\left(R_S + R_{Sh}\right) - V_{OC}\right)}{N_S V_T + \exp\left[\dfrac{I_{Sc}R_S - V_{OC}}{N_S V_T}\right].\left(I_{SC}\left(R_S + R_{Sh}\right) - V_{OC}\right)} \tag{2.24}$$

It is observed that (2.22) is an explicit equation, whereas (2.23) and (2.24) are implicit. V_t, as in (2.22) is a function of known quantities as well as two unknown quantities R_S and R_{Sh}. The values of R_S and R_{Sh} must be known prior to the evaluation of V_T. Therefore, in this case, using Gauss-Seidel method, only two unknowns need to be initialized before V_t is calculated. Next, with the calculated value of V_T, the values of R_S and R_{Sh} can be calculated.

2.3.2.1 Initialization

As seen before, only two unknown parameters, R_S and R_{Sh}, have to be initialized. The value of R_S is generally in the range of milliohms, whereas the value of R_{Sh} is in the range of kilo-ohms. Therefore, R_S and R_{Sh} can be initialized at 0 and 1 kilo-ohm, respectively. In most

cases, convergence is obtained with the above initialization. However, there may be some cases where the Gauss-Seidel method may fail to converge. In that case, the initialization is done randomly with a constraint that R_{Sh} is much greater than R_S. Closer the initialization to the actual value, faster will be the convergence.

2.3.2.2 A Case study

A case study to find the parameters of the PV module produced by Maharishi Solar, India[103], is conducted at STCs as well as varying environmental conditions. A scanned copy of the manufacturer datasheet is given in Fig.2.5, which contains the characteristic curve of the PV module as well as different parameters of the PV module at STCs. For more clarity, the values provided on the data sheet are tabulated in Table 2.1. Table 2.2 gives the values of the unknown parameters computed by the Gauss-Seidel method as discussed above. It can be observed from this Table that, the value of the series resistance is very small compared to the parallel resistance as expected, whereas the photo generated current is equal to the short circuit current.

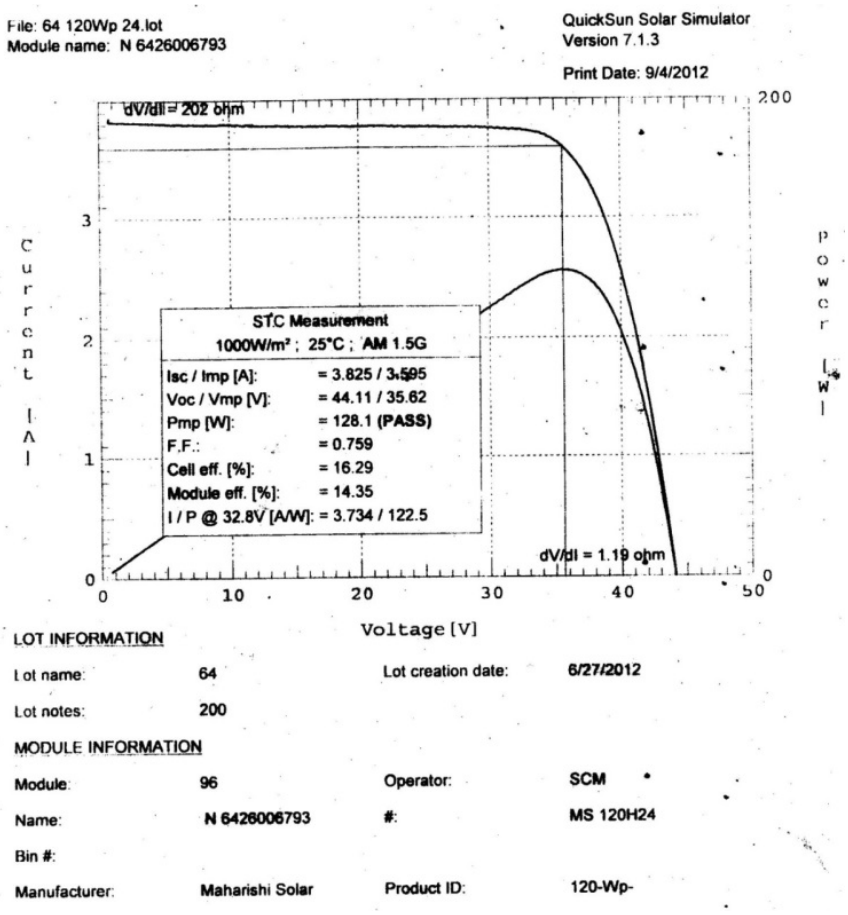

Fig.2.5 : Manufacturer datasheet of PV module [103]

Table 2.1 : Datasheet values of PV module

Short Circuit Current (I_{SC})	3.82 A
Open Circuit Voltage (V_{OC})	44.11 V
Current at MPP (I_{MPP})	3.595 A
Voltage at MPP (V_{MPP})	35.62V
Maximum Power (P_{MPP})	128.1 Watt
Current Temp Coefficient (K_I)	15 $\mu A/cm^2/{}^0C$
Voltage Temp Coefficient (K_V)	-2.10 $mV/cell/{}^0C$

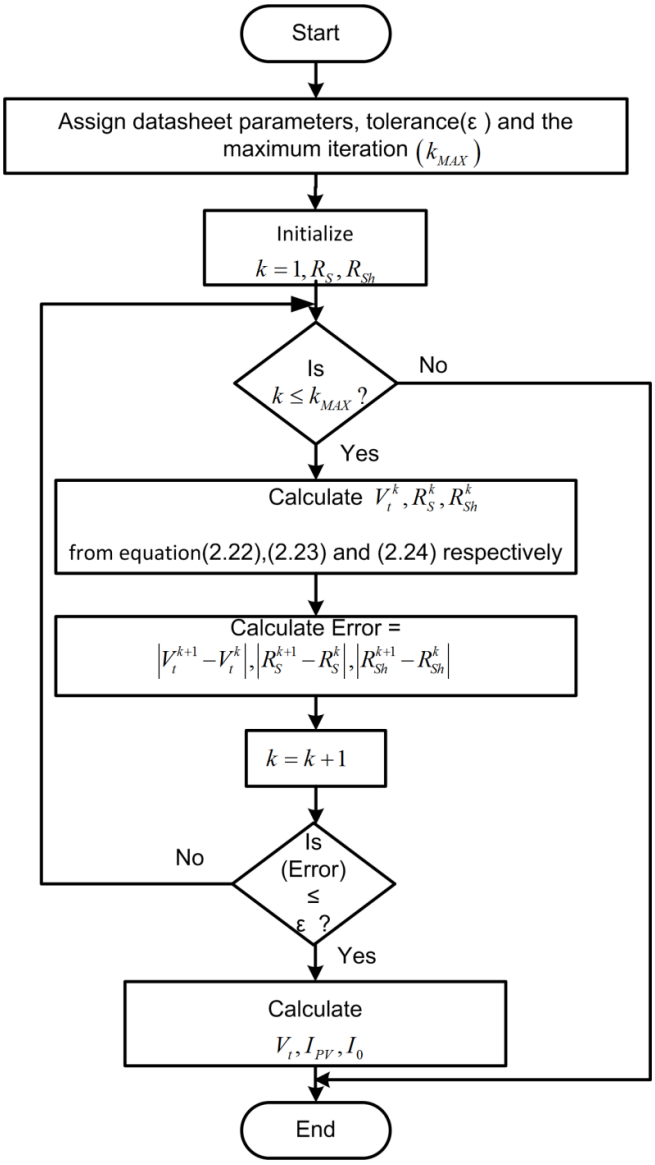

Fig.2.6: Gauss-Seidel algorithm for the determination of unknown parameters

Table 2.2 : Parameters of PV module

Photo generated Current (I_{PV})	3.82 A
Dark Saturation Current (I_0)	0.102 μA
Series Resistance (R_S)	0.31 Ω
Shunt Resistance (R_{Sh})	600 Ω
Diode Ideality Constant (A)	1.2

2.4 Modeling of Strings and Arrays

A PV source is commercially available in the form of a PV module in which number of cells are connected in series. However, for large power and voltage applications, a combination of these modules is needed. A series combination of the modules is called a string. To increase the current rating, these strings are connected in parallel to form an array. A conceptual diagram of a string is shown in Fig.2.7. It shows that the circuit elements which form a series combination in a string can be lumped to give an equivalent single-diode model of the string, which consists of same circuit elements as that of one module, but with different values of parameters, depending on the number of series connected modules [17]. For a string, the value of the equivalent photo-generated current and the dark saturation current remain the same as that of the module. The diode quality factor too remains the same as that of the module. However, the series and parallel resistances of the string acquire values which are as many times the values of the module as there are modules in the string.

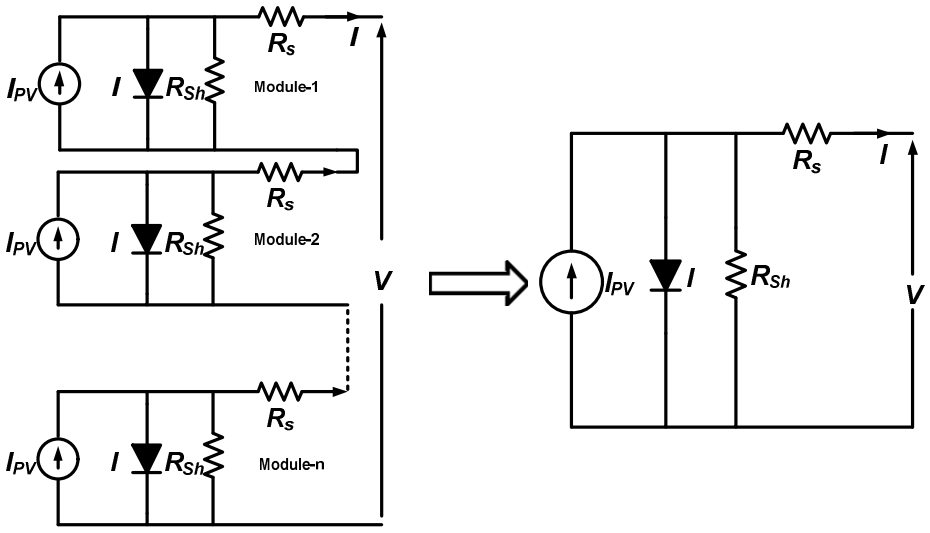

Fig.2.7: Equivalent lumped circuit for a string consisting of modules in series

Similarly, a number of strings connected in parallel to increase the current output of the PV array can be represented by an equivalent lumped circuit, as shown in Fig.2.8 [17]. In this

case, the values of photo-generated current and the dark saturation current of the array are number of strings times the respective value for one string. However, series and parallel resistances get divided by the number of strings in the array, with the diode quality factor remaining the same as that of the string.

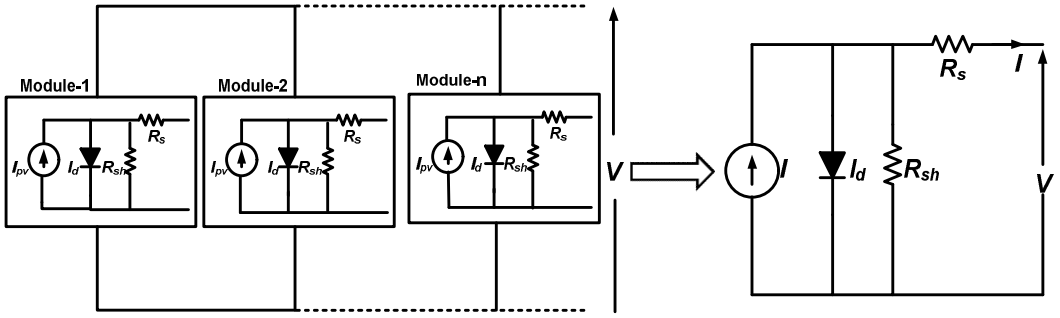

Fig.2.8: Equivalent lumped circuit for an array consisting of strings in parallel

2.5 Design of Array

Let an array be designed for 10 kW. The maximum system voltage specified by the National Electric Code (NEC) is 600 V. The system voltage as defined by NEC is 1.25 times the open circuit voltage at STCs [70]. For PV- N- 6426006793 modules (Maharishi Solar), the open circuit voltage at STC is 44.1 V. Therefore, a maximum of 10 modules can be connected in series to form a string. If the array is controlled to operate at MPP, and if all modules in the array are identical in all respects and assumed to operate under identical environmental conditions, then each module in the array will also operate at MPP. At MPP under STC, the array voltage is 356.2V and the power produced by one module is 128.1 W, and hence by one string is 1.28 kW. Therefore, 8 strings in parallel will be able to produce approximately 10 kW of power.

2.5.1 Array Parameters

Array parameters can be estimated from datasheet values of the module and from the number of modules in series-parallel combination in the array. If the number of modules connected in series in a string is N_{SS} and the number of strings connected in parallel to form an array is N_{PP}, then the specifications of the array will be as shown in Table 2.3, assuming identical characteristics of each module and identical operating conditions.Using the data for the array as given in Table 2.3 and Gauss-Seidel method to determine the parameters, the equivalent lumped parameter model of the array is obtained. For the 10 kW array consisting of PV-N-6426006793 modules of Table 2.1, with 10 modules per string and 8 strings in parallel, the parameters obtained are shown in Table 2.4. From this table, it is seen that an alternative approach can be adopted to estimate the equivalent lumped parameters of an array, where, the parameters of the module are determined first and then, using the

information of the number of modules in a string and the number of strings in parallel, parameters of the array can be calculated [68].

Table 2.3 : Datasheets values of an array in relation to a module

Module Datasheet Values	**Equivalent Array Values**
I_{SC}	$I_{SC} \times N_{PP}$
V_{OC}	$V_{OC} \times N_{SS}$
I_{MPP}	$I_{MPP} \times N_{PP}$
V_{MPP}	$V_{MPP} \times N_{SS}$
n_S	$n_S \times N_{SS}$

Table 2.4: Estimated Parameters of an array in relation to a module

$N_{PP} = 10, N_{SS} = 8$		
Relationship with Module Parameters	Equivalent Array Parameters	
$I_{PV} \times N_{PP}$	I_{PV}	38.2 A
$I_0 \times N_{PP}$	I_0	1.02 μA
A	A	1.2
$R_S \times {N_{SS}}/{N_{PP}}$	R_S	0.248 Ω
$R_{Sh} \times {N_{SS}}/{N_{PP}}$	R_{Sh}	480 Ω

2.6 Temperature and Irradiance Dependence

The photo-generated and dark saturation currents are functions of irradiance and temperature, which further depends on prevailing atmospheric conditions. The photo-generated current of the PV cell as a function of these quantities is given by the following equation[25], [26]–[29]:

$$I_{PV}\left(G,T\right) = \left(I_{PV,STC} + K_I \Delta T\right)\frac{G}{G_{STC}} \tag{2.25}$$

Where $I_{PV,STC}$ (in amperes) is the photo-generated current at the nominal condition (i.e. 25 ^{0}C and 1000 W/m^2),

$\Delta T = T - T_{STC}$ (T and T_{STC} being the actual and nominal temperatures [in Kelvin], respectively),

G (W/m^2) is the irradiation on the device surface, and G_{STC} is the nominal irradiation.

As the short circuit current is directly proportional to the photo-generated current, hence it is also directly proportional to the irradiation. The datasheet of PV module provides temperature coefficient for short-circuit current and open-circuit voltage, K_I and K_V respectively. Short-circuit current and open circuit voltages as functions of temperature are given in equation (2.26) and (2.27), respectively [1].

$$I_{SC}(T) = I_{SC}(T_{STC}) + K_I(T - T_{STC}) \tag{2.26}$$

$$V_{OC}(T) = V_{OC}(T_{STC}) + K_V(T - T_{STC}) \tag{2.27}$$

Open circuit voltage of PV module, however, is not directly proportional to the irradiation. It is obtained by rearranging equation(2.6) as shown in equation (2.28) [1].

$$V_{OC}(G) = n_s V_T \ln\left(\frac{I_{PV}(G)R_{Sh} - V_{OC}(G)}{I_0 R_{Sh}}\right) \tag{2.28}$$

Dark saturation current is a function of temperature alone, and is independent of irradiation. It can be found out from equation(2.11) by expressing the variables as a function of temperature, as shown in equation(2.29) [1].

$$I_0(T) = \left(I_{SC}(T) - \frac{V_{OC}(T) - I_{SC}(T)R_S}{R_{Sh}}\right)\exp\left(-\frac{V_{OC}(T)}{n_s V_T}\right) \tag{2.29}$$

The diode saturation current I_0 and its dependence on the temperature can also be expressed by as shown [12], [14], [15]–[18]:

$$I_0 = I_{0,STC}\left(\frac{T_{STC}}{T}\right)^3 \exp\left[\frac{qE_g}{Ak}\left(\frac{1}{T_{STC}} - \frac{1}{T}\right)\right] \tag{2.30}$$

Where E_g is the band gap energy of the semiconductor ($\left(E_g = 1.12\,eV\right)$ for the polycrystalline Si at 25 ^{0}C [23], [42]), and $I_{0,STC}$ is the nominal saturation current:

$$I_{0,STC} = \frac{I_{sc,STC}}{\exp\left(V_{oc,STC} / AV_{T,STC}\right) - 1} \tag{2.31}$$

With $V_{T,STC}$ being the thermal voltage of N_S series-connected cells at the nominal temperature T_{STC}.

2.7 Simulation of PV Module

In order to validate the model discussed above under different atmospheric conditions, the equations developed in previous sections have been implemented in Matlab Simulink. The PV module is simulated with an equivalent circuit model based on the PV model of Fig.2.2. The data given in Table 2.1 are used for the modelling of PV module. The magnitude of the source current is obtained by numerically solving the $I - V$ equation, which is calculated by V, I, I_0 and I_{PV} as inputs. I_{PV} and I_0 are obtained using equations(2.6) and

(2.11), respectively. The solution of this equation is obtained using a numerical method, implemented in MATLAB embedded programming.The simulation model is used to obtain the I-V and P-V characterisics of module.

The irradiation and temperature dependencies of the PV model's characteristic curve have been obtained by plotting the $P–V$ and $I–V$ characteristics for four different irradiations and temperatures. Fig.2.9 and Fig.2.10 shows the $P–V$ and $I–V$ characteristics of the PV module at varying irradiations and constant temperature, respectively. It can be observed that at STCs the $P-V$ and $I-V$ characteristics of the PV module completely resemble the manufacturer's datasheet curves. From these figures it can be noted that, according to the theory, short-circuit current shows a linear dependence on irradiation, unlike the open-circuit voltage which increases logarithmically with the irradiation. As the variation of current is more as compared to voltage, the PV module power variation largely depends on the PV current output. Similar to other semiconductor devices, PV modules are sensitive to temperature. With increases in temperature the band gap of a semiconductor reduces, thereby most of the semiconductor material parameters are getting affected. The decrease in the band gap of a semiconductor with increasing temperature can be viewed as increase in energy of the electrons. Lower energy is therefore needed to break the bond. Also, the short-circuit current (I_{sc}) decreases with increasing band gap, the open-circuit voltage (V_{oc}) increases as the band gap increases [25]. However, the parameter most affected by temperature is the V_{OC}. Fig.2.11 and Fig.2.12 shows the $P–V$ and $I–V$ characteristics of the PV module at varying temperatures and constant irradiation, respectively. Short-circuit current, open-circuit voltage and maximum power is observed to be in close agreement with the manufacturer data-sheet. The change in the open-circuit voltage and short-circuit current are also in accordance with the temperature coefficients given in the data-sheet. In addition to plot the characteristic curve under varying atmospheric conditions, a Matlab program is also developed to determine the magnitudes of voltage, current and power at MPP. These MPPs are marked on the respective curves and their magnitudes are tabulated in Table 2.5 and Table 2.6 for varying irradiation and temperature conditions respectively.

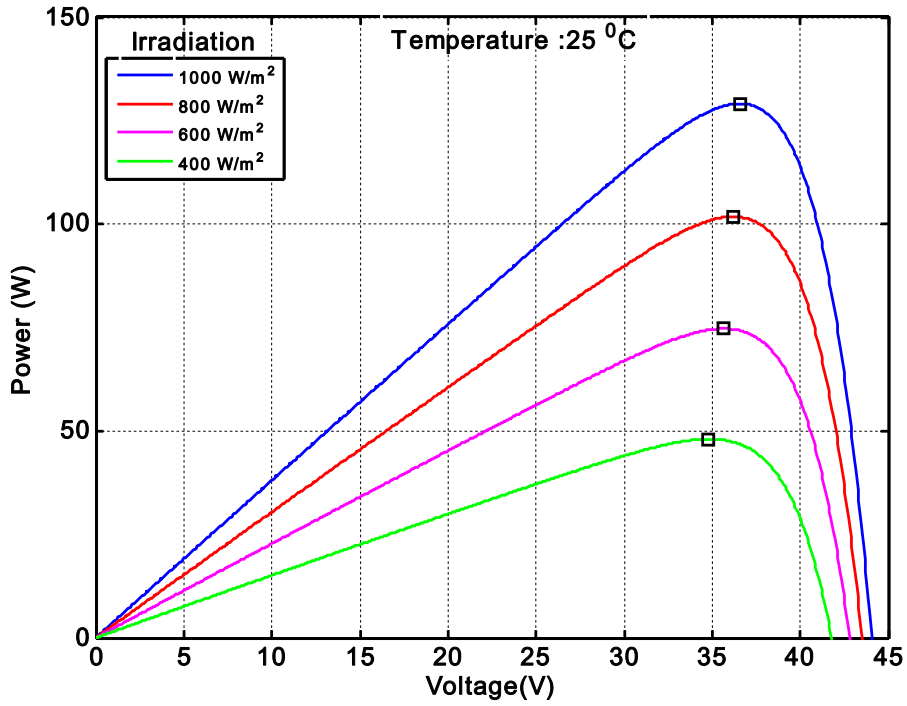

Fig. 2.9: P-V characteristics of the PV module at a temperature of 25 ^{0}C with varying irradiation

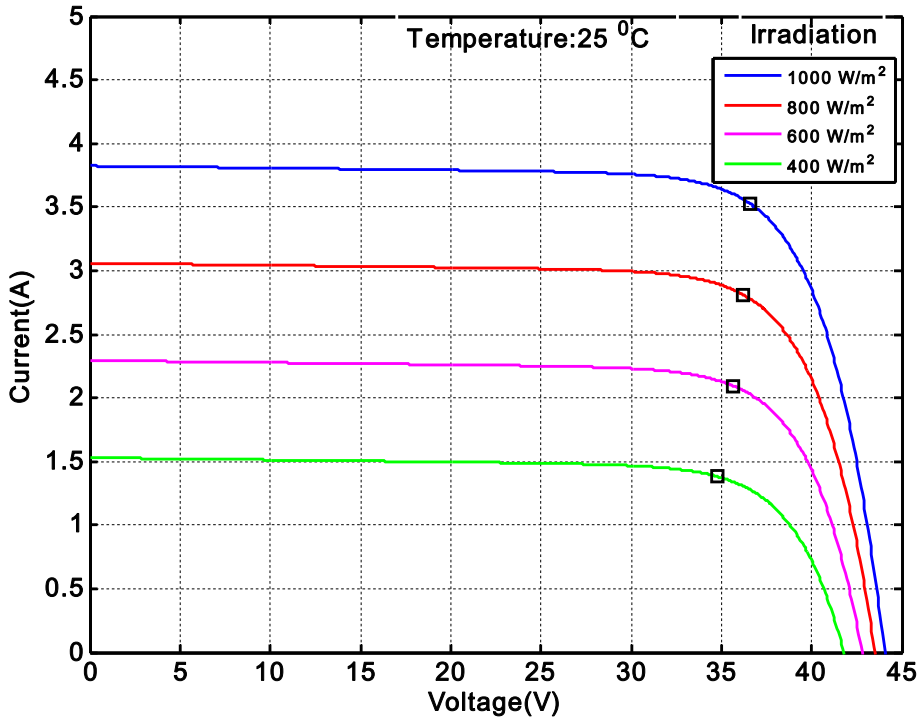

Fig. 2.10: I-V characteristics of the PV module at a temperature of 25 ^{0}C with varying irradiation

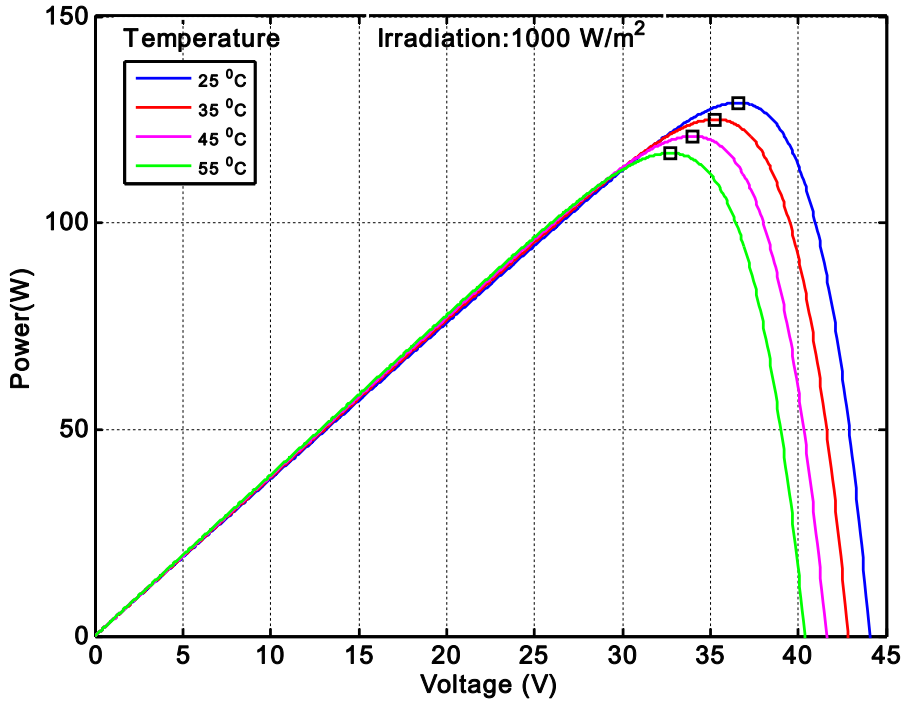

Fig. 2.11: P-V characteristics of the PV module at an irradiation of 1000 W/m^2 with varying temperatures

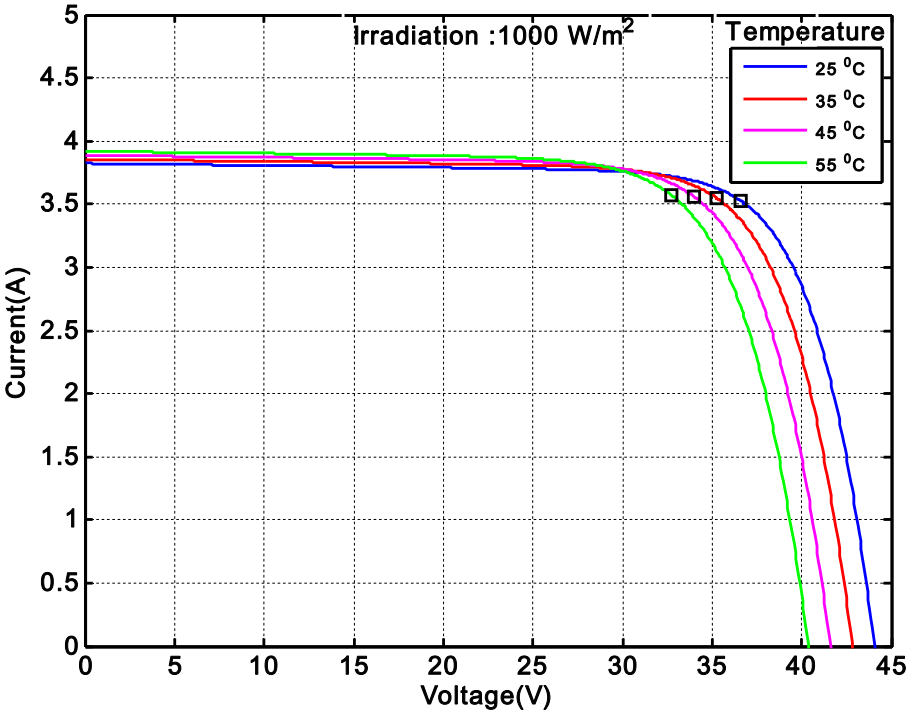

Fig. 2.12: I-V characteristics of the PV module at an irradiation of 1000 W/m^2 with varying temperatures

Table 2.5 : Voltage, Current and Power at MPP during varying Irradiation conditions

Irradiation (W/m^2)	Temperature : 25 ^{0}C		
	V_{MPP}	I_{MPP}	P_{MPP}
1000	36.32	3.526	128.1
800	35.99	2.811	101.2
600	35.53	2.093	74.38
400	34.74	1.379	47.89

Table 2.6 : Voltage, Current and Power at MPP during varying temperature conditions

Temperature (^{0}C)	Irradiation: 1000 W/m^2		
	V_{MPP}	I_{MPP}	P_{MPP}
25	36.32	3.526	128.1
35	35	3.545	124.1
45	33.74	3.556	120
55	32.49	3.567	115.9

Similar to varying atmospheric conditions, the $P-V$ and $I-V$ characteristics of PV module with varying series (R_S) and shunt resistance (R_{Sh}) are plotted under STCs. Fig.2.13 and Fig.2.14 show the case of varying R_S whereas Fig.2.16 and Fig.2.17 show the case of varying R_{Sh}. In Fig. 2.13, as R_S increases, the $P-V$ curve moves to the left and the peak power (P_{MPP}) is achieved as per data sheet value at the series resistance value of 0.31Ω. It can be observed from the characteristic plot that, at open-circuit voltage (V_{OC}) is not affected by the series resistance(R_S). This is due to zero voltage drop in R_S under open circuit conditions. However, near V_{OC}, the $I-V$ curve is strongly affected by R_S.

Low value of R_{Sh} causes power losses in PV modules by providing an alternate current path for the light-generated current. Such a diversion reduces the amount of current flowing through the PV module and reduces the voltage of the PV module. The effect of R_{Sh} is particularly severe at low light levels, since there will be less light-generated current. The loss of this current to the shunt resistance, therefore, has a larger impact. Here, the $P-V$ and $I-V$ characteristic of the PV module is plotted under STCs which are depicted in Fig.2.15 and Fig.2.16 respectively. It can be observed that the impact of shunt resistance on these curves under STCs is very less. Similar to the characteristic curve under varying atmospheric conditions, the MPP points are marked on the respective curves under varying series and shunt resistances. The magnitudes of maximum voltage, current and power at MPP are tabulated in Table 2.7 and Table 2.8 respectively with varying series and shunt resistances.

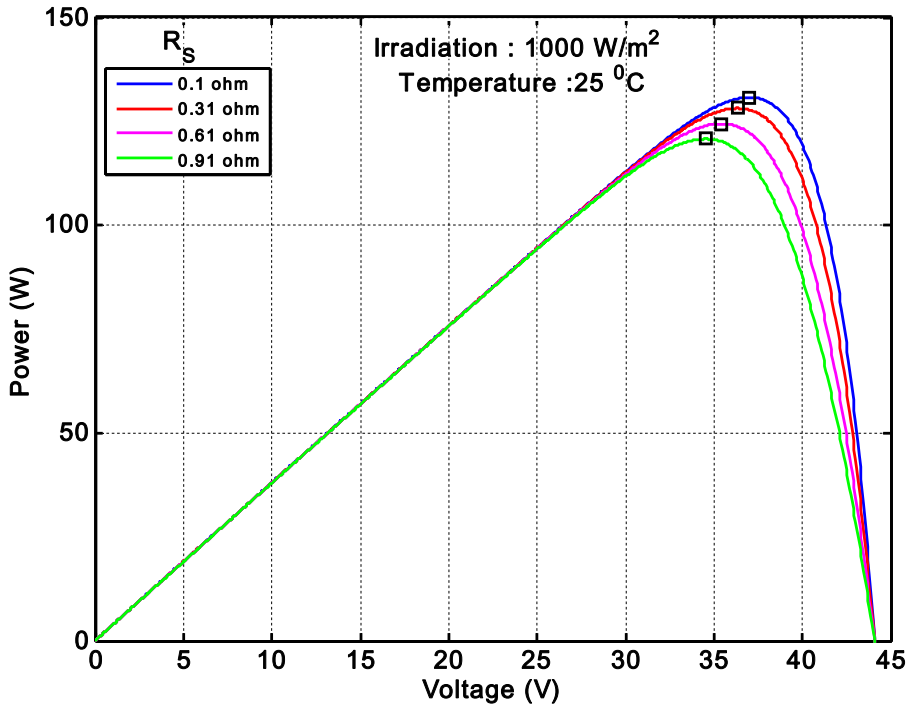

Fig. 2.13: P-V characteristics of the PV module at STC with varying series resistance

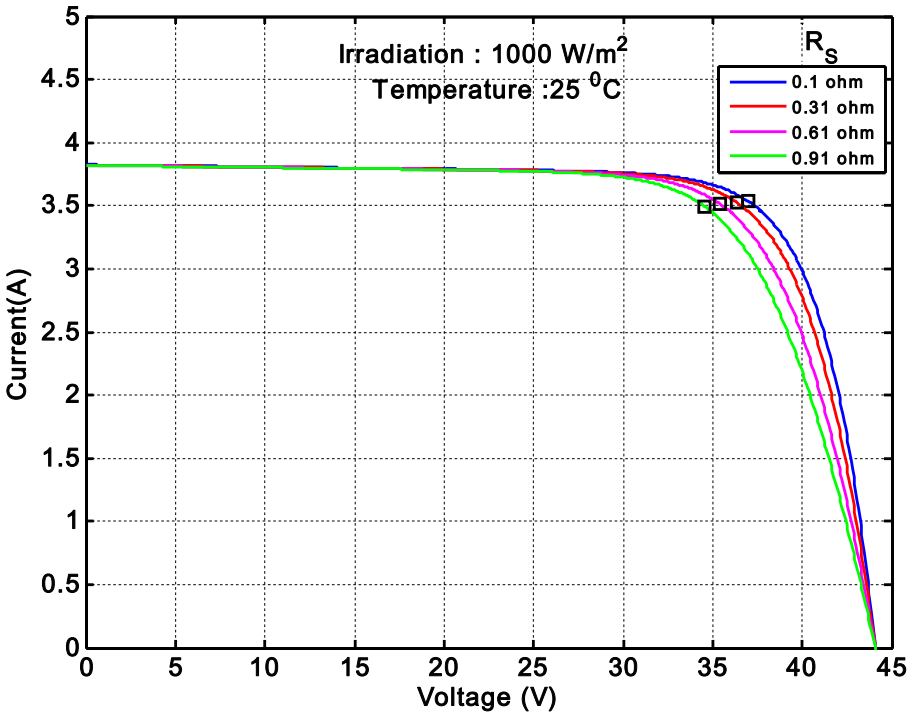

Fig. 2.14: I-V characteristics of the PV module at STC with varying series resistance

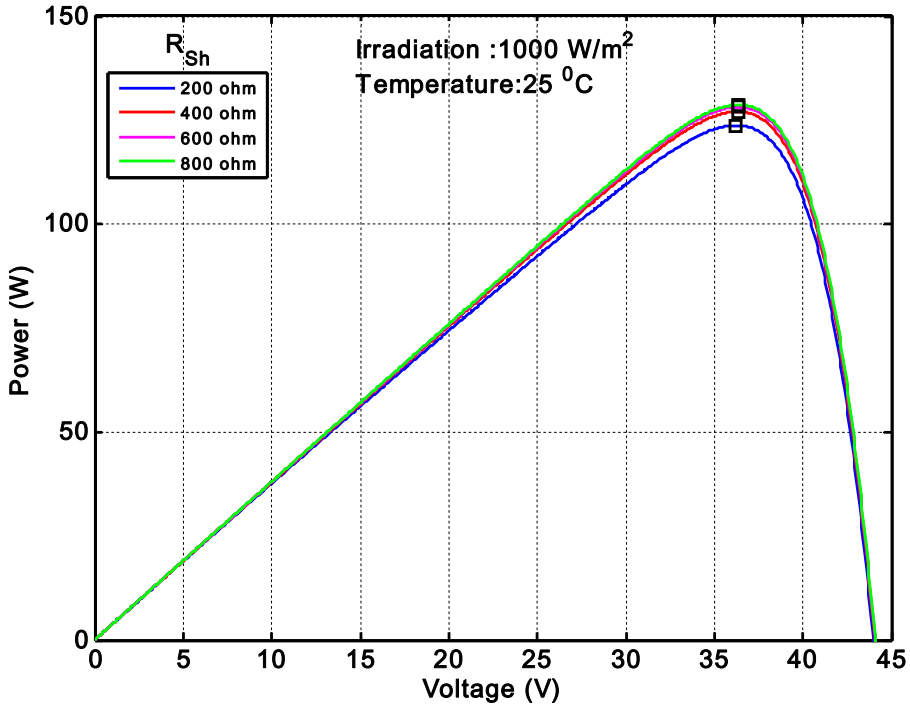

Fig. 2.15: P-V characteristics of the PV module at STC with varying shunt resistance

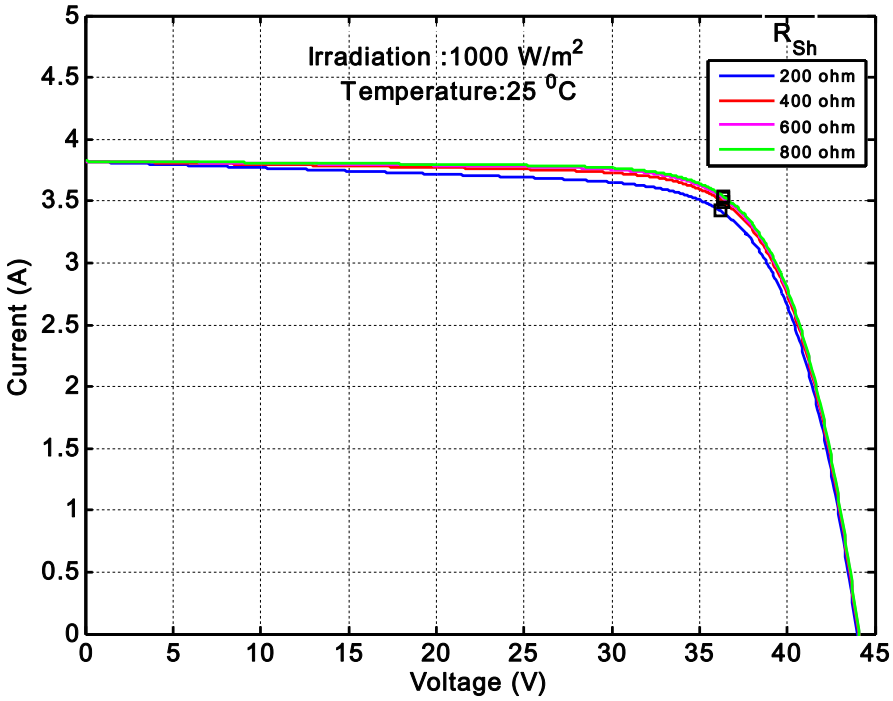

Fig. 2.16: I-V characteristics of the PV module at STC with varying shunt resistance

Table 2.7 :Values of Voltage, Current and Power at MPP at STCs with varying series resistance

Series Resistance (R_S)	Irradiation: 1000 W/m^2 ,Temperature (25 ^{0}C) Shunt Resistance $(R_{Sh} = 600\Omega)$		
	V_{MPP}	I_{MPP}	P_{MPP}
0.1	36.99	3.535	130.8
0.31	36.32	3.526	128.1
0.61	35.40	3.515	124.4
0.91	34.54	3.496	120.7

Table 2.8 :Values of Voltage, Current and Power at MPP at STCs with varying shunt resistance

Series Resistance (R_{Sh})	Irradiation: 1000 W/m^2 ,Temperature (25 ^{0}C) Series Resistance $(R_S = 0.31\Omega)$		
	V_{MPP}	I_{MPP}	P_{MPP}
200	36.192	3.419	123.755
400	36.324	3.494	127.042
600	36.324	3.526	128.1
800	36.39	3.536	128.690

2.8 Maximum Power Point Tracking Control

As discussed in the previous section, a PV module under uniform irradiation exhibits a nonlinear $I-V$ characteristic with a unique maximum power point (MPP), where it produces maximum output power[1]. The $P-V$ and $I-V$ characteristics curve of PV module under varying irradiation and temperature conditions are shown in Fig.2.10 to Fig.2.13. The MPP has also been marked in all these figures. As evidenced from simulation results, the characteristic curve of a PV module, and hence its MPP, changes as a consequence of the variation of the irradiation and temperature[1]. Therefore, it is necessary to track MPP continuously to maximize the power output from a PV module, for an operating conditions. The location of the MPP is not known, but need to be located and for this different MPPT methods have been realized[31]. They vary in "complexity, sensors required for the voltage or current, convergence speed, cost, range of effectiveness and hardware implementation"[31, 54]. These algorithms are based on the measurement of the PV module output voltage and current. Then, it calculates the PV power and determines if the control parameter needs to be increased or decreased. The control parameter could be a reference signal (voltage or current) for the controller or it can be the duty ratio of DC/DC converter. The point at which I_{MPP} and V_{MPP} meet is the maximum power point. The value of load resistance at MPP is given by:

$$R_{MPP} = \frac{V_{MPP}}{I_{MPP}} \tag{2.32}$$

The maximum power point tracker uses the DC/DC converter to adjust the PV voltage at the maximum power point. A boost type converter steps up the PV voltage to high voltage necessary for the inverter in grid connected system. The block diagram is shown in Fig.2.17. The conversion ratio of boost converter is given by the following expression:

$$\frac{V_0}{V_{in}} = \frac{I_{in}}{I_0} = \frac{1}{1-D} \tag{2.33}$$

Where D is the duty cycle. This expression gives us the following relationships:

$$V_{in} = V_0\left(1-D\right) \tag{2.34}$$

$$I_{in} = \frac{I_0}{\left(1-D\right)} \tag{2.35}$$

Knowing V_{in} and I_{in}, we can find the input resistance of the converter. This is given by,

$$R_{in} = \frac{V_{in}}{I_{in}} = \frac{V_0\left(1-D\right)}{I_0 \big/ \left(1-D\right)} = R_0\left(1-D\right)^2 \tag{2.36}$$

Therefore, from the above expression, it can be concluded that by varying the duty cycle of the DC-DC boost converter, it is possible to match the load resistance with R_{MPP} and hence maximum power can be extracted from the PV module.

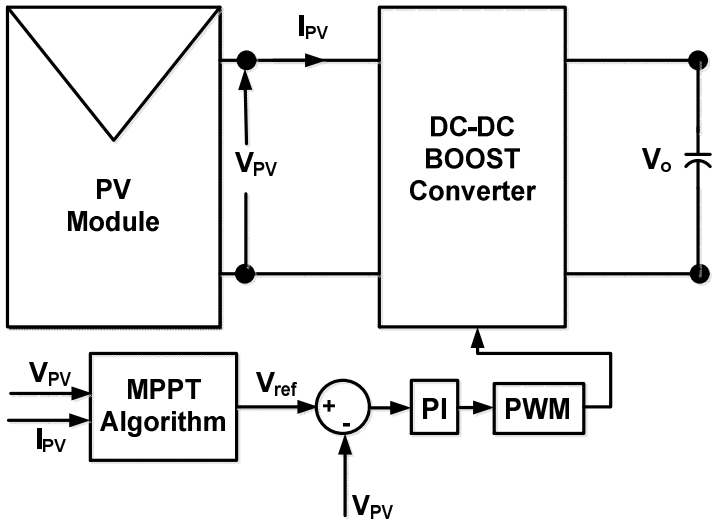

Fig.2.17: Block diagram of MPPT control with DC-DC Converter

For the maximum power point tracking, the reference signal is generated from the MPPT algorithm and is compared with actual PV output voltage. Then the error is processed through a controller to generate the switching pulses for the DC-DC converter and thereby extract the maximum power from the PV module. However, the performance of the MPPT is strongly depends on the performance of the converter control and its ability to regulate the operating point of the PV module. This section addresses the control problem illustrated in Fig.2.17. The PV module feeds the DC-DC boost converter. The output of the converter is

represented by a constant DC voltage source V_0 that represents a DC-link for another cascaded converter. Boost converter serves as an interface between the PV module and the output voltage V_0. The control of the input voltage of boost converter is required for the MPPT of the PV module. In this situation, unlike conventional converters, the output voltage is constant and the input voltage is controlled. The following subsections present the analysis, control and design of the boost converter for MPPT control with the constant output voltage and variable input, which is followed by the MPPT control algorithm to generate the reference voltage for the controller.

2.8.1 DC-DC Boost Converter Modelling

This section presents a brief introduction on a generalized state space averaging (SSA) technique for the modelling of DC-DC converters operating in continuous conduction mode (CCM)[104] which is followed by the modelling of boost converter. In the CCM of DC-DC converter, there exist two switching states in one switching period of a switch. One is during the turn on time interval (dT) and another is during turn off time interval (1-D)T, where D and T are the duty cycle and switching time period respectively.

A small signal model of the boost converter fed from the PV module is developed. The method of average variables is used to obtain small-signal converter transfer functions. These models describe the behaviour of PV module output voltage and current w.r.t duty cycle of the boost converter. Fig.2.18 shows the PV boost converter with average voltages and currents. The bar over a variable name $\left(e.g.\overline{v}_{PV}, \overline{i}_L\right)$ means the discrete-time average value of the variable within one switching period of the boost converter.

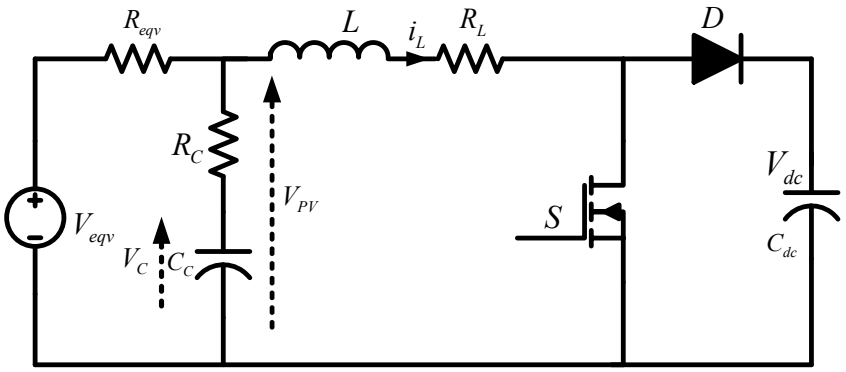

Fig.2.18: Boost Converter with PV array linear model

When the switch is on $\left(dT\right)$, the capacitor and the inductor state equation can be written as,

$$\frac{V_{eqv}-\overline{v}_{PV}}{R_{eqv}}-C\frac{d\overline{v}_C}{dt}-\overline{i}_L=0 \tag{2.37}$$

$$\overline{v}_{PV}-\overline{v}_L-\overline{i}_L R_L=0 \tag{2.38}$$

Similarly, when the switch is in the off state $(1-d)T$, the state equations can be written as,

$$\frac{V_{eqv}-\overline{v}_{PV}}{R_{eqv}}-C\frac{d\overline{v}_C}{dt}-\overline{i}_L=0 \tag{2.39}$$

$$\overline{v}_{PV}-\overline{v}_L-\overline{i}_L R_L-V_{dc}=0 \tag{2.40}$$

Now applying the SSA scheme the average capacitor and average inductor state equation can be written as,

$$C\frac{d\overline{v}_C}{dt}=\frac{V_{eqv}-\overline{v}_{PV}}{R_{eqv}}-\overline{i}_L \tag{2.41}$$

$$\begin{aligned}&\overline{v}_L=\overline{v}_{PV}-\overline{i}_L R_L-(1-d)V_{dc}\\&\Rightarrow L\frac{d\overline{i}_L}{dt}=\overline{v}_{PV}-\overline{i}_L R_L-(1-d)V_{dc}\end{aligned} \tag{2.42}$$

In addition to this, the relation between the input voltage of a boost converter and the capacitor voltage can be written as,

$$\overline{v}_{PV}=R_C\frac{d}{dt}\overline{v}_C+\overline{v}_C \tag{2.43}$$

2.8.2 Small Signal Analysis of boost converter

The objective of modelling the boost converter for input voltage control is to obtain a small-signal transfer function that relates the small-signal PV output voltage $\tilde{v}_{PV}$ and the control variable $\tilde{d}$.

The modelling process essentially consists of following three steps:

- Inserting the small signal variable in the state equation
- Applying the Laplace transformation
- Manipulating the equations in order to find the desired transfer function

The small signal variables are introduced to the following definitions,

$$\left.\begin{aligned}&\overline{v}_C=V_C+\tilde{v}_C\\&\overline{v}_{PV}=V_{PV}+\tilde{v}_{PV}\\&\overline{i}_L=I_L+\tilde{i}_L\\&d=D-\tilde{d}\end{aligned}\right\} \tag{2.44}$$

The minus signal is necessary, because negative variations of duty cycle cause positive change in the input voltage.

By substituting equation (2.44) in the equation(2.41),

$$\begin{aligned}&C\frac{d(V_C+\tilde{v}_C)}{dt}=\frac{V_{eqv}-(V_{PV}+\tilde{v}_{PV})}{R_{eqv}}-(I_L+\tilde{i}_L)\\&\Rightarrow C\frac{d\tilde{v}_C}{dt}=-\frac{\tilde{v}_{PV}}{R_{eqv}}-\tilde{i}_L\end{aligned} \tag{2.45}$$

Now by taking the Laplace transform of (2.45),

$$sC\tilde{v}_c(s) = -\frac{\tilde{v}_{PV}(s)}{R_{eqv}} - \tilde{i}_L(s) \tag{2.46}$$

Similarly, by substituting equation (2.44) in the equation(2.43),

$$\left(V_{PV} + \tilde{v}_{PV}\right) = R_C C \frac{d\left(V_C + \tilde{v}_c\right)}{dt} + \left(V_C + \tilde{v}_C\right) \tag{2.47}$$

Now applying the Laplace transform in the above equation,

$$\begin{aligned} &\tilde{v}_{PV}(s) = sCR_C\tilde{v}_C(s) + \tilde{v}_C(s) \\ &\Rightarrow \tilde{v}_C(s) = \frac{\tilde{v}_{PV}(s)}{1 + sCR_C} \end{aligned} \tag{2.48}$$

By substituting equation (2.48) in (2.46), the small signal inductor current can be expressed as,

$$\tilde{i}_L(s) = -\tilde{v}_{PV}(s)\left[\frac{1}{R_{eqv}} + \frac{sC}{\left(1 + sCR_C\right)}\right] \tag{2.49}$$

Substituting equation (2.49) in the equation(2.42),

$$L\frac{d\left(I_L + \tilde{i}_L\right)}{dt} = \left(V_{PV} + \tilde{v}_{PV}\right) - \left(I_L + \tilde{i}_L\right)R_L - \left(1 - \left(D - \tilde{d}\right)\right)V_{dc} \tag{2.50}$$

Now by taking the Laplace transform of equation(2.50),

$$\tilde{i}_L(s) = \frac{\tilde{v}_{PV}(s) - \tilde{d}(s)V_{dc}}{R_L + sL} \tag{2.51}$$

Finally, by comparing equation,(2.49) and (2.50), the transfer function of input voltage to the duty cycle can be expressed as,

$$\frac{\tilde{v}_{PV}(s)}{\tilde{d}(s)} = \frac{sCR_C R_{eqv} V_{dc} + V_{dc} R_{eqv}}{s^2 LC + s\left[L + R_L C + R_C R_{eqv} C\right] + \left(R_L + R_{eqv}\right)} \tag{2.52}$$

2.8.3 Design of boost converter for MPPT

Voltage at MPP under STCs, $V_{in} = V_{MPP,PV} \times N_{PP} = 35.68 \times 10 = 356.8V$

DC-link voltage of PV inverter, $V_{out} = V_{dc} = 500V$

Maximum PV Output power at STCs, $P_{MPP} = 10260W$

Switching Frequency of DC-DC converter, $f_{sw} = 5kHz$

Maximum Inductor current ripple, $\Delta i_L = 10\%$

The following equation can be used to calculate the inductor L ,

$$\frac{V_{out}}{V_{in}} = \frac{1}{1-D}$$

$$\Rightarrow D = 1 - \frac{V_{in}}{V_{out}} = 1 - \frac{356.8}{500} = 0.2864$$

$$L \geq \frac{V_{out}.D.(1-D)}{f_{sw}.\left|\Delta i_{ripple}\right|} \tag{2.53}$$

Finally the boost converter inductance value can be calculated as, $L \geq$ 4.97 mH

The output current of the boost converter can be given as,

$$I_{out} = \frac{P_{MPP}}{V_{out}} = \frac{10260}{500} = 20.52A \tag{2.54}$$

The load resistance for the boost converter can be calculated as,

$$R_{out} = \frac{V_{out}}{I_{out}} = \frac{500}{20.52} = 24.36\Omega \tag{2.55}$$

Now to calculate the input capacitor the following relation is used,

$$C_{in} \geq \frac{I_{out}D^2}{0.02(1-D)f_{sw}V_{MPP}} \geq 60.10\mu F \tag{2.56}$$

Finally, for the calculation of the output capacitor, the following relation is used,

$$C_{out} \geq \frac{V_{out}D}{f_{sw}\Delta V_{out}R_{out}} \geq 47\mu F \tag{2.57}$$

2.8.4 Open loop Analysis

With the DC-DC boost converter transfer functions, an analysis of the PV boost system can be made that helps in understanding the effects of R_L and R_C in the system. These two parameters are used for the realistic analysis of the input regulated boost converter fed from a PV module. Fig.2.19 illustrates the effect of R_L and R_C on the system response. From this bode plot it can be observed that, R_C introduces a high frequency zero in the system and thereby reduces the system phase lag. The parameters used for system are discussed in the previous section. The GM and PM of the system for the different values of R_C and R_L are tabulated in Table.2.9. Although R_C is undesired in converter design, in the input regulated converter it helps to stabilize the system by increasing the phase margin and significantly reducing the phase lag at high frequency.

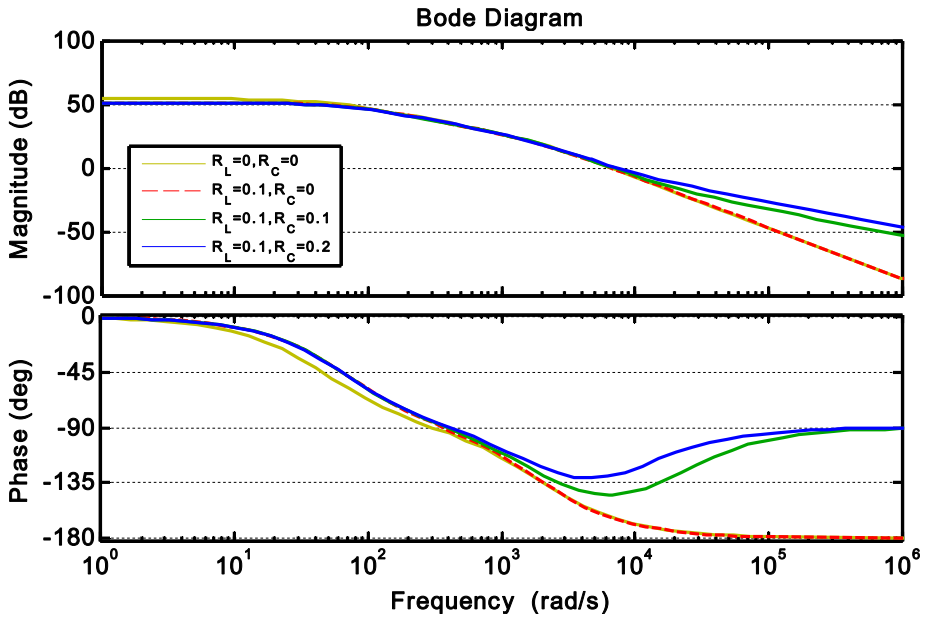

Fig.2.19 : Bode plots of the transfer function $G_{vd}(s)$ with different values of R_L and R_C

2.8.5 Closed loop Analysis

The design of closed-loop controllers for the DC-DC boost converter fed by a PV array is based on the transfer function developed in previous sections. In this section, the input voltage control strategy for the boost converter is presented and is validated by the simulation results. Fig.2.20 shows the bode plot of open loop (G_{vd}(s)) and compensated system. The system is compensated with $(30s+750)/s$ .The compensator places the crossover frequency at $\omega = 3.22\times10^3$ rad/Sec. This warranties good phase margin even when the system operates at a point other than at which it was linearized. Finally, simulation is carried out in MATLAB for the transfer function and physical model for different values of input reference voltage. The parameters used for the simulation is given in section in 2.8.4. The simulation results are given in Fig.2.21. It can be observed that for the different values of reference input voltage the controller is able to track smoothly both for transfer function and physical model.

Table 2.9: Influence of R_C and R_L in open loop transfer function

R_L (Ω)	R_C (Ω)	GM in dB	PM	Frequency in kHz
0	0 Ω	Inf	16.8^0	1.05
0.1	0 Ω	Inf	17.0^0	1.05
0.1	0.1 Ω	Inf	35.4^0	1.09
0.1	0.2 Ω	Inf	51.9^0	1.15

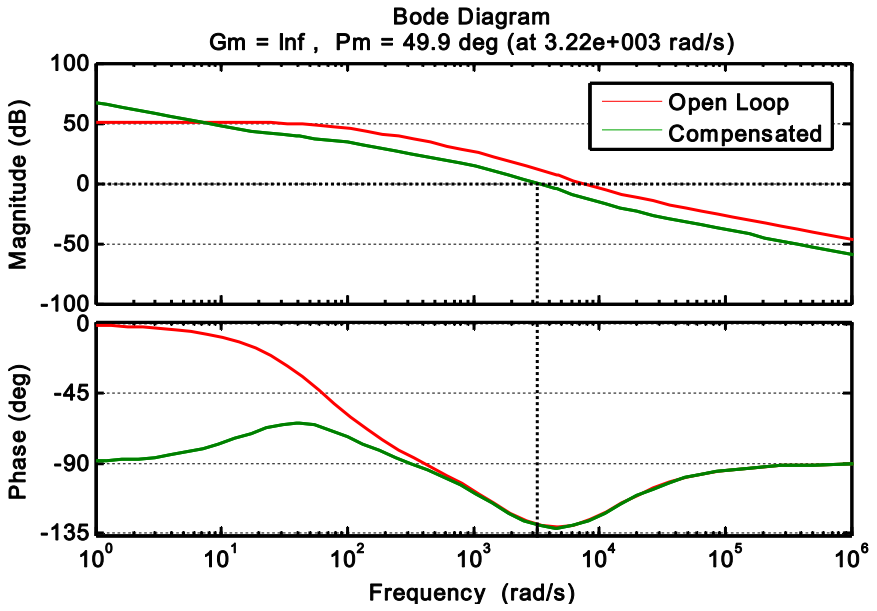

Fig.2.20: Bode plot of the open-loop system and compensated system

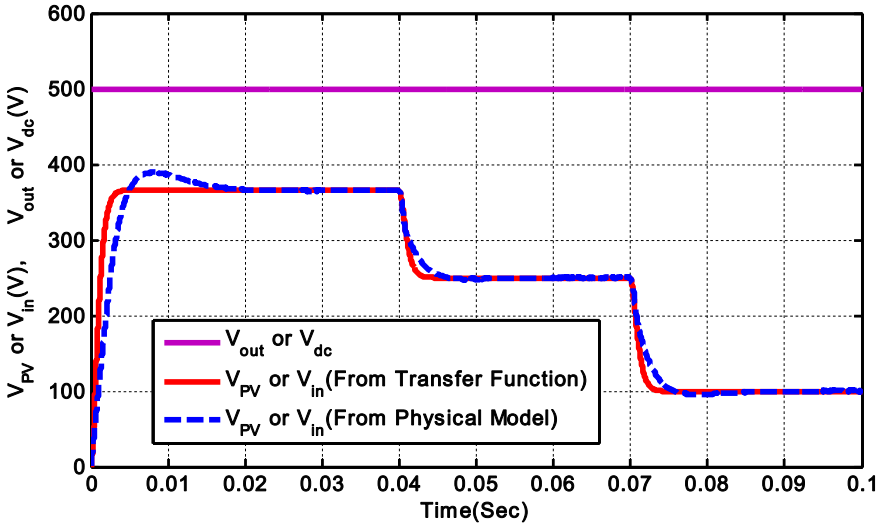

Fig.2.21: Simulation results of input and output voltage of the boost converter with transfer function model and physical model

2.8.6 Perturb and Observe algorithm for MPPT Control

This is one of the most extensively used MPPT control schemes in PV application. It involves a perturbation in PV module output voltage which can be observed from Fig.2.22. Here, a small increment/decrement in the PV module output voltage on the left side of MPP leads to increase/decrease in PV module output power. However, in the right half of MPP, the increase/decrease in PV module output voltage leads to decrease/increase in power respectively. Therefore, if PV module output power is found to be increasing, the succeeding perturbation should be retained in the same direction to reach the MPP. On the other hand, the perturbation needs to be reversed, if there is a reduction in PV module output power. The above mentioned process is repeated in every sampling time until the PV module output

power reaches the MPP. The instant when MPP is reached, the complete system oscillates around that MPP. This leads to power loss across the PV module. This oscillation and hence the power loss can be minimized by taking a reduced value of the step size for the perturbation. However, a small size of perturbation leads to slow response from MPPT controller to reach the MPP. It can be observed from the algorithm that, at t^{th} sampling time, the PV module output voltage ($V_{PV}(t)$) and current ($I_{PV}(t)$) are sensed to compute the PV module output power, $P(t)$, which is compared with the power measured at $(t\text{-}1)^{th}$ sampling instant i.e. $P(t-1)$. If $P(t)$ is found to be more than $P(t-1)$, the output voltage perturbation is made to continue in the same direction. However, if the PV module output power $P(t)$ is found to be of lesser than $P(t-1)$, the output voltage perturbation is reversed. A large value of the step size leads to a fast response of an MPPT algorithm under varying atmospheric condition with an increase in power losses. However, with a small step size, the losses under varying atmospheric conditions can be reduced with a trade of the slow response of MPPT controller under varying atmospheric conditions.

An improved P&O algorithm is used here as a solution to this conflicting problem, which is shown in Fig.2.22. Here, instead of the same perturbation size throughout the process, two step sizes (*k1* and *k2*, *k1>k2*) are used. The operating voltage of the PV module is perturbed and the resulting change in power is measured. Initially, when the error, i.e. $E = P(t) - P(t-1)$ is large the algorithm selects the step size as $k = k1$ to have a fast tracking of MPP. However, at the instant when $E <= \xi$, the step size $k2$ is chosen to have a minimum oscillation at MPP. The exact value of $k1$ is chosen based on the tracking time of MPP and it can be calculated as follows,

Let, t =Maximum tracking time of MPPT controller and T_S =Sampling time of the controller. Number of samples (or iteration) required for the MPPT controller to reach the MPP, $S = t / T_s$. In worst possible condition, the operating point has to cover from 0 V to V_{MPP} V (under STCs) within this S number of iterations. Therefore $k1$ can be calculated as, $k1 = V_{MPP} / S$. However, to minimize the power ripple at MPP, the step size $k2$ is chosen as 1/10 times of *k1.*

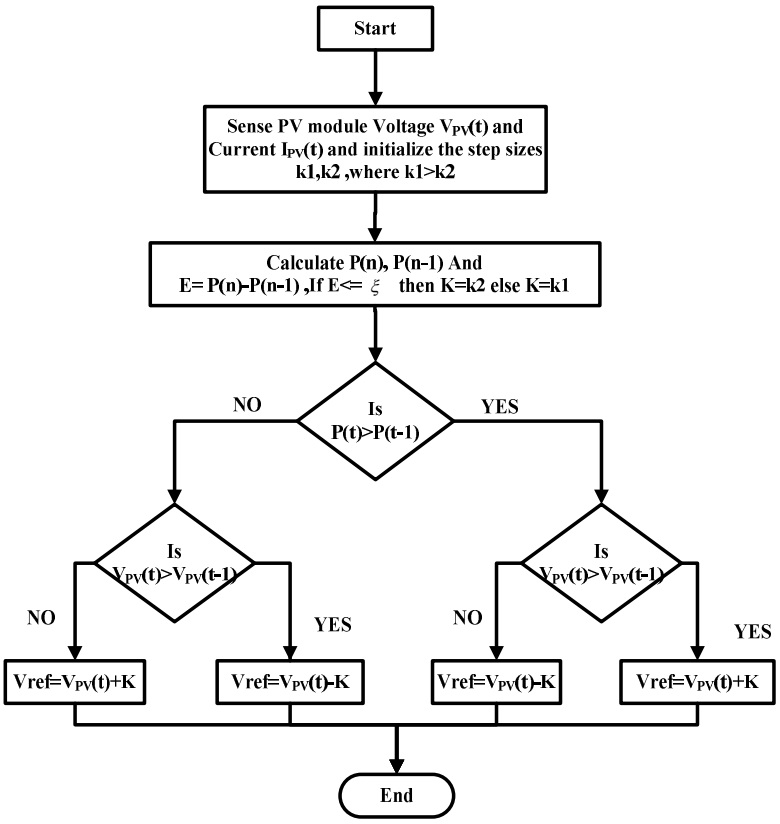

Fig.2.22: Flow Chart of P&O MPPT algorithm

2.8.7 Fuzzy Logic Based MPPT Controller

As discussed in the previous sub-section, the P&O based MPPT controller is the most commonly used algorithm in practice because of simplicity, easy implementation, and low cost. However, it has two major drawbacks.

1) Slow converging to the MPP.

2) At steady-state condition, the amplitude of the PV power is oscillates around the maximum power point that causes system power losses.

Here, a fuzzy-logic-based MPPT controller is proposed for the PV system. The proposed controller is capable of exploiting the advantages of the P&O method and eliminates the above mentioned drawbacks while generating variable stepsize for MPPT control. The detailed description on this is given below:

In this fuzzy logic controller, there are two input variables, which are error and change in error, one output variable which is the duty cycle. Each universe of discourse of the error (E), change in error (CE) and duty cycle (D) is divided into five fuzzy sets. Triangular membership functions have been used here. All the membership functions are shown in Fig.2.23. Fuzzy logic control generally consists of three stages: fuzzyfication, rule base and defuzzification. During fuzzification, numerical input variables are converted into linguistic variable based on a membership function. There are total 25 rules as listed in Table 2.10.

Each control rule can be described using the input variables E, CE and output variables D. For this MPPT, the inputs to the fuzzy logic controller are taken as a change in power with respect to change in voltage, E and change in error, CE. Once E and CE are calculated and converted to the linguistic variables, the fuzzy logic controller output, which is the duty ratio D of the power converter, can be looked up in a rule base table. The linguistic variables assigned to D for the different combinations of E and CE are based on the knowledge of the user. Here the rule base is prepared based on P&O algorithm where the voltage is repeatedly perturbed by a fixed amount in a given direction, and the direction is changed only if it detects a drop in power between steps. In the defuzzification stage, the fuzzy logic controller output is converted from a linguistic variable to a numerical variable still using a membership function. Fuzzy logic based MPPT controller have been shown to perform well under varying atmospheric conditions. However, their effectiveness depends a lot on the knowledge of the user or the control engineer in choosing the right error computation and coming up with the rule base table. The equations for error E and change in error CE are given as follows:

$$E = \frac{P(t) - P(t-1)}{V_{PV}(t) - V_{PV}(t-1)} \tag{2.58}$$

$$CE = E(t) - E(t-1) \tag{2.59}$$

Where E and CE are the inputs and D is the output of the fuzzy logic controller. E and CE is having five membership functions each namely, Negative High (NH), Negative Low (NL), Zero (ZE), Positive Low (PL), Positive High (PB). Similarly, the output D is also having five membership functions, namely, Very Small (VS), small(S), Medium (M), Positive Low (PL), Positive Big (PB).

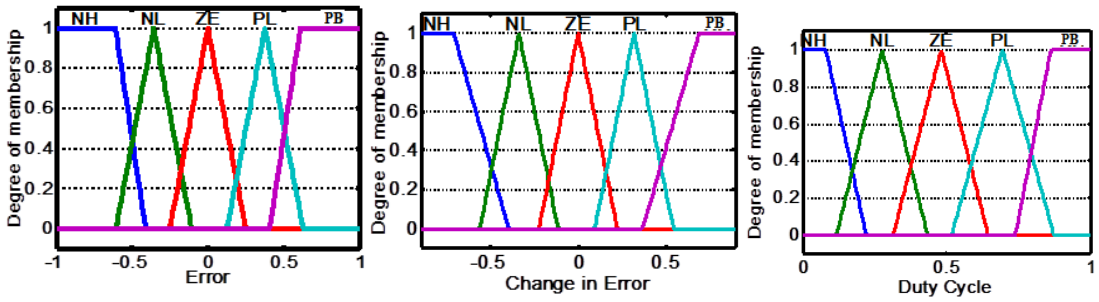

(a) (b) (c)

Fig.2.23: Membership functions for inputs (a) Error (E), (b) Change in Error(CE) and (c) output Duty Cycle (D) in Fuzzy logic controller based MPPT

Table 2.10: Fuzzy rule base for MPPT control

D ↘		CE				
		NH	**NL**	**ZE**	**PL**	**PB**
E	**NH**	PS	PB	PB	PS	M
	NL	S	PS	PB	PB	PB
	ZE	PB	M	M	M	S
	PL	VS	S	S	PB	PB
	PB	VS	VS	PB	PB	PB

The rule base that associates the fuzzy output to the fuzzy inputs is derived by understanding the system behaviour. Here the fuzzy rules are designed to incorporate the following considerations, keeping in view the overall tracking performance.

1. When the PV module output voltage is much greater than the voltage at MPP, then the change in the duty ratio of the DC-DC boost converter so as to bring the terminal voltage to VMPP.

2. When the PV module output voltage is less than the voltage at MPP, then the change in the duty ratio of the DC-DC boost converter is negative and it must be large so as to bring the terminal voltage to VMPP

3. When the PV module output voltage is close to the voltage at MPP, then the incremental duty ratio is small.

4. When the PV module output voltage is near to MPP voltage and is approaching it rapidly, then the change of duty ratio should be zero so as to prevent operating point deviation away from the MPP.

5. When the PV module output voltage is equal to the voltage at MPP, then the change of duty ratio should be maintained at zero.

Taking the above points into consideration the fuzzy rules are derived and the corresponding rule base is given Table 2.2. These rules can be employed in any PV system for MPPT irrespective of size and type of converter used. In the defuzzification process the crisp value of the change of duty cycle is obtained. Here, the center of gravity method is used for defuzzification. The crisp value of control output is computed by the following equation:

$$\Delta D = \frac{\sum_{i=1}^{n} W_i \Delta D_i}{\sum_{i=1}^{n} W_i} \tag{2.60}$$

Where n is the maximum number of effective rules, W_i is the weighting factor and ΔD_i is the value corresponding to the membership function of ΔD. The fuzzy logic based MPPT controller computes the variable step sizes to increment or decrement the duty cycle, therefore the tracking time is less and during steady-state conditions, its performance is much better than the P&O algorithm.

2.8.8 Simulation Results for MPPT control

Fig.2.24 (a) shows the power at maximum power point which is being tracked by P&O MPPT controller at different irradiation and constant temperature conditions. Similarly Fig 2.24(b) shows the power at maximum power point which is being tracked by the P&O MPPT controller at different temperature and constant irradiation conditions. Fig.2.25(a) shows the voltage, current and power at maximum power point which is being tracked by fuzzy MPPT controller at different irradiation and constant temperature conditions. Similarly Fig.2.25(b) shows the voltage, current and power at maximum power point which is being tracked by the fuzzy MPPT controller at different temperature and constant irradiation conditions. Fig.2.26 shows the response time of two MPPT controllers. At standard test condition, i.e. at irradiation of 1000 Watt/m^2 and temperature of 25^0C the P&O MPPT controller is taking 0.04 seconds to track the maximum power point, whereas the fuzzy MPPT controller is taking only 0.014 seconds to track the maximum power point. The fuzzy based MPPT controller can reduce the maximum power tracking time by 66% as compared to conventional perturb and observe based MPPT controller. It can also be observed that the fluctuation in power with fuzzy based MPPT control is quite less compared to conventional P&O based MPPT controller.

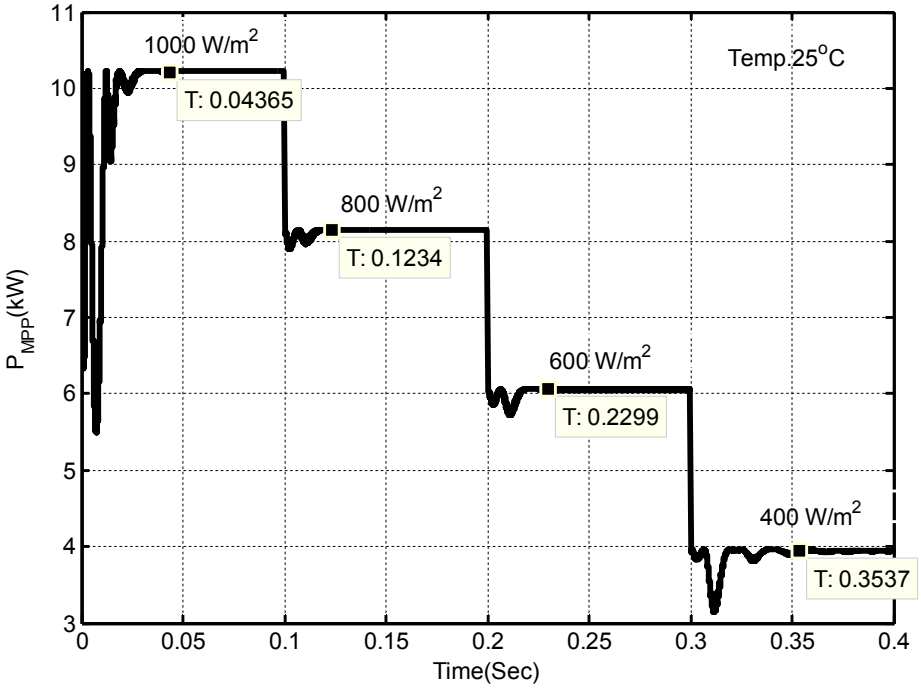

(a)

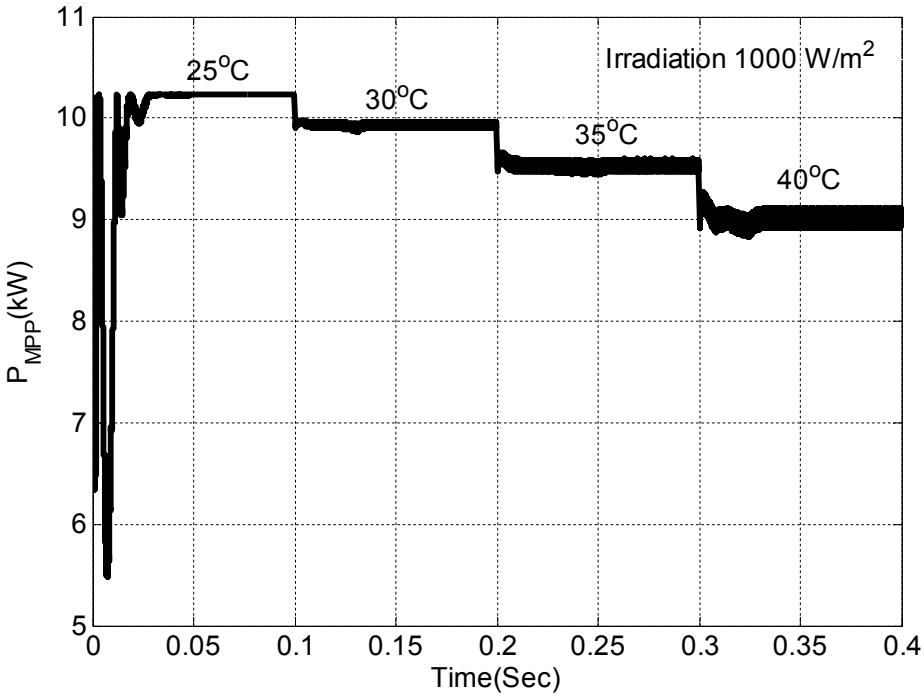

(b)

Fig.2.24: Simulation result of P&O based MPPT controller with (a) Varying irradiation and constant temperature (b) Varying temperature and constant irradiation

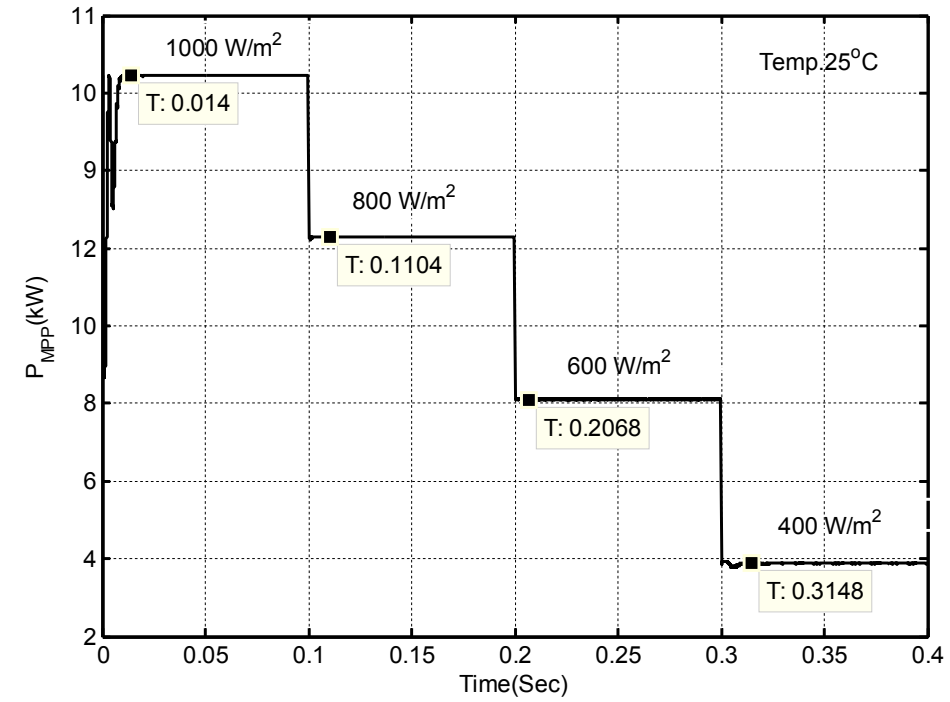

(a)

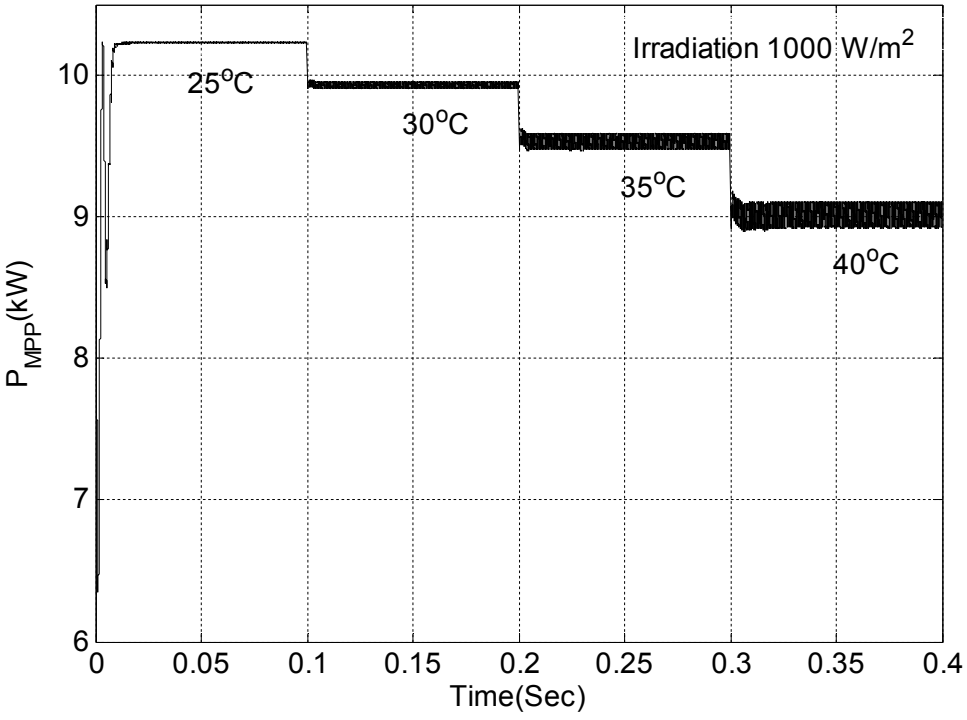

(b)

Fig.2.25: Simulation result of Fuzzy logic based MPPT controller under (a) Varying irradiation and constant temperature (b) Varying temperature and constant irradiation

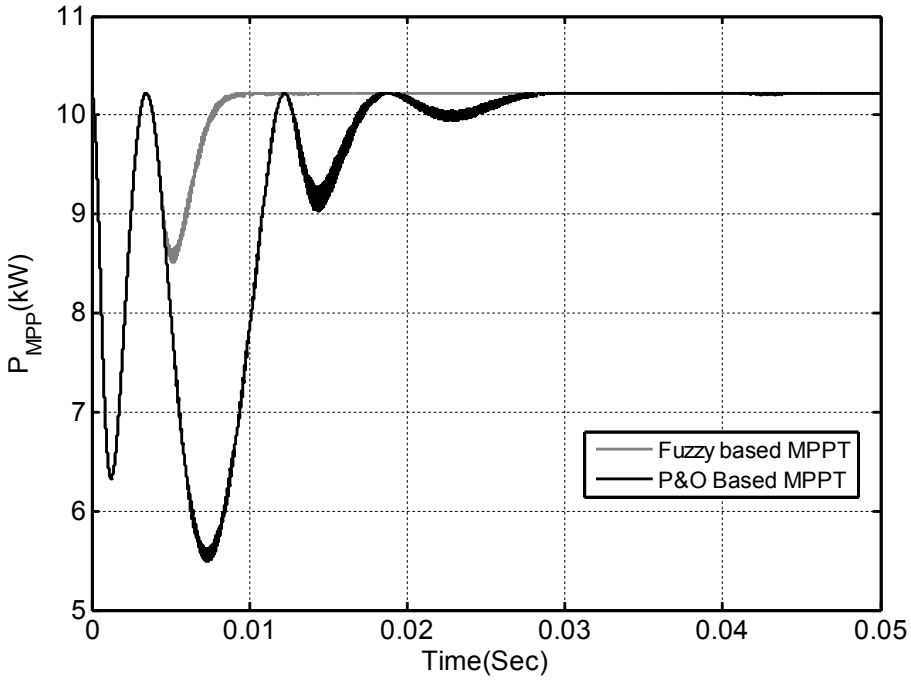

Fig.2.26: Comparative analysis of P&O and fuzzy based MPPT

2.9 Conclusion

This chapter presented a simplified approach of PV modelling under varying atmospheric conditions. All the parameters required for the modelling purpose are not provided by the manufacturer. However, some of the parameters required for the modelling of PV module are found in the manufacturer's data sheets. A step by step approach for the determination of unknown parameters is given in this chapter. A method has been developed using Gauss-Seidel iterative method to determine equivalent model parameters of the PV array. In order to validate the effectiveness of the aforementioned modelling scheme of PV module, a simulation program was developed in Matlab. The $I-V$ and $P-V$ characteristics for different temperatures, irradiations and circuit resistances were plotted and validated with the manufacturer's data sheet. The modelling of PV module is followed by the development of DC-DC boost converter transfer function for the input voltage control of the boost converter operating with duty cycle control. The transfer functions reveal important dynamic characteristics of the input controlled boost converter when it is fed by a PV module and with these transfer function the feedback controller for the control of the input voltage of the boost converter is designed. For the optimal use of PV module, a fuzzy-logic based MPPT controller is proposed. The rule base for the fuzzy controller is prepared based on the principle of P&O controller. A Simulink model is developed for both P&O and fuzzy based MPPT controller and based on these simulation results a comparative analysis is made. The results of the proposed fuzzy based MPPT exhibit a faster MPPT and less oscillation around the MPP under steady-state conditions.

Chapter 3: TWO STAGE TWO- LEVEL PVDG SYSTEM WITH IMPROVED POWER QUALITY FEATURES

[This chapter presents a 1-ϕ 230 V, 50Hz, two-level PV inverter system for power injection, harmonic elimination and reactive power compensation in 1-ϕ PV distributed generation (PVDG) system. Exhaustive simulation results are presented to investigate the performance of the PVDG system during different modes of controller action, varying atmospheric as well as varying load conditions. This chapter further investigates the performance of the PVDG system for night -mode operation.]

3.1 Introduction

Power electronics-based equipment forms the key components of power processing in distributed generation (DG) system because of the various benefits offered by them. These nonlinear devices/loads draw non-sinusoidal currents from the generation system, thereby leading to non-sinusoidal voltage at the Point of Common Coupling (PCC). This affects the operation of other loads, which require high quality of power. Therefore, a DG system has to deal with such harmonic current pollution. In addition to this, sometimes the DG system has to supply reactive power. These features of power quality can be conveniently integrated, in the DG system to compensate the reactive power and the local nonlinear load current harmonics. Here an effort has been made to develop a PV inverter with the features of real power injection as well as with the power quality enhancement (PQE) capability.

In a PVDG system, the demand of local load is fulfilled by the combined action of the PV inverter and the grid, based on the prevailing atmospheric and load conditions. During favourable atmospheric condition or light load condition, the local load demand is fulfilled by the PV inverter and the surplus power is fed to the grid. Similarly, during the unfavourable atmospheric condition or overload condition, both PV inverter and the grid jointly meet the load demand. Thus, in both the aforementioned conditions the quality of the grid current is decided by the load. Hence, with a nonlinear type local load in PVDG system, a proper control strategy has to be adopted to ensure that the grid current satisfies the required standards for grid interfaced system [67, 105, 106]. This chapter addresses the application of PQE scheme for the control of reactive power as well as harmonic current elimination in a 1-ϕ PVDG system.

To compensate the load current related power quality problems, shunts APFs are usually employed. Recently, many research papers have shown a substantial advancement in the performance of APF for 3-ϕ systems[107, 108]. Lately, power quality problems in 1-ϕ systems have drawn a lot of attention. The major concerns for a 1-ϕ system are current harmonics and reactive power, which are also the major issues in the modern DG system. Many control schemes have been proposed in a 1-ϕ system to overcome these PQ problems. The instantaneous reactive power (IRP) theory, which was initially implemented in 3-ϕ systems by Akagi et.al. [10], is one of the most appropriate theory for generation of

instantaneous reference compensating signal for APF. This theory gives an acceptable steady state and dynamic response for 3-ϕ systems and has been successfully extended by Lui et al. [11] thereby using the theory of instantaneous active and reactive power separation in αβ-coordinates for 1-ϕ system. The main goal of this chapter is to formulate and implement the 1-ϕ IRP theory in the PVDG system for the enhancement of power quality. Two possible ways to implement this PQE scheme in PVDG system are given in the following sections:

3.1.1 Power quality enhancement of PVDG System by an external APF

In this topology, an external APF is interfaced at the PCC to inject the compensating current for the reactive power and load current harmonic compensation. Fig.3.1 shows the implementation of an external APF based PVDG system for the PQE. Here the PV inverter is only used for the active power flow and shunt APF is responsible for the power Quality enhancement.

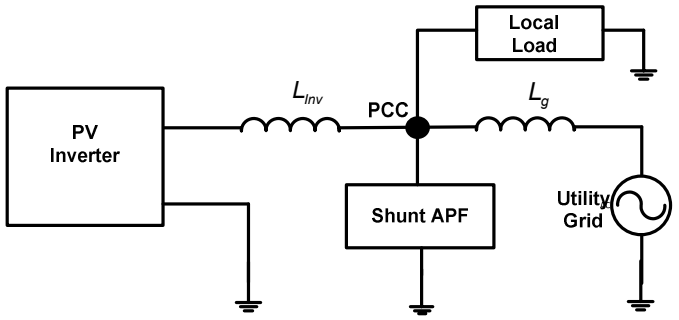

Fig.3.1: Single line diagram of a PVDG system with an external shunt APF at PCC

3.1.2 Power quality enhancement of PVDG System by PV Inverter

The main drawbacks of a PVDG system with an external APF topology for achieving PV power injection with harmonics and reactive power compensation are the high cost and the underutilization of the hardware circuits[109]. To decrease the complexity and for the optimal utilization of the hardware circuits, the complete PVDG system can be integrated with an APF capability. With this approach, the PV inverter regulates the active power flow between the PV module and the grid. In addition to this, the system also carries out the compensation of reactive power and load current harmonics thereby keeping the grid current sinusoidal. Here, the main idea is to maximize the utilization of the inverter rating, which is underutilized due to the intermittent nature of solar energy. In this topology a control scheme for active power filtering is integrated in the PV inverter itself to enhance the power quality of PVDG system. The single line diagram of such PVDG system with an integrated filtering mechanism is shown in Fig.3.2.

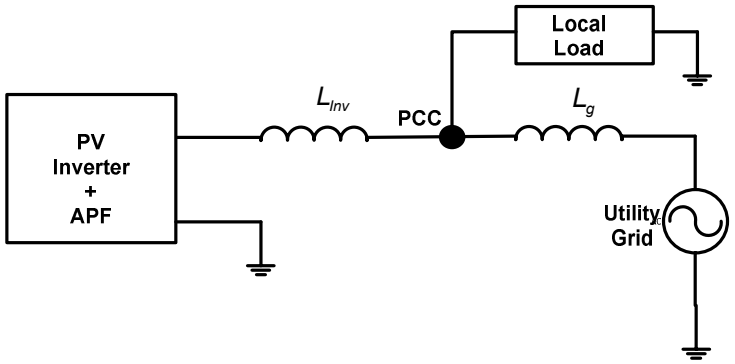

Fig.3.2 : Single line diagram of a PVDG system

Moreover, the PV inverter generates real power only during the daytime, with completely idle state at night time[110, 111]. This leads to underutilization of such an expensive system in the night time. Therefore, the PV inverter as a shunt APF has also been presented in this chapter to address this issue of underutilization of the PVDG system during night time.

The main objectives of this work are to effectively utilize the PV inverter in distributed generation system to achieve the following,

- To transmit the maximum possible real power from the PV module
- To meet the real power demanded by the local load
- To compensate for the reactive and harmonic components of load current at PCC
- To utilize the PV inverter as a shunt APF during night time.

Thus, with an adequate control of PV inverter, all the above-mentioned objectives can be achieved either separately or simultaneously. Hence, the power quality requirements as per the utility standards at the PCC[67] can be accomplished without requiring any additional hardware circuits.

3.2 Block Diagram of System Controller

The block diagram of the above mentioned PVDG system with an integrated PQE capability is depicted in Fig.3.3. The key components of the system are PV array, two-stage converter comprising of boost type DC-DC converter and DC-AC inverter, local load (linear/non-linear) and the grid. The PV array is connected to the boost converter through a capacitor (C_{PV}), which helps in controlling PV voltage, thereby extracting maximum power from it by using MPPT algorithm. The DC-DC converter is connected to DC-AC inverter via a DC-link capacitor (C_{dc}). The voltage across (C_{dc}) is maintained constant through the outer voltage control loop of DC-AC inverter to facilitate complete active and reactive power transfer to the AC side of the inverter. The grid voltage (v_g), connected at the PCC is assumed to be capable of absorbing both active and reactive power whenever the generated power from the PV system is more in comparison to the local load power demand and vice-

versa. The DC-AC inverter is the key element of the PVDG system as it interfaces with the PV module to the grid and delivers the generated power with improved power quality features. PV inverter control with aforementioned features is achieved with the following controllers, load current (i_L) analyser, which comprises of demanded load real power, reactive power, and harmonic components, DC-link voltage controller, which is used to maintain constant DC-link voltage during varying atmospheric, and load conditions and finally the reference inverter current (i_{ref}) estimator. This reference inverter current (i_{ref}) is used for the control of the inverter using PWM scheme to feed active and reactive power to the local load and the grid with improved power quality features.

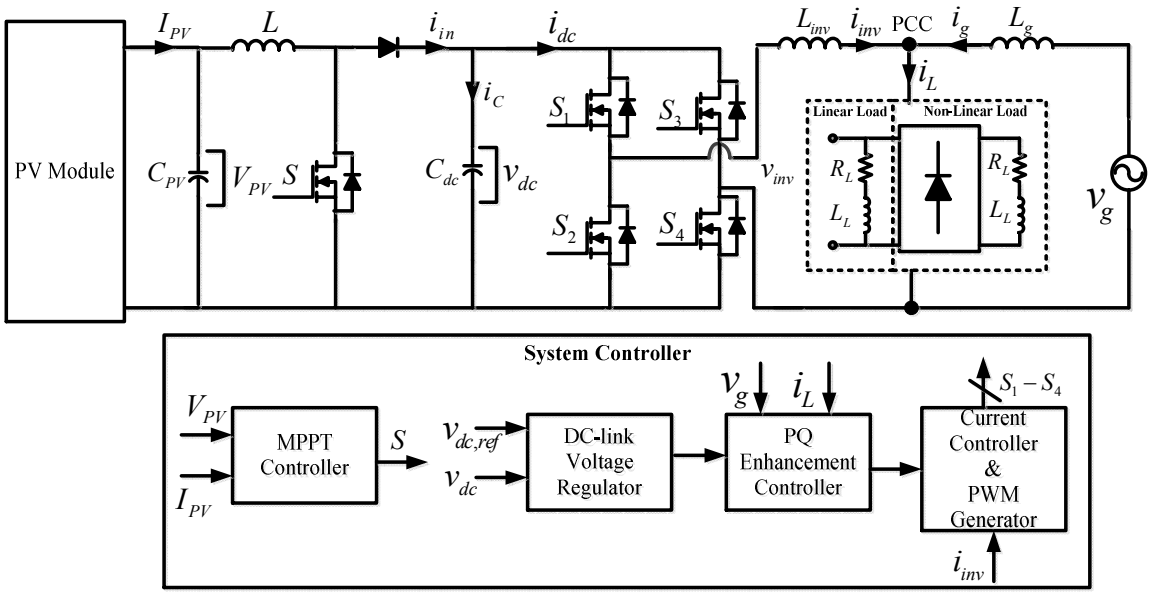

Fig.3.3: Block diagram of two-stage 2-level PVDG system with an enhanced PQ feature

3.3 Control Scheme of PV Inverter

The 1-ϕ two-level PV inverter used in PVDG system is shown in Fig.3.3. DC-link of PV inverter is fed from a PV module through a boost type DC-DC converter for MPPT control. The AC side of the inverter circuit results in the output terminal voltage as, v_{inv}, which is given as,

$$v_{inv} = S.v_{dc} \tag{3.1}$$

Where, $S = S_1S_4 - S_2S_3$, with S_i, $i = 1,2,3,4$ is the state of each switch which is having two discrete values: '1' when the switch is turned on and '0' when it is turned off. Therefore S is having two discrete values -1 and 1 which gives an inverter output voltage as $-v_{dc}$ and v_{dc}

respectively. Moreover, the considered PV inverter can be completely described by the following two differential equations:

$$L_{inv}\frac{di_{inv}}{dt} = S.v_{dc} - v_g \tag{3.2}$$

$$C_{dc}\frac{dv_{dc}}{dt} = i_{in} - S.i_{inv} \tag{3.3}$$

The grid tie inverter control in PVDG system mainly consists of two cascaded control loops[112]. One is the internal current loop, which controls the current and the other one is DC-link voltage control loop, which regulates the DC-link voltage [Ref]. For the issues related to power quality current loop is responsible. Therefore, harmonic and reactive power compensation is the key properties of the current controller. However, the DC-link voltage controllers are designed for the power flow balancing in the PVDG system. The control logic of the 1-ϕ PV inverter control scheme with enhanced power quality features is depicted in Fig.3.4, which consists of following three control blocks,

- DC-link voltage controller
- Grid synchronization controller
- Reference current estimator
- Current controller and firing pulse generator

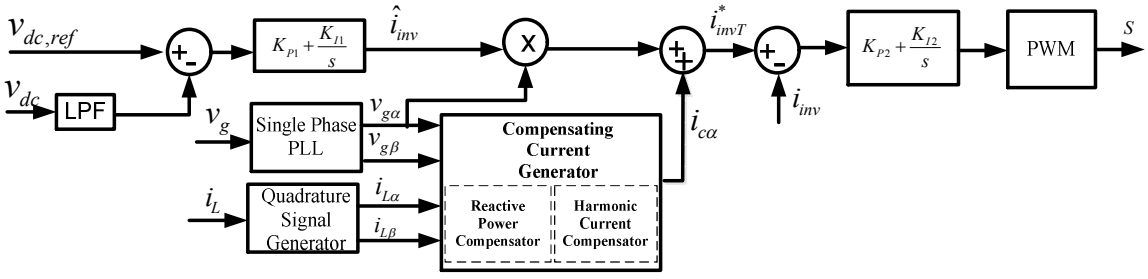

Fig. 3.4: System Controller for 1-ϕ PVDG System

The detailed descriptions of each block are discussed as follows,

3.3.1 DC-link Voltage Controller

Power generated by PV module is of varying nature. Therefore the DC-link plays a vital role in transferring this variable power from the PV module to the grid. Power generated by PV module is represented as a current source connected to the DC-link of a PV inverter. The power transferred from the PV module to the grid through the DC-link is represented by an equivalent circuit shown in Fig.3.5.The generated PV current injected into the DC-link at a voltage level V_{dc} can be given as,

$$i_{in} = \frac{P_{PV}}{v_{dc}} \tag{3.4}$$

Where P_{PV} is the generated power from the PV Module

The current flowing to the other side of the DC-link can be represented as,

$$i_{dc} = \frac{P_{inv}}{v_{dc}} = \frac{P_g + P_{Loss}}{v_{dc}} \tag{3.5}$$

Where P_{inv} : Total power input to the inverter side

P_g : Total power supplied to the grid

P_{Loss} : Inverter loss

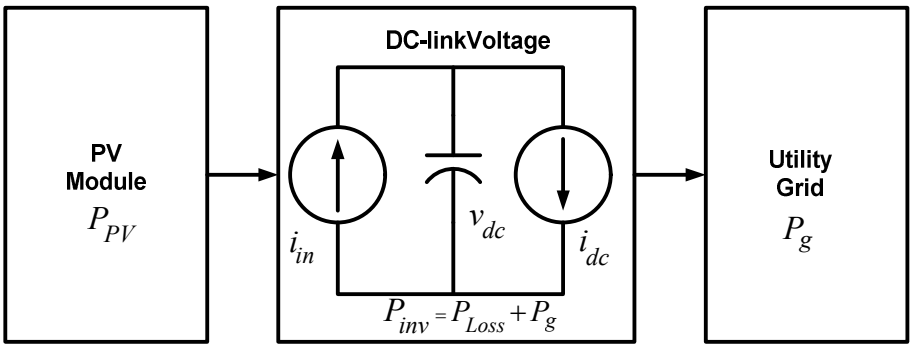

Fig.3.5: Equivalent diagram of DC-link

The control of DC-link voltage carries the information regarding the exchange of active power in between the PV module and the grid. Thus the output of a DC-link voltage controller results in an active current $(\hat{i}_{inv})$ .Throughout this thesis, $\hat{x}$ indicates the maximum value of x .For the calculation of $\hat{i}_{inv}$, the power balance between the input and the output of the PV inverter is used. The following expression defines P_{in} and P_{out}, where the losses in the capacitor and MOSFET have been neglected.

$$P_{in} = i_{in} v_{dc} - \frac{1}{2} R \hat{i}_{inv}^2 \tag{3.6}$$

$$P_{out} = \frac{1}{2} \hat{v}_g \hat{i}_{inv} \tag{3.7}$$

Where R is the resistance of filter inductor

Considering that , $P_{in} = P_{out}$, we have,

$$i_{in} v_{dc} - \frac{1}{2} R \hat{i}_{inv}^2 = \frac{1}{2} \hat{i}_{inv} \hat{v}_g \tag{3.8}$$

Finally the expression for $\hat{i}_{inv}$ is obtained as,

$$\hat{i}_{inv} = -\frac{\hat{v}_g}{2R} + \sqrt{\frac{\hat{v}_g^2}{4R^2} + \frac{2i_{in}v_{dc}}{R}} \tag{3.9}$$

The block diagram of DC-link voltage controller for 1-ϕ two-level PV inverter is given in Fig.3.4. Here the actual DC-link voltage of PV inverter is sensed and passed through a first-order low pass filter (LPF) to eliminate the presence of switching ripples in the DC-link voltages. The difference of this filtered DC-link voltage and reference DC-link voltage (v_{dc}^*) is given to a discrete-PI regulator to maintain a constant DC-link voltage under varying atmospheric and load conditions.

The DC-link voltage error (Δv_{err}) in n^{th} sampling instant is given as:

$$\Delta v_{err}(n) = v_{dc}^*(n) - v_{dc}(n) \tag{3.10}$$

The output of the discrete-PI regulator at n^{th} sampling instant is expressed as,

$$i_{inv}(n) = i_{inv}(n-1) + K_{P1}(\Delta v_{err}(n) - \Delta v_{err}(n-1)) + K_{I1}\Delta v_{err}(n) \tag{3.11}$$

Where K_{P1} and K_{I1} are proportional and integral gains of the DC-link voltage regulator.

In order to design the voltage controller, a suitable transfer function is obtained by the linearization of the equation (3.11). In this case it is considered that the PV module operates at STCs.

By considering only the DC component of the term Si_{inv}, equation(3.3) is equivalent to,

$$S\hat{i}_{inv} = i_{in} - C_{dc}\frac{dv_{dc}}{dt} \tag{3.12}$$

In order to simplify the transfer function, the input currents to the DC-link i_{in} is considered as disturbances and the term S constant. Under this assumption, the following transfer function is obtained:

$$\frac{\hat{v}_{dc}(s)}{\hat{i}_{inv}(s)} = -\frac{S}{sC_{dc}} \tag{3.13}$$

Where C_{dc} and the term S is defined for STCs.

3.3.2 Grid Synchronization Controller

Synchronization between the PV inverter and the grid means that both will have the same phase angle, frequency and amplitude. In order to accomplish this, a 1-ϕ phase locked loop (PLL) is used. It is a feedback control system which automatically adjusts the phase of a locally generated signal to match the phase of an input signal and hence provide a unity power factor operation. In a grid connected PV system the objective of the PLL is to synchronize the inverter output current with the grid voltage. The schematic diagram of the 1-ϕ PLL is shown in Fig. 3.6. Here the input to the PLL structure is the grid voltage and output

is its phase angle. This phase angle is used to generate the sine wave which acts as a reference signal to the control system. The time required for the synchronization is dependent on the PI block parameters, which are computed below.

From the schematic diagram (Fig.3.6), it can be observed that the error in the PI controller of the PLL structure is given by,

$$e = V_g \sin\theta_g \cos\theta - V_g \cos\theta_g \sin\theta = V_g \sin(\theta_g - \theta) \tag{3.14}$$

Where θ_g and θ are phase angles of the grid and the PLL respectively.

In order to tune the parameters of PI controller, the input to the PI controller is linearized around a working point. Under steady state operation, the error in PI controller is zero and the linearized error in PI controller can be expressed by Taylor series as,

$$f(x) \approx f(x_0) + f'(x_0).(x - x_0) \Leftrightarrow \sin(x)\big|_{x=0} = \cos(0)(x-0) = x \tag{3.15}$$

Thus, the error in PI controller becomes,

$$\varepsilon = V_g(\theta_g - \theta) \tag{3.16}$$

The linearized small signal transfer function of the PLL is given by,

$$Pll(s) = \frac{V_g\left(K_P + \frac{K_I}{s}\right)\frac{1}{s}}{1 + V_g\left(K_P + \frac{K_I}{s}\right)\frac{1}{s}} = \frac{V_g\left(\frac{K_P}{K_I}\right)(1 + s K_I)}{s^2 + V_g K_P s + V_g\left(\frac{K_P}{K_I}\right)} \tag{3.17}$$

This is a second order system with one real zero. K_P is the proportional gain and K_I is the integral gain. The natural frequency and damping ratio can thus be stated as, $\omega_n = \sqrt{\frac{V_g K_P}{K_I}}$ and $\xi = \sqrt{\frac{V_g K_P K_I}{4}}$ respectively. The relationship between the natural frequency and the rise time for a second order system is known to be $t_r \approx \frac{1.8}{\omega_n}$ [113]. The parameters describing the PI controller can then be specified in terms of rise time and grid voltage amplitude, $K_I \approx \frac{\sqrt{2}}{\omega_n} \approx 0.79 t_r$ and $K_P \approx \frac{\omega_n \sqrt{2}}{\hat{V}_g} \approx \frac{2.55}{t_r V_g}$ [ref]. For a rise time of five msec, with optimal damping the parameters of the PI controller equals, $K_P = 12.75$ and $K_I = 3.95 \times 10^{-3}$.

However, if the grid frequency differs from the nominal 50 Hz, the output from delay block in Fig. 3.6 is $\cos(\theta_g) + A\sin(\theta_g)$. Assuming that a cosine trigonometric function is used to compute the $\cos(\theta)$ and the error into the PI controller becomes,

$$Err = V_g \sin(\theta_g - \theta) - V_g A \sin(\theta_g).\sin(\theta) \tag{3.18}$$

Which contains an additional AC component at $(\omega_g + \omega) rad/\sec$. This would lead to an error in PLL output, which is the major drawback of the conventional transport delay based PLL. A modified PLL is developed to cancel out errors because of input frequency variation. In modified PLL, the cosine of the PLL in feedback path is replaced by a sine function with another 5 msec delay block. With this dual transport delay based PLL (DTDPLL), the error into the PI controller becomes:

$$\begin{aligned} Err &= V_g \sin(\theta_g)\left[\cos(\theta) + A\sin(\theta)\right] - V_g\left[\cos(\theta_g) + A\sin(\theta_g)\right].\sin(\theta) \\ &= V_g \sin(\theta_g - \theta) \end{aligned} \tag{3.19}$$

From the equation (3.19), it is observed that the error due to input frequency variation is cancelled out by feedback transport delay block.

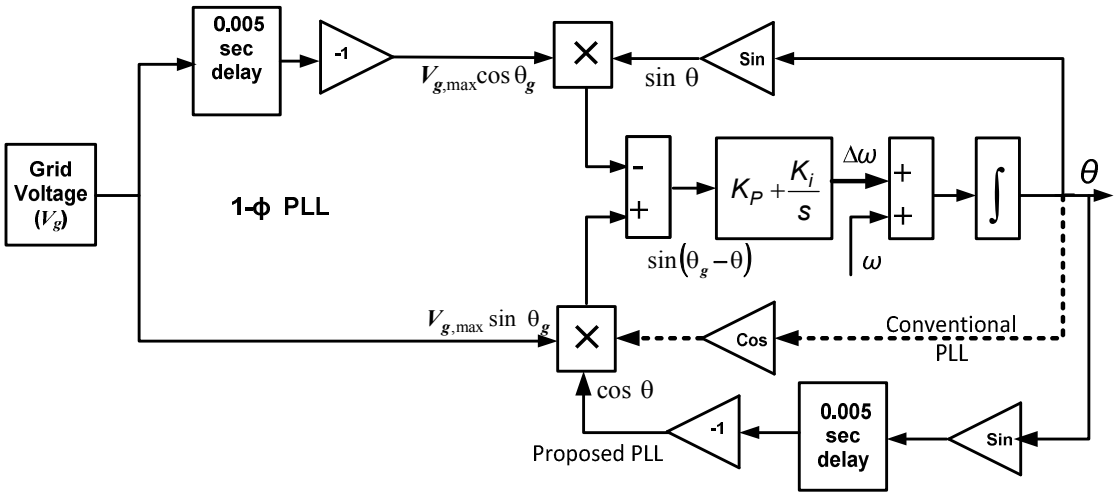

Fig. 3.6: Controller for grid synchronization

In order to validate the efficacy of DTDPLL for frequency other than 50 Hz input, the proposed PLL is simulated with an input frequency of 45 Hz which is far more than normal frequency variation. Initially conventional PLL is employed and after 0.04 seconds, the proposed PLL is employed. The corresponding simulation results are shown in Fig. 3.7. Fig. 3.7(a) shows the output phase angle of the PLL in rad/Sec whereas Fig. 3.7(b) shows the i/p and o/p signal. It can be observed that, with conventional TDPLL the error is found to be significant when an input signal is having other than 50 Hz frequency. However, with proposed DTDPLL, the error is almost zero and input and output signals are found to be exactly in phase with each other. In order to show the dynamic performance of the proposed PLL under frequency variation, simulation results of input and output signal under different frequency inputs are shown in Fig. 3.8.

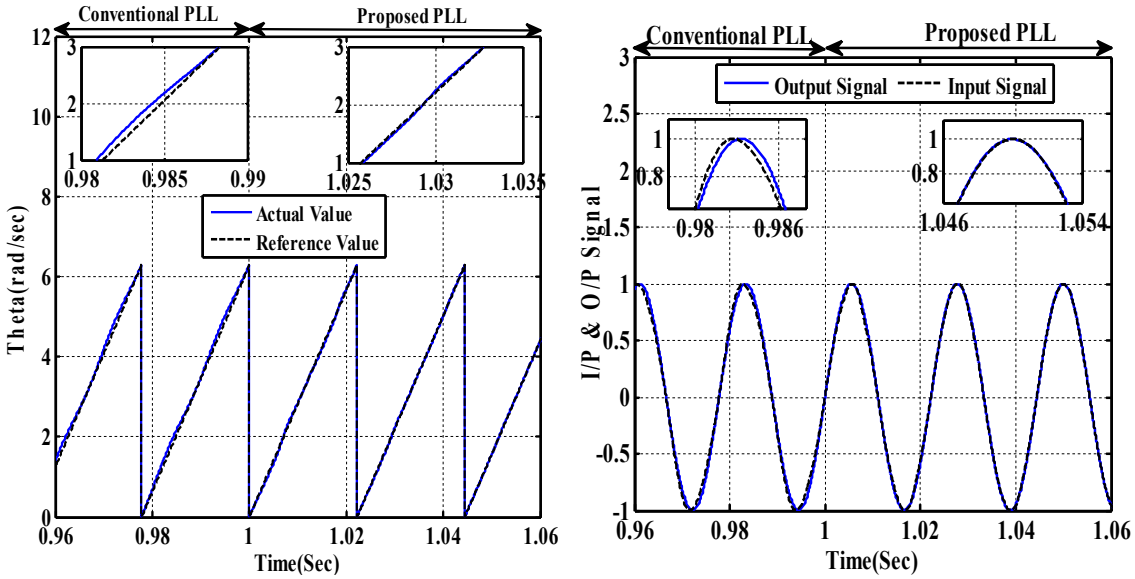

Fig. 3.7: (a) Output phase angle (b) input and output signal with conventional and proposed PLL when input signal frequency other than 50Hz

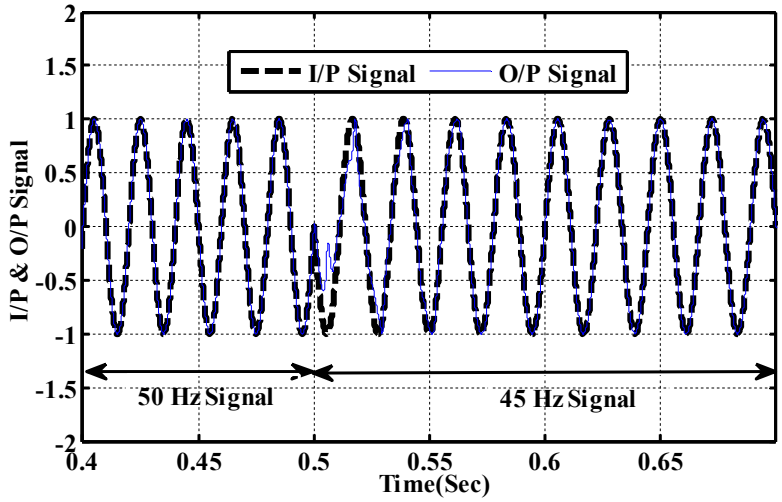

Fig. 3.8: Input and output signal of proposed PLL with frequency variation

3.3.3 PV Inverter Reference Current estimator

The nonlinear load is shown in Fig.3.9. In general, the current drawn by such type of load from the source can be divided into following three parts,

i_{Lp} : Real Power Component

i_{Lq} : Reactive Power Component

i_{Lh} : Harmonic Component

This reference current estimator has the task of calcuating these components of current that has to be generated by the PV inverter. The grid voltage (v_g), DC-link capacitor voltage (v_{dc}), and load current (i_L) are measured to obtain reference compensating current (i_{ref}). One of the key points for proper estimation of i_{ref} is to use a reliable estimation method.The IRP theory is one of the well accepted theories for the estimation of reference compensating current for shunt active power filter. The extension of the 1-ϕ IRP theory[114] is used here for estimating the reference compensating current (i_{ref}).The IRP theory is based on a set of instantaneous powers defined in the time domain.

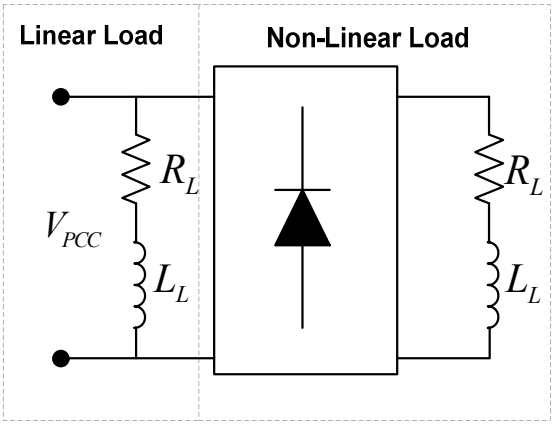

Fig.3.9 : Test load used in this work

Let the 1-ϕ grid voltage be given as,

$$V_g = V_m \sin \omega t \tag{3.20}$$

and the local non-linear load current in PVDG system be given as,

$$i_{_L} = \sum i_{Ln} \sin\left(\left(n\omega t\right) + \phi_g\right) \tag{3.21}$$

The IRP theory starts with the transformation of source voltage and currents into $\alpha\beta -$ stationary reference frame. The 1-ϕ grid voltage and load current representation in $\alpha\beta -$ coordinates with a $\pi / 2$ lead is given by,

$$\begin{bmatrix} v_{g\alpha}(\omega t) \\ v_{g\beta}(\omega t) \end{bmatrix} = \begin{bmatrix} v_g(\omega t) \\ v_g\left(\omega t + \frac{\pi}{2}\right) \end{bmatrix} = \begin{bmatrix} \sqrt{2}V_g \, sin\, \omega t \\ \sqrt{2}V_g \cos \omega t \end{bmatrix} \tag{3.22}$$

$$\begin{bmatrix} i_{L\alpha}(\omega t) \\ i_{L\beta}(\omega t) \end{bmatrix} = \begin{bmatrix} i_L\left(\omega t + \phi_g\right) \\ i_L\left(\omega t + \phi_g + \frac{\pi}{2}\right) \end{bmatrix} \tag{3.23}$$

The instantaneous real power (p) and the instantaneous reactive power (q) are defined from instantaneous grid voltages and load currents on the $\alpha\beta-$ axes as,

$$p(\omega t) = v_{g\alpha}(\omega t) i_{L\alpha}(\omega t) + v_{g\beta}(\omega t) i_{L\beta}(\omega t) \tag{3.24}$$

$$q(\omega t) = -v_{g\beta}(\omega t) i_{L\alpha}(\omega t) + v_{g\alpha}(\omega t) i_{L\beta}(\omega t) \tag{3.25}$$

Equations (3.24) and (3.25) can be written in matrix form as,

$$\begin{bmatrix} p(\omega t) \\ q(\omega t) \end{bmatrix} = \begin{bmatrix} v_{g\alpha}(\omega t) & v_{g\beta}(\omega t) \\ -v_{g\beta}(\omega t) & v_{g\alpha}(\omega t) \end{bmatrix} \begin{bmatrix} i_{L\alpha}(\omega t) \\ i_{L\beta}(\omega t) \end{bmatrix} \tag{3.26}$$

The Instantaneous active (p) and reactive (q) powers can be decomposed into an average (DC) and an oscillatory component (AC) as,

$$p(\omega t) = \bar{p}(\omega t) + \tilde{p}(\omega t) \tag{3.27}$$

$$q(\omega t) = \bar{q}(\omega t) + \tilde{q}(\omega t) \tag{3.28}$$

The above power components can be defined as,

$\bar{p}(\omega t) =$ DC component of the instantaneous power $p(\omega t)$, which is related to the conventional fundamental active current.

$\tilde{p}(\omega t) =$ AC component of the instantaneous power $p(\omega t)$ having zero average value, which is related to the harmonic currents caused by the AC component of the instantaneous real power.

$\bar{q}(\omega t) =$ DC component of the imaginary instantaneous power $q(\omega t)$, which is related to the reactive power generated by the fundamental components of voltages and currents.

$\tilde{q}(\omega t) =$ AC component of the instantaneous imaginary power $q(\omega t)$, which is related to the harmonic currents caused by the AC component of instantaneous reactive power.

Once the calculated real and reactive powers are separated into their average and oscillating parts, the undesired portions of the real and imaginary powers of the load that should be compensated by PV inverter can be selected.

Let p_C and q_C be the powers to be generated by the PV inverter to compensate the harmonic and reactive power of the system, then the compensating currents can be calculated in *αβ*-reference frame as,

$$\begin{bmatrix} i^*_{C\alpha}(\omega t) \\ i^*_{C\beta}(\omega t) \end{bmatrix} = \begin{bmatrix} v_{g\alpha}(\omega t) & v_{g\beta}(\omega t) \\ v_{g\beta}(\omega t) & -v_{g\alpha}(\omega t) \end{bmatrix}^{-1} \begin{bmatrix} p_C(\omega t) \\ q_C(\omega t) \end{bmatrix} \tag{3.29}$$

As the PV inverter has to deliver the total load active as well as reactive power demand of the load, hence the above equation (3.29)can also be expressed as,

$$\begin{bmatrix} i^*_{C\alpha}(\omega t) \\ i^*_{C\beta}(\omega t) \end{bmatrix} = \frac{1}{v^2_{g\alpha} + v^2_{g\beta}} \begin{bmatrix} v_{g\alpha}(\omega t) & v_{g\beta}(\omega t) \\ v_{g\beta}(\omega t) & -v_{g\alpha}(\omega t) \end{bmatrix} \begin{bmatrix} p_L(\omega t) \\ q_L(\omega t) \end{bmatrix} \quad (3.30)$$

Therefore, the reference current for PV inverter in the single phase PVDG system with power quality enhancement capabilities can be expressed as,

$$i^*_{C\alpha}(\omega t) = \frac{1}{v^2_{g\alpha} + v^2_{g\beta}} \left[-v_{g\alpha}(\omega t) \cdot \tilde{p}(\omega t) + v_{g\alpha} \cdot \bar{p}(\omega t) + v_{g\beta}(\omega t) \cdot \tilde{q}(\omega t) + v_{g\beta}(\omega t) \cdot \bar{q}(\omega t) \right] \quad (3.31)$$

Where $\frac{1}{v^2_{g\alpha} + v^2_{g\beta}}$ and the term $\bar{p}(\omega t)$ represents the total amount of active power that the PV inverter can deliver to the grid or local load by regulating the DC bus.

3.3.4 Current Controller and Firing Pulse Generator

The DC-link voltage controller output is multiplied with the grid voltage template and then added to the reference compensating current calculated from the equation (3.31) to generate the total reference current of the PV inverter. This reference current (i_{refT}) is compared with the actual inverter current (i_{inv}) and the error is processed in a controller. The outputs of the controller set the 1-ϕ reference signals (modulating signals) for the PWM technique implemented in the controller. To produce PWM switching patterns for the switching devices, the PWM controller compares the modulating signals with triangle carrier signal. The switching operation of the power switches forces the PV inverter current to follow the generated reference current.

3.4 Design of DC Capacitor

The energy storage capability of the DC-bus of the PV inverter should be sufficient to sustain disturbances arising due to atmospheric and load variations. The value of DC-link voltage (v_{dc}) could overshoot the reference DC-link voltage (v^*_{dc}) upon decrease in value of the load or instant increase in solar irradiation. On the other hand, v_{dc} could go below v^*_{dc}, upon an increase in value of the load or decrease in solar radiation. Therefore, during these transient conditions, the DC bus voltage of the PV inverter exhibits two extreme possible values. If the DC-link voltage is allowed to change by $\pm 10\%$,then corresponding to the instant application of load or decrease in solar irradiation the value of $v_{dc} = 0.9 v^*_{dc}$. On the other hand, during load withdrawal or increase in solar irradiation the value of $v_{dc} = 1.1 v^*_{dc}$.

The energy exchange (Δe) between the PV inverter and load can be expressed as,

$$\Delta e = \frac{1}{2} C_{dc} {v_{dc}}^2 = \frac{1}{2} C \left[(v^*_{dc} - v_{dc}).(v^*_{dc} + v_{dc}) \right] \quad (3.32)$$

Here, a factor of 1.53 is considered and, thus, the 326 V (peak) grid voltages give a reference DC bus voltage (v_{dc}^{*}) of 500 V[84]. The $\frac{\pi}{2}$ phase shift between $\alpha\beta$ -axis quantities results in a minimum 60^{0} delay in computation (ζ_d) of instantaneous load active and reactive power demands[114]. For the rated load of 10kVA, the energy exchange during transient conditions can be determined (with a maximum active power demand of 7.5 kW) as,

$$\Delta e = \zeta_d \times P_{Max} = (3.33msec) \times 7500 = 25J$$

Substituting, $\Delta e = 25J$, $v_{dc}^{*} = 500V$, $v_{dc} = 1.01v_{dc}^{*} = 505V$ and $v_{dc} = 0.99v_{dc}^{*} = 495V$ in equation (3.32)gives,952 or 1092 μF respectively. In the simulation model, the value of the DC-link capacitor (C_{dc}) is considered as 2200 μF .

3.5 Result and Discussion

Computer simulation studies under different atmospheric and load conditions have been carried out to evaluate the performance of the 1- ϕ two-stage two-level PVDG system for harmonic elimination and reactive power compensation. The simulation of the entire system has been carried out in a MATLAB/Simulink environment, and the simulation model of the entire system is shown in Fig.3.10.

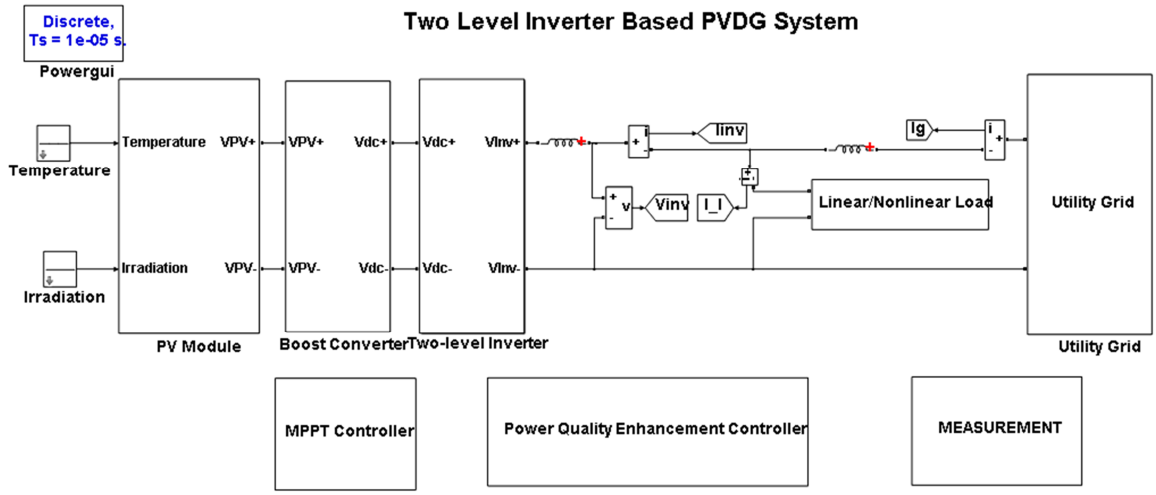

Fig.3.10: Simulink model of 2-level Inverter based PVDG System

The control algorithm for the PVDG system is modelled in MATLAB/Simulink. Here the reference compensating current is derived from the IRP theory discussed in section.3.3.3 by using the measured grid voltage, load current and the DC-link capacitor voltage of the two-level PV inverter. A PWM current controller has been used to generate the gating signals for the MOSFETs of the two-level PV inverter. The parameters used in the simulation are given in Table.3.1. A non-linear load consisting of an uncontrolled rectifier with a RL element on the DC side, has been considered as the local load for the PV inverter. Two different

combinations of RL element have been taken for the analysis of the system, which are mentioned in Table.3.1.Extensive simulation studies have been carried out to investigate the performance of the PVDG system for harmonic elimination and reactive power compensation under different loading and atmospheric conditions.

Table 3.1. Parameters used in the simulation study

Parameter	Value
Grid voltage	Single-phase, 230 V, 50 Hz
PV Array	10.2 kW
DC bus reference voltage	500 V (for PV Inverter)
DC bus capacitance	2200 μF
Coupling inductor of PV Inverter	L_{inv} = 1 mH
Grid side inductance	L_g = 0.1 mH
PWM switching frequency	3 kHz
PI controller parameters	For DC-link voltage control: K_p= 1.3, K_i = 0.8 For Current Control: K_p= 0.1, K_i = 0
Load	Single-phase uncontrolled rectifier, **Load-1**: R_{dc} = 10 Ω, L_{dc} = 21 mH (Light Load) **Load-2**: R_{dc} = 3.306 Ω, L_{dc} = 10.5 mH(Over Load)

3.5.1 PVDG system without and with PQEC

This section presents simulation results of PVDG system in different modes of operation of PQEC. These results pertain to STCs for PV modules while employing the MPPT controller, with a non-linear load (Load-1) connected across PCC. In order to study the steady state and transient performance of the system for these conditions, the following events are considered to take place.

At *t* = 0 Sec., PQEC is off (disabled mode).

At *t* =0.4 Sec., PQEC is on (enabled mode).

The simulation results of the PVDG system under this condition are given in Fig.3.11. The waveforms of grid voltage (v_g), PV inverter current (i_{inv}), load current (i_L), grid current (i_g) and DC-link voltage (V_{dc}) are shown in Fig.3.11 (a) and from these simulation results, following observations are made:

1. Initially the PQEC is in disabled mode. During this condition, the load current demand is less than that generated by PV inverter and hence, the surplus current is fed to the grid. This can be observed from Fig.3.11(a), where grid current is out of phase with the grid voltage. As the PQEC is in disabled mode, the PV inverter generates

sinusoidal current as per the PWM scheme. However, the non-linear load connected across the PV inverter, draws a distorted current from the PV inverter, which leads to the injection of distorted current into the grid. Therefore, in this condition, even though the PV inverter generates a sinusoidal current, the non-linear nature of load forces the grid current to be non-sinusoidal.

2. With the PQEC is enabled at t=0.4 Sec., the controller generates a reference current for the PV inverter which includes both harmonics and reactive components of load current. Therefore, in this condition the PV inverter generates a non-sinusoidal current to compensate the harmonics and reactive components of load current, thereby feeds a pure sinusoidal current to the grid. This demonstrates the capability of the PVDG system for harmonic compensation. Similar to a previous condition, as the load current demand is less than that generated by PV inverter, the surplus current is fed to the grid. This can be observed from Fig.3.11(a), where grid current is out of phase with grid voltage.

3. With the implementation of Power Quality Enhancement (PQE) scheme, the reactive component of current required by the local load is completely supplied by the PV inverter. Thus, the grid current is found to have a unity displacement factor with the grid voltage, thereby demonstrating the reactive power compensation capability of PQEC.

4. At the instant when the PQEC is enabled the DC capacitor voltage of PV inverter drops from its reference value to compensate the load current harmonics. This drop in capacitor voltage is restored in 4-5 cycles, as can be observed from Fig.3.11(a). The DC-link voltage regulator has ensures the regulation of the capacitor voltage.

Fig.3.11 (b) and Fig.3.11 (c) shows the generated active and reactive power curves of the PVDG system under these two different modes of operation of PQEC. From these simulation results following observations are made,

1. It can be observed from the power curve depicted in Fig.3.11(b) that, with the implementation of the MPPT control scheme, the generated PV power is found to reach the maximum power .

2. Fig.3.11(b) shows that, under both modes of operation of PQEC, the generated PV power is more than load demand. Thus, the surplus PV power is fed to the grid. The positive value of the active power supplied by the PV inverter implies that power flows from PV inverter towards PCC, whereas the negative value of grid active power implies that the grid absorbs power.

3. Similarly, it can be observed from the reactive power plots depicted in Fig.3.11(c) that, when PQEC is disabled, the reactive power demanded by the local load is

completely supplied by the grid. However, at the instant when PQEC is enabled, the PV inverter starts feeding the reactive power to the local load thereby making the grid reactive power zero. This implies that, with PQEC the PV inverter supplies all the reactive power demanded by the load. This leads to unity displacement factor at the point of common coupling (PCC), as can be observed from Fig.3.11(a).

Finally, the harmonic spectrum of PV inverter current, load current and grid current are shown in Fig.3.11(d), Fig.3.11(e), and Fig.3.11(f) respectively. The load current THD is 26.63%. Before the application of PQEC, the THD of PV Inverter current and grid current are found out to be 1.73%and 27.92 % respectively. Similarly, when the PQEC is enabled the THD of PV Inverter current and grid current are found out to be 22.65% and 3.15% respectively. It can be observed that the grid current THD is well within the limits of IEEE 1547 and IEC 61727 recommended value of 5% with the application of PQEC.

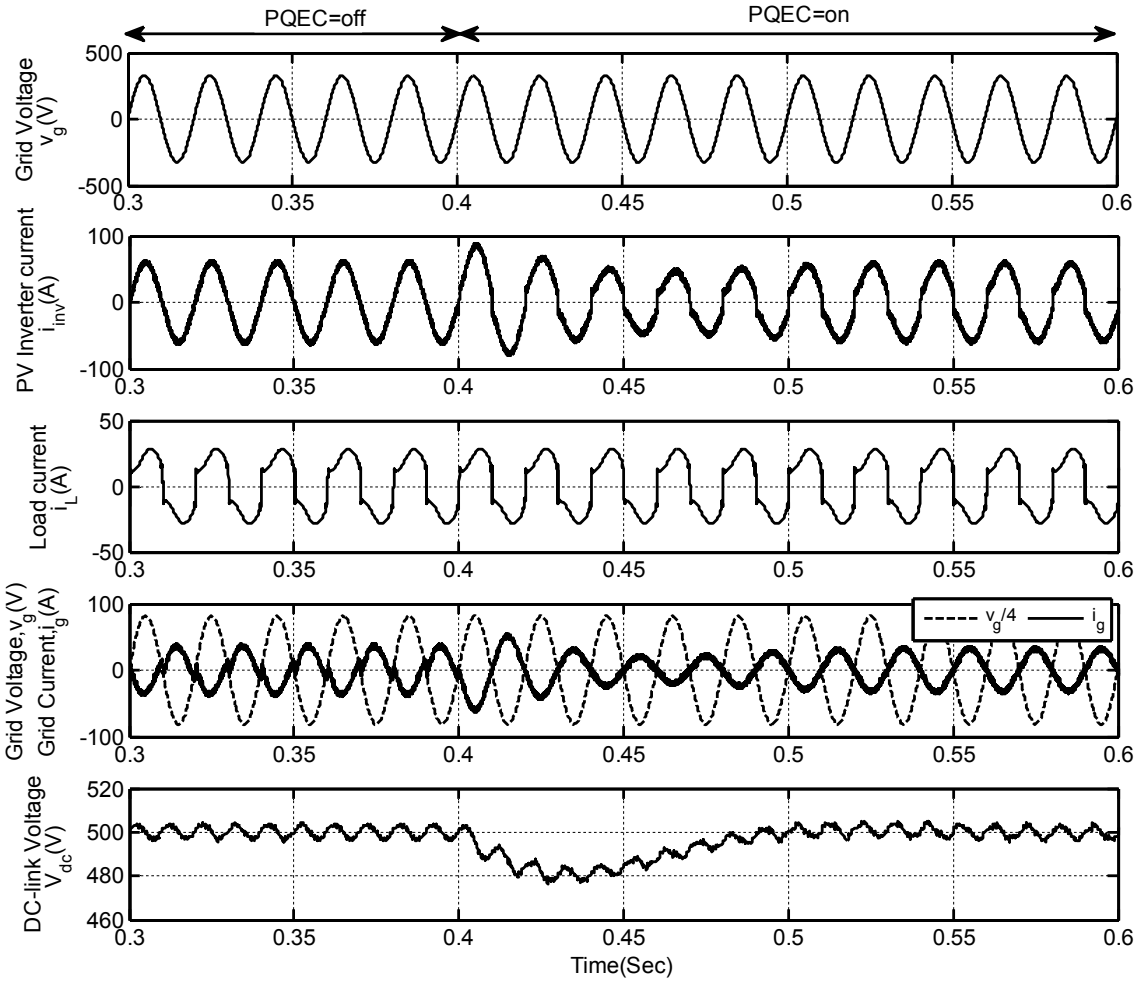

Fig.3.11.(a): Grid Voltage, PV inverter current, load current, grid current and DC-link voltage of PVDG system under disabled and enabled modes of operation of PQEC

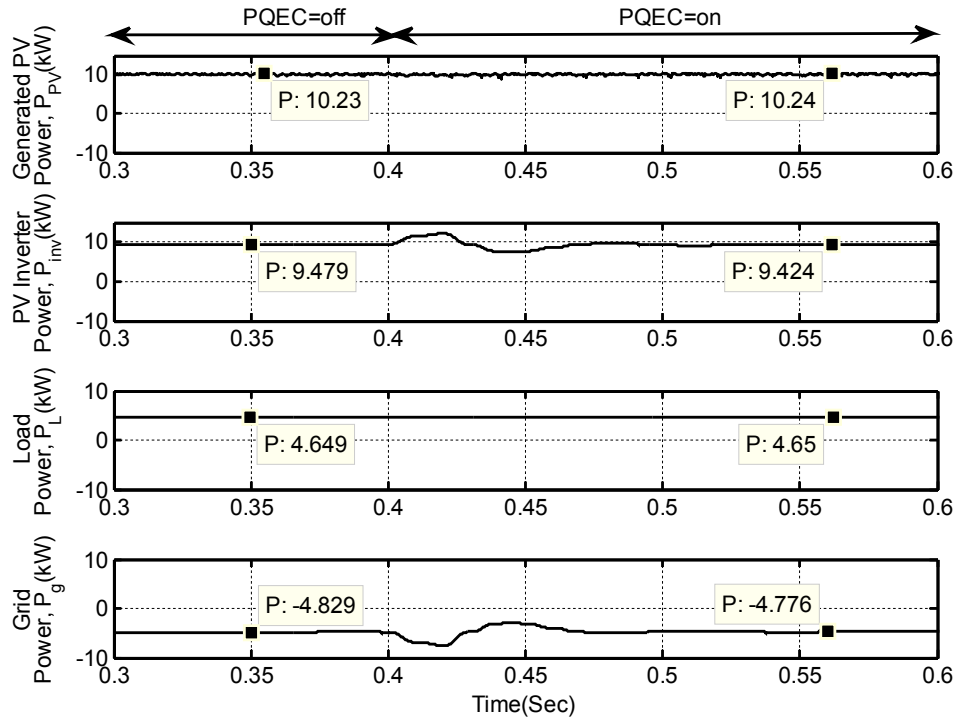

Fig.3.11(b): Active Power curves of PVDG System

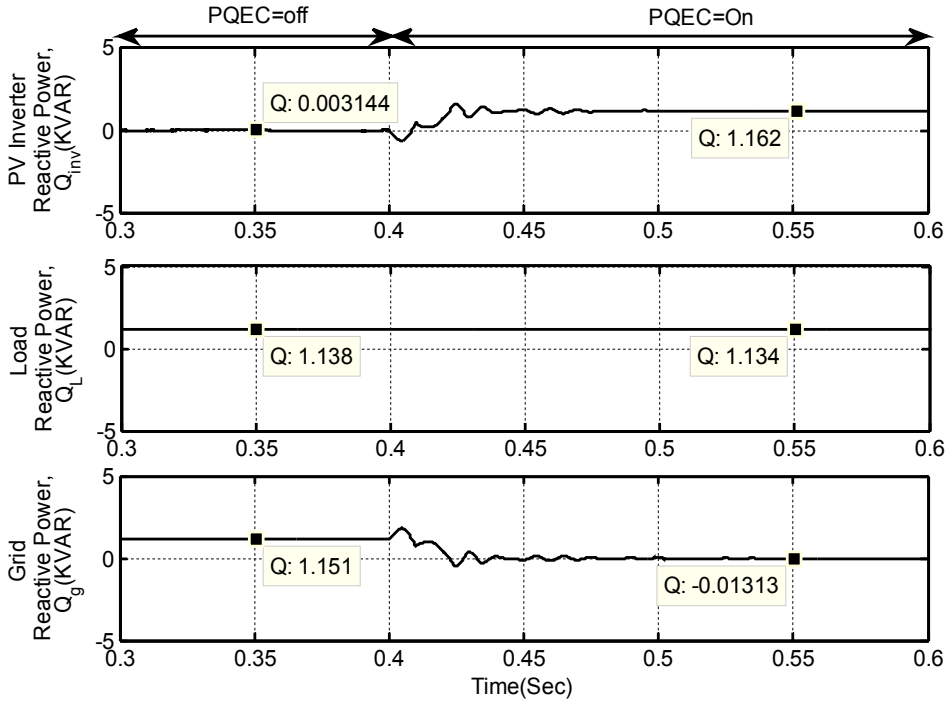

Fig.3.11(c): Reactive Power curves of PVDG System

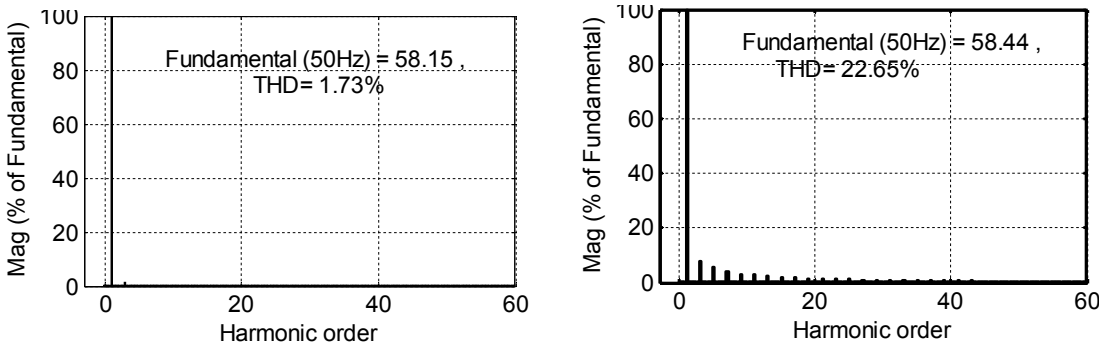

(i) (ii)

Fig.3.11 (d): THD of PV Inverter Current (i) without PQEC (ii) with PQEC

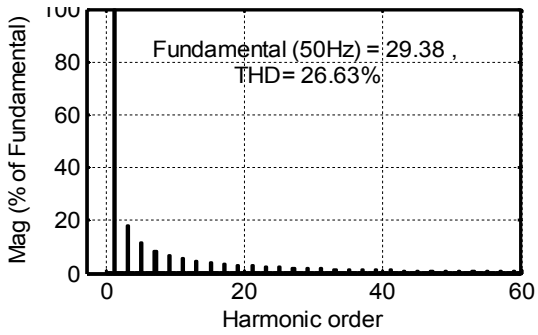

Fig.3.11 (e): THD of Load Current

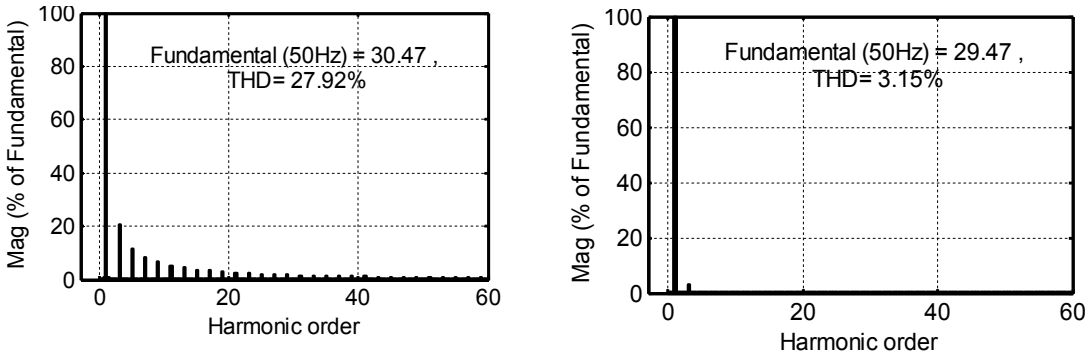

(i) (ii)

Fig.3.11 (f): THD of Grid Current (i) Without PQEC (ii) With PQEC

Fig.3.11.: Simulation results two-stage 2-level PVDG system under different modes of PQEC

3.5.2 PVDG system under varying load conditions

This section presents simulation results of PVDG system under two extreme loading conditions- namely light load and overload. These results pertain to STCs for PV modules while employing both MPPT controller and PQEC. In order to study the steady state and transient performance of the system for these conditions, the following events are considered in PVDG system:

At *t* = 0 Sec., a light load (Load-1) is present on the PV Inverter.

At *t* =0. 4 Sec., an overload (Load-2) condition is created in the PV Inverter.

The simulation results of the PVDG system under these conditions are given in Fig.3.12. The simulated waveforms of grid voltage (v_g), PV inverter current (i_{inv}), load current (i_L), grid current (i_g) and DC-link voltage (V_{dc}) for the PVDG system under this load varying condition are shown in Fig.3.12 (a) and from these simulation results, following observations are made:

1. Initially there is a light non-linear load on the system. During this condition, the load current demand is less than that generated by PV inverter and hence, the surplus current is fed to the grid. This can be observed from Fig.3.12(a), where grid current is 180^0 out of phase with PV inverter as well as the load current. However, this non-linear load draws a distorted current from the PV inverter. As the PQEC is enabled during this condition, the PV inverter generates a non-sinusoidal current consisting of fundamental, harmonics and reactive components of a load current. So, under this condition the non-sinusoidal component of the load current is completely supplied by the PV inverter, thereby relieving the grid from the supply of harmonics.
2. Similarly, when the load is increased at t=0.4 Sec., to create an overload condition, the load current demand is more than that generated by PV inverter and hence, the rest of the load current demand is met from the grid. This is verified from Fig.3.12(a), where grid current is in phase with both PV inverter and load current. Similar to light load condition, the harmonic components of the load current still continue to be supplied by the PV inverter thereby making the grid current purely sinusoidal. This demonstrates the capability of the PVDG system to fully compensate the harmonics.
3. With the implementation of PQE scheme, the reactive component of current required by the local load is completely supplied by the PV inverter. Thus, the grid current is found to have a unity displacement factor with the grid voltage under both, light and overload conditions, thereby demonstrating the reactive power compensation capability of the scheme also.
4. At the instant when the load demand increases the DC capacitor voltage of PV inverter drops from its reference value to compensate the increased load current.

This drop in capacitor voltage is restored in 3-4 cycles, as can be observed from Fig.3.12(a). The DC-link voltage regulator has ensured the regulation of the capacitor voltage.

Fig.3.12 (b) and Fig.3.12 (c) shows the generated active and reactive power curves of the PVDG system under varying load condition respectively. From these simulation results the following observations are made,

1. The power curve is shown in Fig.3.12 (b). With the implementation of the MPPT control scheme, the generated PV power is found to reach the maximum power point.
2. Fig.3.12(b) shows that, under light load condition, the generated PV power is more than the power demand of the load. Thus, the surplus PV power is fed to the grid. The positive value of the active power supplied by the PV inverter implies that power flows from PV inverter towards PCC, whereas a negative value of grid active power implies that the grid absorbs power. Moreover, during overload condition, the generated PV power is unable to meet the load demand and hence, both PV inverter and the grid share the load.
3. Similarly, it can be observed from the reactive power plots depicted in Fig.3.12(c) that, under both light load and overload condition, the grid reactive power is zero, thereby implying that the reactive power demanded by the load is met by the PV inverter. This leads to unity displacement factor at the point of common coupling (PCC), as can be observed from Fig.3.12(a).

Finally, the harmonic spectrum of PV inverter current, load current and grid current, under light load and overload conditions, are shown in Fig.3.12(d), Fig.3.12(e), and Fig.3.12(f) respectively. Under light load condition, the THD of PV Inverter current, load current, and grid current are found out to be 22.65 %, 26.63%, and 3.15% respectively. Similarly, during overload condition the THD of PV Inverter current, load current and grid current are found out to be 38.10 %, 31.82 % and 4.36 % respectively. It can be observed that the grid current THD is well within the limits of IEEE 1547 and IEC 61727recommended value of 5% under both light and overload conditions.

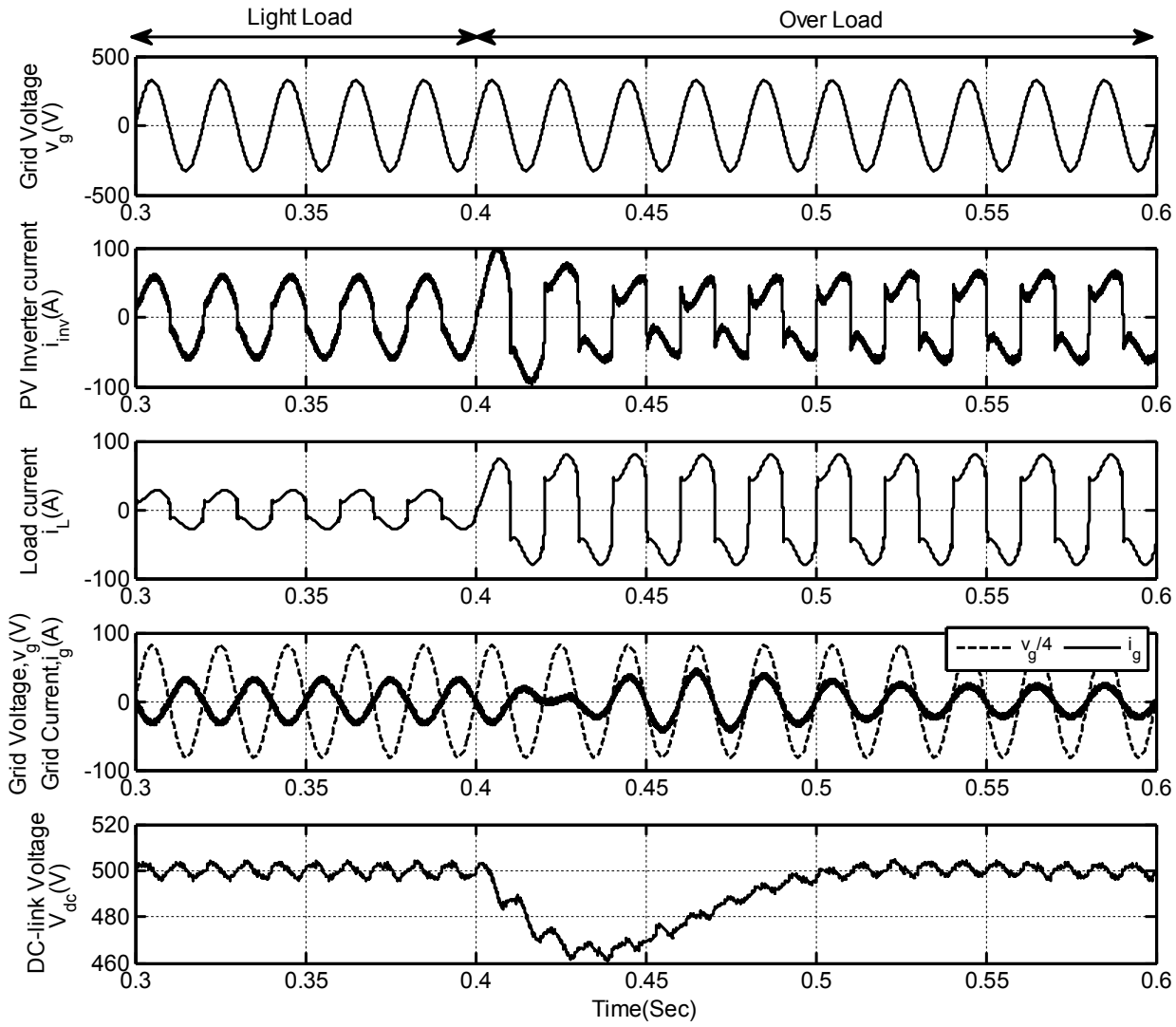

Fig.3.12 (a): Grid Voltage, PV inverter current, load current, grid current and DC-link voltage of PVDG system under varying load condition.

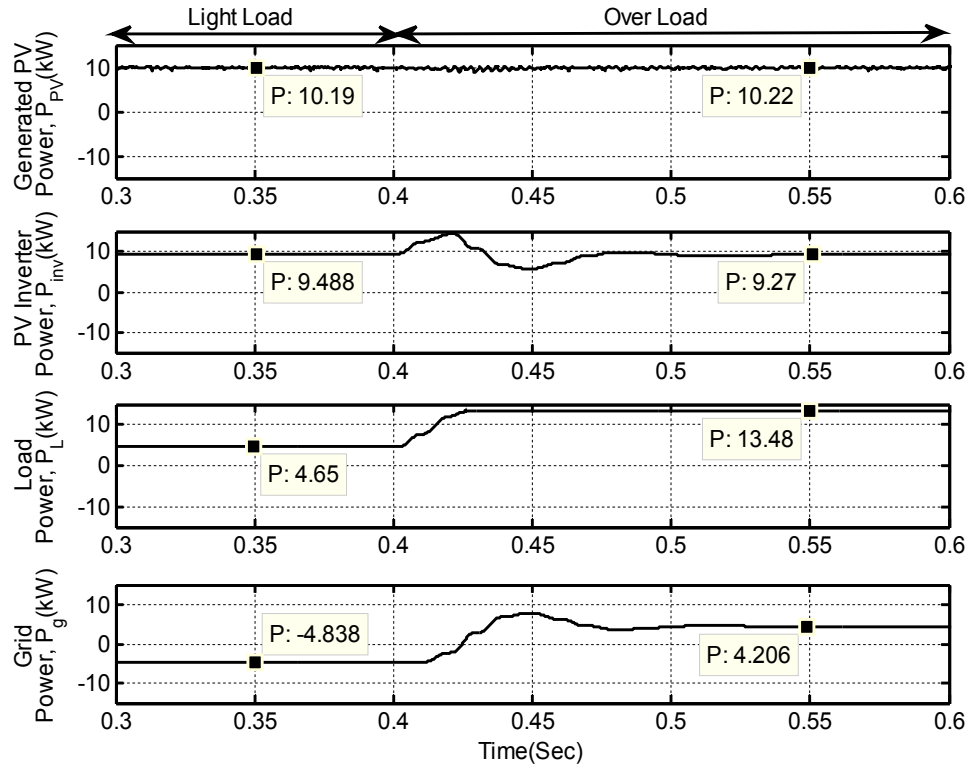

Fig. 3.12(b) Active Power curves of PVDG System

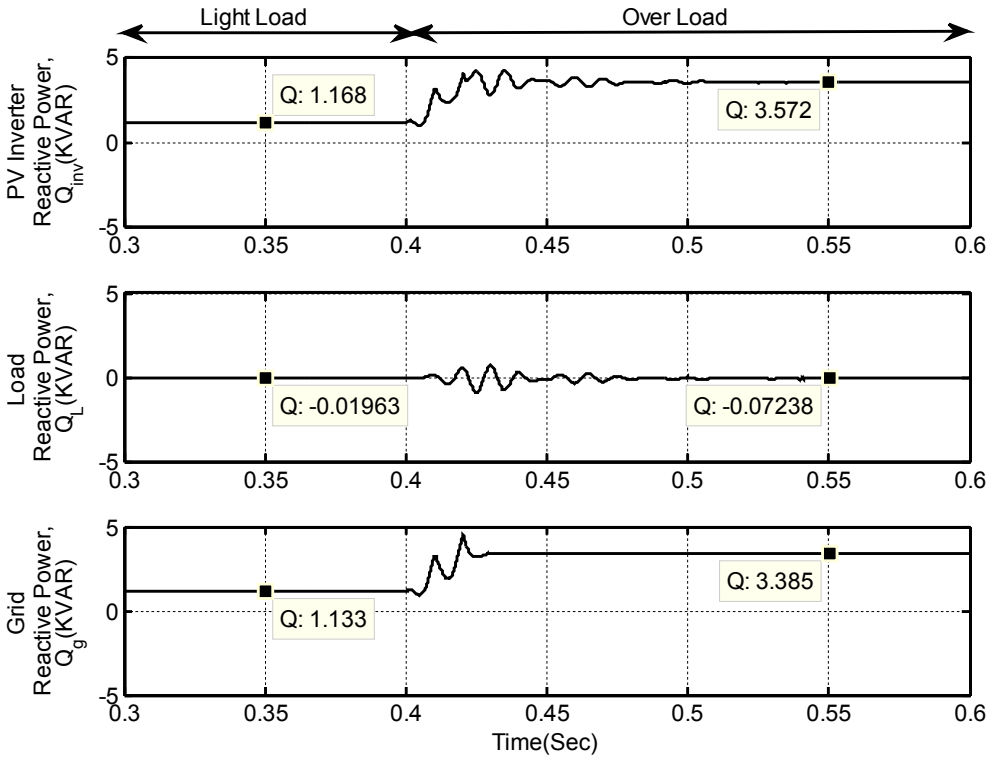

Fig. 3.12(c) Reactive Power curves of PVDG System

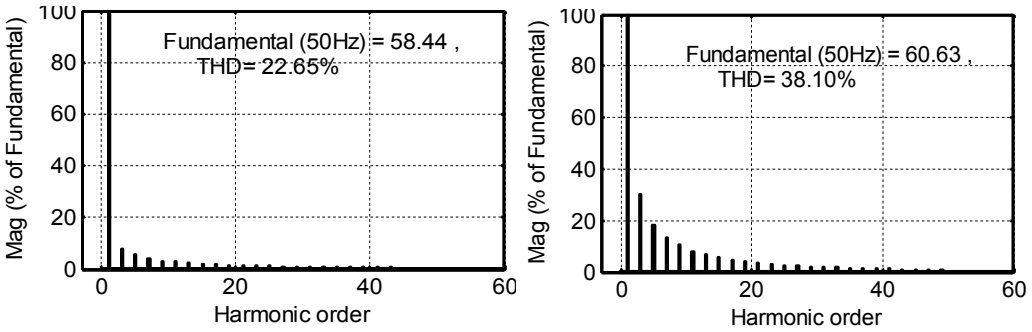

(i) (ii)

Fig. 3.12 (d): THD of PV Inverter Current (i) Light load (ii) Overload Condition

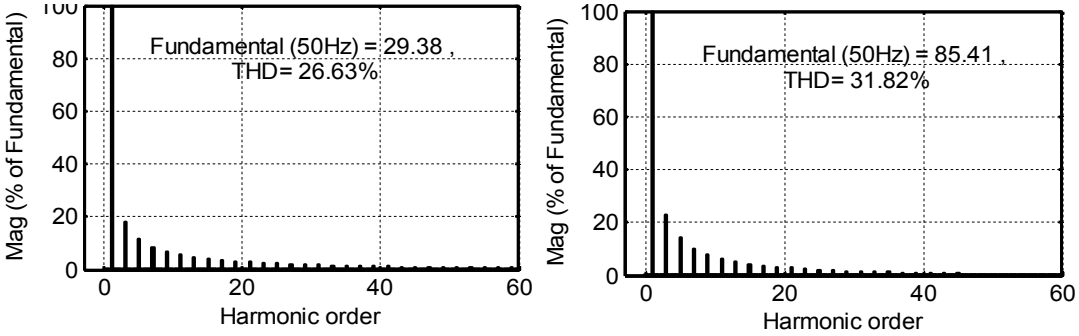

(i) (ii)

Fig. 3.12(e): THD of Load Current (i) Light Load (ii) Overload condition

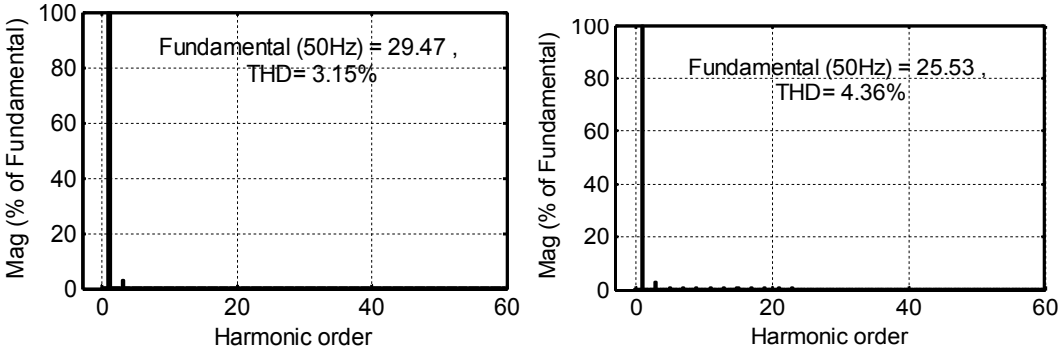

(i) (ii)

Fig. 3.12 (f): THD of Grid Current (i) Light load (ii) Overload condition

Fig.3.12: Simulation results of two-stage 2-level of PVDG system under varying load condition.

3.5.3 PVDG system under varying atmospheric conditions

This section presents simulation results of the PVDG system under varying atmospheric conditions. The analysis of the system is made with both MPPT and PQEC are enabled and , with a non-linear load (Load-1) connected across PCC throughout. In order to study the steady-state and transient performance of the system under these conditions, the following events have been designed to occur in PVDG system:

At t = 0 Sec., the irradiation level of the PV module is set as 1000 W/m^2.

At t =0. 4 Sec., irradiation level is reduced to 300 W/m^2

The simulation results of the PVDG system under these above mentioned conditions are given in Fig.3.13. The simulated waveforms of grid voltage, PV inverter current, load current, grid current, and DC-link voltage for the PVDG system under this varying atmospheric condition are shown in Fig.3.13(a) and from these simulation results, following observations are made:

1. Initially the PVDG system is operated at the irradiation level of 1000 W/m^2. During this condition, the load current demand is less than that generated by PV inverter and hence, the surplus current is fed to the grid. This can be observed from Fig. 3.13(a), where grid current is 180^0 out of phase with PV inverter as well as the load current. However, this non-linear load draws a distorted current from the PV inverter. As the PQEC is enabled during this condition, the PV inverter generates a non-sinusoidal current consisting of fundamental, harmonics and reactive components of a load current. So, under this condition the non-sinusoidal component of the load current is completely supplied by the PV inverter, thereby relieving the grid from the supply of harmonics.
2. However, when the irradiation level is decreased to 300 W/m^2 at t=0.4 Sec., to create an unfavorable atmospheric condition for the PVDG system, the generated PV inverter current is not sufficient to meet the load current demand and hence, the rest of the load current demand is met by the grid. This is verified from Fig. 3.13(a), where grid current is in phase with both PV inverter and the load currents. Similar to favorable atmospheric condition, the harmonic components of the load current still continue to be supplied by the PV inverter thereby making the grid current purely sinusoidal. This demonstrates the capability of PVDG system to fully compensate for harmonic.
3. With the implementation of PQE scheme, the grid current is found to be in phase with the grid voltage under both, favourable and unfavourable atmospheric conditions thereby confirming the compensation of reactive power.
4. At the instant when the solar irradiation is decreased from 1000 W/m^{2}to 300 W/m^2 the DC capacitor voltage of PV Inverter drops from its reference value to maintain the load current demand. This drop in capacitor voltage is restored in 4-5 cycles, as

can be observed from Fig.3.13(a). The DC-link voltage regulator has ensured the regulation of the capacitor voltage.

Fig.3.13 (b) and Fig.3.13(c) shows the generated active and reactive power curves of the PVDG system under varying atmospheric condition respectively. From these simulation results following observations are made,

1. Fig.3.13(b) shows that, under favorable atmospheric condition, i.e. at the irradiation level of 1000 W/m^2, the generated PV power is more than the power demand of the load. Thus, the surplus PV power is fed to the grid. The positive value of the active power supplied by the PV inverter implies that power flows from PV inverter towards PCC, whereas a negative value of grid active power implies that the grid absorbs power. Moreover, during low irradiation condition, the generated PV power is unable to meet the load demand and hence, both PV inverter and the grid share the load.
2. Similarly, it can be observed from the reactive power plots depicted in Fig.3.13(c) that, under both high and low irradiation conditions, the grid reactive power is zero, thereby implying that, the PV inverter supplies the reactive power demanded by the load. This leads to unity displacement factor at the point of common coupling (PCC), as can be observed from Fig.3.13(a).

Finally, the harmonic spectrum of PV inverter current, load current and grid current, under favourable (1000 W/m^2) and unfavourable (300 W/m^2) atmospheric conditions, are shown in Fig.3.13(d), Fig.3.13(e), and Fig.3.13(f) respectively. The load current THD is 26.63%. Under favorable atmospheric condition, the THD of PV Inverter current and grid current are found out to be 22.65 %, and 3.15% respectively. Similarly, during unfavorable atmospheric condition the THD of PV inverter current, load current and grid current are found out to be 31.58 % and 4.88 % respectively. It can be observed that the grid current THD is well within the limits of IEEE 1547 and IEC 61727recommended value of 5% under both aforementioned conditions.

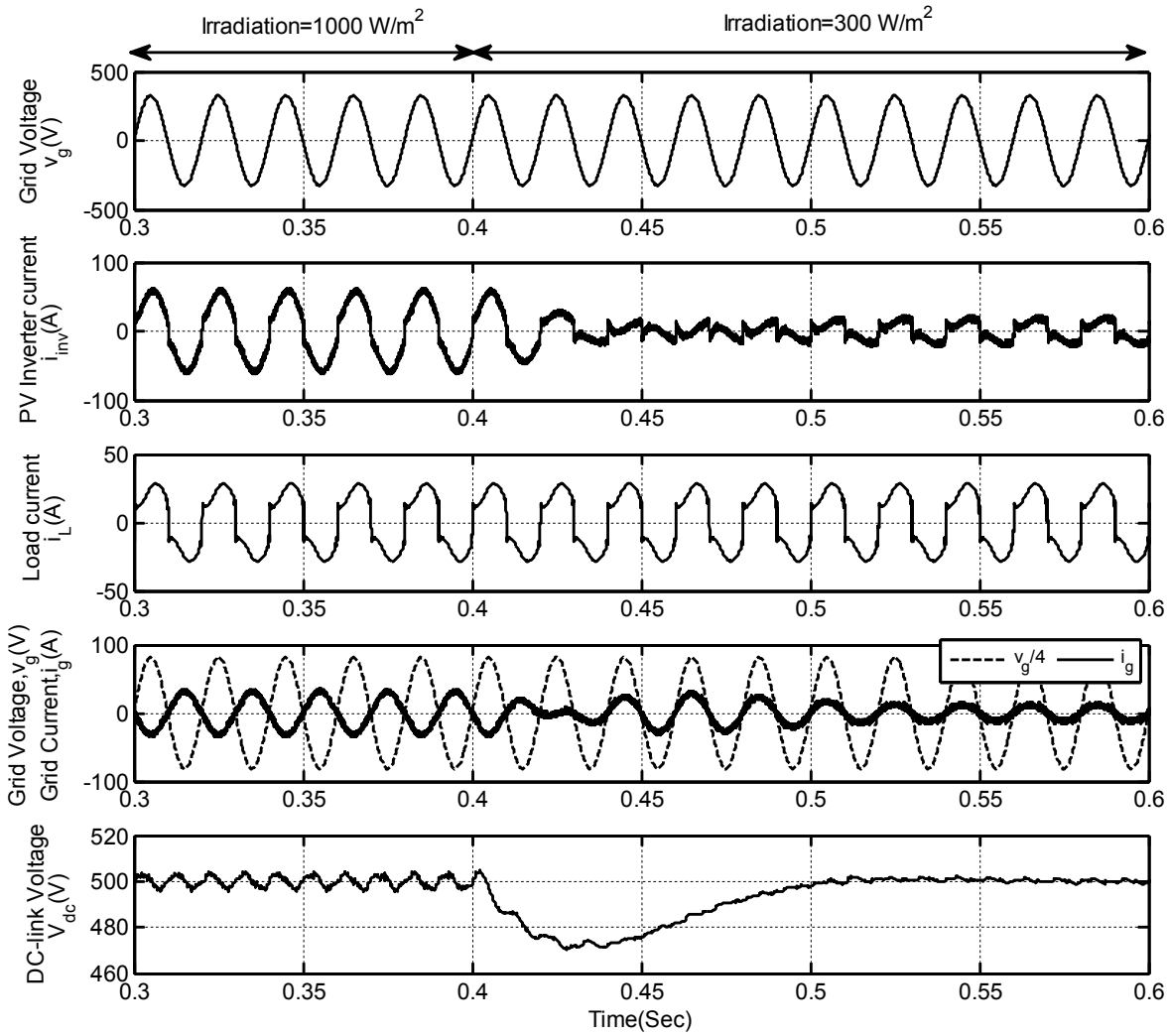

Fig.3.13 (a): Grid Voltage, PV inverter current, load current, grid current and DC-link voltage of PVDG system under varying atmospheric condition.

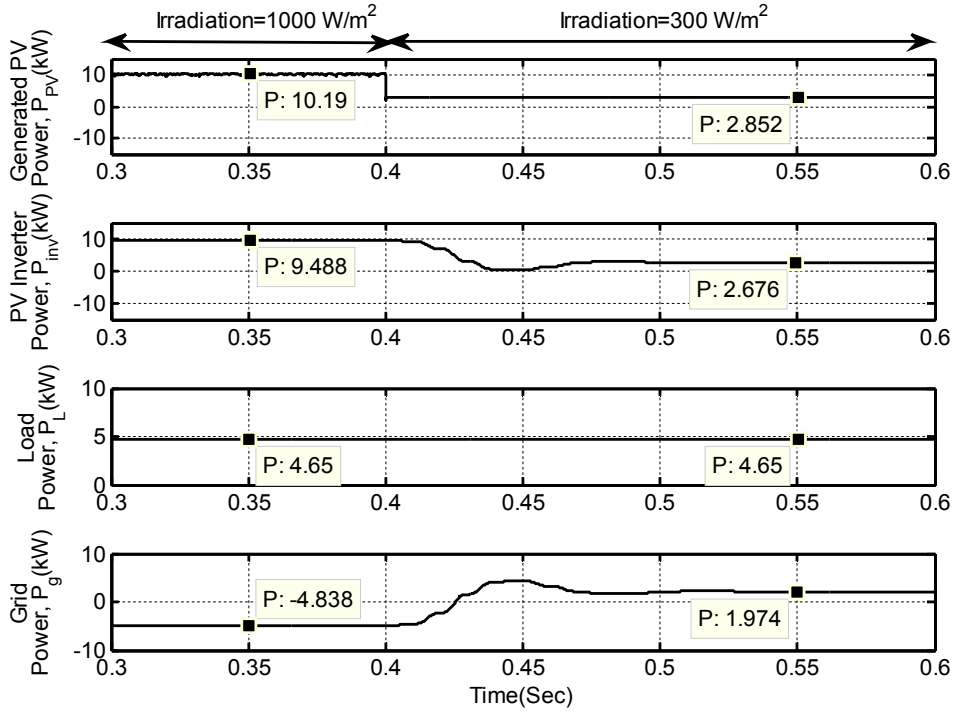

Fig.3.13(b): Active Power curves of PVDG System under varying atmospheric condition

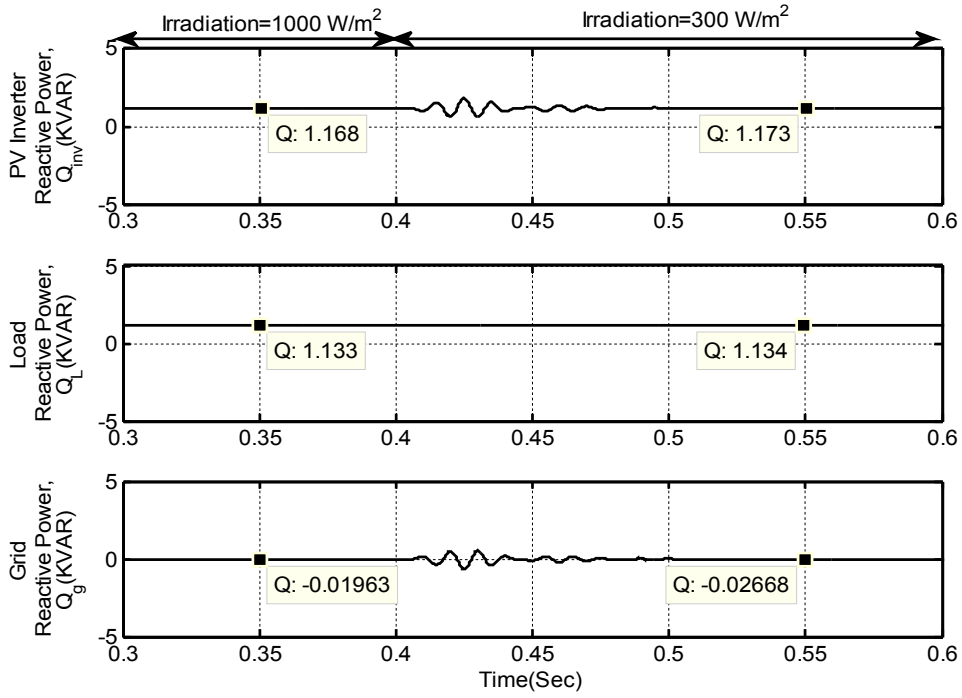

Fig.3.13 (c): Reactive Power curves of PVDG System under varying atmospheric condition

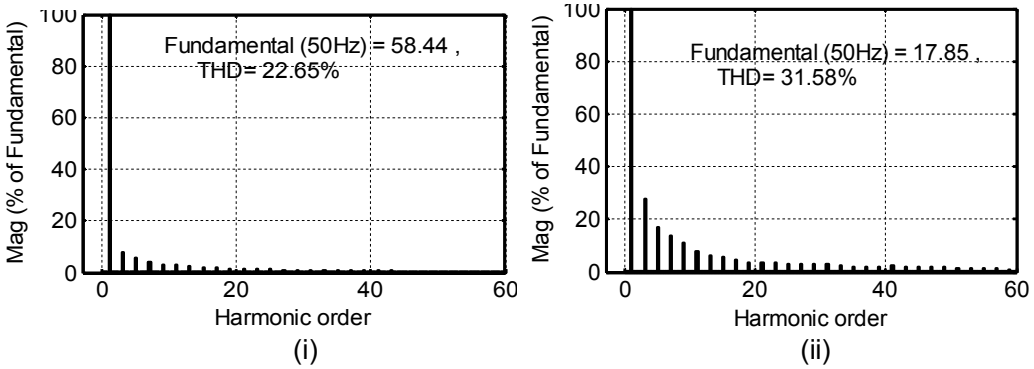

(i) (ii)

Fig.3.13(d): THD of PV Inverter Current (i) at 1000 W/m^2 (ii) at 300 W/m^2

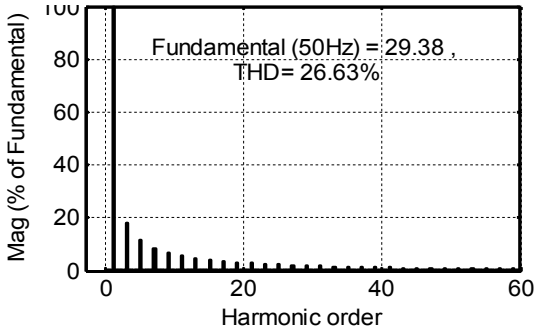

Fig.3.13(e): THD of Load Current

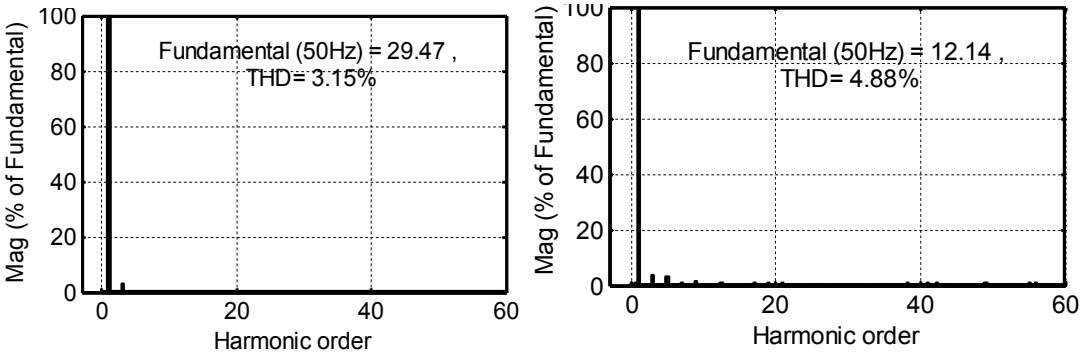

(i) (ii)

Fig.3.13 (f): THD of grid Current (i) at 1000 W/m^2 (ii) at 300 W/m^2

Fig.3.13: Simulation results of two-stage 2-level PVDG system under varying atmospheric condition

3.5.4 PVDG system under night mode operation

This section presents simulation results of the PVDG system while operating it during nighttime. The system is validated under disabled and enabled modes of PQEC. The irradiation and temperature level for PV panels are fixed at 0 W/m^2 and 15 ^{0}C respectively, with a non-linear load (Load-1) connected across PCC. In order to study the steady state and transient performance of the system for these conditions, the following events are considered to occur in PVDG system:

At *t* = 0 Sec., PQEC is off (disabled mode).

At *t* =0.4 Sec., PQEC is on (enabled mode).

The simulation results of the PVDG system under this condition is given in Fig.3.14. The simulated waveforms of grid voltage (v_g), PV inverter current (i_{Inv}), load current (i_L), grid current (i_g) and DC-link voltage (V_{dc}) for the PVDG system under different modes of operation of PQEC are shown in Fig.3.14(a) and from these simulation results, following observations are made:

1. At night time, as the PV module is unable to generate any active power, the load current demand is completely met by the grid. This can be observed from Fig.3.14(a), where PV inverter current is having zero value, while grid current is in phase with load current. As the PQEC is in disabled mode, with a non-linear load connected across the PV inverter, the grid generating a non-sinusoidal current as per the demand of local load. Therefore, in this condition, with disable mode of PQEC, the non-linear nature of load forces the grid current to be non-sinusoidal.

2. At the instant when the PQEC is enabled at t=0.4 Sec., the controller generates a reference current for the PV inverter which consists of both harmonics and reactive components of load current. Consequently, the PV inverter generates only the compensating current to mitigate the harmonic and reactive components of the load current thereby making the grid current pure sinusoidal. Moreover, in this condition, the grid supplies the active component of the load current, the PV inverter only feed the compensating current. Moreover, the PV inverter also draws some active current from the PV inverter to meet the switching losses. This demonstrates the capability of the PVDG system to fully compensate the harmonic.

3. With the implementation of PQE scheme, the reactive component of current required by the local load is completely supplied by the PV inverter. Thus, the grid current is found to have a unity displacement factor with the grid voltage, thereby demonstrating the reactive power compensation capability of PQEC even in the night mode operation of PVDG system.

4. At the instant when the PQEC is enabled the DC capacitor voltage of PV inverter drops from its reference value to compensate the load current harmonics, which in turn increased power, demanded from the PV inverter. This drop in capacitor voltage is restored in 3-4 cycles, as can be observed from Fig.3.14(a). The DC-link voltage regulator has ensured the regulation of the capacitor voltage.

Fig.3.14(b) and Fig.3.14(c) shows the generated active and reactive power curves of the PVDG system under these two different modes of operation of PQEC. From these simulation results following observations are made,

1. It can be observed from the power curve depicted in Fig.3.14(b) that, as the PV module is operated in night mode, the generated PV power is zero. It also shows that, under both modes of operation of PQEC, as the PV module unable to generate any active power, the grid supplies the required load active power. The positive value of the active power supplied by the grid implies that power flows from the grid towards PCC.
2. Similarly, it can be observed from the reactive power plots depicted in Fig.3.14(c) that, under the disabled mode of operation of PQEC, the reactive power demanded by the local load is completely supplied by the grid. However, at the instant when PQEC is enabled, the PV inverter starts feeding the reactive power to the local load thereby making the grid reactive power zero. This implies that, with PQEC only the PV inverter supplies the reactive power demanded by the load. This leads to unity displacement factor at the point of common coupling (PCC).

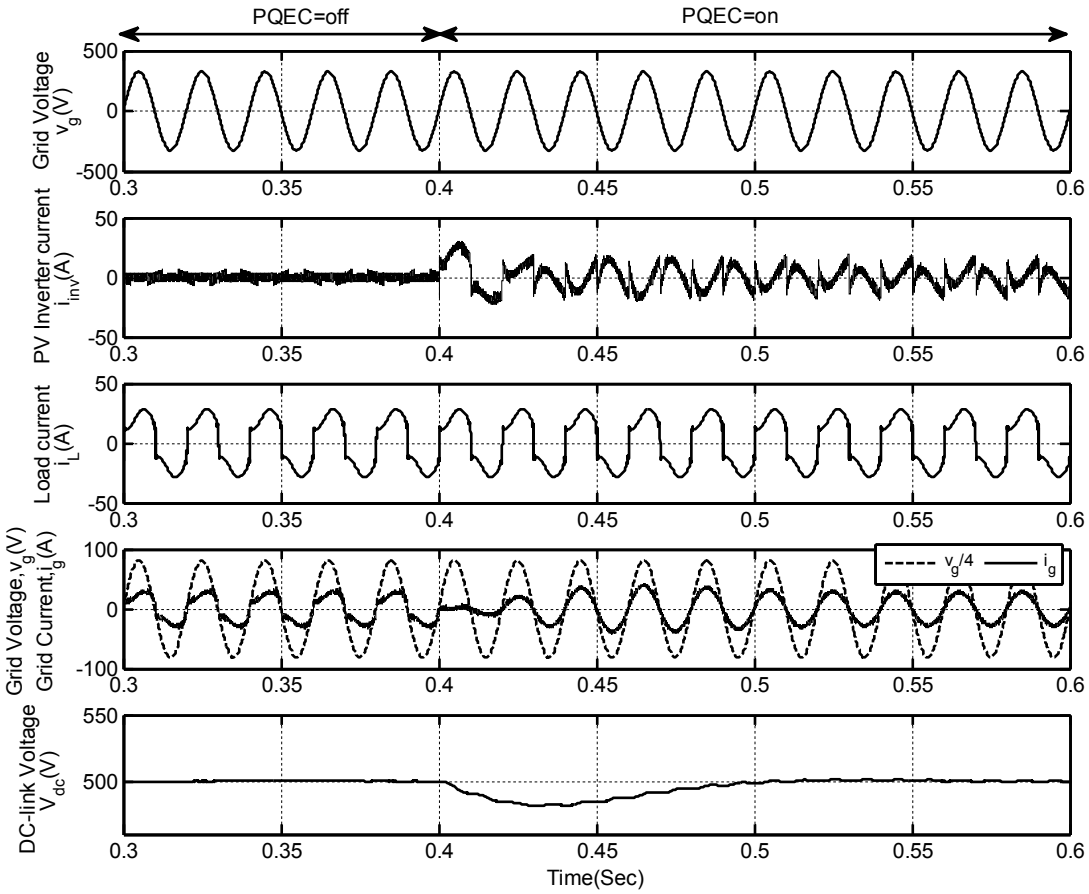

Fig.3.14 (a): Grid Voltage, PV inverter current, load current, grid current and DC-link voltage of PVDG system during night mode.

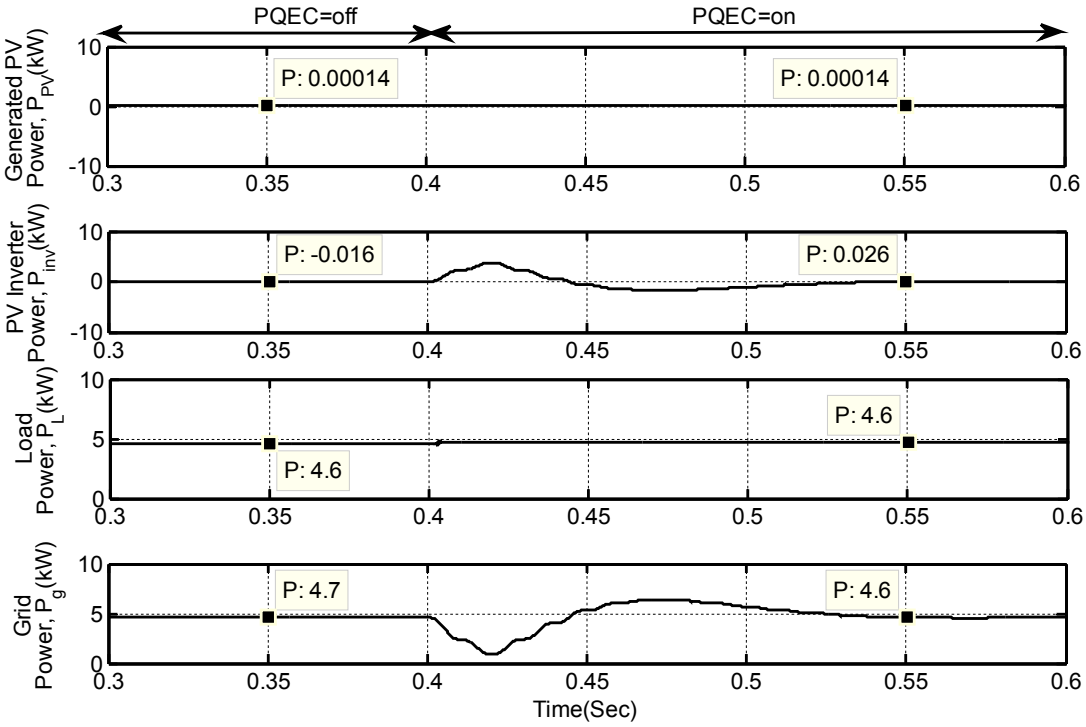

Fig. 3.14(b): Active Power curves of PVDG System during night mode.

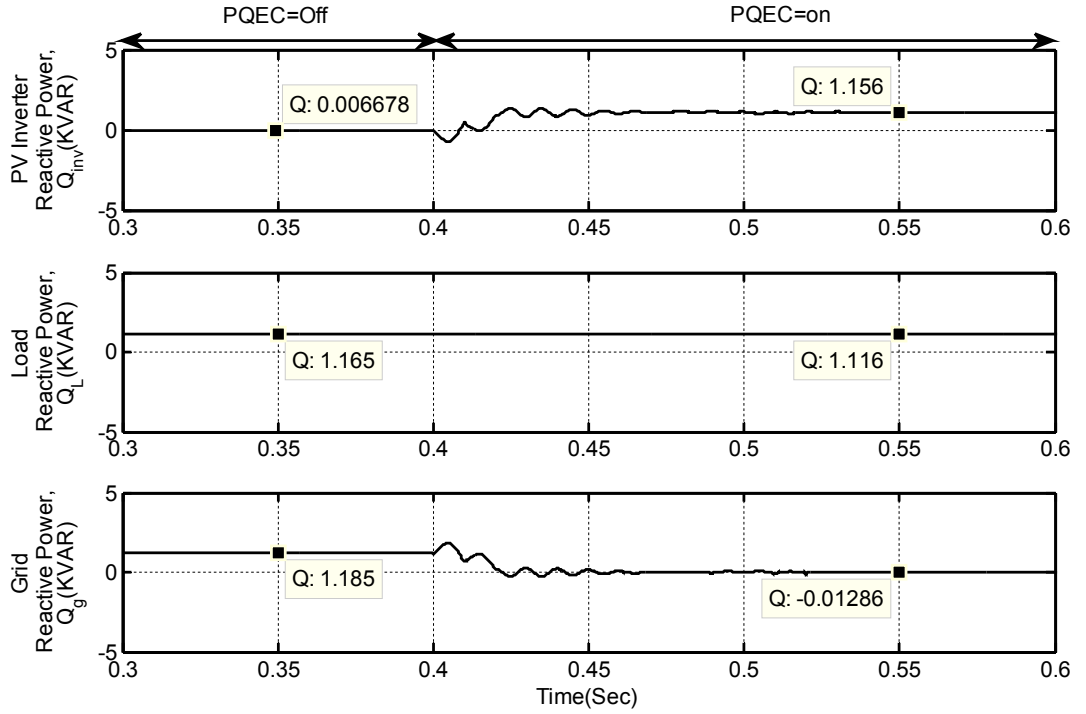

Fig. 3.14(c): Reactive Power curves of PVDG System during night mode.

Finally, the harmonic spectrum of grid current, during night mode operation without and with the application of PQEC is shown in Fig.3.14(d). It can be observed that without PQEC, the grid current THD is 26.51%. After the application of PQEC, the grid current THD is found to be 2.88%, which is well within the limits of IEEE 1547 and IEC 61727recommended value of 5% even under night mode operation.

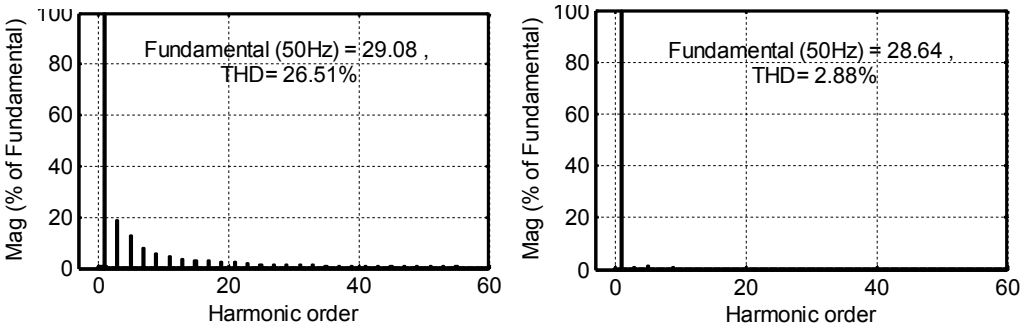

(i) (ii)

Fig. 3.14(d): THD of Grid Current (i) without PQEC (ii) with PQEC

Fig.3.14: Simulation results of PVDG system during night mode.

3.6 Conclusion

The main goal of this chapter was to develop a power quality enhancement scheme for a 1-ϕ two stage PVDG system. The current control scheme of PV inverter includes a compensating current generator based on instantaneous reactive power theory to obtain the aforementioned objective. The PV inverter with the proposed control scheme is utilized to inject the generated PV power to the grid with an integrated shunt APF capability to eliminate the need of an extra converter to improve power quality of the system at PCC. Exhaustive simulation results are presented to investigate the performance of the PVDG system during different conditions of loading and irradiation level. The idle state of PV inverter at night time leads to the underutilization of such an expensive system. This issue of PVDG system has also been considered and hence, the concept of the utilization of the PV inverter as a shunt APF during night time has also been presented in this chapter. Rigorous simulation study under different conditions such as with and without PQEC, light and overload condition, low and high solar irradiation level, and night mode operation are presented to demonstrate the effectiveness of this system.

[A 1-ϕ five-level CHBMLI based two-stage and single stage PVDG system with an improved power quality feature is presented in this chapter. These topologies consist of two H-bridge PV inverter cells connected in series. In case of a two-stage PVDG system, DC-DC converter is used for MPPT and CHBMLI is responsible for the power flow operation. Whereas, in single-stage PVDG system the CHBMLI is in charge of both power flow and MPPT operation. Exhaustive simulation results are presented to investigate the performance of the CHBMLI based PVDG system during varying atmospheric and varying load as well as different control modes. Comparative analysis of 1-ϕ single stage CHBMLI based PVDG system with two-stage two-level and CHBMLI based topology is also presented]

4.1 Introduction

As discussed in the preceding chapters, a 1-ϕ PVDG system is well suited for clean power generation and distribution system. However, the power generated by the PV module is still considered to be expensive and wider use of the PVDG system is largely dependent on cost effective technologies. In general, the ongoing research for the improvement of the overall efficacy of the PVDG system includes the following areas:

- Efficiency improvement of PV module
- Cost reduction of PV module
- Efficiency improvement of the overall PV system while focusing on the power conditioning units

A lot of research work is going to obtain an efficient and cheaper PV module based on new cell material and manufacturing technologies. In addition, the overall cost of PVDG system can be reduced by increasing the efficiency of the whole system using the power conditioning system and also by introducing an improved power quality feature in its control system. The primary goal of a power conditioning unit in PVDG system is to increase the energy injection to the utility grid by optimizing the energy extraction process from the PV module by keeping track of maximum power point (MPP), by operating at a lower switching frequency thereby reducing the switching losses At present the most commonly used converter topology for PVDG system is the two level multistring inverter which is discussed in Chapter.3. This PV inverter consists of several PV strings that are connected with DC-DC converters to a common DC-AC inverter. This topology has advantages of independent tracking of the MPP of each string. A PQE scheme for such two-stage two-level PV inverter topology is presented in Chapter.3. With this control scheme, it is possible to inject a high quality of PV power to the grid. For the further improvement of power quality and also to increase the power a multilevel inverter topology is introduced in place of the two-level inverter. The important features of such inverter topologies are,

(i) They can generate high quality of voltage waveform with each power switch operating at lower frequencies.

(ii) The MLIs feature several DC-links which allow independent voltage control and tracking of the MPP in each string. This characteristic can increase the efficiency of the PV system in case of mismatch in the strings due to unequal solar irradiation, ageing of the PV panels and different type of cells or accumulation of dust on the panel surface.

(iii) With an option of multiple DC-link voltage in the input side, the MLI can synthesize a high quality of output voltage waveform. This leads to reduction of harmonics in the generated current and hence reduces the size of filter at the output.

Among all the available MLI topologies, the modular structure of CHBMLI makes it best suited for PV application. Additionally, this topology employs power semiconductors with a lower rating than the standard two-level configuration, which allows cost saving. Last but not the least, MLI topologies feature several degrees of freedom that make possible the operation of CHBMLI based PV system even under faulty conditions, increasing in this way the reliability of the whole system. This chapter deals with the power flow control of the CHBMLI based PVDG system. In the first part of this chapter a two-stage CHBMLI based PVDG system is discussed. The power flow control in such type of PVDG system requires two control loops. The inner current control loop is used to modulate the output current of the PV CHBMLI to meet magnitude and phases of waveform whereas the outer voltage control loop regulates the output power of the PV inverter according to the MPP of PV modules. These two control loops are realized by two stages of power conversion. One is a DC to DC converter with MPPT control and the other is a DC to AC inverter. But two stage operation leads to more power loss than that of a single stage conversion. In single stage PVDG system, both the control loops are realized in one power conversion stage, thus simplifying the system topology and hence increases the overall power conversion of the system. The second part of this chapter presents a single stage CHBMLI based PVDG system.

These 1-ϕ 5-level CHBMLI based two-stage and single-stage PVDG system is controlled in such a way to inject an optimum and improved quality of power to the distribution network to meet the required standards set by IEEE, IEC[67, 68] for distributed generation system and are tested under both varying atmospheric and non-linear load conditions.

The main objectives of this chapter are to effectively utilize the CHBMLI based PV inverter in two-stage and single stage distributed generation system to achieve the following three important functions:

- To transmit the maximum possible active power from the PV module
- To supply the reactive power demand of local load
- To compensate the current harmonics at PCC

With an adequate control of PV CHBMLI, all the above mentioned objectives can be achieved either separately or simultaneously. The power quality issues in PVDG system such as harmonic and reactive power compensation at the PCC can be addressed without requiring any additional hardware circuits. A detailed description of above mentioned two-stage and single stage PVDG system is presented in section 4.2 and 4.3 respectively.

4.2 Two-stage CHBMLI based PVDG System

The schematic diagram of a 1-ϕ two-stage CHBMLI based PVDG system with an enhanced power quality features is depicted in Fig.4.1. The key components of the system are PV modules, two stage converter comprising of boost type DC-DC converter and 5-level CHBMLI based DC-AC inverter, local load (linear/non-linear) and the grid. Each PV module is connected to an individual boost converter through a capacitor which helps in controlling PV voltage, thereby extracting maximum power from it by using MPPT algorithm. Each DC-DC converter is connected to a separate H-bridge cell via a DC-link capacitor. The voltage across each DC-link capacitor is maintained constant through the outer voltage control loop of CHBMLI to facilitate active and reactive power transfer to the utility grid. The CHBMLI is the key element of the proposed PVDG system as it interfaces the PV source to the grid and delivers the generated power with improved power quality features. CHBMLI control with aforementioned features is achieved with the following controllers, load current (i_L) analyzer which comprises of demanded load real power, reactive power and harmonic components, DC-link voltage controller, which is used to regulate the DC-link voltages of each H-bridge cell during varying atmospheric and load conditions and the reference CHBMLI current (i_{ref}) estimator. This reference current (i_{ref}) is used for the control of the CHBMLI using a modulation scheme to feed active and reactive power to the local load. The two-stage CHBMLI based PVDG system comprises of an isolated MPPT controller to extract maximum power from the PV module with two cascaded current and voltage control loops [1]. The internal current control loop controls the grid current and the DC-link voltage control loop regulates the DC-link voltage of each H-bridge [2, 3]. For the issues related to power quality current loop is responsible. Therefore, harmonic and reactive power compensation is the key functions of the current controller. However, the DC-link voltage controllers are designed for the power flow balancing in the PVDG system. The descriptions of all the control blocks required for the proposed system are discussed below.

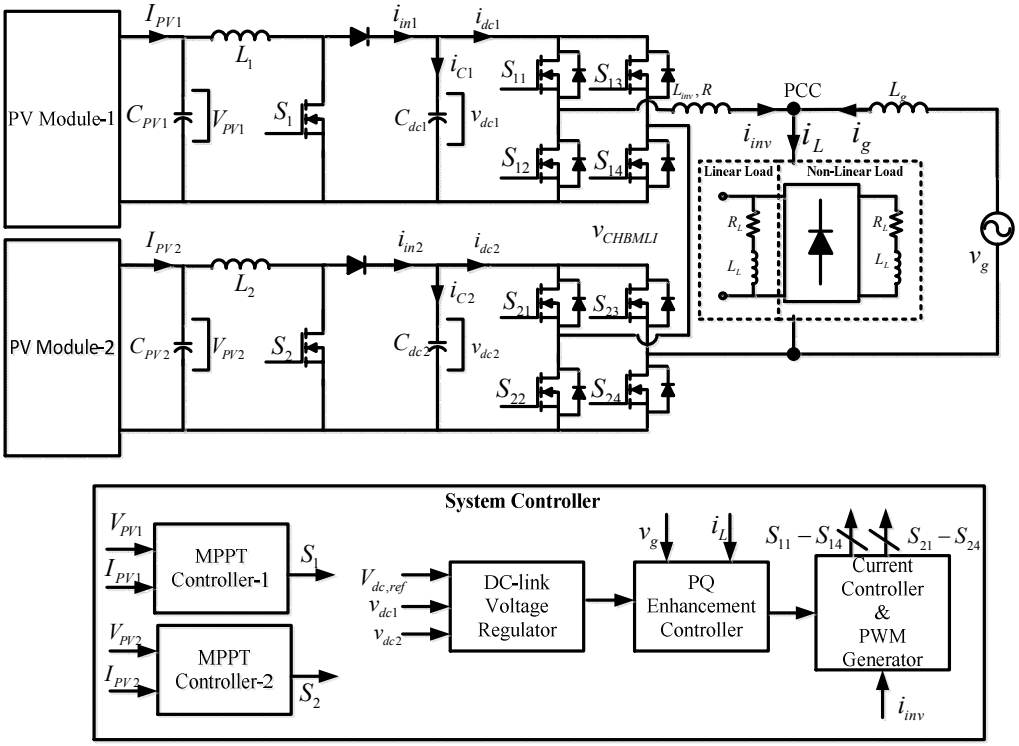

Fig.4.1: Schematic diagram of two-stage CHBMLI based PVDG system with improved power quality features

4.2.1 CHBMLI Control Scheme

The 1-ϕ 5-level PV CHBMLI is shown in Fig.4.1. DC-link of each H-bridge cell is fed from a PV module through a boost type DC-DC converter. The AC sides of the CHBMLI circuits are connected in series, which results in the output terminal voltage as, $v_{CHBMLI} = v_{H1} + v_{H2}$

The output voltage of each H-bridge in CHBMLI can be written as,

$$v_{Hi} = S_i . v_{dci}, \quad i = 1, 2 \tag{4.1}$$

Where, $S_1 = S_{11}S_{14} - S_{12}S_{13}$ and $S_2 = S_{21}S_{24} - S_{23}S_{24}$

With S_{xx} is the state of each switch which presents two discrete values: '1' when the switch is turned on and '0' when it is turned off. Therefore S_i is having three discrete values 1, 0 and -1 giving the output voltage of each H-bridge as $v_{dc}, 0$ and $-v_{dc}$ respectively by assuming $v_{dc1} = v_{dc2} = v_{dc}$. The considered PV CHBMLI can be completely described by the following three differential equations:

$$L_{inv} \frac{di_{inv}}{dt} = S_1 v_{dc1} + S_2 v_{dc2} - v_g \tag{4.2}$$

While considering $v_{PCC} = v_g$

$$C_1 \frac{dv_{dc1}}{dt} = i_{in1} - S_1 i_{inv} \tag{4.3}$$

$$C_2 \frac{dv_{dc2}}{dt} = i_{in2} - S_2 i_{inv} \tag{4.4}$$

The DC-link of CHBMLI plays a vital role in transferring variable power from the individual PV module to the grid. Energy generated from each PV module is represented as a current source connected to the DC-link of a grid interfacing CHBMLI. The power transfer from the PV module to the grid through the DC-link is depicted by a systematic representation in Fig.4.2.The generated PV current from each PV module which is injected into the DC-link at a voltage level v_{dc1} and v_{dc2} can be written as,

$$i_{dc1} = \frac{P_{PV1}}{v_{dc1}} \tag{4.5}$$

$$i_{dc2} = \frac{P_{PV2}}{v_{dc2}} \tag{4.6}$$

Where P_{PV1}, P_{PV2} are the generated power from PV module-1 and module-2 respectively.

The current flowing into the other side of the DC-link can be represented as,

$$i_{dc} = \frac{P_{inv}}{v_{dc1} + v_{dc2}} = \frac{P_g + P_{loss}}{v_{dc1} + v_{dc2}} \tag{4.7}$$

Where P_{inv} : Total power available at grid interfacing CHBMLIside

P_g : Total power supplied to the grid

P_{Loss} : CHBMLI loss

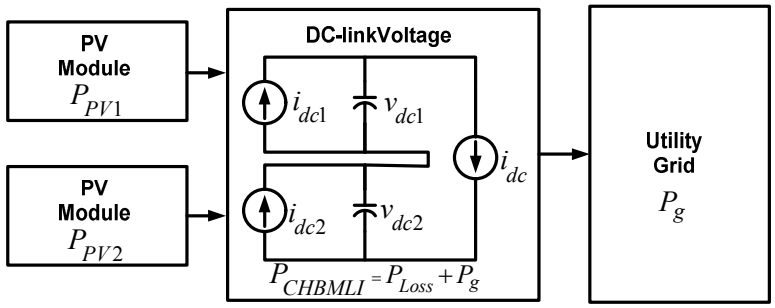

Fig.4.2:Equivalent DC-link for two-stage CHBMLI

The control of DC-link voltages carry the information regarding the exchange of active power between the PV module and the grid. Thus the output of a DC-link voltage regulator results in maximum value of active current $(\hat{i}_{inv})$. For the calculation of $\hat{i}_{inv}$, the power balance between the input and the output of the CHBMLI is used. The following expression defines P_{in} and P_{out}, where the losses in the capacitor and MOSFET have been neglected.

$$P_{in} = i_{in1} v_{dc1} + i_{in2} v_{dc2} - \frac{1}{2} R \hat{i}_{inv}^2 \tag{4.8}$$

Where R is the resistance of filter inductor

$$P_{out} = \frac{1}{2}\hat{v}_g \hat{i}_{inv} \tag{4.9}$$

Considering that both PV modules are working in the same operating point, $P_{in} = P_{out}$

$$2i_{in}v_{dc} - \frac{1}{2}R\hat{i}_{inv}^2 = \frac{1}{2}\hat{i}_{inv}\hat{v}_g \tag{4.10}$$

Finally the following expression for $\hat{i}_{inv}$ is obtained as,

$$\hat{i}_{inv} = -\frac{\hat{v}_g}{2R} + \sqrt{\frac{\hat{v}_g^2}{4R^2} + \frac{4i_{in}v_{dc}}{R}} \tag{4.11}$$

4.2.2 DC Voltage Regulation

Fig.4.3 shows two different schemes of DC-link voltage controller for DC voltage regulation for an 5-level CHBMLI based PVDG system which are discussed as follows,

1) Cluster voltage balancing control
2) Individual voltage balancing control

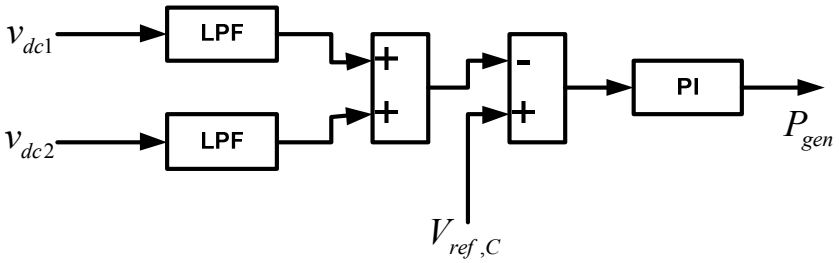

(a)

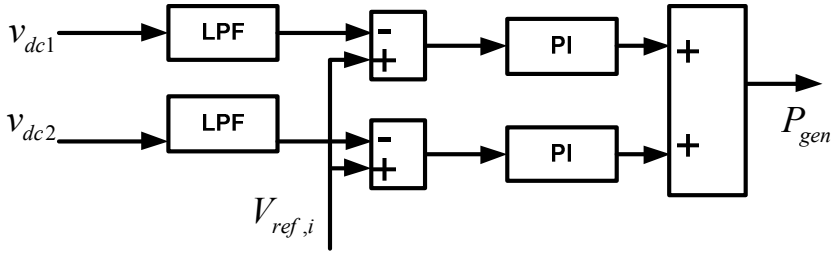

(b)

Fig.4.3: DC voltage controller for a 5-level CHBMLI based PVDG system (a) cluster voltage balancing control; (b) individual voltage balancing control.

4.2.2.1 Cluster Voltage Balancing Control

Fig.4.3 (a) shows the block diagram of the cluster voltage balancing control. This controller forces the DC-link voltage of the cluster formed by capacitor voltages of H-bridge-1 (v_{dc1}) and H-bridge-2 (v_{dc2}), to follow the reference cluster voltage $(V_{ref,c})$. The cluster voltage is defined as:

$$V_{dc} = v_{dc1} + v_{dc2} \tag{4.12}$$

Here, v_{dc1} and v_{dc2} are the instantaneous capacitor voltages consisting of both AC and DC components. It is desirable to extract only the dc components because the existence of the AC components deteriorates the controllability. Low-pass filters with a cut-off frequency of 15 Hz have been used to eliminate the dominant 100Hz component from the measured dc voltages [115, 116]. In cluster balancing control, the cluster voltage is calculated and compared with the cluster reference voltage $(V_{ref,c})$. The cluster reference voltage $\left(V_{ref,c}\right)$ can be calculated by adding the individual DC voltage references of the H-bridge cells in the cluster i.e.

$$V_{ref,c} = N \times V_{ref,H_i} \tag{4.13}$$

Where N=Number of cells of CHBMLI

The errors between the cluster voltages and $V_{ref,c}$ is processed through a PI controller and its output decides the amount of the current corresponds to the real power generated by the PV CHBMLI to keep the cluster voltages at their corresponding reference values. When DC voltage reference is greater than the cluster voltage, an amount of active power flows into that particular cluster, thus leading to enhancement of cluster voltage. On the other hand, when DC voltage reference is lower than the cluster voltage, then an amount of active power is drawn from that particular cluster, thus leading to a reduction in cluster voltage. For the two-stage CHBMLI based PVDG system this type of voltage controller is used.

The block diagram of DC-link voltage controller for two-stage 5-level 1-ϕ CHBMLI is given in Fig. 4.4. Here the actual DC-link voltage of each H-bridge cell (v_{dc1}, v_{dc2}) is sensed and passed through a first-order low pass filter (LPF) to eliminate the presence of switching ripples on the DC-link voltages and in the generated reference current signals. The difference of this filtered DC-link voltage and reference DC-link voltage $(v_{ref,C})$ is given to a discrete-PI regulator to maintain a constant DC-link voltage under varying atmospheric and load conditions.

The DC-link voltage error (Δv_{err}) in n^{th} sampling instant is given as:

$$\Delta v_{err}(n) = v_{ref,c}(n) - v_{dc1}(n) - v_{dc2}(n) \tag{4.14}$$

The output of the discrete PI regulator at n^{th} sampling instant is expressed as,

$$i_{inv}(n) = i_{inv}(n-1) + K_{P1}(\Delta v_{err}(n) - \Delta v_{err}(n-1)) + K_{I1}\Delta v_{err}(n) \tag{4.15}$$

Where K_{P1} and K_{I1} are proportional and integral gains of DC-link voltage regulator.

In order to design the voltage controllers, suitable transfer functions are obtained by the linearization of the equation (4.3) and (4.4). In this case it is considered that the PV module operates at STCs.

Adding equation (4.3) and (4.4)yields,

$$S_1 i_{inv} + S_2 i_{inv} = i_{in1} + i_{in2} - C_1 \frac{dv_{dc1}}{dt} - C_2 \frac{dv_{dc2}}{dt} \tag{4.16}$$

By considering only the DC component of the term $(S_1 + S_2) i_{inv}$, equation (4.16) is equivalent to,

$$\frac{(S_1 + S_2)\hat{i}_{inv}}{2} = i_{in1} + i_{in2} - C_1 \frac{dv_{dc1}}{dt} - C_2 \frac{dv_{dc2}}{dt} \tag{4.17}$$

In order to simplify the transfer function, the input currents to the DC-link i_{in1} and i_{in2} will be considered as disturbances and the term $S_1 + S_2$ constant. Under this assumption, the following transfer function is obtained:

$$\frac{V_{dc1}(s) + V_{dc2}(s)}{\hat{i}_{inv}(s)} = -\frac{S_1 + S_2}{2Cs} \tag{4.18}$$

Where $C_1 = C_2 = C$ and the term $S_1 + S_2$ is defined for STCs.

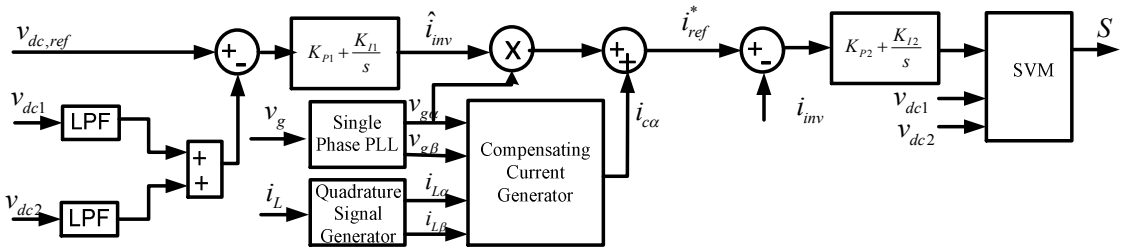

Fig.4.4:Schematic diagram of PV CHBMLI control scheme

4.2.2.2 Individual Voltage Balancing Control

Fig.4.3(b) shows the block diagram for the individual DC-link voltage balancing control. With individual voltage balancing control, each capacitor voltage is compared with the DC reference voltage ($V_{ref,Hi}$). The error is processed in a PI controller and its output decides the amount of real power required to keep that particular capacitor voltage at its reference value. When DC voltage reference is greater than the capacitor voltage, an amount of active power flows into that particular capacitor, thus leading to enhancement of capacitor voltage. On the other hand, when DC voltage reference is lower than the capacitor voltage, an amount of active power is drawn from that particular capacitor, thereby bringing down the capacitor voltage to its reference value. The sum of the outputs of the PI controllers is the total amount of real power generated by PV CHBMLI while keeping the capacitor voltages of individual H-bridges at their corresponding reference values. The gains of the PI controllers have been selected to give the optimum performance. For the single-stage PVDG system such type of DC-link voltage controller is used.

4.2.3 Reference current estimator for PV Inverter

To calculate the reference current a similar procedure has been followed here which was used for two-stage two-level PVDG system and is given by the following expression,

$$i_C^* = \frac{1}{v_{g\alpha}^2 + v_{g\beta}^2}\left[-v_{g\alpha}(\omega t)\cdot \tilde{p}(\omega t) + v_{g\alpha}\cdot \bar{p}(\omega t) + v_{g\beta}(\omega t)\cdot q(\omega t)\right] \quad (4.19)$$

Where $\frac{1}{v_{g\alpha}^2 + v_{g\beta}^2}$ and the term $\bar{p}(\omega t)$ represents the total amount of active power that the PV inverter is capable to deliver the utility grid or local load by regulating the DC bus.

4.2.4 Current Controller and Firing Pulse Generator for two-stage PVDG system

The reference PV CHBMLI current calculated in the equation (4.19) is added with DC-link voltage controller output and then compared with the actual CHBMLI current. The difference of this current is processed in a controller. The output of the controller set the 1-ϕ reference signal for the modulation scheme implemented in the controller. To produce the switching patterns for the devices, a single phase SVM based controller is used and is discussed in detail in the following subsection.

4.2.5 Modulation Scheme for 5-level CHBMLI

Many modulation techniques have been developed for controlling the output voltage of a CHBMLI. They are aimed at generating a stepped waveform that approximates an arbitrary reference signal with adjustable amplitude, frequency, and phase of a fundamental component that is usually a sinusoidal in steady state[117].The modulation algorithms are divided into two main groups depending on the domain in which they operate: the state-space vector domain, in which the operating principle is based on the voltage vector generation, and the time-domain, in which the method is based on the voltage level generation over a time frame.

The state-space vector domain algorithms such as Space Vector Modulation (SVM) based modulation algorithms for multilevel inverters are reported in [118], but, they are not the dominant modulation schemes found in industrial applications[119] as a SVM is a computationally intensive method and its complexities increase with increasing number of levels in the inverter [118]. However, these methods have advantages but usually at the expense of more complex implementation. The time-domain approaches such as carrier based pulse width modulation (PWM) techniques are the extensions of the classical modulation methods used for two-level VSI [119, 120]. Other time-domain modulation methods that have also been derived from the two-level VSI are multilevel selective harmonic elimination[121], selective harmonic mitigation[122] and synchronized optimum PWM. These three techniques require offline computations and need to be stored in lookup tables in the digital interface control board. These methods have the advantage in achieving better

efficiency. On the negative side, low dynamic performance and calculation burden with higher number of levels limit their applications. In contrast with the high amount of recently introduced multilevel modulation schemes, no new schemes have made their way to industrial applications, despite the great amount of recent contributions and advances on this topic [119]. The main reason could be that manufacturers favour the proven technology and simplicity of carrier-based PWM schemes[123] over new methods that have advantages but usually at the expense of more complex implementation [119, 120].

4.2.5.1 Single Phase Space Vector Modulation Scheme for CHBMLI

The space vector modulation scheme is based on the generation of reference voltage that was determined by the controller as the average of discrete output voltages that can be achieved by the power converter. This technique takes advantage of the degrees of freedom, as the selection of the switching sequence can be made in order to improve some power converter features, such as the number of commutation or voltage balance. However, both the PWM and SVM methods have the problems when the CHBMLI is operated with uncontrolled DC-link voltages. With CHBMLI, if the DC-link voltages are not of the correct magnitude and the modulators do not considered these voltage errors, there will be distortion in the output waveforms. This problem can be avoided in 1-ϕ CHBMLI using the SVM technique.

4.2.5.2 Control Region of 2-Cell 1-ϕ CHBMLI under balanced condition

The schematic diagram of a two-Cell 1-ϕ CHBMLI is shown in Fig.4.5. The output voltage of this CHBMLI depends on the output voltage of each cell which can be expressed as, $V_o = V_{H1} + V_{H2}$

Where, V_{H1}, V_{H2} are the output voltages of the H-bridge cell-1 and H-bridge cell-2 respectively.

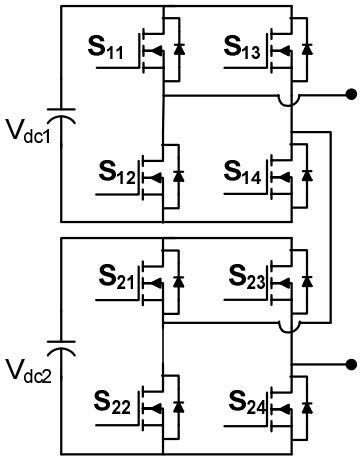

Fig.4.5: Schematic diagram of a 1-ϕ 2-cell CHBMLI

Three possible output voltage levels of each H-bridge cell are $-V_{dc,i}, 0, V_{dc,i}$, where i represent the H-bridge cell number. These voltage levels can be obtained by applying the switching vectors (0, 1, 2) which are shown in Table.4.1. As the output voltage is composed of the sum of individual H-bridge cell voltages, five output voltage levels can be achieved while considering equal DC-link voltages of each H-bridge cell. These output voltage levels are shown in Table.4.1.Some redundant switching states appear in the CHBMLI, because the same output voltage can be achieved using different combination of individual H-bridge states. Using Table.4.2, it is possible to represent the control region of the single phase two-cell CHBMLI. Output voltage is used as a component to plotted. In addition to this, the different states can be placed on one-dimensional representation, taking into their contribution to the output voltage. Finally the control region of two-cell CHBMLI under balanced condition of DC-link voltage is represented in Fig.4.7(a). State vectors UL means that the upper cell or H-bridge-1 has state 'U' and the lower cell or H-bridge-2 has state 'L'. The presence of redundant state vectors is clear using this representation, because different H-bridge states are located at the same point of the control region.

Table 4.1. Possible Switching vectors and the corresponding output voltage of H-bridge inverter

Switching Vectors	Switching Pulses to individual switch				Output Voltage
	S_{21} or S_{11}	S_{22} or S_{12}	S_{23} or S_{13}	S_{24} or S_{14}	
0	0	1	1	0	$-V_{dc}$
1	0	0	0	0	0
2	1	0	0	1	V_{dc}

Table 4.2: Different voltage levels under balanced and unbalanced condition

1st H-Bridge	**2nd H-bridge**	**Output Voltage**		
		$V_{dc1}=V_{dc2}=V_{dc}$	**$V_{dc1}>V_{dc2}$**	**$V_{dc1}<V_{dc2}$**
0	0	$-2V_{dc}$	$-V_{dc1}-V_{dc2}$	$-V_{dc1}-V_{dc2}$
0	1	$-V_{dc}$	$-V_{dc1}$	$-V_{dc1}$
1	0	$-V_{dc}$	$-V_{dc2}$	$-V_{dc2}$
0	2	0	$-V_{dc1}+V_{dc2}$ (<0)	$-V_{dc1}+V_{dc2}$(>0)
1	1	0	0	0
2	0	0	$V_{dc1}-V_{dc2}$ (>0)	$V_{dc1}-V_{dc2}$ (<0)
1	2	V_{dc}	V_{dc2}	V_{dc2}
2	1	V_{dc}	V_{dc1}	V_{dc1}
2	2	$2V_{dc}$	$V_{dc1}+V_{dc2}$	$V_{dc1}+V_{dc2}$

4.2.5.3 Selection of switching vector and estimation of switching duty cycle

Using the one-dimensional control region introduced for two-cell single phase CHBMLI with equal DC-link voltages, a one dimensional SVM strategy can be developed using the nearest two-vector method. The algorithm for the single phase SVM is given in Fig.4.6. As mentioned in the algorithm, the DC-link voltages of each cell are sensed. Based on these sensed voltages, possible voltage levels are estimated. Then a bubble sort algorithm is used to sort all the available voltage levels of CHBMLI in ascending order. In every sampling period, the position of the reference voltage is determined and based on the position two consecutive voltage vectors are applied to the CHBMLI. The algorithm is demonstrated as follows: Let the two H-bridge inverter has been applied with a DC voltage of V_{dc} each and the reference sinusoidal voltage is having maximum values $V_{\max}$, where $V_{dc} < V_{\max} < 2V_{dc}$. The vector diagram for this case is shown in Fig.4.7(a). At any time if the instantaneous value of reference voltage is V_1 Volt such that, $0 < V_1 < V_{dc}$, then from Fig.4.7(a) it is clear that the two adjacent voltage levels requires to achieve the reference value are 0 and V_{dc}.

Now $R = \dfrac{V_1}{V_{dc} - 0} = a.b$

Finally the output voltage, $V_0 = V_{dc}.T_1 + 0.T_2$

Where $T_1 = 0.b$ and $T_2 = 1 - 0.b$

To write it in a more general way, the switching sequence is formed by the states, U_1L_1 and U_2L_2 with duty cycles T_1 and T_2 respectively. The redundancy of the H-bridge is not taken into account and one possible space vector is chosen.

4.2.5.4 Control Region of 2-Cell 1-ϕ CHBMLI under un-balanced condition

However, there is always a chance of input DC-link voltage unbalance in CHBMLI when fed from PV module. The main cause of voltage unbalance in PV application are the partial shading, dust collection and PV ageing. This voltage unbalance in CHBMLI, leads to distortion in the output voltages and currents of the CHBMLI. Therefore the balance of the DC voltages is one of the important issues in the control of CHBMLI when used for PV application. By considering each H-bridge with different DC-link voltage V_{dci}, nine possible output voltage levels are possible for the CHBMLI which are summarized in Table.4.2. In this generalized case, the control region can again be represented using one dimension, mapping the states created by the variation in the DC voltages of the H-bridge cells. In case of single phase two-cell CHBMLI, the movement of the state vectors from voltage balanced condition to unbalanced voltage condition is shown in Fig.4.7. In unbalanced condition, four

different cases appear, because depending on the instantaneous voltage unbalance, the state vectors from the most negative to the most positive are different.

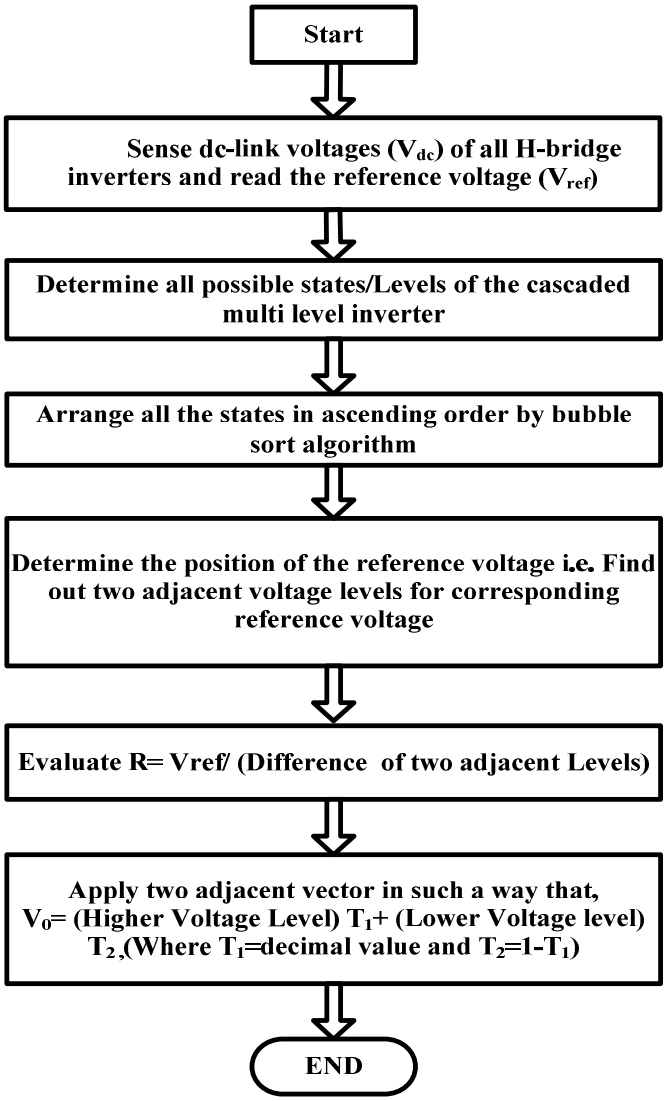

Fig.4.6: Flow Chart for single phase SVM

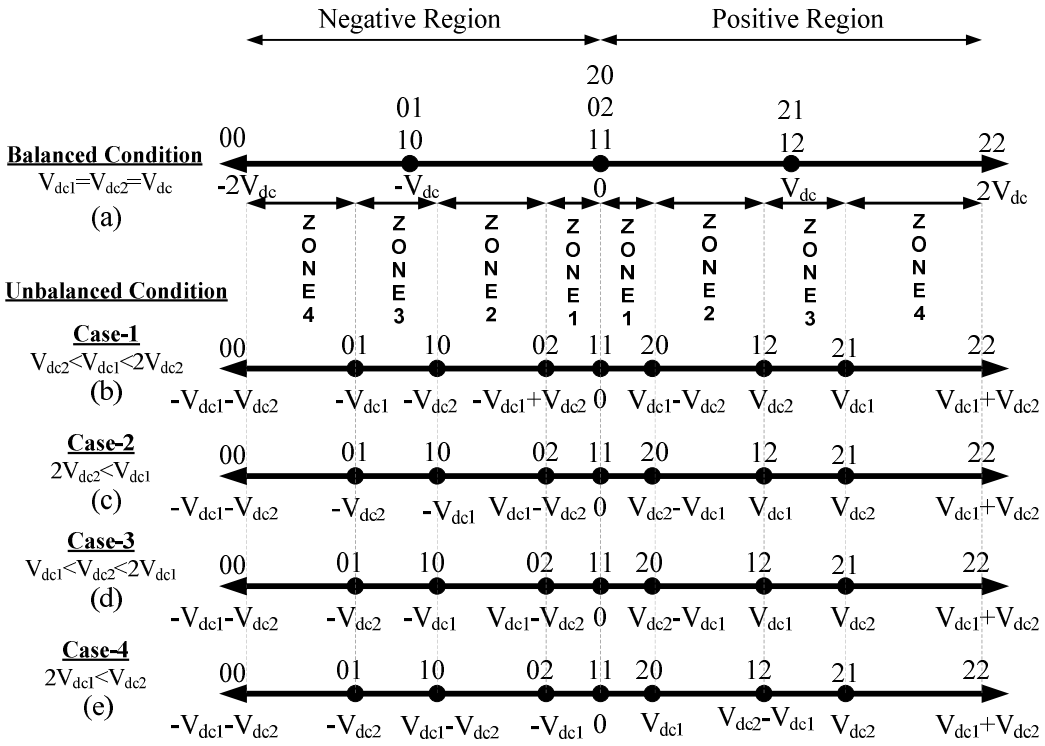

Fig.4.7: Control region for balanced and unbalanced DC-link voltage condition

4.2.5.5 Selection of switching vector and Estimation of switching duty cycle under unbalanced condition

The step by step procedure of one-dimensional space vector modulation scheme under both balanced and unbalanced condition of DC-link voltage is given below:

Step-1: Read reference and DC-link voltages

Step.2: Normalization of reference voltage at every sampling time, $V_{nor} = \dfrac{V_{ref}}{V_{dc1} + V_{dc2}}$

Step-3: Determination of all possible voltage levels

Step-4: Sorting of all voltage levels in normalized form using the bubble sort algorithm

Step-5: Evaluation of different zones (z_i) and their zone width (w_{di}, difference in magnitude of consecutive voltage levels) in both positive and negative regions of reference voltage.

Step-6: Selection of reference point in each zone

Step-7: Calculation of duty cycles, $T_1 = \left| \dfrac{V_{nor} - V_{ref,Z_i}}{w_{di}} \right|$, $T_2 = 1 - T_1$

Where T_1 and T_2 is the time for upper switching states and lower switching states for H-bridge-1 and H-bridge-2 respectively

Step-8: Selection of appropriate switching vectors of upper and lower H-bridge cells

Table 4.3. Calculation of reference point, zone width and switching sequence during unbalanced condition

Zone	Case	Reference Point		Zone Width ω_d		Switching Sequence	
		+ve Region	-ve Region	+ve Region	-ve Region	+ve Region	-ve Region
1	1	0	$\frac{V_{dc2}-V_{dc1}}{V_{dc1}+V_{dc2}}$	$\frac{V_{dc1}-V_{dc2}}{V_{dc1}+V_{dc2}}$	$\frac{V_{dc2}-V_{dc1}}{V_{dc1}+V_{dc2}}$	20-11	11-02
	2	$\frac{V_{dc1}-V_{dc2}}{V_{dc1}+V_{dc2}}$	$\frac{V_{dc1}-V_{dc2}}{V_{dc1}+V_{dc2}}$	$\frac{V_{dc2}-V_{dc1}}{V_{dc1}+V_{dc2}}$	$\frac{V_{dc2}-V_{dc1}}{V_{dc1}+V_{dc2}}$	12-20	11-10
	3	$\frac{V_{dc2}}{V_{dc1}+V_{dc2}}$	$\frac{V_{dc1}-V_{dc2}}{V_{dc1}+V_{dc2}}$	$\frac{V_{dc2}-V_{dc1}}{V_{dc1}+V_{dc2}}$	$\frac{V_{dc1}-V_{dc2}}{V_{dc1}+V_{dc2}}$	21-12	11-20
	4	$\frac{V_{dc1}}{V_{dc1}+V_{dc2}}$	$\frac{V_{dc1}}{V_{dc1}+V_{dc2}}$	$\frac{V_{dc1}}{V_{dc1}+V_{dc2}}$	$\frac{V_{dc1}}{V_{dc1}+V_{dc2}}$	22-21	11-01
2	1	0	$\frac{V_{dc2}}{V_{dc1}+V_{dc2}}$	$\frac{2V_{dc2}-V_{dc1}}{V_{dc1}+V_{dc2}}$	$\frac{V_{dc1}-2V_{dc2}}{V_{dc1}+V_{dc2}}$	20-11	02-10
	2	$\frac{V_{dc2}-V_{dc1}}{V_{dc1}+V_{dc2}}$	$\frac{V_{dc1}}{V_{dc1}+V_{dc2}}$	$\frac{2V_{dc1}-V_{dc2}}{V_{dc1}+V_{dc2}}$	$\frac{V_{dc2}-2V_{dc1}}{V_{dc1}+V_{dc2}}$	12-20	10-02
	3	$\frac{V_{dc2}}{V_{dc1}+V_{dc2}}$	$\frac{V_{dc1}}{V_{dc1}+V_{dc2}}$	$\frac{V_{dc2}}{V_{dc1}+V_{dc2}}$	$\frac{V_{dc2}-2V_{dc1}}{V_{dc1}+V_{dc2}}$	21-12	20-01
	4	$\frac{V_{dc1}}{V_{dc1}+V_{dc2}}$	$\frac{V_{dc1}-V_{dc2}}{V_{dc1}+V_{dc2}}$	$\frac{V_{dc2}-2V_{dc1}}{V_{dc1}+V_{dc2}}$	$\frac{2V_{dc1}-V_{dc2}}{V_{dc1}+V_{dc2}}$	22-21	01-20
3	1	0	$\frac{V_{dc1}}{V_{dc1}+V_{dc2}}$	$\frac{V_{dc1}-V_{dc2}}{V_{dc1}+V_{dc2}}$	$\frac{V_{dc2}-V_{dc1}}{V_{dc1}+V_{dc2}}$	20-11	10-01
	2	$\frac{V_{dc2}-V_{dc1}}{V_{dc1}+V_{dc2}}$	$\frac{V_{dc2}}{V_{dc1}+V_{dc2}}$	$\frac{V_{dc2}-V_{dc1}}{V_{dc1}+V_{dc2}}$	$\frac{V_{dc1}-V_{dc2}}{V_{dc1}+V_{dc2}}$	12-20	02-01
	3	$\frac{V_{dc2}}{V_{dc1}+V_{dc2}}$	$\frac{V_{dc2}}{V_{dc1}+V_{dc2}}$	$\frac{V_{dc2}-V_{dc1}}{V_{dc1}+V_{dc2}}$	$\frac{V_{dc1}-V_{dc2}}{V_{dc1}+V_{dc2}}$	21-12	01-10
	4	$\frac{V_{dc1}}{V_{dc1}+V_{dc2}}$	$\frac{V_{dc2}}{V_{dc1}+V_{dc2}}$	$\frac{V_{dc1}}{V_{dc1}+V_{dc2}}$	$\frac{V_{dc1}}{V_{dc1}+V_{dc2}}$	22-21	20-10
4	1	0	-1	$\frac{V_{dc2}}{V_{dc1}+V_{dc2}}$	$\frac{V_{dc2}}{V_{dc1}+V_{dc2}}$	20-11	01-00
	2	$\frac{V_{dc1}}{V_{dc1}+V_{dc2}}$	-1	$\frac{V_{dc1}}{V_{dc1}+V_{dc2}}$	$\frac{V_{dc1}}{V_{dc1}+V_{dc2}}$	12-20	01-00
	3	$\frac{V_{dc2}}{V_{dc1}+V_{dc2}}$	-1	$\frac{V_{dc1}}{V_{dc1}+V_{dc2}}$	$\frac{V_{dc1}}{V_{dc1}+V_{dc2}}$	21-12	10-00
	4	$\frac{V_{dc1}}{V_{dc1}+V_{dc2}}$	-1	$\frac{V_{dc1}}{V_{dc1}+V_{dc2}}$	$\frac{V_{dc1}}{V_{dc1}+V_{dc2}}$	22-21	10-00

4.2.5.6 Simulation Results of 1-ϕ SVM scheme for 2-cell CHBMLI with any DC-link voltage ratio

In order to validate the 1-ϕ space vector modulation scheme under both balanced and unbalanced DC voltages, simulation results have been obtained in a two-cell CHBMLI topology. For the validation of 1-ϕ SVM scheme, a reference voltage of 230 V (326 V (peak)) is chosen.The switching frequency is selected as 3 kHz. The test is carried out for three different cases of DC-link voltage ratio of two H-bridge cells, such as 1:1, 2:1 and 3:1. In these three cases, the DC-link voltage ratios are chosen as 300:300, 300:150 and 300:100 respectively. As discussed earlier, the generalized space vector modulation scheme for any DC-link voltage ratio is based on the calculation of the control region of the CHBMLI by accounting the instantaneous value of each DC-link capacitor voltages. The evaluation of the switching sequence and the duty cycle is made by using the control region which was determined online. The complete algorithm of SVM is developed in the embedded MATLAB function block of MATLAB Simulink software. The simulation results of duty cycle for H-bridge-1, H-bridge-2 for three different cases of DC-link voltage ratio is shown in Fig. 4.8. The output voltage and its harmonic spectrum of the three above mentioned cases of voltage ratio are shown in Fig.4.9 and Fig. 4.10 respectively. For the DC voltage ratio of 1:1, with, the output modulated voltage and its harmonic spectrum are shown in Fig.4.9 (a) and Fig. 4.10(a) respectively. Under this condition, the number of levels in the output voltage is found to be 5. The rms value of output voltage and its THD are found to be 325 V and 31.68% respectively. Similarly for the unbalanced condition, (i.e. DC-link voltage ratio of 2:1), the output modulated voltage and its harmonic spectrum are shown in Fig.4.9(b) and Fig. 4.10(b) respectively. In this case the number of levels of the output voltage waveform has increased from 5 (in case of 1:1) to 7. With the increment in number of levels, the THD of out voltage waveform is reduced from 31.68% (in case of 1:1) to 17.54%. Similar to the previous case, the rms value of output voltage found to be 325 V which is found to follow the reference voltage. Finally, the simulation results of output voltage and its harmonic spectrum for the DC voltage ratio of 3:1, is presented in Fig.4.9(c) and Fig. 4.10(c) respectively. In this case the number of levels of the output voltage waveform is increased to 9 and with this increase in number of levels; the THD of out voltage waveform is found to 12.26 %.Therefore, using this modulation scheme, any DC voltage ratio in the CHBMLI input can be accommodated in the modulation process to generate the reference voltage. The SVM controller determines the best output voltage of the CHBMLI and this voltage is generated by the controller even under extreme DC-link voltage unbalance situations.

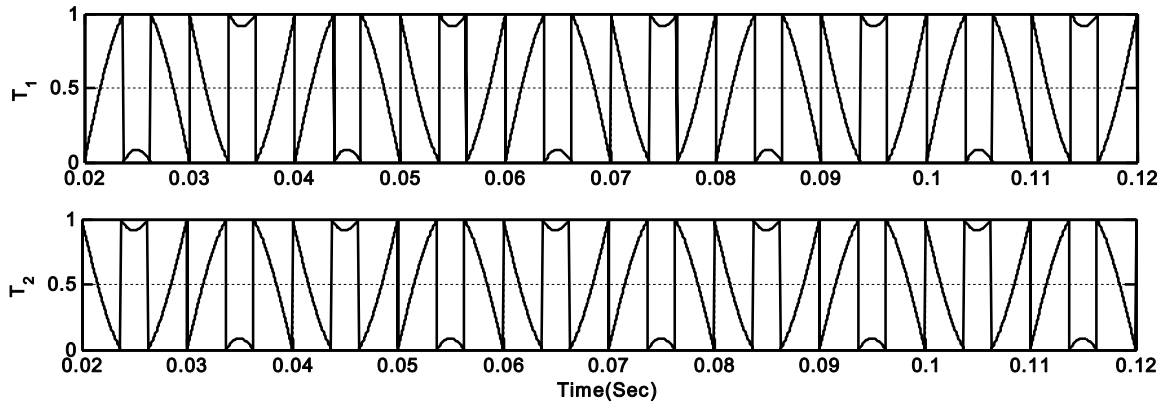

(a)

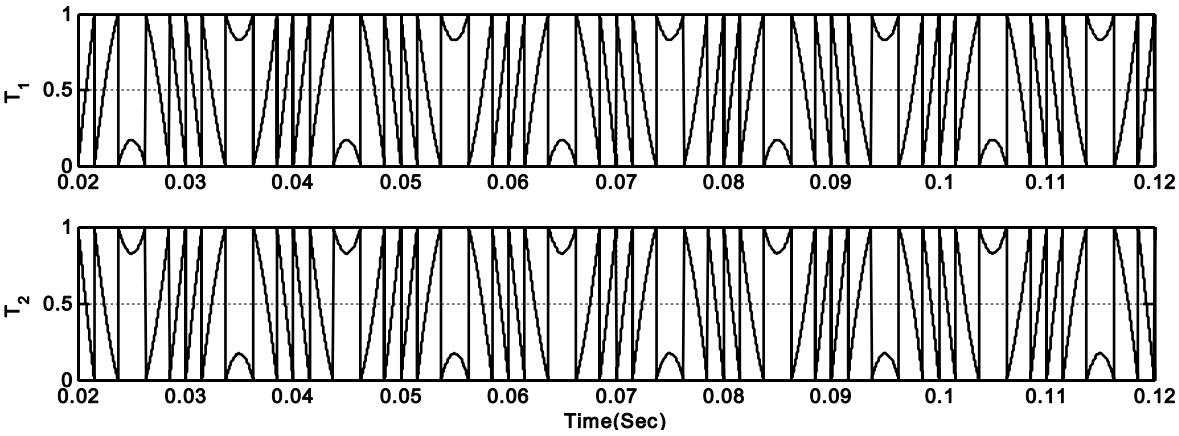

(b)

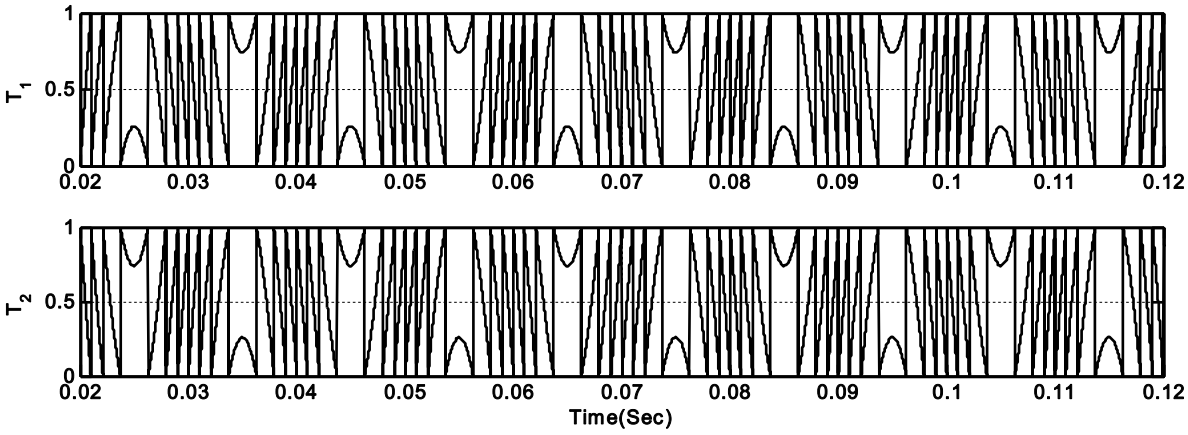

(c)

Fig. 4.8:Duty cycle (T_1 and T_2) for the upper and lower state of H-bridge-1,H-bridge-2 respectively, while the DC-link voltage ratio is (a) 1:1 (b) 2:1 (c) 3:1

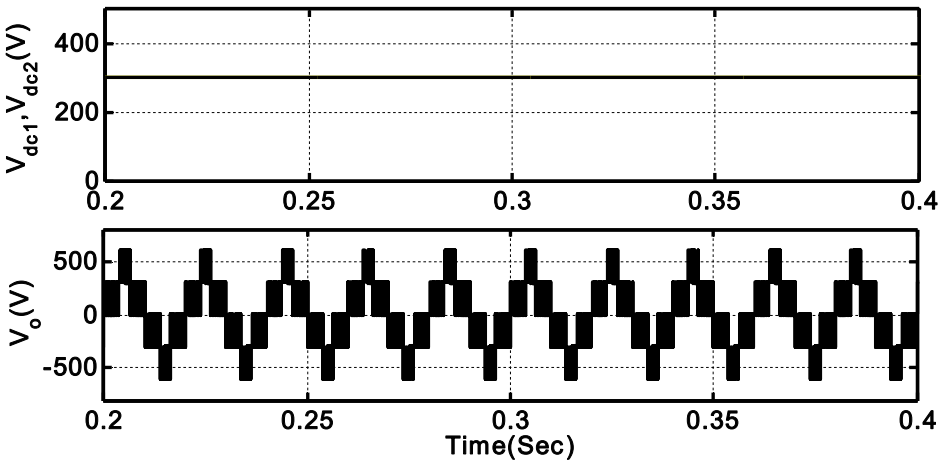

(a)

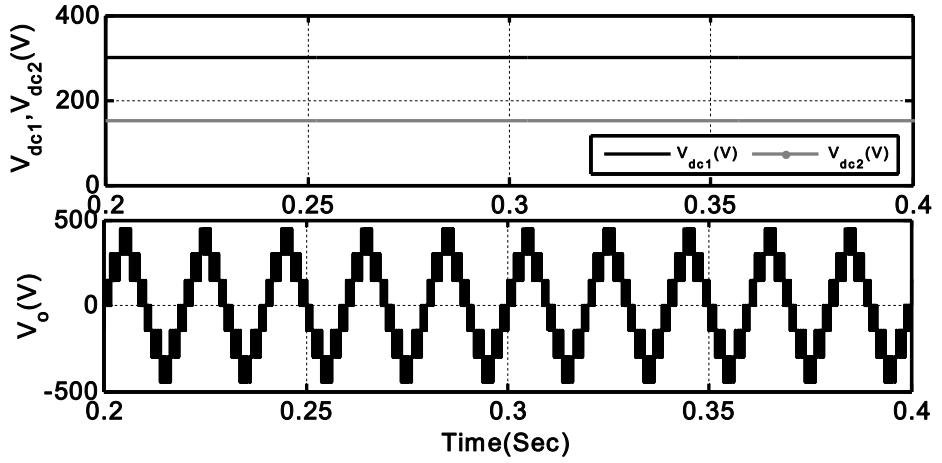

(b)

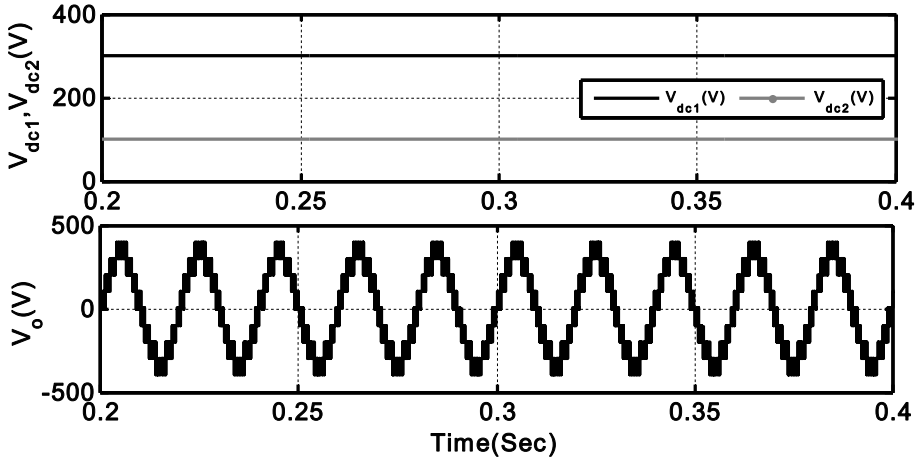

(c)

Fig.4.9: DC link voltages and CHBMLI output voltage when DC-link voltage ratio is (a)1:1(b)2:1 (c)3:1

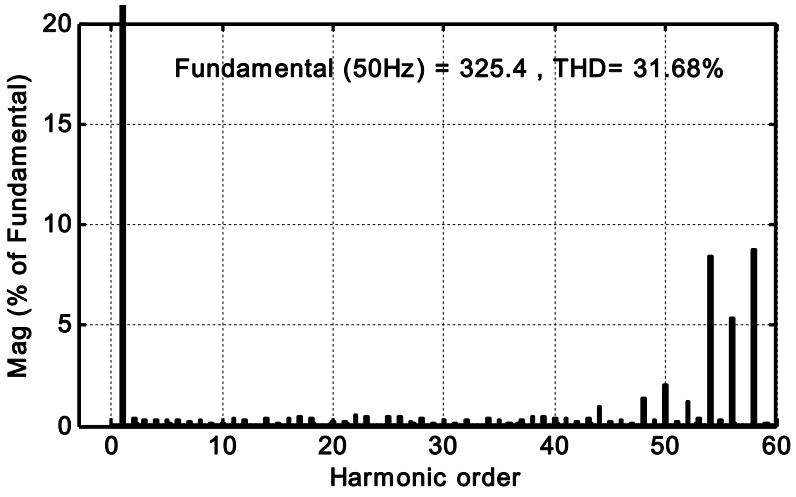

(a)

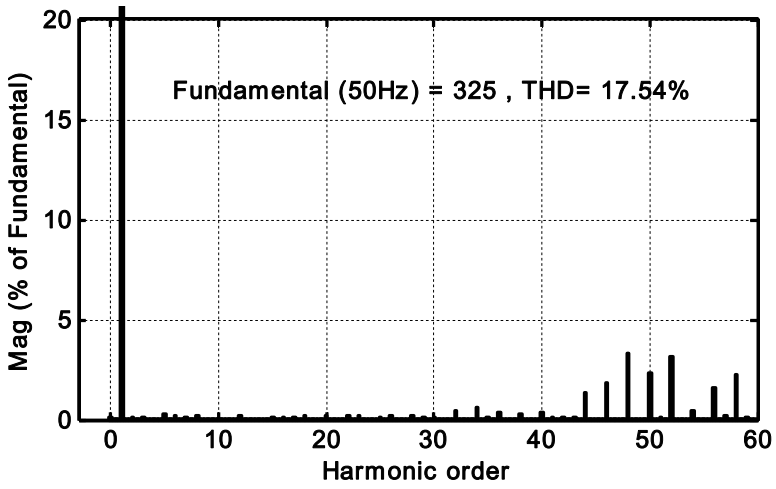

(b)

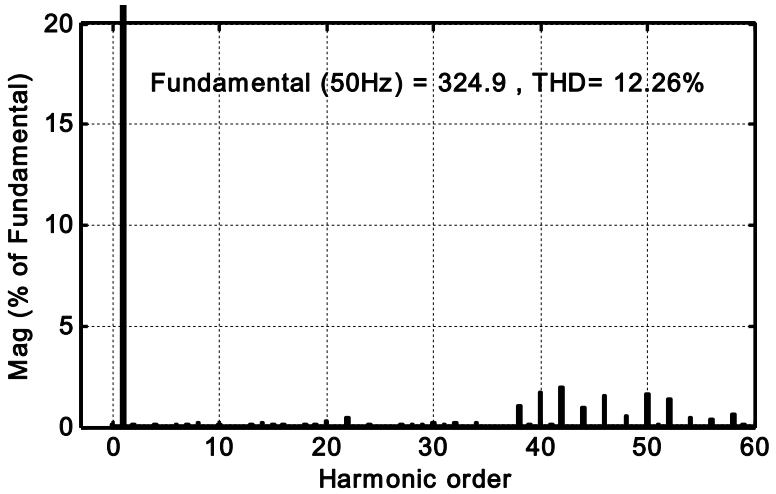

(c)

Fig. 4.10: Harmonic spectrum of output voltage of CHBMLI when DC-link voltage ratio is (a)1:1(b)2:1 (c)3:1

4.3 Single Stage CHBMLI based PVDG System

The configuration of proposed single-stage CHBMLI based PVDG system consists of two PV arrays, a CHBMLI, interfacing inductor, MPPT controllers, and PQEC is shown in Fig.4.11. PV array consists of series and parallel combination of small PV modules to match the required power rating. The 5-level CHBMLI topology consists of two H-bridge inverter connected in series. DC-link of each H-bridge cell of CHBMLI is fed from separate PV array and interfaced with the utility grid. Similar to the two-stage PVDG system, a linear/non-linear load is connected at PCC and the objective here is to control the CHBMLI in such a way to achieve the following functions in PVDG system,

1. MPPT Control
2. Power Flow Control
3. Load Current harmonic Compensation
4. Load Reactive power Compensation

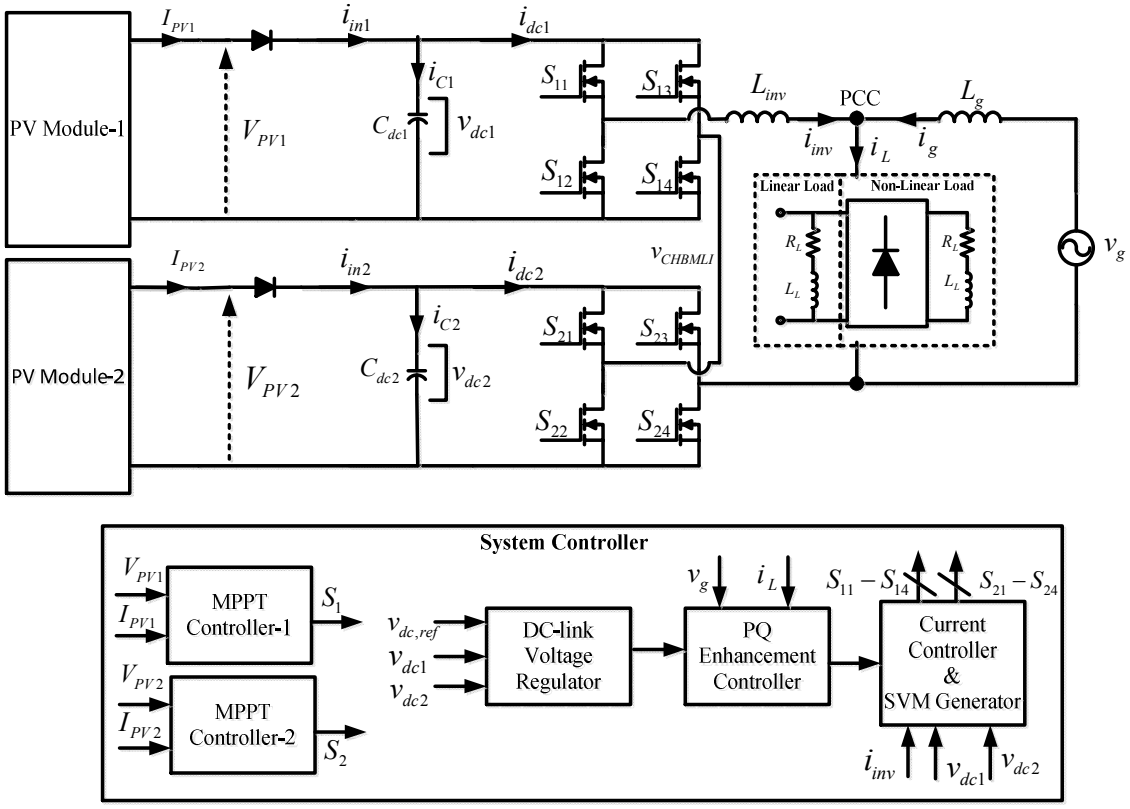

Fig.4.11: Schematic diagram of single-stage CHBMLI based PVDG system

The controllers required for obtaining above mentioned objectives in single-stage PVDG system are shown in Fig.4.4. The complete system controller in the proposed PVDG system consists of two main subdivisions such as (i) MPPT controller, which determines the reference DC-link voltage and (ii) current controller for PV CHBMLI which consists of control functions including the power flow operation, load current and reactive power compensation. The PV module voltage is maintained at reference voltage, which is decided by MPPT

algorithm using a PI controller. Therefore, the DC-link of such system is of floating type, unlike the two-stage topology where the DC-link is maintained at a fixed voltage level. In addition to that for the load current harmonics and reactive power compensation a PQEC is used whose operation is similar to that used in two-stage topology.

4.3.1 Development of MPPT with CHBMLI

Instead of using the boost converter, each H-bridge cell of CHBMLI is controlled independently for MPPT control. Here, a perturb and observe (P&O) based MPPT algorithm is used. In the proposed single-stage CHBMLI based PVDG system; the DC-link voltage of each H-bridge cell is equal to the corresponding PV module voltage. Therefore, to achieve MPPT for each PV module, the DC -link voltage of corresponding H-bridge cell is controlled such that PV module operates at its maximum power point (MPP). To control the DC-link voltages of CHBMLI, the reference value of DC-link voltage is adjusted. Under steady state, the reference DC-link voltage is equal to voltage at maximum power point i.e. (V_{MPP}). The flow chart for the MPPT controller is given in Fig.4.12. From the algorithm, it can be noticed that at first the present samples of PV array voltages $(V_{PV1}(k), V_{PV2}(k))$ and current $(I_{PV1}(k), I_{PV2}(k))$ are sensed to calculate the PV array output power $(P_1(k), P_2(k))$ and $\left(P_1(k-1), P_2(k-1)\right)$ at k^{th} and $(k^{th}, (k-1)^{th})$ sampling instant respectively. The governing equations for P&O based MPPT controllers are,

At MPP,

$$\frac{P(k)-P(k-1)}{V(k)-V(k-1)}=0 \tag{4.20}$$

Similarly on, the left side of MPP in $V-P$ curve,

$$\frac{P(k)-P(k-1)}{V(k)-V(k-1)}>0 \tag{4.21}$$

And on the right side of MPP in $V-P$ curve,

$$\frac{P(k)-P(k-1)}{V(k)-V(k-1)}<0 \tag{4.22}$$

In reference to above three conditions, the reference DC-link voltages of both H-bridge cells are updated at every sampling period to operate the whole system at MPP and finally the sensed DC-link voltages are controlled using a voltage regulator to follow the reference DC-link voltage. The updating of reference DC-link voltages as per the governing equation mentioned above are,

If the operating point is at MPP i.e. if equation (4.20) is satisfied then,

$$V_{dc1,refnew} = V_{dc1,ref}$$
$$V_{dc2,refnew} = V_{dc2,ref} \quad (4.23)$$

If the operating point is on the left side of MPP i.e. if equation (4.21) is satisfied then,

$$V_{dc1,refnew} = V_{dc1,ref} - \Delta V$$
$$else \quad (4.24)$$
$$V_{dc2,refnew} = V_{dc2,ref} + \Delta V$$

Finally, If the operating point is on the right side of MPP i.e. if the equation (4.22) is satisfied then,

$$V_{dc1,refnew} = V_{dc1,ref} + \Delta V$$
$$else \quad (4.25)$$
$$V_{dc2,refnew} = V_{dc2,ref} - \Delta V$$

Where $V_{dc1,refnew}, V_{dc2,refnew}, V_{dc1,ref}, V_{dc2,ref}$ are the new and old values of reference DC-link voltages for H-bridge-1 and H-bridge-2 respectively. ΔV is the step size for the iteration.

Finally the values of each PV arrays voltages and currents at $(k-1)^{th}$ are updated for the next iteration. The variations in reference DC-link voltages and hence the regulation of DC-link voltage ensures the operation of each PV array at MPP. For the proper operation of the CHBMLI based PVDG system, the sum of the DC-link voltages of two H-bridge cell should be little higher than the peak of the grid voltage.

4.3.2 DC-link Voltage Controller for Single Stage PVDG System

The DC-link voltage control of single stage CHBMLI based PVDG system is done by Individual Voltage Balancing Control which is discussed in Section.4.2.2.2. The only difference in single stage topology is that the reference DC-link voltage is of variable nature as it is generated from the MPPT controller unlike in two-stage topology where the reference DC-link voltage is of fixed value. Here the reference voltage $(V_{dc1,ref}, V_{dc2,ref})$ generated by the MPPT controller is compared with actual DC-link voltage (in this topology, it is PV array voltage) and then processed through two PI controllers. Each PI controller output gives the information about the power flow capability of the corresponding PV array. Basically, it gives a current which the PV array is capable to deliver. The output of two PI controllers is added to evaluate the reference value of active current for the PV CHBMLI.

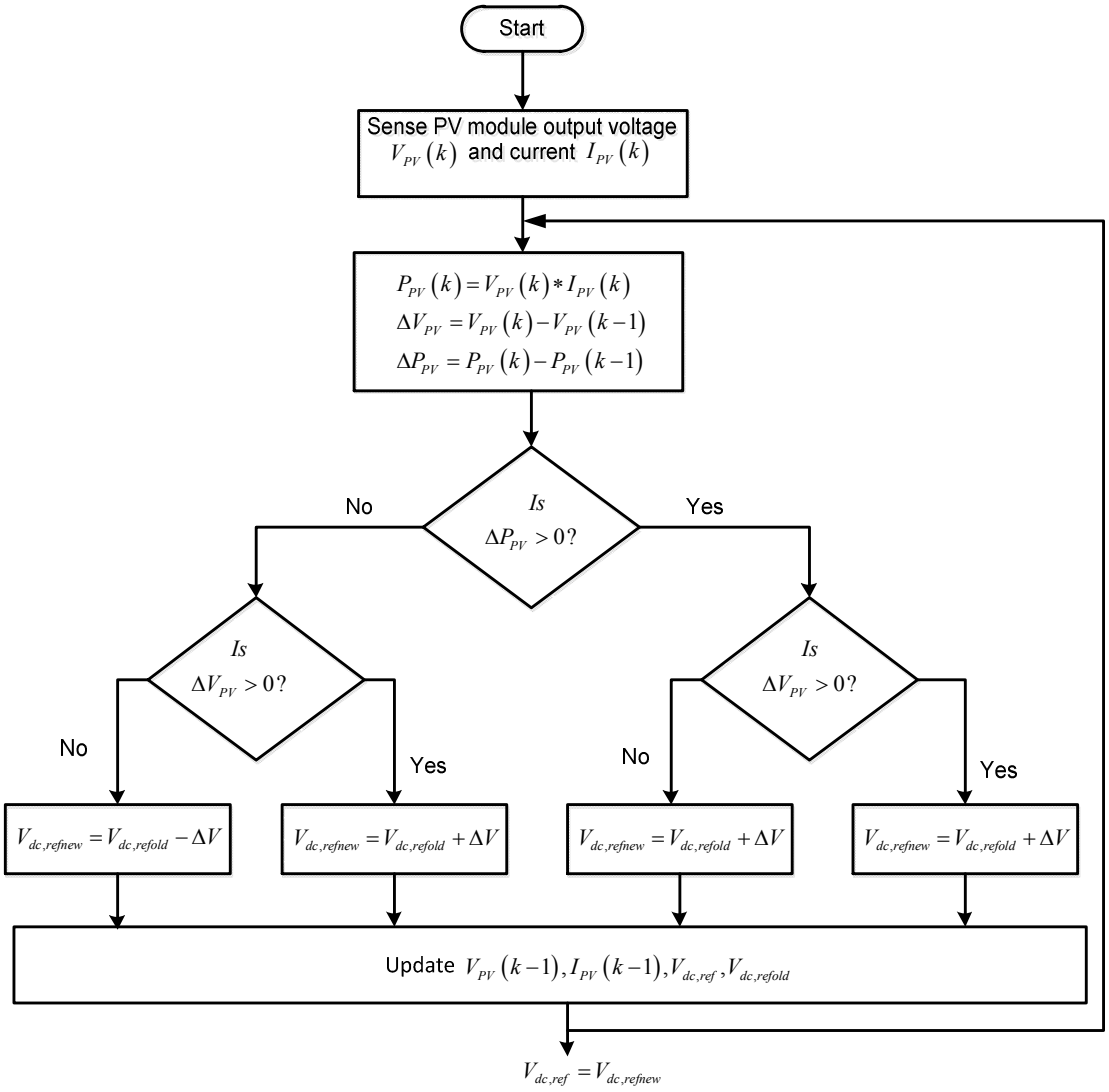

Fig.4.12: P&O based MPPT algorithm for single-stage PVDG system

4.3.3 Control of CHBMLI for single stage PVDG system

Similar to two-stage CHBMLI topology, the reference compensating current calculated in equation (4.19) is added to the DC-link voltage controller output to generate the total reference current for the CHBMLI. This reference current (i_{ref}^{*}) is compared with the actual inverter current (i_{inv}) and the error is processed in a controller. The outputs of the controller set the 1-ϕ reference signal for the SVM controller and produces the switching patterns for the power devices.. The switching operation of the power devices forces the PV CHBMLI current to follow the generated reference current.

4.4 Design of 1-ϕ 230V CHBMLI based PVDG system

To design a CHBMLI based PVDG system, let N be the cascaded number, i.e. the number of cascaded voltage source H-bridge inverter. Now, according to [115], the voltage (V_{dc}) required to be maintained in each capacitor of the H-bridge cell for proper operation of PVDG system with an enhanced power quality features is given as,

$$V_{dc} = k\frac{V_g}{N} \tag{4.26}$$

Where, V_g is the rms value of grid voltage and *k* is the design parameter.

The value of k should be properly selected as the performance of the PVDG system depends on it. The minimum value of k is $\sqrt{2}$ but, for optimal performance k is selected from the range 1.5 to 2.5 [124].

4.4.1 Selection of Cascade Number (*N*) for a 1-phase utility System

The cascade number is one of the most important design parameters, which accounts for the blocking voltage of the switching devices used in the PV CHBMLI. It also directly affects the cost, size and performance of the PV CHBMLI. With a cascade number N, the AC output voltage has a $(2N+1)$ level waveform. If the cascade number is low, then the required DC voltage reference is high and expensive switching devices are required. On the other hand, if the cascade number is very high, then the required DC voltage reference is low but more number of switching devices are necessary. Hence, an optimum value of cascade number should be selected.

Here a cascade number of *N* = 2 has been chosen, considering %THD, the PV module requirement and the voltage rating of the power switches to be used. With $N=2$, the DC voltage of individual H-bridge cells can be kept between 170 to 280 V.

4.4.2 Selection of Reference DC Voltage for each H-bridge Cell

For the optimum performance of PV CHBMLI, the value of reference DC voltage for each H-bridge cell $(V_{dc,i})$ must be carefully selected. For $k=2$, the reference DC voltage for each H-bridge cell is calculated to be 230 V. Thus, $V_{ref,i}$ of the value of 250 V is selected or for the cluster type DC-link voltages control the total reference DC-link voltage $(V_{ref,C})$ is chosen as 500 V. This allows the use of 460 V MOSFET for each H-bridge cell, which are available in the market at a reasonable cost.

4.4.3 Selection of Passive Parameters for PV CHBMLI

Based on the specific application, operating requirements, system configurations and control strategies, ratings of various components of PVDG system such as DC capacitor and inductance of coupling reactors have been selected [125-128].

The design of these components is based on the following assumptions [125]:

1. The grid voltage is sinusoidal.
2. Grid side current distortion is assumed to be less than 5% after compensation with PV CHBMLI having integrated shunt APF capability.
3. Fixed capability of reactive power compensation of PV CHBMLI.
4. Modulation scheme for the CHBMLI is assumed to operate in the linear modulation mode.
5. The coupling inductor resistance, R is neglected.

4.4.3.1 Selection of DC Capacitors

The energy exchange (Δe) in joules between each H-bridge cell of PV CHBMLI and load can be expressed as[125-128]:,

$$\Delta e = \frac{1}{2} C_{dc,i} \left(V_{c\max}^2 - V_{c\min}^2 \right) \tag{4.27}$$

Where $C_{dc,i}$ is the DC-link capacitor of i^{th} H-bridge cell

Where $V_{c\max}$ and $V_{c\min}$ (in volts) are the maximum and minimum capacitor voltages, respectively. From the principle of energy transformation equation (4.27) can be written as [127]:

$$\frac{1}{2} C_{dc,i} \left(V_{ref,i}^2 - V_{dc,\min}^2 \right) = V(aI)t \tag{4.28}$$

In equation(4.28),

$C_{dc,i} =$ Capacitance of the capacitor of each H-bridge cell (in farads),

$V_{dc,Min} =$ Minimum voltage level of the DC bus voltage of H-bridge cell,

$V =$ AC voltage of the each H-bridge cell (in rms) $= \frac{V_g}{2}$,

$I =$ Rated current of PV CHBMLI,

$t =$ Response time of the PV CHBMLI[127, 128],

$a =$ Over loading factor [127, 128].

Considering $V_{dc,\min} = 240V$ (considering 4% ripple in DC capacitor voltages), $V = \frac{230}{2} V = 115V$, $I = \frac{10*10\text{^}3}{230} = 43.47A$, t = 300 μsec, and $a = 1.2$, the calculated value of $C_{dc,i}$ is 734 μF.

4.4.3.2 Selection of Coupling Inductor

PV CHBMLI generates undesirable current harmonics around the switching frequency and its multiples. If the switching frequency of the PWM based PV CHBMLI is sufficiently high, these undesirable current harmonics can be easily filtered out by the filter inductor. The filter inductor $\left(L_{inv}\right)$ is one of the key components which determine the performance of the PV CHBMLI with an improved power quality features[125]. The connection of the coupling inductor to the PCC point is shown in Fig.4.1.

The selection of the AC inductance depends on the current ripple $i_{inv,(P-P)}$ and switching frequency of the PV inverter, f_{sw} .The approximate value of the ac inductance is given as [127]:

$$L_{inv} = \frac{m_a V_{CHBMLI}}{12 a f_{sw} i_{inv,(p-p)}} \tag{4.29}$$

Considering 5% peak-to-peak PV CHBMLI current ripple $\left(i_{inv,(p-p)}\right)$ to be 2.17 A (rms), the switching frequency of the PV CHBMLI $f_{sw} = 2Nf_{cr} = 2 \times 2 \times 3$ kHz = 12 kHz, amplitude modulation index $m_a = 1$, output voltage of the PVCHBMLI $\left(V_{CHBMLI}\right) = N * V_{ref,i} = 2 * 250 = 500V$ and overload factor (a) = 1.2, the value is calculated to be 1.3 mH. On one hand, for a better harmonic cancellation and reactive power compensation a higher value of inductance is preferable. However, on the other hand, a very high value of inductance will result in slow dynamic response of the PV CHBMLI and it would not be possible to compensate some of the load harmonics [125]. For the simulation of proposed CHBMLI based PVDG system the inductance value is chosen as 0.8 mH

4.5 Simulation Results and Discussion

In order to verify the proposed control approach for CHBMLI based two-stage and single-stage PVDG system an extensive simulation is carried out using MATLAB/Simulink software and their simulation model are shown in Fig.4.13(a) and Fig.4.13(b) respectively. Both two-stage and single-stage PVDG system are actively controlled to achieve sinusoidal grid current at unity displacement factor in spite of highly non-linear load connected at PCC under varying atmospheric and load conditions.

The control algorithms of both the two-stage and single-stage PVDG systems are modelled in MATLAB/Simulink. As discussed in the earlier section the MPPT control in two-stage PVDG system is accomplished by DC-DC converter, whereas in single-stage PVDG system it is achieved by each H-bridge cell of CHBMLI. The algorithm for the MPPT controller is developed in the embedded Matlab function block. In a PVDG system, The reference compensating current for the power flow control is derived from the instantaneous reactive power theory discussed in Section.4.3 by using the measured grid voltage, load

current and DC-link voltages of the individual capacitors of the H-bridge cells. A 1-ϕ SVM based current controller has been used to generate the gating signals for the MOSFETs of the two cell CHBMLI. The parameters used in the simulation are given in Table 4.4. A non-linear load consisting of an uncontrolled rectifier and a RL element on the DC-side, have been used for the analysis of the system. The system is validated for different modes of controller action as well as atmospheric condition. Finally, based on the simulation results a comparative analysis is made between two-level and CHBMLI based PVDG system with single-stage CHBMLI based topology.

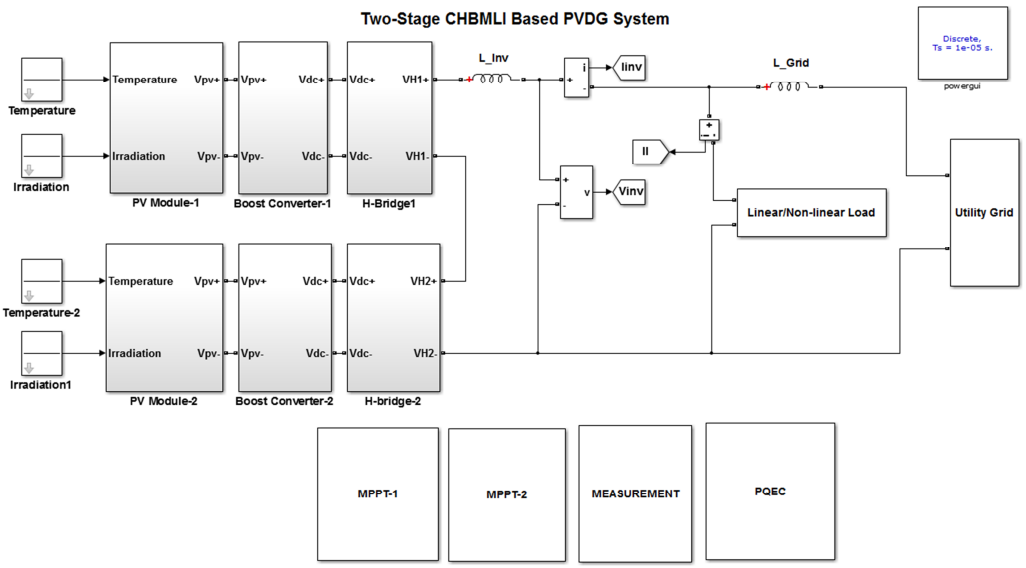

(a)

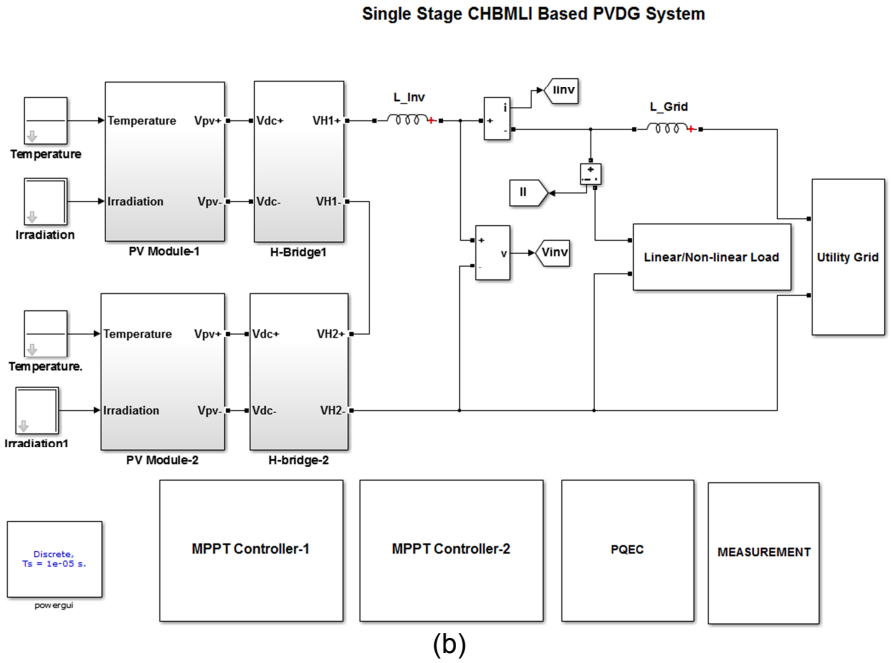

(b)

Fig.4.13: Matlab Simulink model of (a) Two-stage CHBMLI based PVDG System (b) Single-stage CHBMLI based PVDG System

Table 4.4: Parameters used in the simulation study.

Parameter	Value
Grid voltage	1-ϕ, 230 V, 50 Hz
DC bus reference voltage for 2-stage PVDG System	250 V (for each capacitor in the H-bridge cell)
DC bus capacitance	800μF (for each capacitor in the H-bridge cell)
Coupling inductor of PV CHBMLI	L_{inv} = 0.8 mH
Grid side inductance	L_g = 0.1 mH
Switching frequency	3 kHz
PI controller parameters	For two-stage PVDG System: K_p= 1.3, K_i = 0.8 For Single-stage PVDG System: K_p= 1.1, K_i = 1.5.
Load	Single-phase uncontrolled rectifier , Load-1: = 10 Ω, = 21 mH (Light Load) Load-2: = 3.306 Ω, = 10.5 mH (Over Load)
PV Array (For each H-bridge)	Total Power:5120 W Number of PV module in series:10 Number of PV module in parallel: 8

4.5.1 CHBMLI based PVDG system without and with PQEC

This section shows the system behaviour of two-stage and single-stage CHBMLI based PVDG system with different modes of operation of PQEC. These results pertain to STCs for PV modules while employing the MPPT controller, with a non-linear load (Load-1), connected across the PCC. In order to study the steady state and transient performance of these topologies for different modes of PQEC, the following events are considered to take place.

At t = 0 Sec., PQEC is off (disabled mode)

At t =0.4 Sec., PQEC is on (enabled mode)

The simulation results of two-stage and single-stage system under this condition are given in Fig.4.14 and Fig.4.15 respectively. The waveforms of grid voltage (v_g), PV CHBMLI current (i_{inv}), load current (i_L), grid current (i_g) and DC-link voltages (V_{dc1}, V_{dc2}) for two-stage and single-stage CHBMLI based PVDG system are shown in Fig.4.14(a) and Fig.4.15(a) respectively. Finally, based on these simulation results, the following observations are made:

1. Initially the PQEC is in disabled mode. During this state, the load current demand is less than that generated by PV CHBMLI and hence, the surplus current is fed to the grid. This can be observed from Fig.4.14(a) and Fig.4.15(a), where grid current is out of phase with the grid voltage in both the topologies. As the PQEC is in disabled mode, the PV CHBMLI in both the cases generates sinusoidal current as per the modulation scheme. However, the non-linear load connected at the PCC, draws a distorted current from the PV CHBMLI, which

leads to the injection of distorted current to the grid. Therefore, in this condition, even though the PV CHBMLI generates a sinusoidal current, the non-linear nature of load forces the grid current to be non-sinusoidal in both the CHBMLI based topologies.

2. With the PQEC is enabled at t=0.4 Sec., the controller generates a reference current for the PV CHBMLI which includes both harmonics and reactive components of a load current. Therefore, in this situation the PV CHBMLI generates a non-sinusoidal current to compensate the harmonics and reactive components of load current, thereby feeds a pure sinusoidal current to the grid. This demonstrates the capability of both two-stage and single-stage CHBMLI based PVDG system for harmonic compensation. Similar to a previous condition, as the load current demand is less than that generated by PV CHBMLI, the surplus current is fed to the grid. This can be observed from Fig.4.14(a) and Fig.4.15(a), for two-stage and single-stage topology respectively, where grid current is out of phase with grid voltage.
3. With the implementation of PQE scheme, the reactive component of current required by the load is completely supplied by the PV CHBMLI. Thus, the grid current is found to have a unity displacement factor with the grid voltage in both two-stage and single-stage topology, thereby demonstrating the reactive power compensation capability of PQEC in both two-stage and single-stage topology.
4. At the instant when the PQEC is enabled the DC capacitor voltages of each H-bridge cell of PV CHBMLI drops from its reference value to compensate the load current harmonics. This drop in capacitor voltages is restored by the DC-link voltage controller in both the cases. This ensures the effectiveness of the DC-link voltage controller under different modes of PQEC. However, it is found that the restoration time in the two-stage system is quite less compared to single-stage topology.

Fig.4.14(b) and Fig.4.15(b) shows the generated active power curves of two-stage and single-stage CHBMLI based PVDG system under different modes of operation of PQEC respectively. From these simulation results following observations are made,

1. It can be observed that, with the implementation of the MPPT control scheme in both two-stage and single-stage CHBMLI based PVDG system, the generated PV power is found to reach the maximum power as mentioned in the datasheet of PV module, which is given in Table 2.1. In case of two-stage topology, as the MPPT is achieved by boost converter, change of modes in PQEC doesn't affect the PV module output. Here, the MPPT controller action is not influenced by

PQEC because both controllers are completely isolated from each other. However, in single-stage CHBMLI based topology; the MPPT controller generates the reference voltage for the DC-link capacitor for each H-bridge cells. Therefore, when the PQEC is enabled from disabled mode, the DC-link capacitor of each H-bridge cells are discharged to accommodate the load current demand. This change in capacitor voltage, alter the operating point in PV module which was earlier in MPP. To regain the same MPP, the controller takes some time in case of single-stage CHBMLI based PVDG system.

2. The other three subplots of Fig.4.14(b) and Fig.4.15(b) shows the generated PV CHBMLI power, load power and grid power of two-stage and single-stage CHBMLI based topology respectively, under both modes of operation of PQEC. As the generated PV power is more than load demand, the surplus PV power is fed to the grid. The positive value of the active power supplied by the PV CHBMLI implies that power flows from PV CHBMLI towards PCC, whereas negative value of grid active power implies that the grid absorbs the surplus power. It can be observed that the power generated by PV CHBMLI in two-stage and single-stage topology is 9.7 kW and 9.8 kW respectively. This increase in power with single-stage topology leads to more power transfer in case of single-stage topology compared to two-stage topology.
3. Similarly, the reactive power plots of two-stage and single-stage CHBMLI based topology are depicted in Fig.4.14(c) and Fig.4.15(c) respectively. When PQEC is disabled, the reactive power demanded by the load is completely supplied by the grid. However, at the instant when PQEC is enabled, the PV CHBMLI starts feeding the reactive power to the load thereby making the grid reactive power zero. This implies that, with PQEC the PV CHBMLI in both topologies supplies the reactive power demanded by the load. This leads to unity displacement factor at the PCC.

Finally, the harmonic spectrum of PV CHBMLI current, load current and grid current, before and after the application of PQEC, in case of two-stage CHBMLI based topology are shown in Fig.4.14(d), Fig.4.14(e), and Fig.4.14(f) respectively. Similarly, the corresponding harmonic spectrums in single-stage topology are shown in Fig.4.15(d), Fig.4.15(e) and Fig.4.15(f). Before compensation, the THD of PV CHBMLI current, load current, and grid current in two-stage topology are found to be 1.72 %, 24.90%, and 24.25 %, respectively, whereas with single-stage topology the corresponding current THD are found as 21.14 %, 24.90% and 2.96% respectively. Similarly, when the PQEC is enabled the THD of PV CHBMLI current, load current and grid current in two-stage topology are found out to be 23.31%, 31.22% and 3.65%, respectively, while with single-stage topology the corresponding current THD are found out to be 23.94%, 32.07% and 3.76%. It can be observed that the

grid current THD with both the topologies is well within the limits of IEEE 1547 and IEC 61727 recommended value of 5% with the application of PQEC.

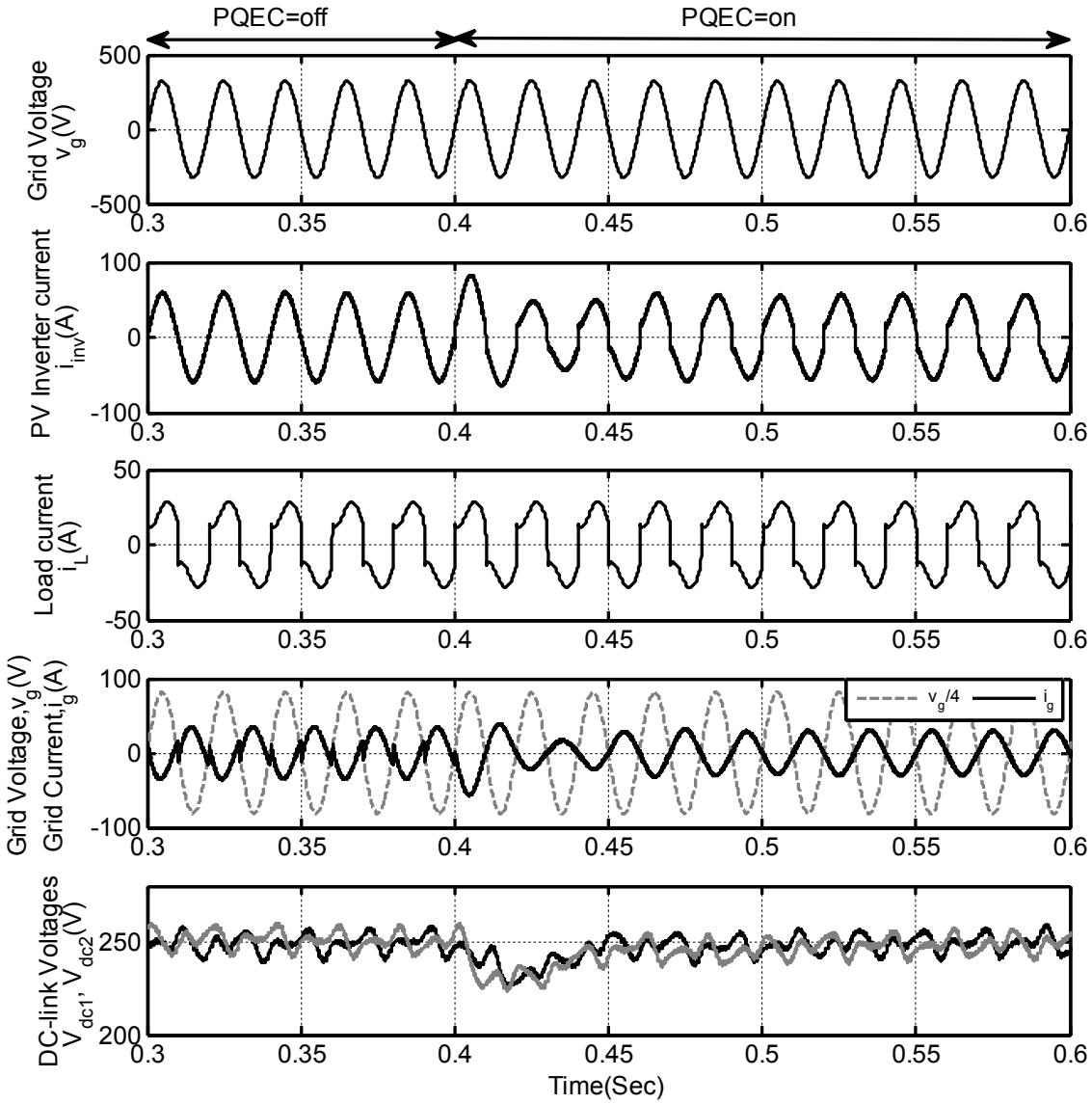

Fig.4.14 (a):Grid Voltage, PV inverter current, load current, grid current and DC-link voltage of two-stage CHBMLI based PVDG system under disabled and enabled modes of PQEC

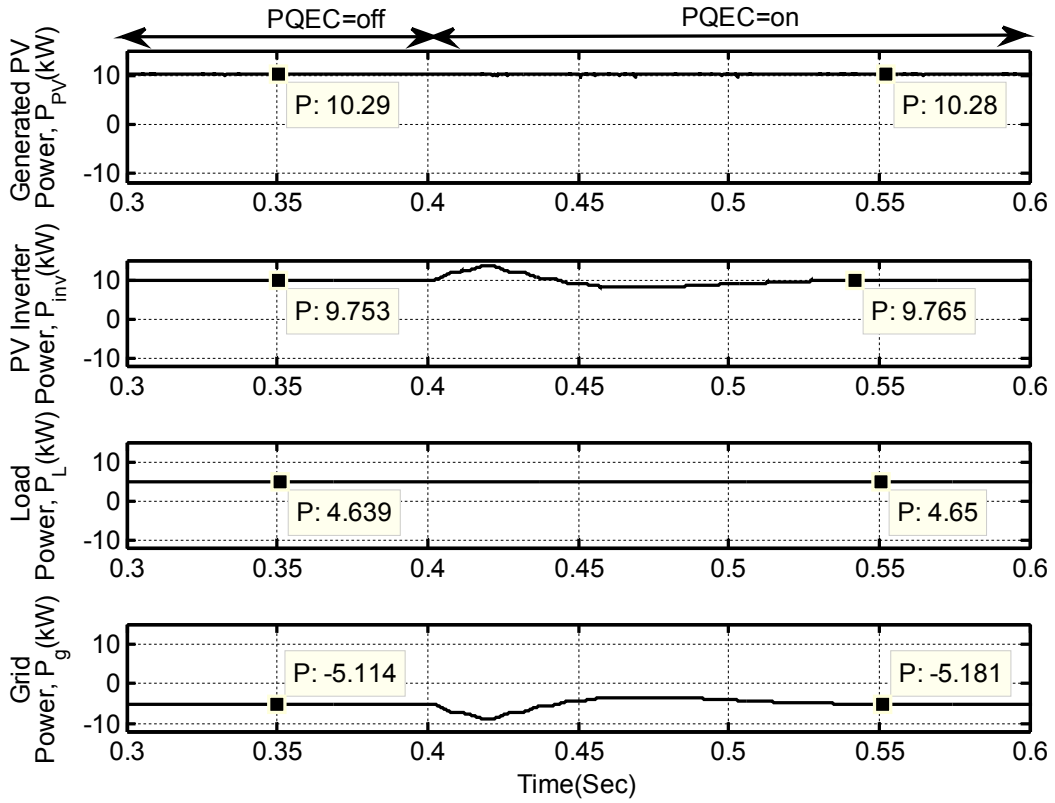

Fig.4.14 (b): Active Power curves of two-stage CHBMLI based PVDG System

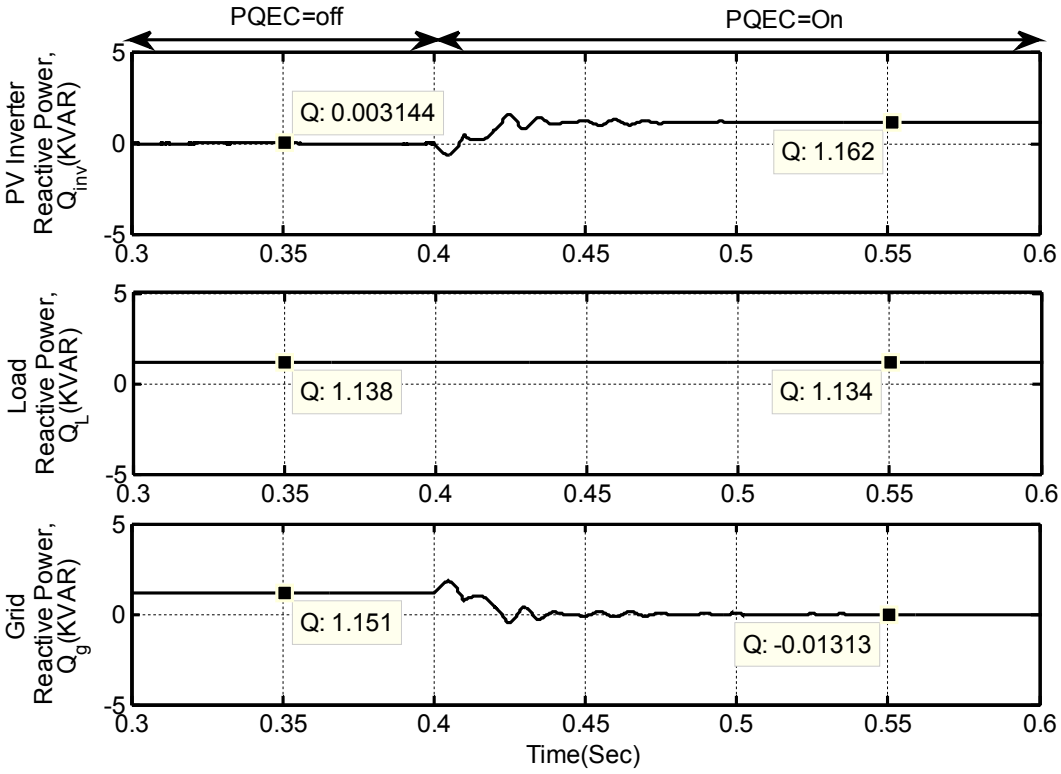

Fig. 4.14 (c): Reactive Power curves of two-stage CHBMLI based PVDG System

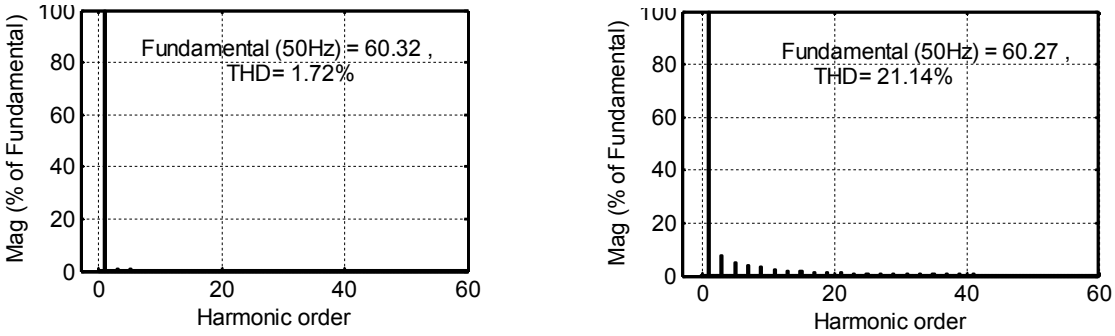

(i) (ii)

Fig. 4.14(d) :THD of PV CHBMLI current (i) without PQEC (ii) with PQEC for two-stage CHBMLI based PVDG system

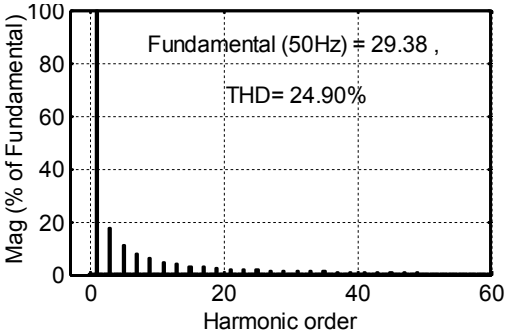

Fig. 4.14(e):THD of Load current

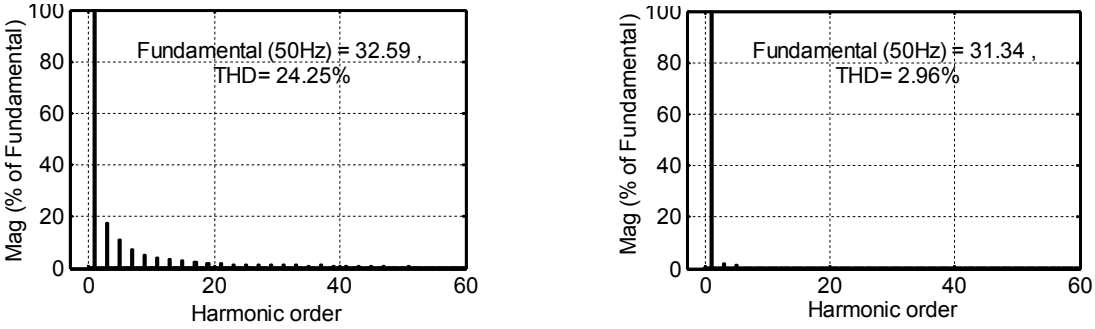

(i) (ii)

Fig. 4.14(f): THD of grid current (i) without PQEC (ii) with PQEC for two-stage CHBMLI based PVDG system

Fig.4.14: Simulation results of two-stage CHBMLI based PVDG system under different modes of PQEC

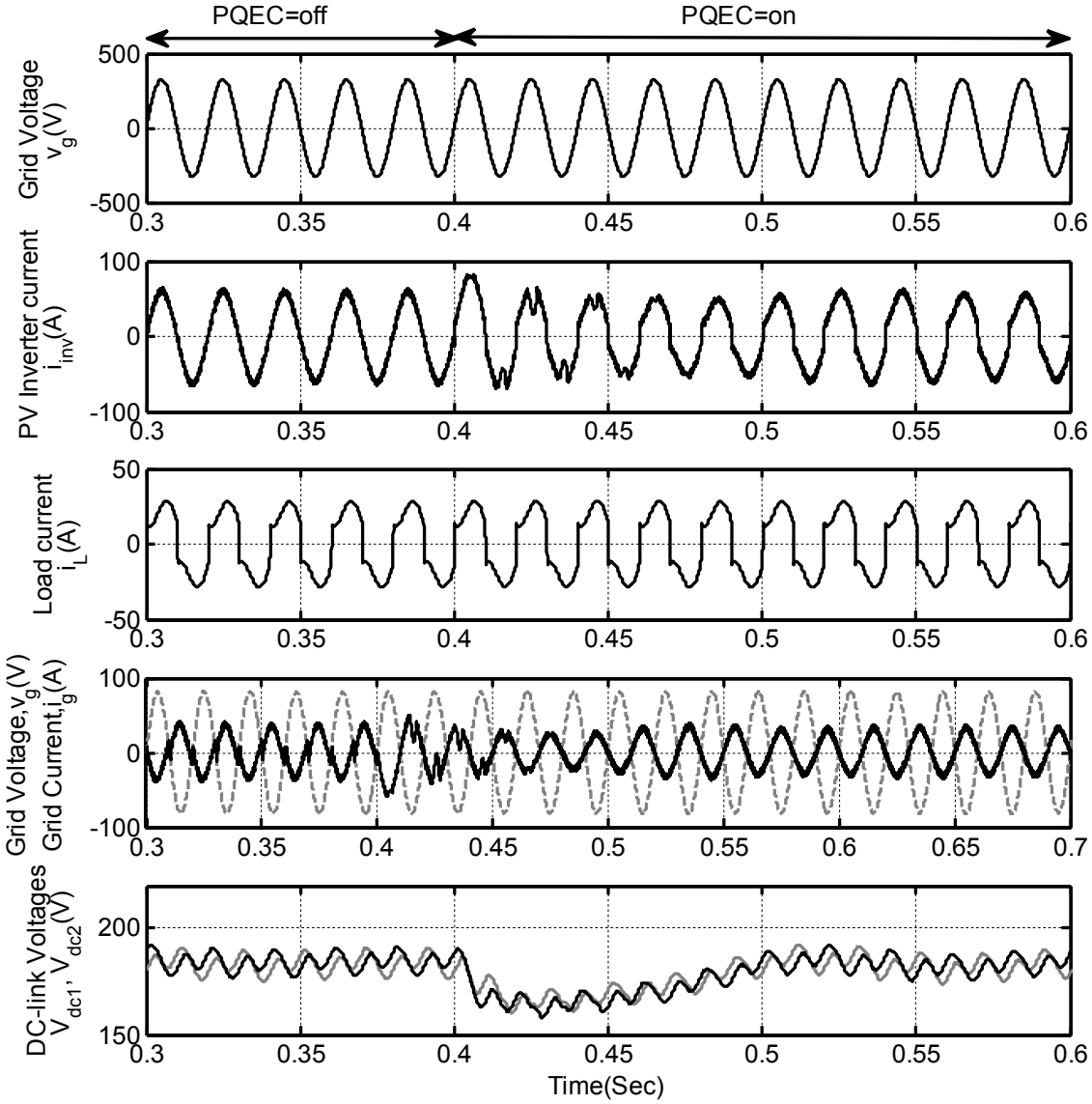

Fig.4.15 (a): Grid Voltage, PV CHBMLI current, load current, grid current and DC-link voltage of single-stage CHBMLI based PVDG system under different modes of PQEC

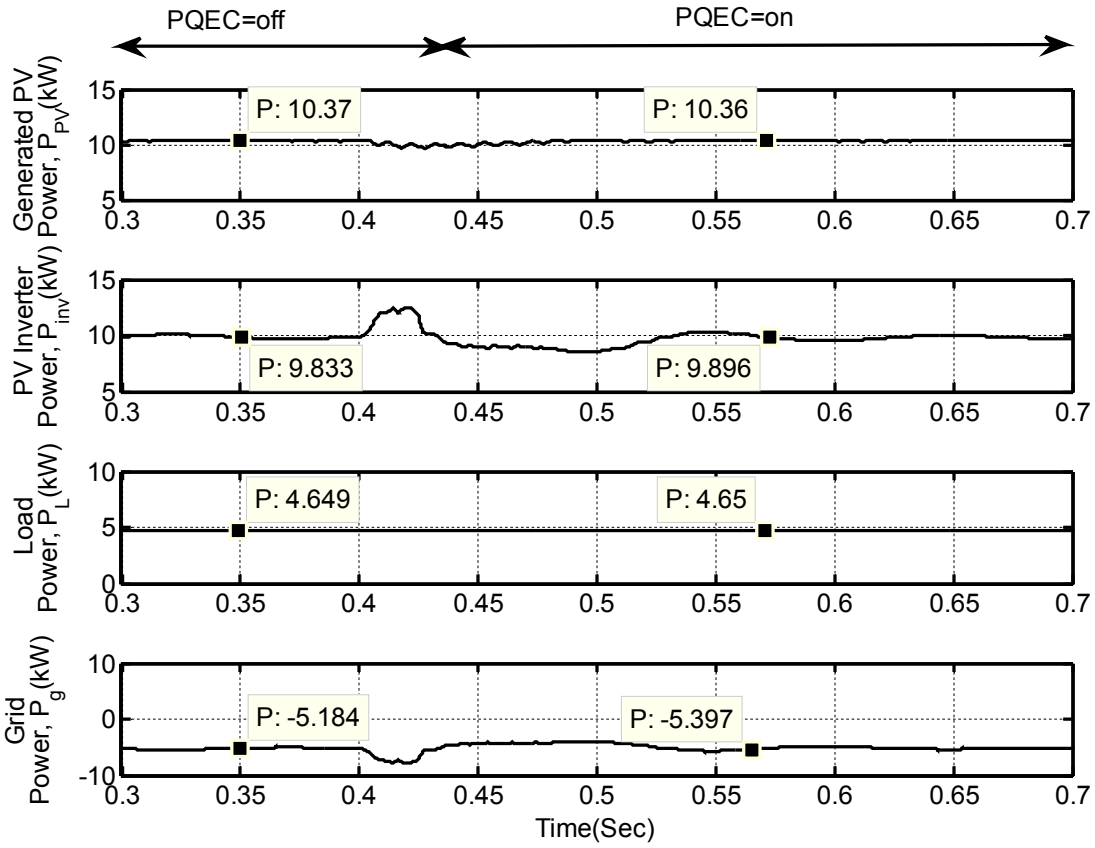

Fig.4.15(b): Active Power Curves of single-stage PVDG system under disabled and enabled modes of operation of PQEC

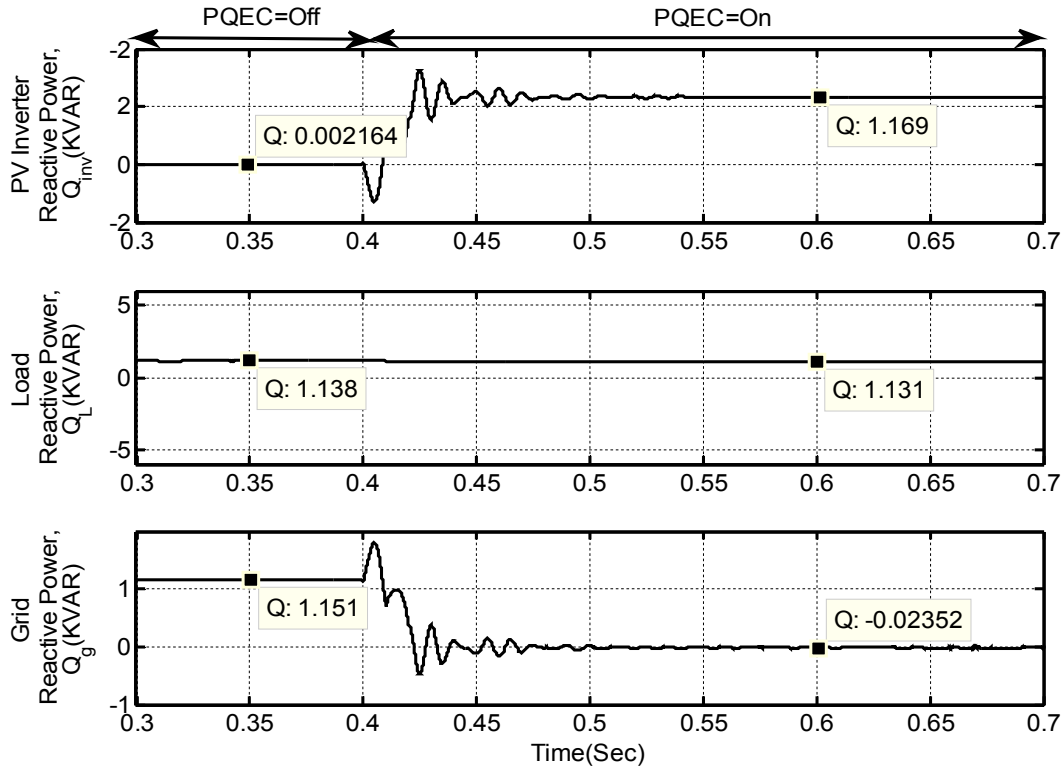

Fig.4.15(c): Reactive Power Curves of single-stage PVDG system under disabled and enabled modes of operation of PQEC.

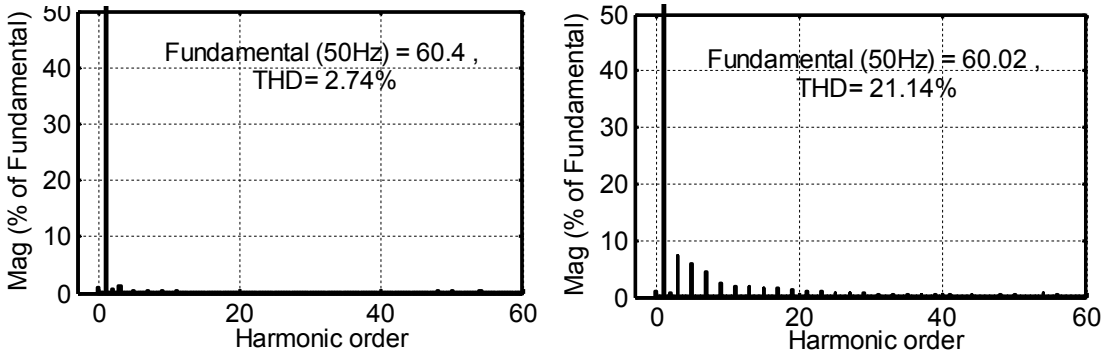

(i) (ii)

Fig.4.15 (d): THD of PV CHBMLI current (i) without PQEC (ii) with PQEC for single-stage CHBMLI based PVDG system

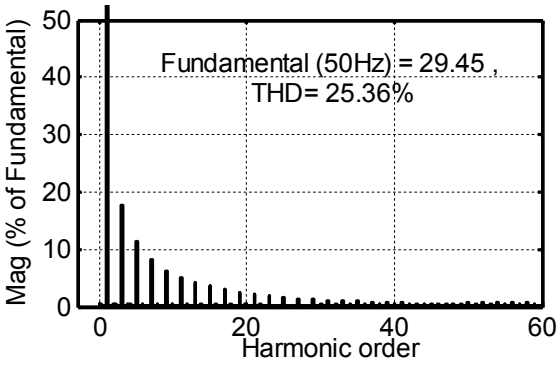

Fig.4.15 (e): THD of PV Load current for single-stage CHBMLI based PVDG system

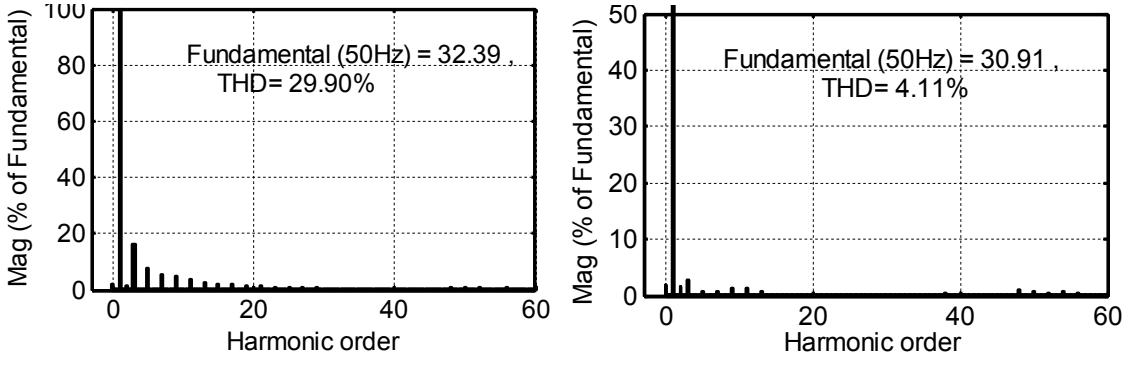

(i) (ii)

Fig.4.15(f): THD of grid current (i) without PQEC (ii) with PQEC for single-stage CHBMLI based PVDG system

Fig.4.15: Simulation results of single-stage CHBMLI based PVDG system under different modes of PQEC

4.5.2 CHBMLI based PVDG system under varying load conditions

This section presents simulation results of two-stage and single-stage CHBMLI based PVDG system under two extreme loading conditions- namely light load and overload. These results pertain to STCs for PV arrays while employing both MPPT and PQEC. In order to study the steady state and transient performance of the system for these conditions, the following events are considered in PVDG system:

At *t* = 0 Sec., a light load (Load-1) is connected across the PCC.

At *t* =0.4 Sec., an overload (Load-2) condition is created at the PCC.

The simulation results of the PVDG system under these conditions with two-stage and single-stage topology are given in Fig.4.16 and Fig.4.17 respectively. The simulated waveforms of grid voltage (v_g), PV CHBMLI current (i_{inv}), load current (i_L), grid current (i_g) and DC-link voltages (V_{dc1}, V_{dc2}) for two-stage and single-stage CHBMLI based PVDG system under varying load condition are shown in Fig.4.16(a) and Fig.4.17(a) respectively. Based on these simulation results, the following observations are made:

1. Initially there is a light non-linear load (load-1) on the system. During this condition, the load current demand is less than that generated by PV CHBMLI and hence, the surplus current is fed to the grid. This can be observed from Fig.4.16(a) and Fig.4.17 (a) that in case of two-stage and single-stage topology, where grid current is out of phase with PV CHBMLI as well as the load current. As the PQEC is enabled, the PV CHBMLI of both the topologies generates a non-sinusoidal current consisting of fundamental, harmonics and reactive components of a load current. Therefore, under this condition the non-sinusoidal component of the load current is completely supplied by the PV CHBMLI, thereby relieving the grid from the supply of harmonics.

2. When the load is increased at t=0.4 Sec., to create an overload condition, the load current demand is more than that generated by PV CHBMLI and hence, the rest of the load current demand is met from the grid. This is verified from Fig.4.16(a) and Fig.4.17(a) for two-stage and single-stage topology respectively, where grid current is in phase with both PV inverter and the load current. Similar to light load condition, the harmonic components of the load current are supplied by the PV CHBMLI thereby making the grid current purely sinusoidal. This demonstrates the capability of the PVDG system to fully compensate the harmonics in both two-stage and single-stage system.

3. With the implementation of the PQE scheme, the reactive component of current required by the load is completely supplied by the PV CHBMLI. Thus, the grid current is found to have a unity displacement factor with the grid

voltage under both, light and overload conditions, thereby demonstrating the reactive power compensation capability of the scheme with both the topologies.

4. At the instant when the load demand increases the DC capacitor voltages of each H-bridge cell of PV CHBMLI drops from its reference value to compensate the increased load current. This drop in capacitor voltages is restored in 2-3 cycles; in case of two-stage topology which can be observed from Fig.4.16 (a). However, in single stage topology the restoration process takes around 4-5 cycles. The DC-link voltage regulator has ensured the regulation of the capacitor voltages in both the topologies.

Fig.4.16 (b) and Fig.4.17 (b) shows the generated active power curves of two-stage and single-stage CHBMLI based PVDG system under varying load condition respectively. From these simulation results the following observations are made,

1. With the implementation of the MPPT control scheme, the generated PV power in both the topologies are found to reach the MPP. In case of two-stage topology the load variation doesn't affect the PV module output, which can be observed from the first sub-plot of Fig.4.17(b). In this topology the MPPT is accomplished with the help of DC-DC converter and the MPPT control action are completely independent from the power flow operation of PV CHBMLI. However, in single-stage topology the load variation directly affects the PV module output. In steady state, when the system was feeding power to a light load, each PV module was operating at MPP.
2. The instant when, the load is changed the operating point on each PV module is deviated from MPP and after a few iterations in MPPT algorithm each PV module again start operating at the MPP. This effect of load variation on the PV module output in single-stage is shown in the first sub-plot of Fig.4.17 (b).
3. The generated PV CHBMLI power, load power and grid power of two-stage and single-stage CHBMLI based topology under varying load conditions are shown in the other three subplots of Fig.4.16 (b) and Fig.4.17(b) respectively. Under light load condition, the generated PV power is more than the power demand of the load. Thus, the surplus PV power is fed to the grid. The Positive value of the active power supplied by the PV CHBMLI implies that power flows from PV CHBMLI towards PCC, whereas a negative value of grid active power implies that the grid absorbs power. Moreover, during overload condition, the generated PV power is unable to meet the load demand and hence, both PV CHBMLI and the grid share the load. Here the

positive value of grid power implies that the power flow is from the grid towards PCC. It can be observed that the power generated by PV CHBMLI in two-stage and single-stage topology is 9.7 kW and 9.8 kW respectively. This increase in power with single-stage topology leads to more power transfer to the grid in case of single-stage topology compared to two-stage topology under light load condition. Whereas during overload condition the share of grid power in two-stage topology is more compared to single-stage topology.

4. Similarly, the reactive power plots of two-stage and single-stage CHBMLI based topology under varying load conditions are depicted in Fig.4.16(c) and Fig.4.17(c) respectively. Under both light load and overload condition, with both the topologies the grid reactive power is zero, thereby implying that the reactive power demand of the load is met by the PV CHBMLI. This leads to unity displacement factor at the point of common coupling (PCC).

Finally, in case of two-stage CHBMLI based topology, the harmonic spectrum of PV CHBMLI current, load current and grid current, under light load and overload conditions, are shown in Fig.4.16(d), Fig.4.16(e), and Fig.4.16(f) respectively. Similarly, the corresponding harmonic spectrums in single-stage topology are shown in Fig.4.17(d), Fig.4.17(e) and Fig.4.17(f). Under light load condition, the THD of PV CHBMLI current, load current, and grid current in two-stage topology are found to be 23.31%, 31.22%, and 3.65% respectively whereas with single-stage topology the corresponding current THD are found as 23.94%, 34.27% and 3.76% respectively. Similarly, under overload condition the THD of PV CHBMLI current, load current and grid current in two-stage topology are found out to be 45.81%, 33.91% and 3.94% respectively, while with single-stage topology the corresponding current THD are found out to be 46.73%, 33.91% and 3.96%. It can be observed that the grid current THD with both the topologies is well within the limits of IEEE 1547 and IEC 61727recommended value of 5% with the PQEC.

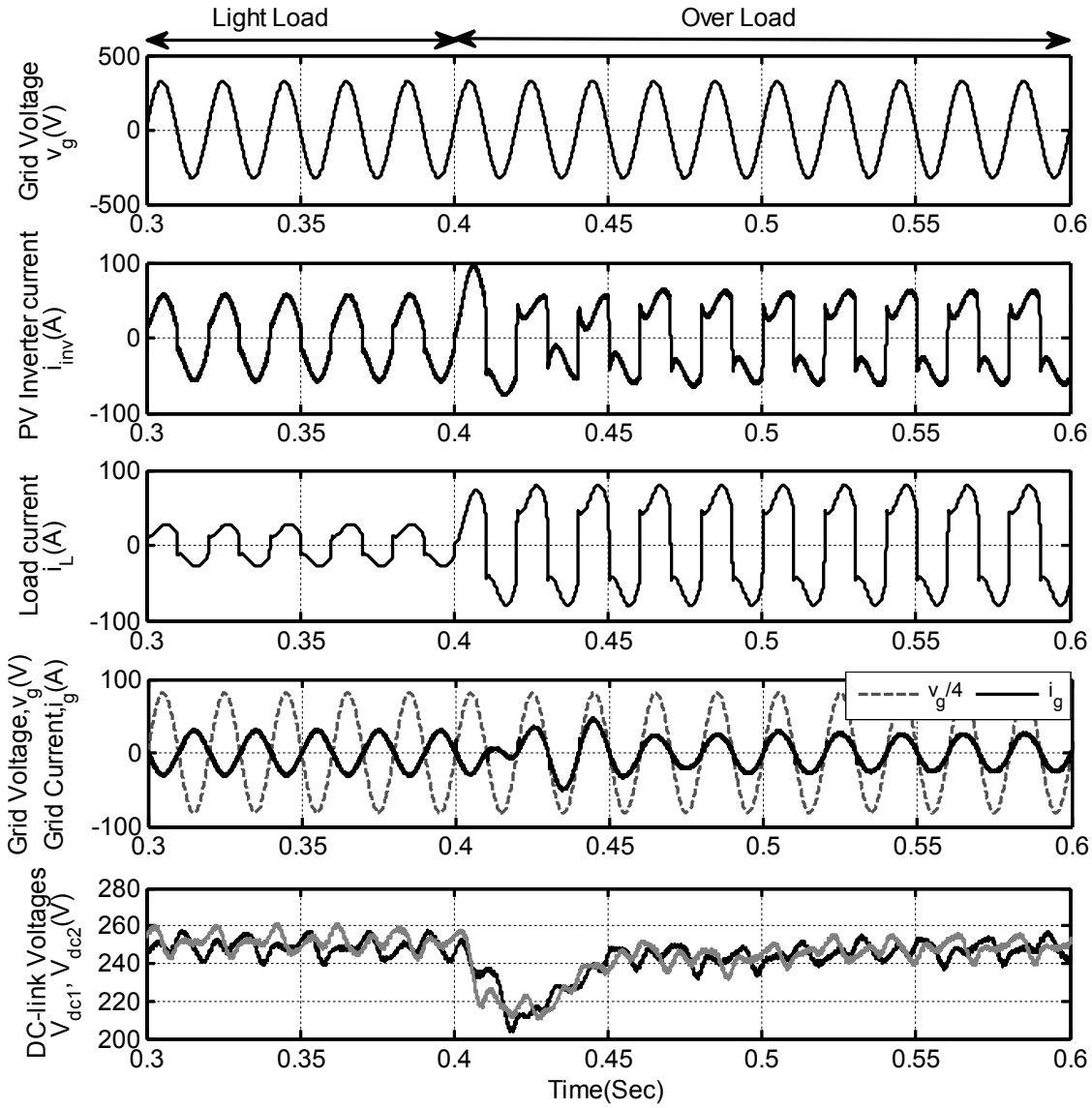

Fig.4.16 (a): Grid Voltage, PV CHBMLI current, load current, grid current and DC-link voltage of PVDG system under varying load condition

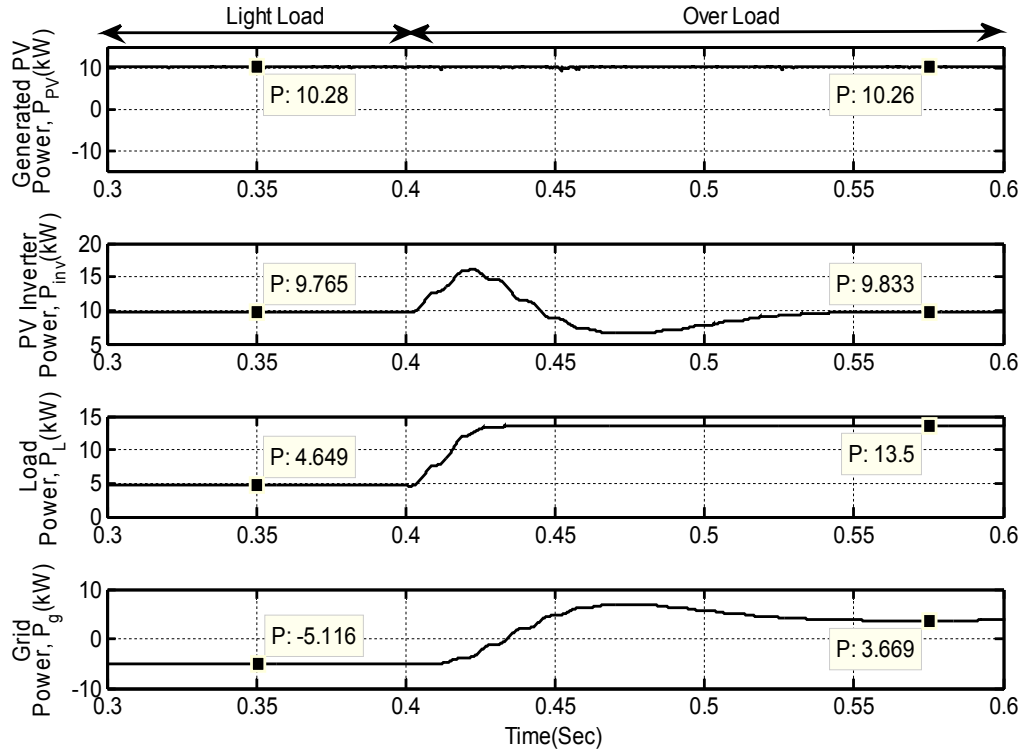

Fig. 4.16(b) Active Power of two-stage CHBMLI based PVDG System under varying load conditions

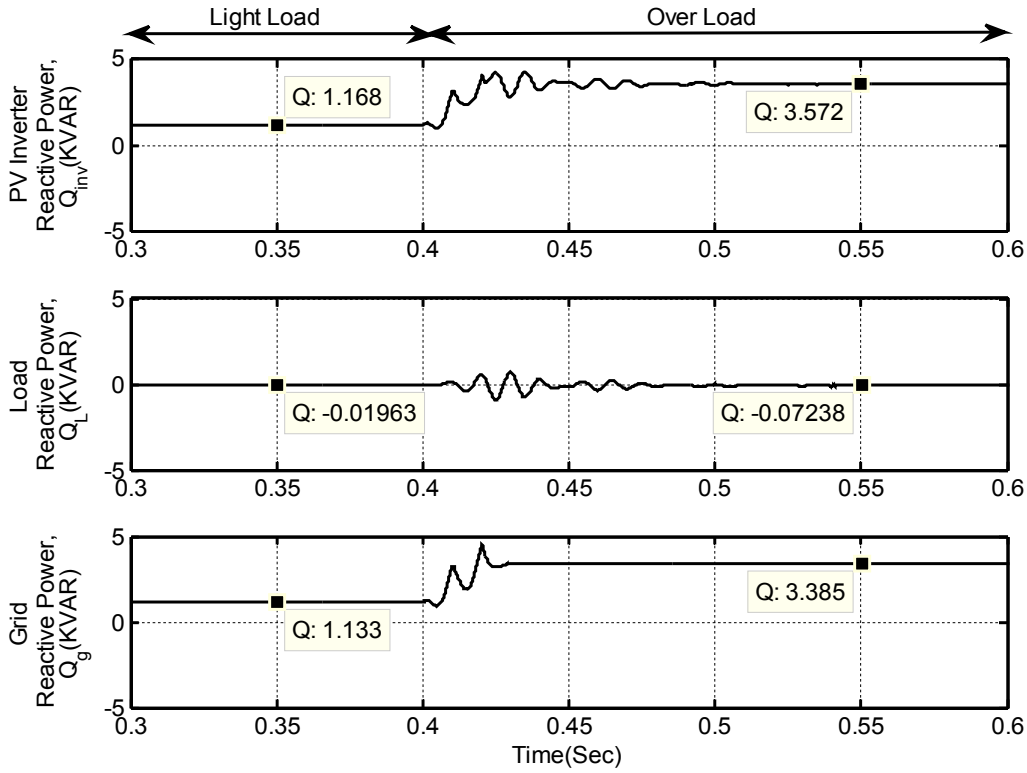

Fig. 4.16(c) Reactive Power curves of two-stage CHBMLI based PVDG System under varying load condition

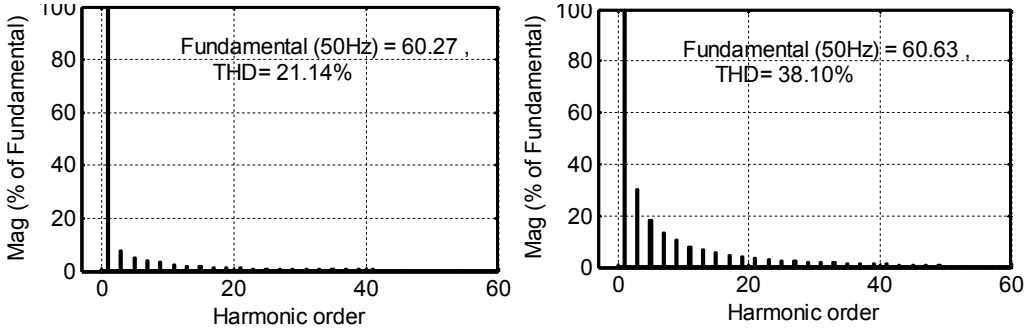

(i) (ii)

Fig.4.16 (d): THD of PV CHBMLI current under (i) light load (ii) overload condition for two-stage PVDG system

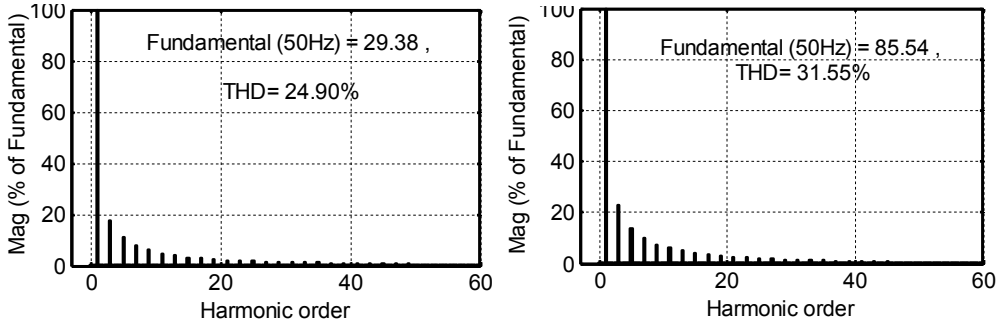

(i) (ii)

Fig.4.16 (e): THD of load current under (i) light load (ii) overload condition for two-stage PVDG system

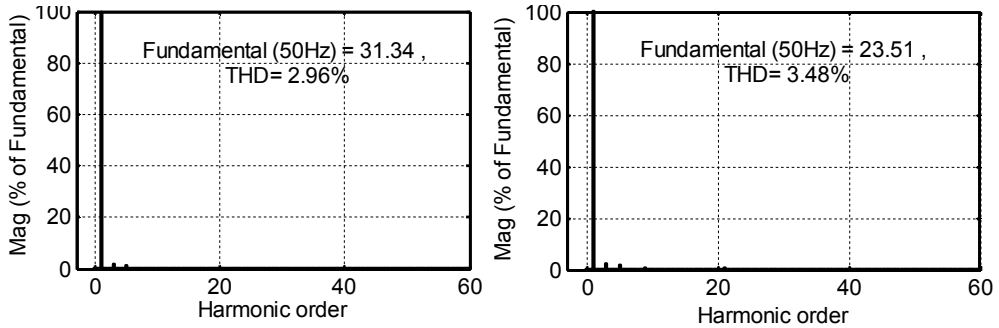

(i) (ii)

Fig.4.16 (f): THD of grid current under (i) light load (ii) under overload conditions for the two-stage PVDG system

Fig.4.16: Simulation results of two-stage CHBMLI based PVDG system under varying load condition

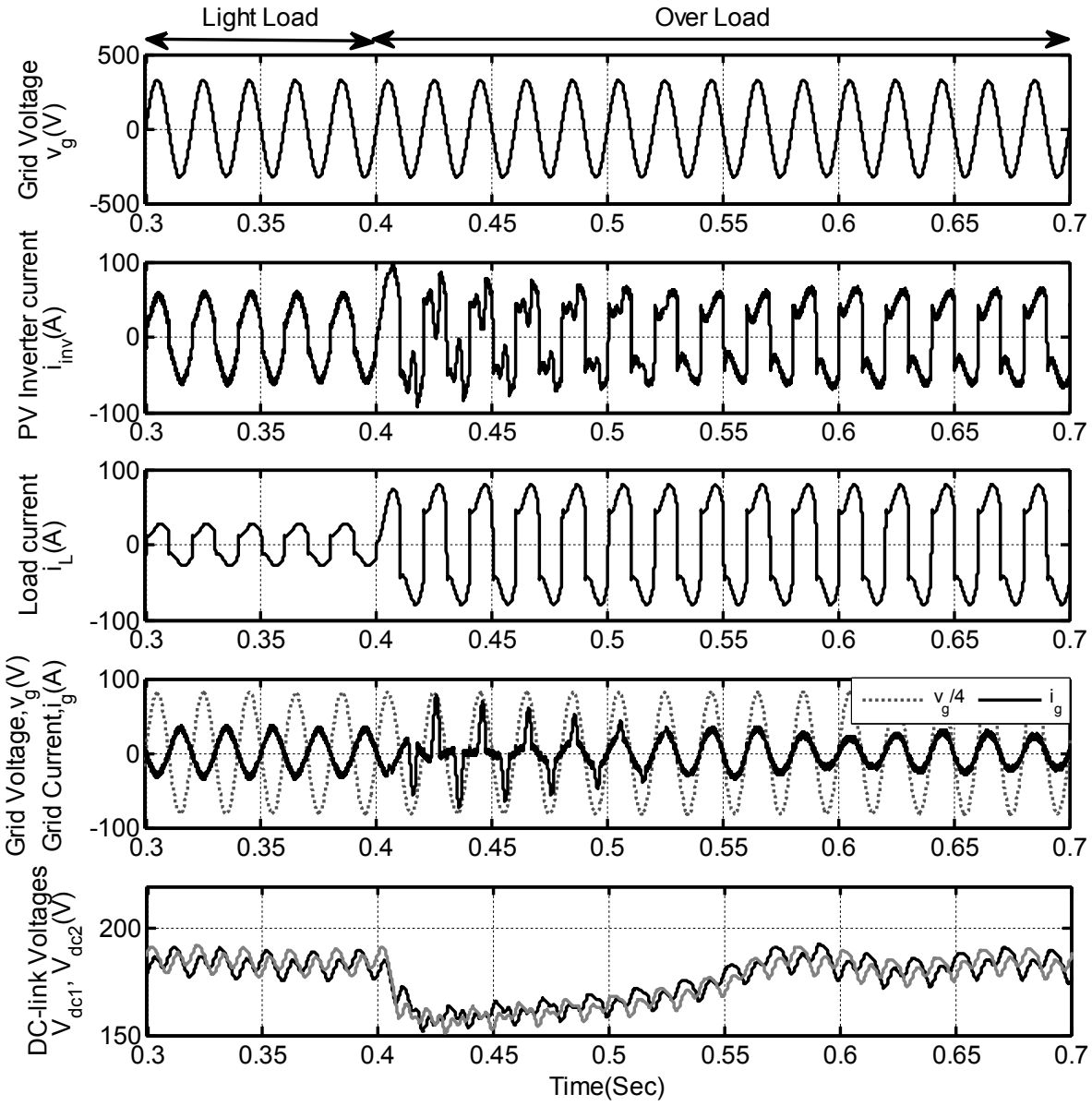

Fig.4.17 (a): Grid Voltage, PV inverter current, load current, grid current and DC-link voltage of single-stage CHBMLI based PVDG system under varying load conditions

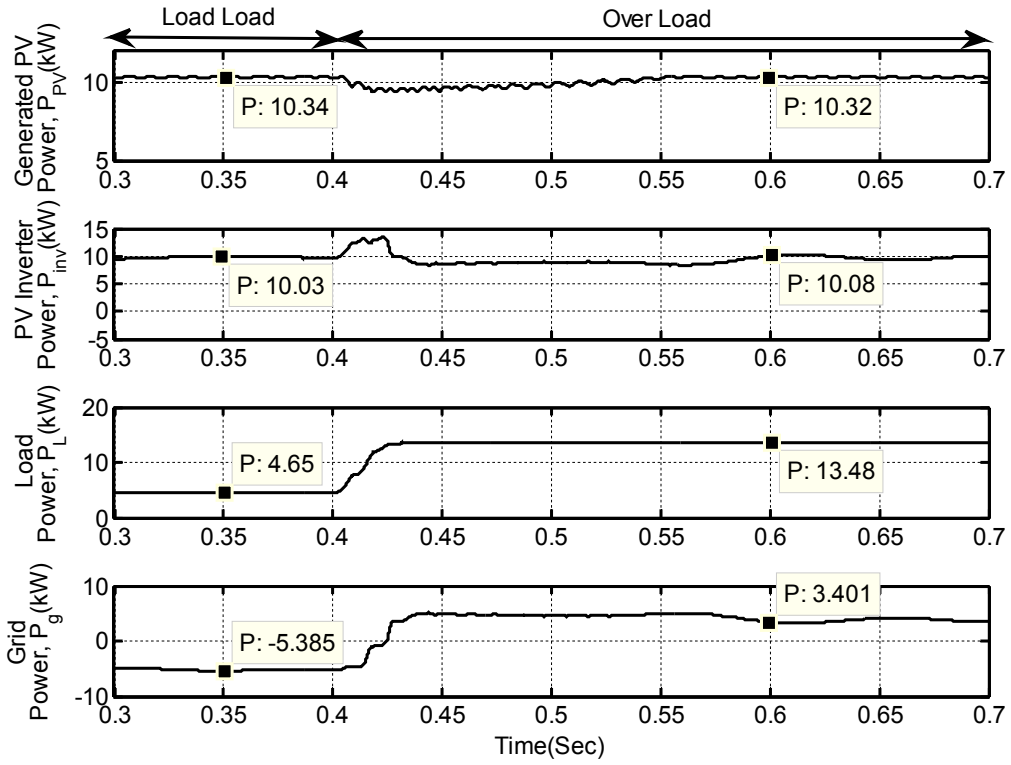

Fig. 4.17(b): Active Power Curves of single-stage CHBMLI based PVDG system under varying load condition

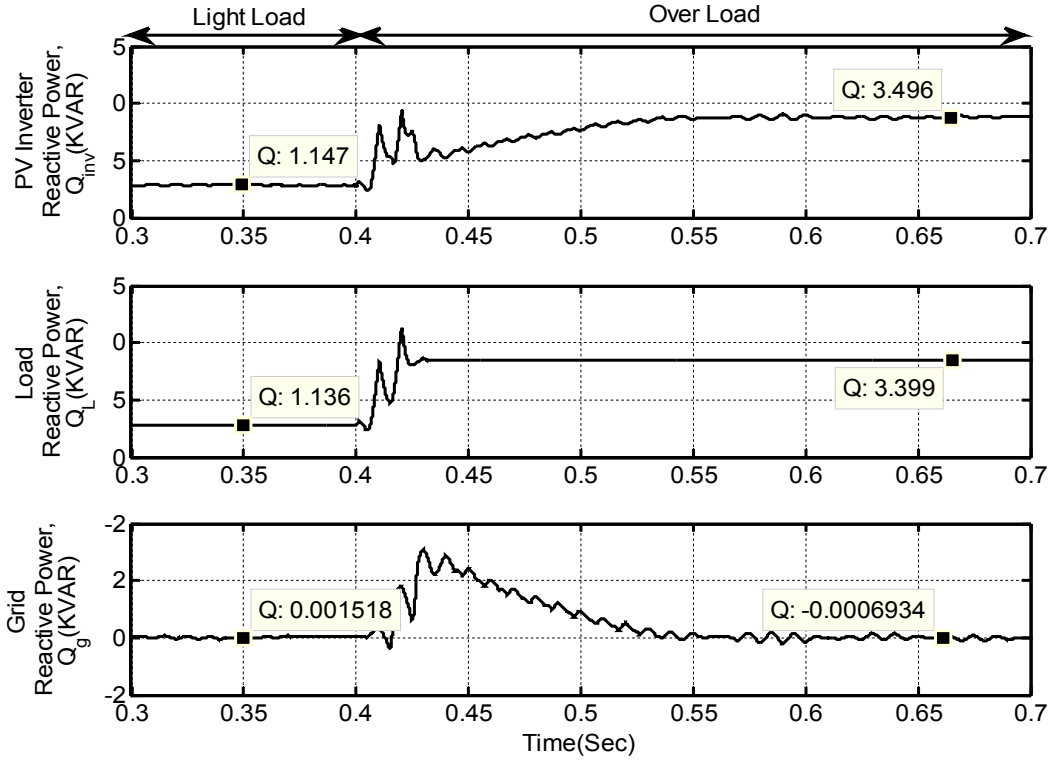

Fig.4.17(c): Reactive Power Curves of single-stage CHBMLI based PVDG system under varying load condition

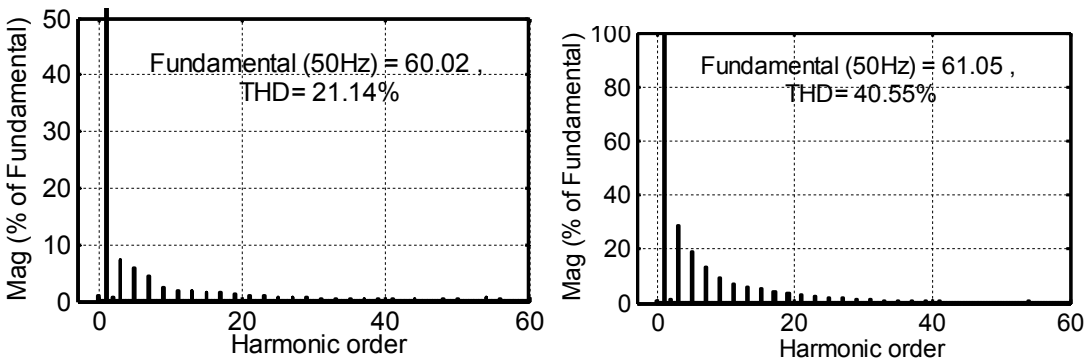

(i) (ii)

Fig.4.17 (d): THD of PV CHBMLI current under (i) light load (ii) overload condition for single-stage PVDG system

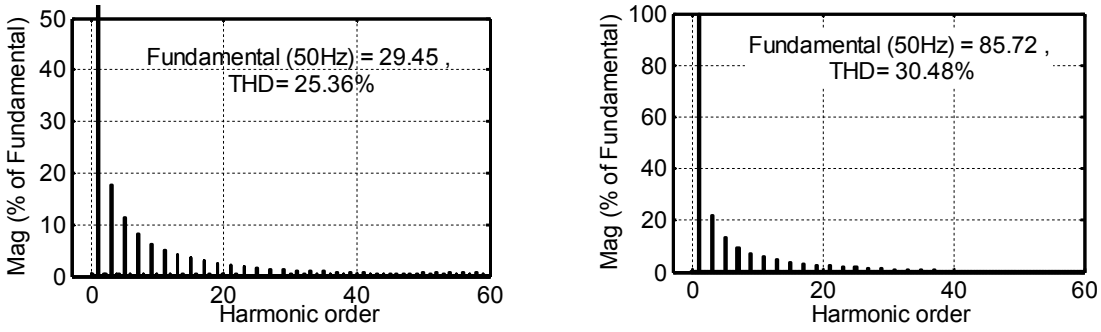

(i) (ii)

Fig.4.17 (e): THD of load current under (i) light load (ii) overload condition for single-stage PVDG system

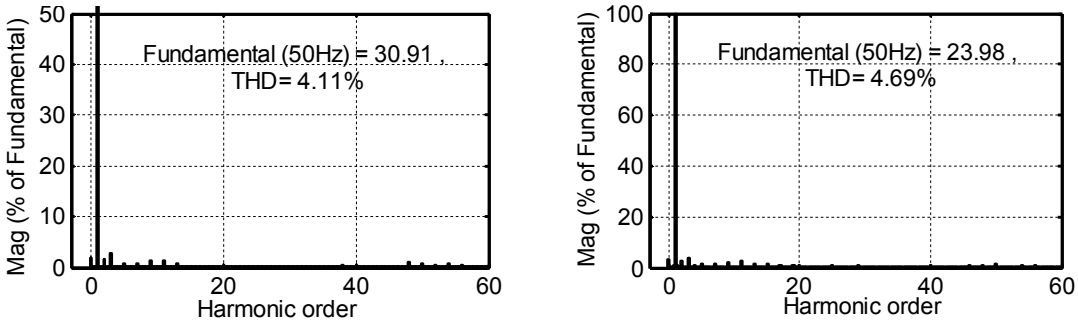

(i) (ii)

Fig.4.17 (f): THD of grid current under (i) light load (ii) Overload condition for single-stage PVDG system

Fig.4.17: Simulation results of single-stage CHBMLI based PVDG system under varying load conditions

4.5.3 CHBMLI based PVDG system under varying atmospheric conditions

This section presents the response of two-stage and single-stage CHBMLI based PVDG system under varying atmospheric conditions. The analysis of the system is made with both MPPT and PQEC are enabled throughout the test with a non-linear load (Load-1), is connected across the PCC. In order to study the steady-state and transient performance of the system under these conditions, the following events have been designed to occur in PVDG system:

At t = 0 Sec., the irradiation level of the PV module is set as 1000 W/m^2.

At t =0.4 Sec., irradiation level is reduced to 300 W/m^2

The simulation results of two-stage and single-stage CHBMLI based PVDG system under these above mentioned conditions are given in Fig.4.18 and Fig.4.19 respectively. The simulated waveforms of grid voltage, PV CHBMLI current, load current, grid current, and DC-link voltages for two-stage and single stage CHBMLI based PVDG system under this varying atmospheric conditions are shown in Fig.4.18 (a) and Fig.4.19 (a) respectively and from these simulation results, following observations are made:

1. Initially the system is operated at the irradiation level of 1000 W/m^2. During this condition, the load current demand is less than that generated by PV CHBMLI and hence, the surplus current is fed to the grid. This can be observed from Fig.4.18(a) and Fig.4.19 (a) where grid current in both the topologies are out of phase with PV CHBMLI as well as the load current. However, this non-linear load draws a distorted current from the PV CHBMLI. As the PQEC is enabled during this condition, the PV CHBMLI generates a non-sinusoidal current consisting of fundamental, harmonics and reactive components of a load current. Therefore, under this condition the non-sinusoidal component of the load current is completely supplied by the PV CHBMLI, thereby relieving the grid from the supply of harmonics.

2. However, when the irradiation level is decreased to 300 W/m^2 at t=0.4 Sec., to create an unfavourable atmospheric condition for the PVDG system, the generated PV CHBMLI current is not sufficient to meet the load current demand and hence, the rest of the load current demand is met by the grid. This is verified from Fig.4.18(a) and Fig.4.19(a) where grid current is in phase with both PV CHBMLI and the load current. Similar to favourable atmospheric condition(i.e. at STCs), the harmonic components of the load current is supplied by the PV CHBMLI thereby making the grid current purely sinusoidal. This demonstrates the capability of both two-stage and single-stage CHBMLI based PVDG system to fully compensate for harmonic.

3. With the implementation of PQE scheme, the grid current is found to be in phase with the grid voltage under both, favourable and unfavourable atmospheric conditions thereby confirming the compensation of reactive power.

4. At the instant when the irradiation is decreased from 1000 W/m^2 to 300 W/m^2 the DC capacitor voltages of each H-bridge cell of CHBMLI drops from its reference value to maintain the load current demand. This drop in each DC-link capacitor voltages are restored to the reference value in 2-3 cycles in two-stage CHBMLI based topology which can be observed from Fig.4.18 (a). However, in case of single-stage system as the solar irradiation changes, the PV module start to operates at new operating point, as per the reference DC-link voltage value generated by MPPT algorithm.

Fig.4.18 (b) and Fig.4.19 (b) shows the generated active power curves of two-stage and single-stage CHBMLI based PVDG system under varying atmospheric conditions respectively. From these simulation results the following observations are made,

1. With the enabled mode of MPPT controller, the generated PV power in both the topologies are found to reach the maximum power point at 1000 W/m^2. In both two-stage and single-stage topology with the variation of solar irradiation from 1000 W/m^2 to 300 W/m^2 the PV module connected at each H-bridge cell starts generating the maximum power corresponding to the irradiation value. This PV power generation under varying irradiation condition under two-stage and single-stage topology is given in the first sub-plot of Fig.4.18 (b) and Fig.4.19 (b) respectively.

2. The generated PV CHBMLI power, load power and grid power of two-stage and single-stage CHBMLI based topology under varying irradiation conditions are shown in the other three subplots of Fig.4.18(b) and Fig.4.19(b) respectively. At the irradiation level of 1000 W/m^2, the generated PV power is more than the power demand of the load. Thus, the surplus PV power is fed to the grid. The positive value of the active power supplied by the PV CHBMLI implies that power flows from PV CHBMLI towards PCC, whereas a negative value of grid active power implies that the grid absorbs power. Moreover, during low irradiation condition, i.e. at 300 W/m^2, the generated PV power is unable to meet the load demand and hence, both PV CHBMLI and the grid share the load. Here the positive value of grid power implies that the power flow is from

the grid towards PCC. It can be observed that the power generated by PV CHBMLI in two-stage and single-stage topology is 9742.5 Watt and 9846 W respectively at the irradiation level of 1000 W/m^2 whereas at the irradiation level of 300 W/m^2 the CHBMLI generates 4504 W and 4807 W with two-stage and single-stage topology respectively. This increase in power generation with single-stage topology leads to more power transfer to the grid in case of single-stage topology compared to two-stage topology under favourable atmospheric condition. Whereas during low irradiation condition the share of grid power in two-stage topology is more compared to single-stage topology.

3. Similarly, the reactive power plots of two-stage and single-stage CHBMLI based topology under varying load conditions are shown in Fig.4.18(c) and Fig.4.19(c) respectively. Under two irradiation levels, with both the topologies the grid reactive power is zero, thereby implying that the reactive power demanded by the load is met by the PV CHBMLI. This implies that, with an enabling mode of PQEC the PV CHBMLI in both topologies supplies all the reactive power. This leads to unity displacement factor at the PCC.

Finally, the harmonic spectrum of PV CHBMLI current, load current and grid current, under varying atmospheric conditions, in case of two-stage CHBMLI based topology are shown in Fig.4.18(d), Fig.4.18(e), and Fig.4.18(f) respectively. Similarly, the corresponding harmonic spectrum in single-stage topology is shown in Fig.4.19(d), Fig.4.19(e) and Fig.4.19(f). Under favourable atmospheric condition, the THD of PV CHBMLI current, load current, and grid current in two-stage topology are found to be 23.31%, 31.22%, and 3.65 %, respectively, whereas with single-stage topology the corresponding current THD are found as 23.94%,34.27% and 3.76% respectively. Similarly, under unfavourable atmospheric condition the THD of PV CHBMLI current, load current and grid current in two-stage topology are found out to be 46.54%, 31.22% and 3.51 % respectively, while with single-stage topology the corresponding current THD is found out to be 47.94%, 34.27% and 4.23%. It can be observed that the grid current THD with both the topologies is well within the limits of IEEE 1547 and IEC 61727 recommended value of 5% with the application of PQEC.

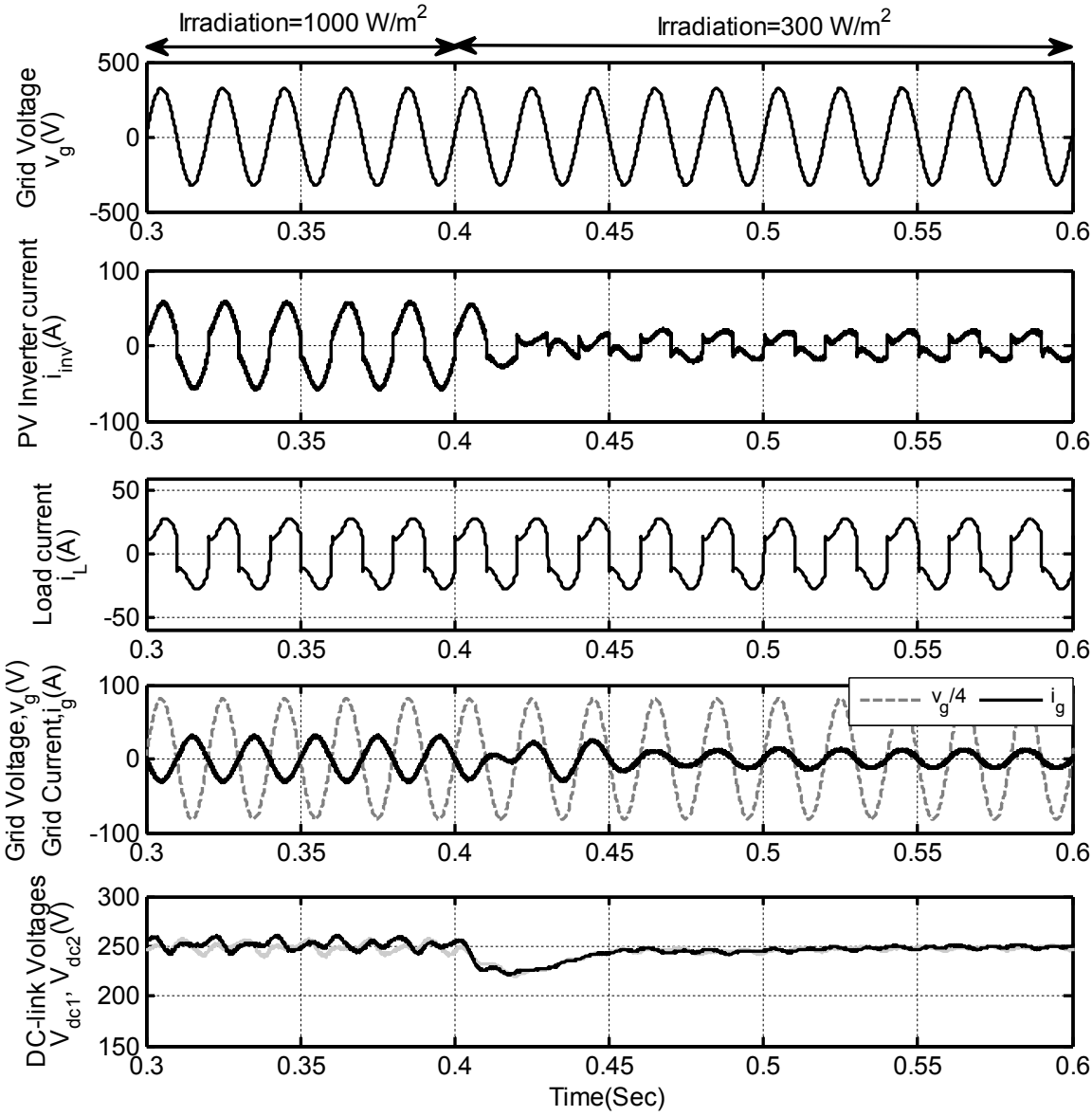

Fig.4.18 (a): Grid Voltage, PV inverter current, load current, grid current and DC-link voltage of two-stage CHBMLI based PVDG system under varying atmospheric condition.

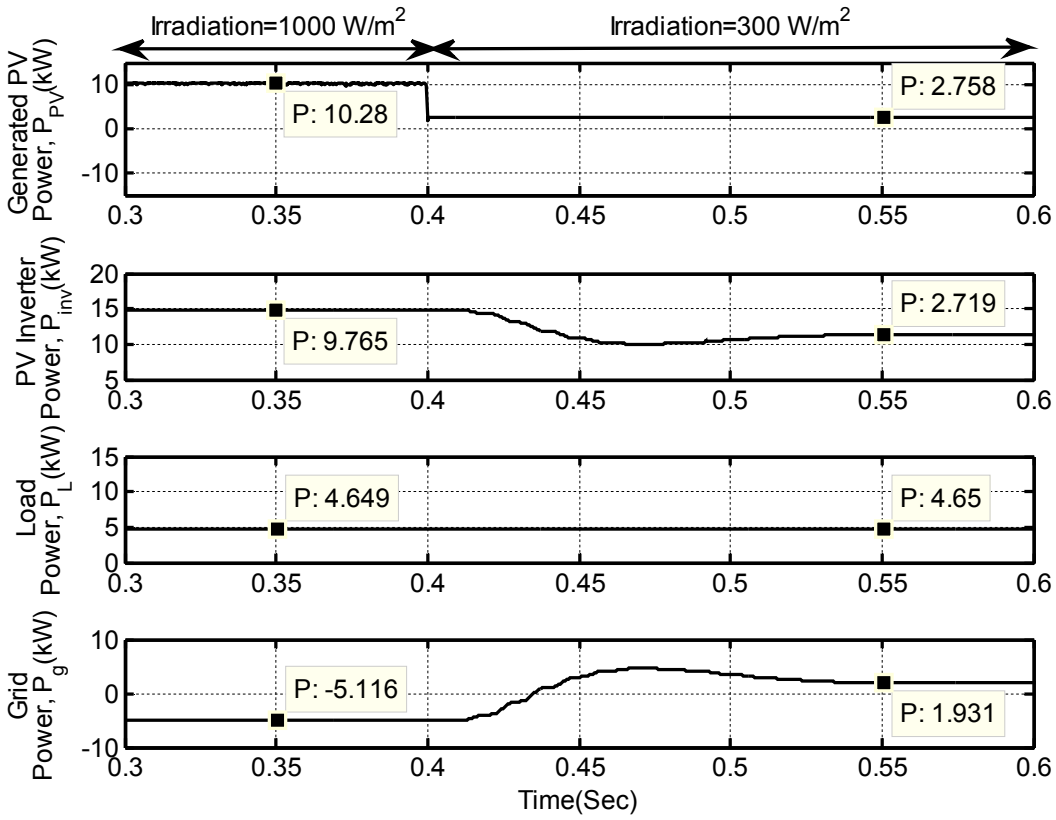

Fig.4.18(b): Active Power curves of two-stage CHBMLI based PVDG System under varying atmospheric condition

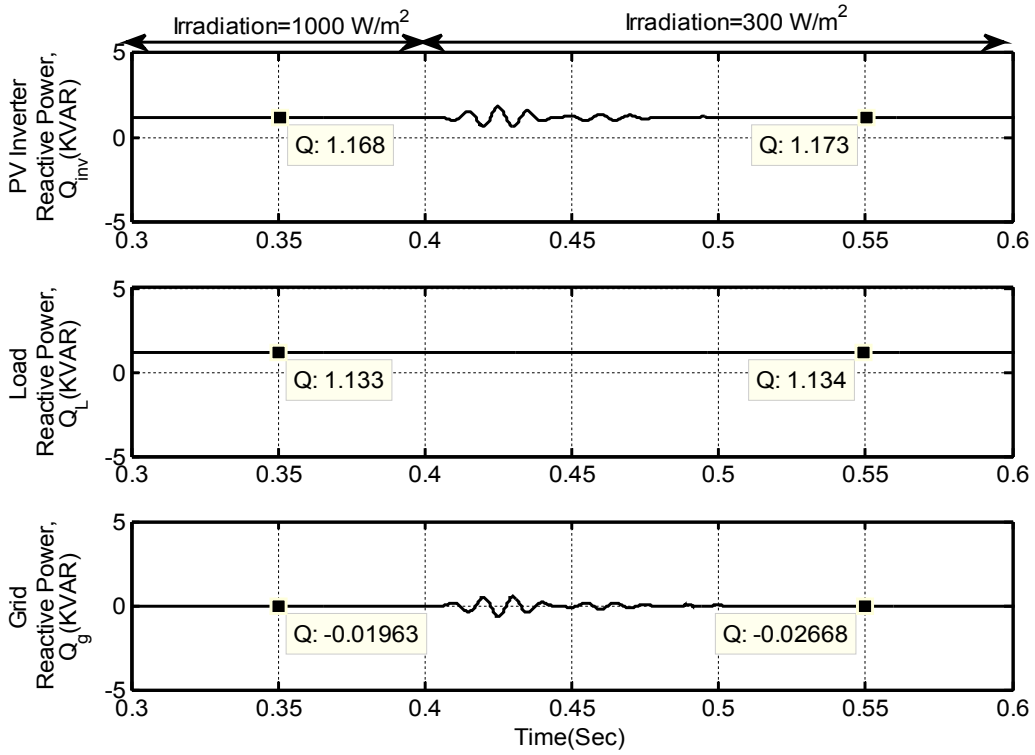

Fig.4.18(c): Reactive Power curves of two-stage CHBMLI based PVDG System under varying atmospheric condition

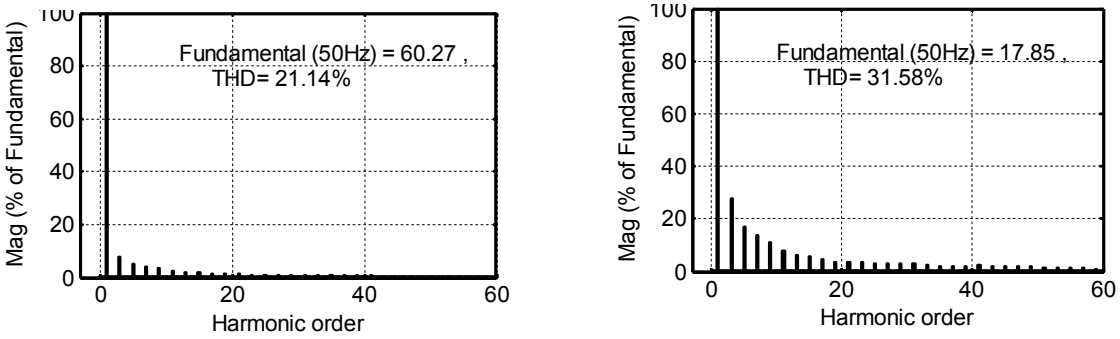

(i) (ii)

Fig.4.18 (d): THD of PV CHBMLI current (i) at irradiation level of 1000 W/m^2 (ii) at irradiation level of 300 W/m2 for two-stage PVDG system

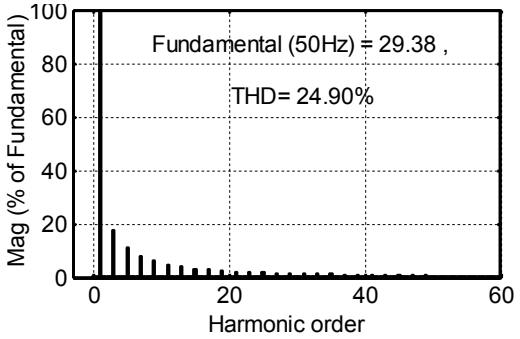

Fig.4.18 (e): THD of load current

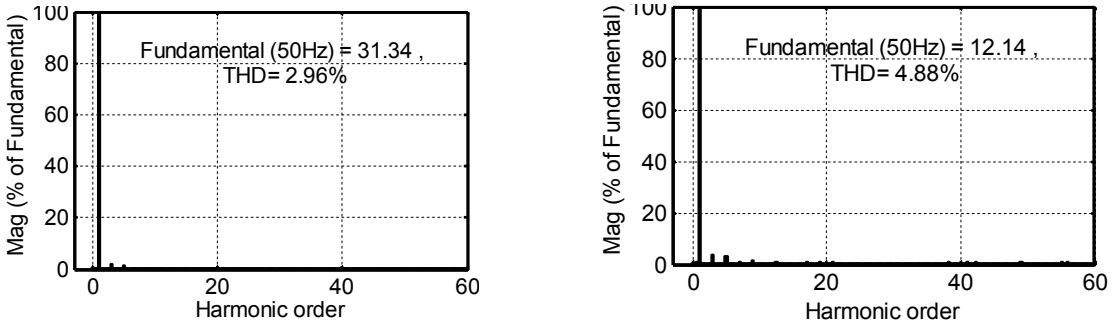

(i) (ii)

Fig.4.18(f): THD of grid current at irradiation level of (i) 1000 W/m^2 (ii) 300 W/m^2 for two-stage PVDG system

Fig.4.18: Simulation results of two-stage CHBMLI based PVDG system under varying atmospheric condition

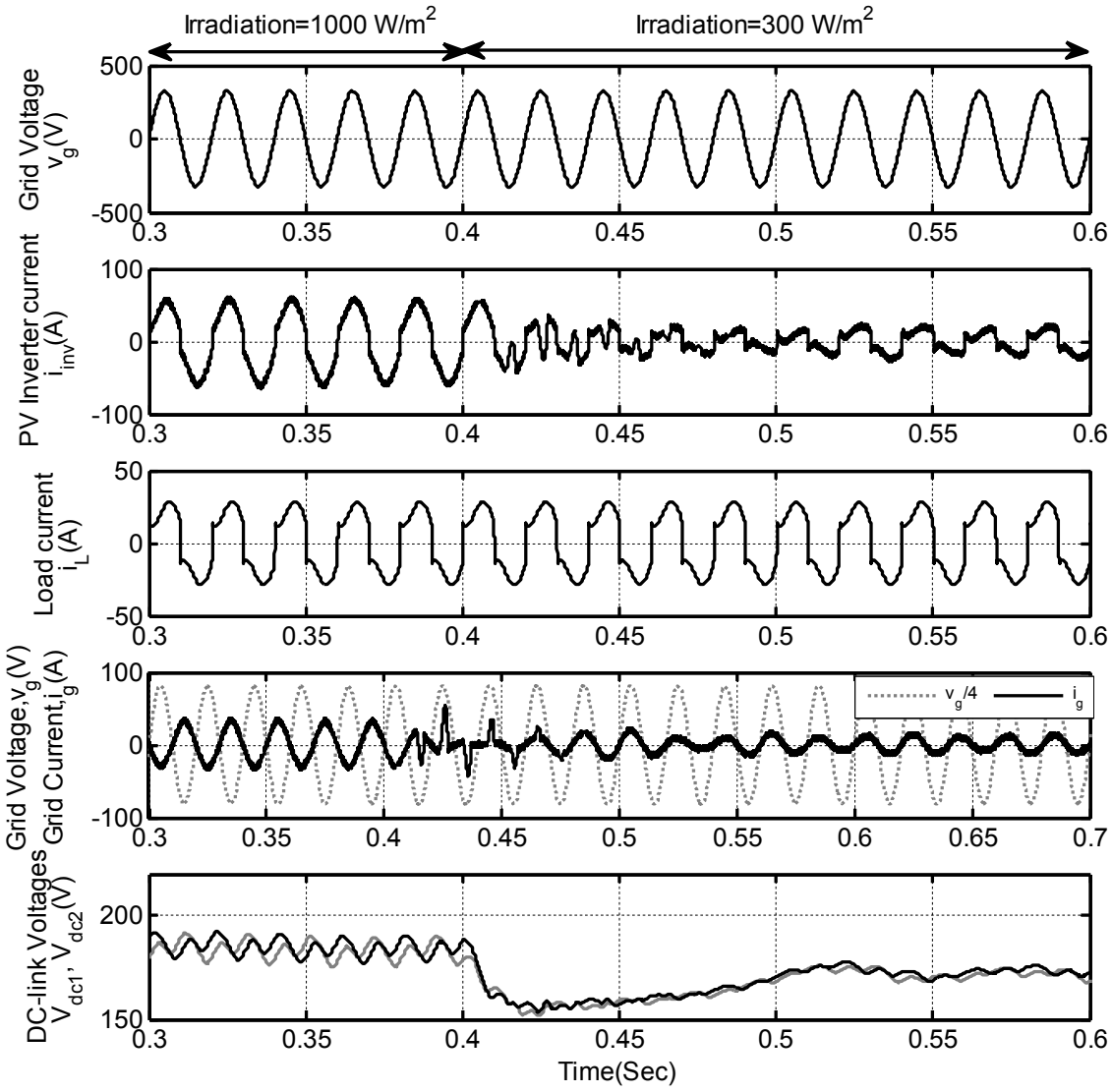

Fig.4.19 (a): Grid Voltage, PV inverter current, load current, grid current and DC-link voltage of single-stage CHBMLI based PVDG system under varying atmospheric conditions.

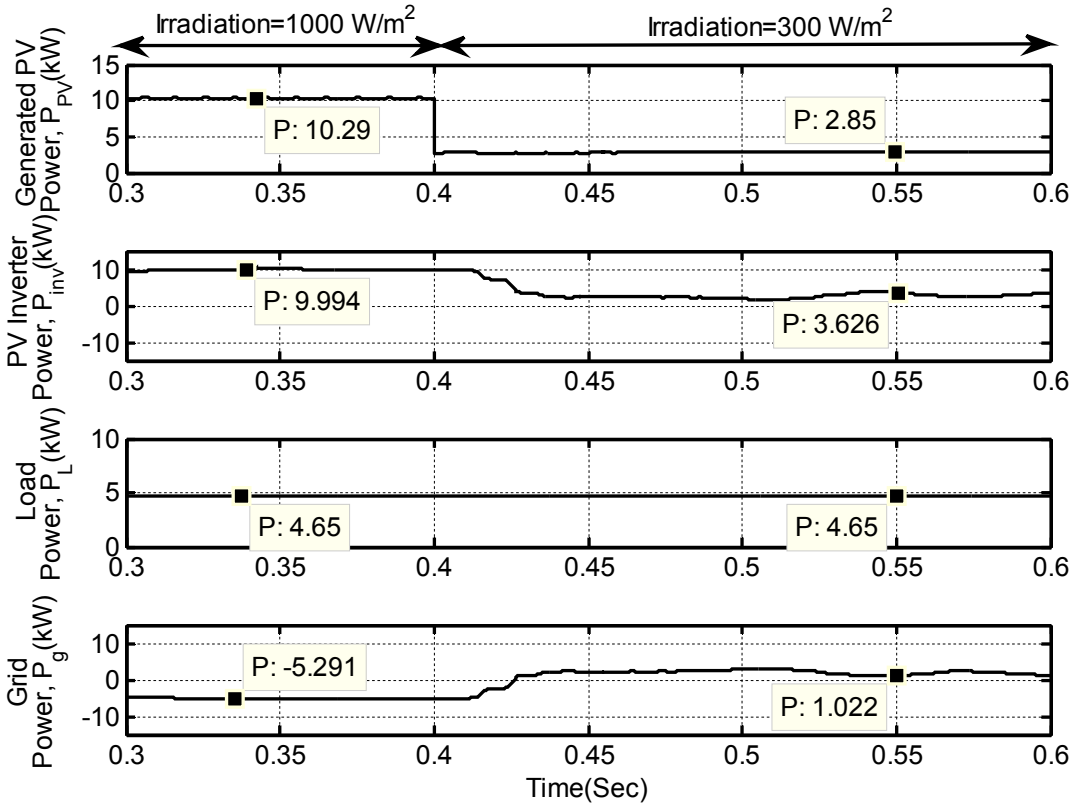

Fig. 4.19(b): Active Power Curves of single-stage CHBMLI based PVDG system under varying atmospheric condition

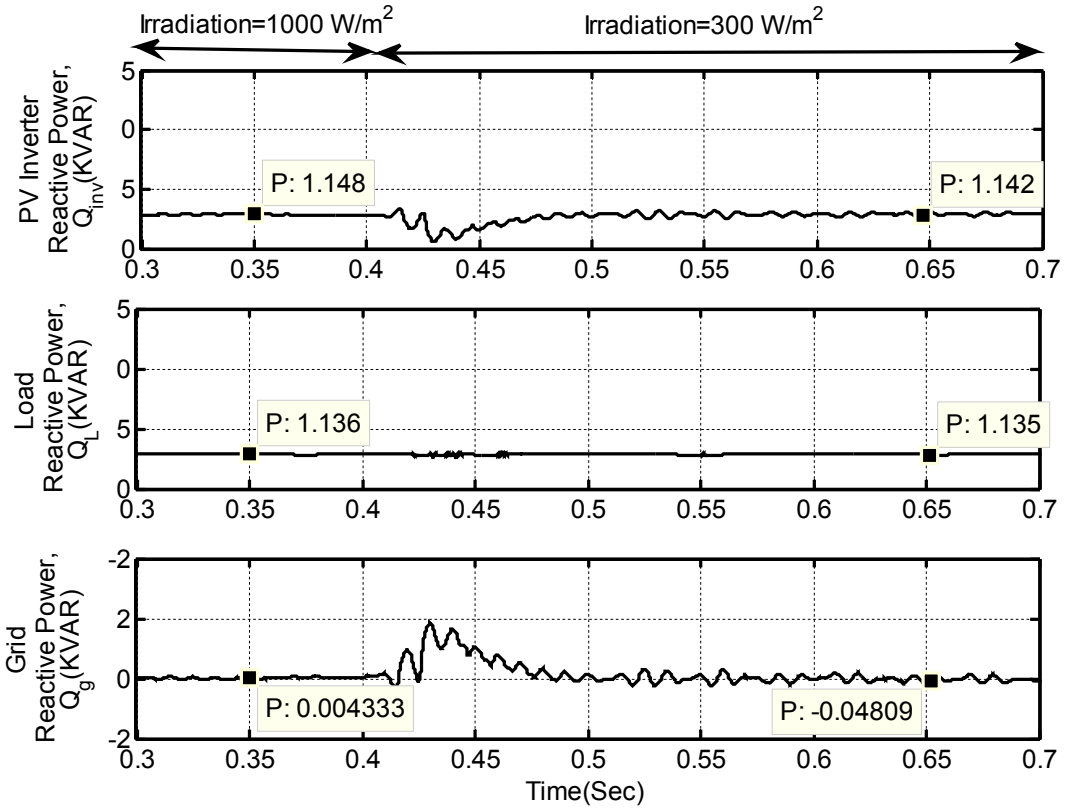

Fig. 4.19(c): Reactive Power Curves of single-stage CHBMLI based PVDG system under varying atmospheric condition

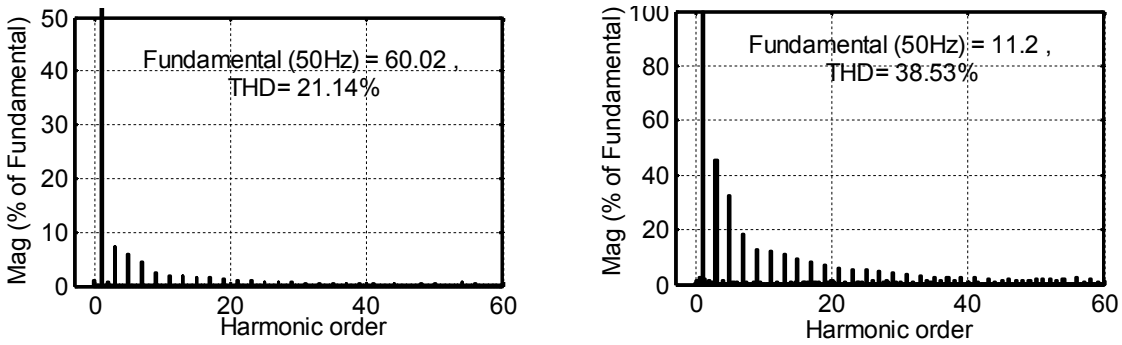

(i) (ii)

Fig.4.19 (d): THD of PV CHBMLI current (i) at irradiation level of 1000 W/m^2 (ii) at irradiation level of 300 W/m^2 for single-stage PVDG system

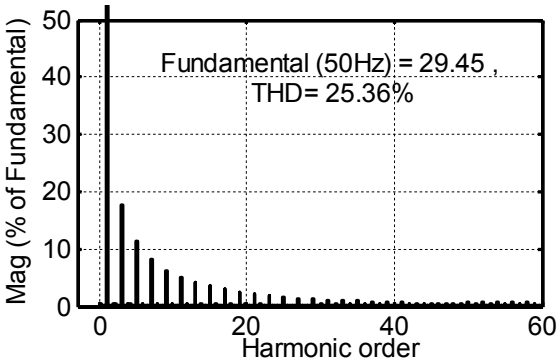

Fig.4.19 (e): THD of load current

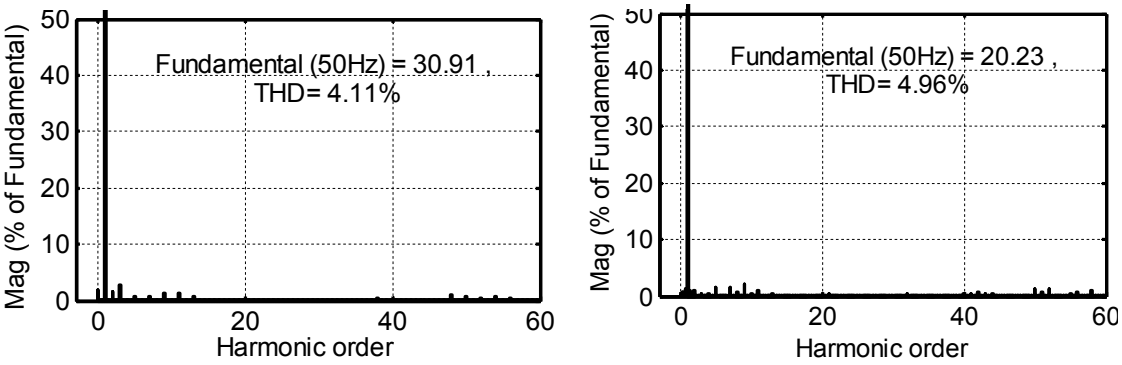

(i) (ii)

Fig.4.19 (f): THD of grid current (i) at irradiation level of 1000 W/m^2 (ii) at irradiation level of 300 W/m^2 for single-stage PVDG system

Fig.4.19: Simulation results of single-stage CHBMLI based PVDG system under varying atmospheric conditions

4.6 Comparative Analysis

Table 4.5 presents a comparative values of active power flow in the PVDG system for the three different topologies of the PVDG system under different atmospheric conditions.The analysis is made with a non-linear load (load-1)(P_L:4650 W) connected across the PCC with PQEC and the MPPT controller is in enabled mode. Positive sign of active power implies that the source is giving power, whereas negative sign implies that the source is receiving power.

Table 4.5:Generated PV inverter Power and Grid Power under different Irradiation level for three different topologies of PVDG System

MPPT and PQEC are Enabled	2-Stage 2-level PV Inverter **(Reference)**		2-Stage PV CHBMLI		1-Stage PV CHBMLI	
Irradiation in W/m^2	**P_{Inv}(w)**	**P_g(w)**	**P_{inv}(w)**	**P_g(w)**	**P_{inv}(w)**	**P_g(w)**
400	3649	1001	3745	905	3939	711
600	5732	-1082	5829	-1179	5949	-1299
800	7694	-3044	7750	-3100	7915	-3265
1000	9450	-4800	9786	-5136	9851	-5201

From Table 4.5, it can be observed that with 2-stage CHBMLI based PVDG system the percentage increase of power generation is 2.14 % (Avg. Value) compared to 2-stage 2-level PVDG system. Whereas, there is 4.70 % (Avg. Value) increase of power generation is possible in case of 1-stage CHBMLI based PVDG system as compared to 2-stage 2-level PVDG system. As per the manufacturer's datasheet given in chapter.2 (Fig.2.4), the efficiency of the PV module is only 14%[103]. Therefore, with 4.70% (Avg. Value) increase of power generation in 1-stage CHBMLI based PVDG system, the overall efficiency of the system can be improved

Similarly, Table 4.6 presents a comparative analysis of % THD of PV inverter current, load current and grid current in the PVDG system for the three different topologies of the PVDG system under different test conditions. It can be observed that with CHBMLI based topology the THD of grid current is quite less compared to 2-level topology. However, in single stage topology the grid current THD is found to be slightly on the higher side compared to 2-stage topology. This is because of the continuous fluctuation of the input DC-link voltage in single stage topology. Table.4.7 presents a comparative analysis of active powers for the three different topologies of PVDG system under different test conditions. It can be observed that with single stage CHBMLI based topology the generated active power is quite high compared to other two topologies.

Table 4.6: Inverter current, load current and grid current THD under different modes of operation for three different topologies of PVDG System

Topology		THD in %								
		2-Stage 2-level PV Inverter			2-Stage 5-level PV CHBMLI			1-Stage 5-level PV CHBMLI		
Mode of Operation		i_{inv}	i_L	$\boldsymbol{i_g}$	i_{inv}	i_L	$\boldsymbol{i_g}$	i_{inv}	i_L	$\boldsymbol{i_g}$
Irradiation (MPPT&PQEC Enabled)	1000 W/m^2	22.65	26.63	3.15	21.14	24.90	2.96	21.14	25.36	4.11
	300 W/m^2	31.58	26.63	4.88	31.558	24.90	4.88	38.53	25.36	4.96
PQEC (At STCs MPPT Enabled)	Off	1.73	26.63	27.92	1.72	24.90	24.25	2.74	25.36	29.90
	On	22.65	26.63	3.15	21.14	24.90	2.96	21.14	25.36	4.11
Varying Non-linear Load (At STCs, MPPT &PQEC Enabled)	Light	22.65	26.63	3.15	21.14	24.90	2.96	21.14	25.36	4.11
	Over	38.10	31.82	4.36	38.10	31.55	3.48	40.55	30.48	4.69

Table 4.7: Inverter Power, load Power and grid Power under different modes of operation for three different topologies of PVDG System

Topology		Active Power in kW								
		2-Stage 2-level PV Inverter			2-Stage 5-level PV CHBMLI			1-Stage 5-level PV CHBMLI		
Mode of Operation		P_{inv}	P_L	$\boldsymbol{P_g}$	P_{inv}	P_L	P_g	P_{inv}	P_L	P_g
Irradiation (MPPT&PQEC Enabled)	1000 W/m^2	9.488	4.65	-4.838	9.765	4.649	-5.116	9.994	4.65	-5.291
	300 W/m^2	2.676	4.65	1.974	2.719	4.65	1.931	3.626	4.65	1.022
PQEC (At STCs MPPT Enabled)	Off	9.479	4.649	-4.829	9.753	4.649	-5.114	9.833	4.649	-5.184
	On	9.424	4.65	-4.774	9.765	4.65	-5.181	9.896	4.65	-5.397
Varying Non-linear Load (At STCs, MPPT &PQEC Enabled)	Light	9.488	4.65	-4.838	9.765	4.649	5.116	10.03	4.65	-5.385
	Over	9.27	13.48	4.206	9.833	13.5	3.669	10.08	13.48	3.401

4.7 Conclusion

1-ϕ two-stage and single-stage CHBMLI based PVDG system with an improved power quality features is developed and simulation results are presented. The CHBMLI based topology advantage of improved quality of currents. The current control scheme of PV CHBMLI includes a compensating current generator based on instantaneous reactive power theory to obtain the aforementioned objective. Both two-stage and single-stage PVDG system is controlled in such a way to inject the maximum PV power to the grid while compensating the load reactive power and harmonic components. Exhaustive simulation results are presented to investigate the performance of the PVDG system during varying atmospheric as well as varying load conditions. With single-stage topology, the need of DC-DC converter for MPPT is eliminated. This leads to more power injection to the grid as compared to two-stage system. The performance of both two-stage and single-stage PVDG system along with harmonic and reactive power compensation has been found satisfactory and meeting IEEE standards of the PVDG system.

[Prototype hardware system comprising of PV Inverter, dSPACE–DS1104 interfacing and related control circuits has been developed for two-stage two-level, two-stage and single-stage CHBMLI based PVDG system. The simulation results presented in previous chapters are validated through those hardware system]

5.1 Introduction

To verify the simulations of 1-ϕ, 230 V, 15 KVA, two-level and 5-level CHBMLI based PVDG system, the following prototypes have been developed in the laboratory.

1. Enhanced PQ based two-stage 2-level inverter based PVDG System.
2. Enhanced PQ based two-stage 5-level CHBMLI based PVDG System.
3. Enhanced PQ based single-stage CHBMLI based PVDG System.

As a first step in hardware development, two 128 W PV modules manufactured by Maharishi Solar, India[103] are installed at the rooftop of the laboratory. As discussed in the earlier chapter, for two-stage topology, two independent boost converters are used for the MPPT of each PV module, whereas in case of single stage system the PV inverter itself is responsible for both MPPT and power flow control.

A 1-ϕ downscaled two level PV inverter and 5-level PV CHBMLI rated at 100 V, 500 VA has been designed and constructed to realize the above mentioned PVDG topologies. The power circuit of two-stage 2-level inverter based PVDG system consists of a 2-level PV inverter which requires 4 power semiconductor devices. The PV module is interfaced with this PV inverter through a boost type DC-DC converter, which is responsible for MPPT control. However, for the development of the CHBMLI based PVDG system, two H-bridge cells are connected in a cascaded manner. These CHBMLI based topology requires 8 switching devices having reduced voltage and current ratings. These 8 switching devices are used to realize 2-H-bridge cells and each cell is equipped with a galvanically isolated PV module in case of a single stage system, whereas in two-stage system each H-bridge cell is connected to an individual PV module through boost type DC-DC converter. These two H-bridge cells are used for the synthesis of 1-ϕ inverter. As a result, it produces 5-level output voltage waveform under balanced input DC-link voltage condition. For the development of the power circuit, MOSFETs (IRFP460) has been used as the switching devices for realizing the PV inverter and boost converter.

The other hardware components required for the operation of the experimental set-up such as pulse amplification circuit, isolation circuit, dead-band circuit, voltage and current sensor circuits, non-linear/reactive loads have been designed and developed in the laboratory. The complete schematic diagram for the realization of two-stage 2-level inverter,

two-stage and single-stage CHBMLI based PVDG system are shown in Fig.5.1, Fig.5.2 and Fig.5.3 respectively.

A Digital Signal Processor (DSP) DS1104 of dSPACE has been used for the real-time implementation of control algorithms. By using the Real-Time Workshop (RTW) of MATLAB and Real-Time Interface (RTI) feature of dSPACE–DS1104, the simulink models of the various controllers of the prototypes have been implemented. The control algorithm is first designed in the MATLAB/Simulink software. The RTW of MATLAB generates the optimized C-code for real-time implementation. The interface between MATLAB/Simulink and Digital Signal Processor (DSP, DS1104 of dSPACE) allows the control algorithm to be run on the hardware. The master bit I/O is used to generate the required gate pulses and Analog to Digital Converters (ADCs) are used to interface the sensed PV modules, voltage and current, PV inverter current, load current, grid voltage and DC-bus capacitor voltages. The development of different hardware components as required for the operation of the hardware prototypes are discussed in the next section.

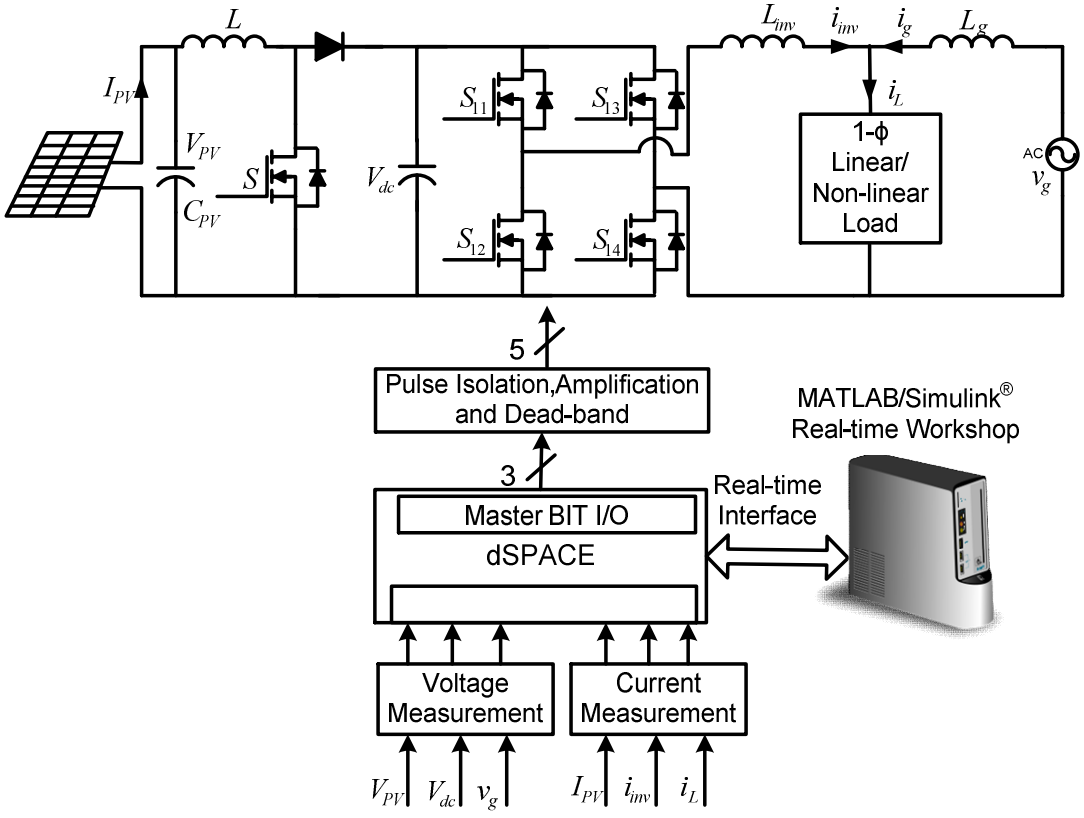

Fig.5.1: Schematic diagram for hardware implementation of two-stage 2-level PVDG system.

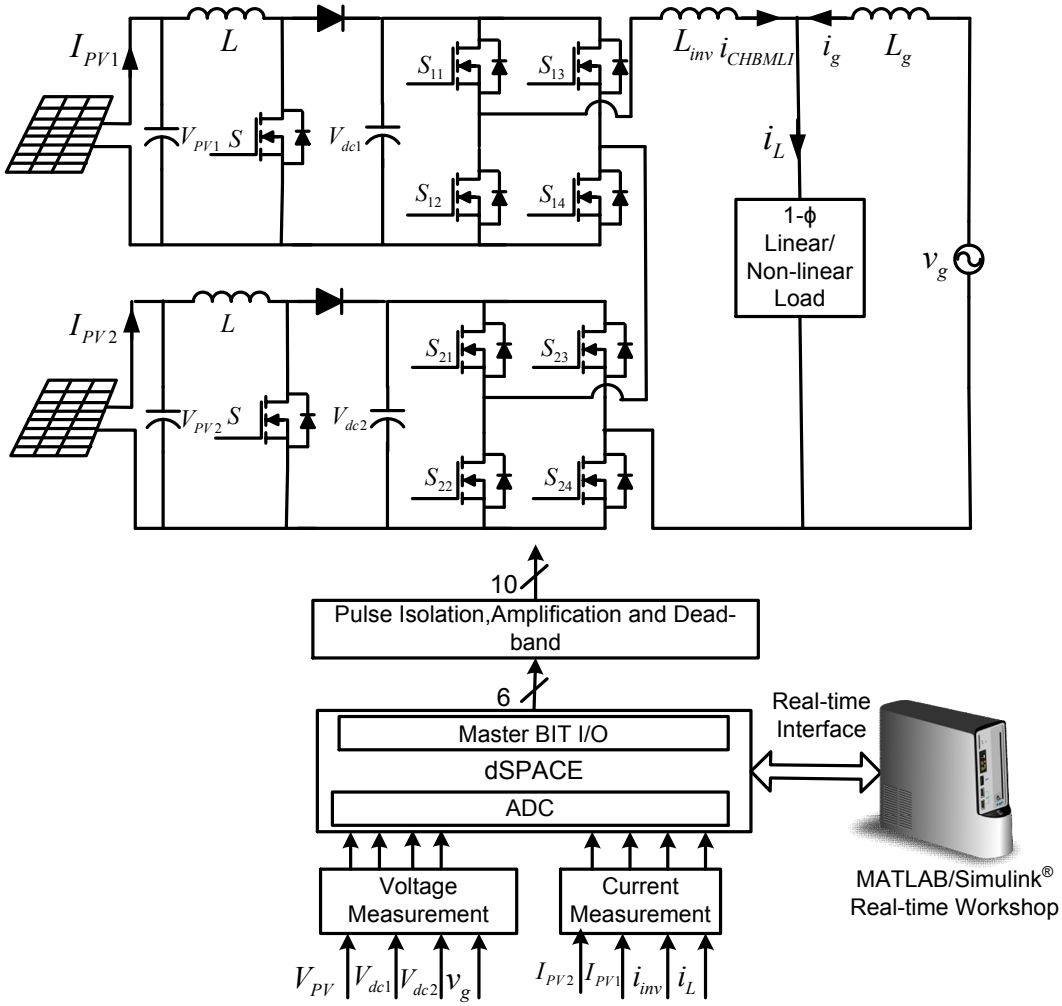

Fig.5.2: Schematic diagram for hardware implementation of two-stage CHBMLI based PVDG system.

5.2 Development of System Hardware

The developed experimental prototype is comprised of the following parts:

1. Power circuit of DC-DC converter for MPPT in two-stage topology and 2- level , 5- level PV inverter for grid interfacing
2. Measurement circuits
   - PV module output voltage and current
   - PV Inverter current, load current
   - Grid Voltage and DC-link voltages of the H-bridge cell
3. System software
4. Control hardware
   - MOSFET driver circuit for Isolation and Amplification
   - Dead-band circuit

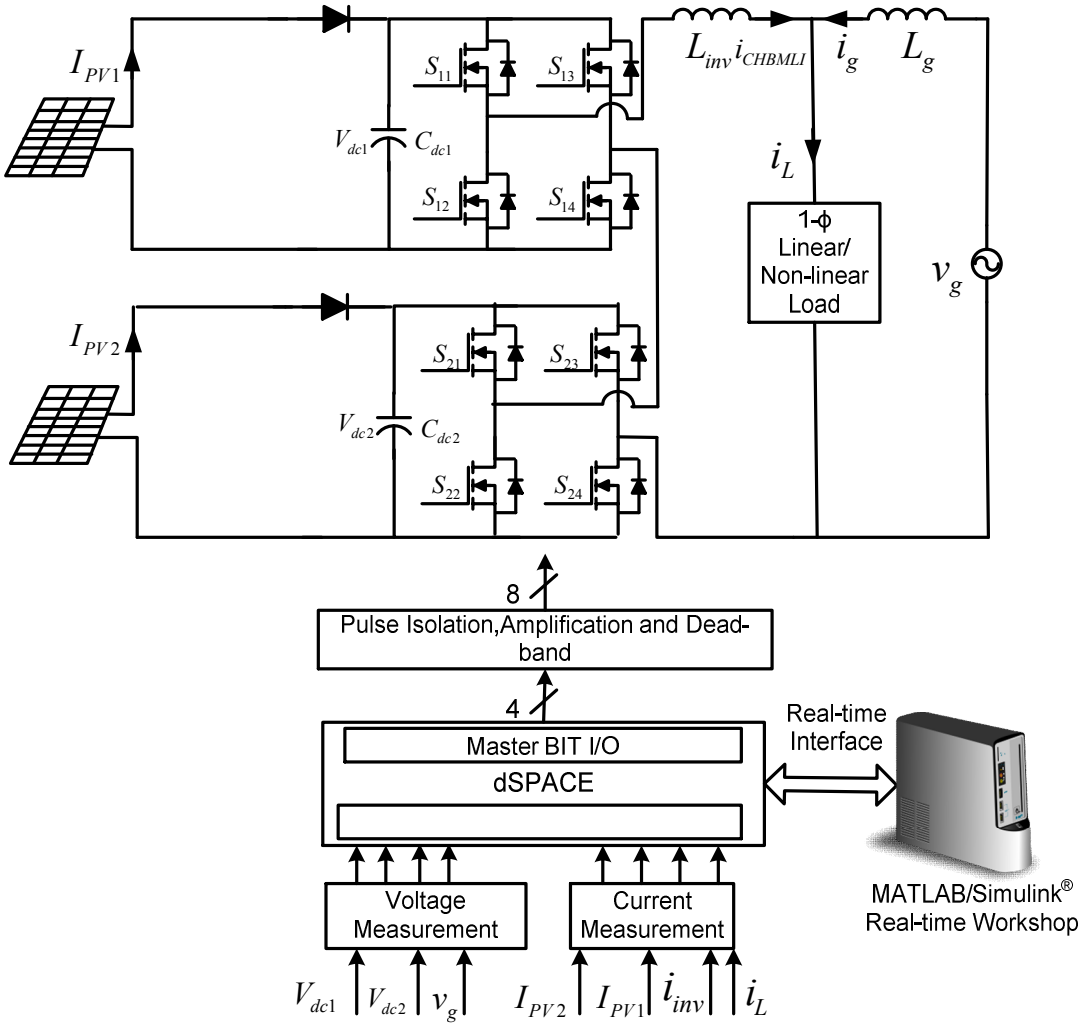

Fig.5.3: Schematic diagram for hardware implementation of single-stage CHBMLI based PVDG system.

5.2.1 Development of Power Circuit

A single-phase 2- level and 5- level PV inverter with suitably designed filter inductor (L_{inv}) on its AC side have been developed in the laboratory. As mentioned earlier, in the two-stage PVDG system, for the MPPT, boost converter is used and is developed by properly designing its required passive elements. The self-commutated power semiconductor switches required for the development of a boost converter and PV inverter are realized by the MOSFETs (IRFP460). To protect each switching device, a suitably designed snubber circuit is connected across it. The snubber comprises of a parallel combination of a resistor and a capacitor connected across a Metal-Oxide Varistor (MOV). The devices are mounted on heat sinks to ensure proper heat dissipation. Various parameters and rating of passive components are designed as per the design criterion discussed in Chapter.3 and Chapter 4.

5.2.2 Measurement Circuits

For the accurate and reliable operation of a system in closed loop, measurement of various system parameters and their conditioning is required. The measurement system must fulfil the following requirements:

- High accuracy
- Galvanic isolation with power circuit
- Linearity and fast response
- Ease of installation and operation

With the availability of Hall-effect current sensors and isolation amplifiers, these requirements are fulfilled to a large extent. In order to implement the control algorithm of 1-ϕ PVDG system in closed loop, following signals have been sensed.

1. PV module output voltage and current
2. Load current, PV inverter currents and grid voltage for reference current generation and synchronization
3. DC voltages of the H-bridge cells (required for the operation of DC voltage regulator).

5.2.2.1 Sensing of AC Current

The PV module output current and AC source currents have been sensed using the PCB-mounted Hall-effect current sensors (TELCON HTP50). The HTP50 is a closed loop Hall effect current transformer suitable for measuring currents up to 50 A. This device provides an output current into an external load resistance. These current sensors provide the galvanic isolation between the high voltage power circuit and the low voltage control circuit and require a nominal supply voltage of the range ±12V to ±15V. It has a transformation ratio of 1000:1 and thus, its output is scaled properly to obtain the desired value of measurement. The circuit diagram of the current sensing scheme is shown in Fig.5.4.

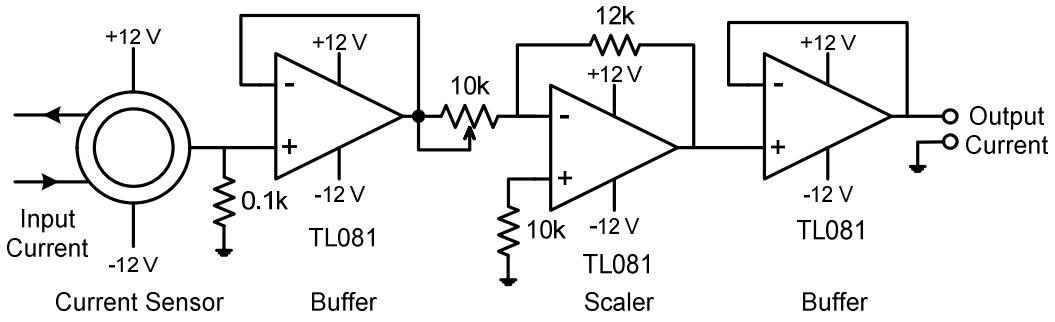

Fig.5.4: AC current sensing circuit.

5.2.2.2 Sensing of Voltage

The voltages are normally sensed using isolation amplifiers and among them, AD202 is a general purpose, two-port, transformer-coupled isolation amplifier that can be used for measuring both AC and DC voltages. The other main features of the AD202 isolation amplifier are:

1. Small physical size
2. High accuracy
3. Low power consumption
4. Wide bandwidth
5. Excellent common-mode performance

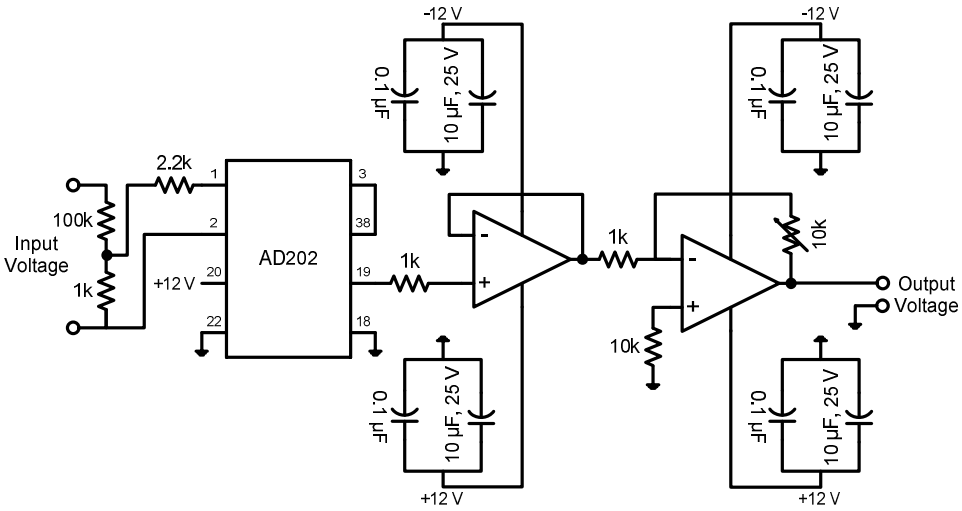

Fig.5.5: AC/DC voltage sensing circuit.

This voltage sensor can sense voltages in the range of ±1 kV (peak) and it requires a nominal supply voltage range of ±12V to ±15V. Fig.5.5 shows the circuit diagram for the voltage sensing scheme, which uses AD202 isolation amplifier. The voltage (AC or DC) to be sensed is applied between the terminals 1 and 2 (across a voltage divider comprising of 100 kΩ and 1 kΩ) and the voltage input to the sensor is available at the pins 1 and 2 of AD202 via a resistance of 2.2 kΩ. The isolated sensed voltage is available at the output terminal 19 of AD202. The output of voltage sensor is scaled properly to meet the requirement of the control circuit and is fed to the dSPACE via its ADC channel for further processing.

5.2.3 Development of System Software

Historically, control software was developed using assembly language. In recent years, industry began to adopt MATLAB/Simulink and Real-Time Workshop (RTW) platform based method, which provides a more systematic way to develop control software. Fig.5.6 shows the Total Development Environment (TDE) of dSPACE and its major component blocks are explained as below:

- MATLAB is widely used as an interactive tool for modelling, analysis and visualization of systems, which itself contains more than 600 mathematical functions and supports additional toolboxes to make it more comprehensive.
- Simulink is a MATLAB add-on software that enables block diagram based modelling and analysis of linear, nonlinear, discrete, and continuous and hybrid systems.
- RTW is Simulink add-on software that enables automatic C-code generation from the Simulink model. The generated optimized code can be executed on PC, microcontrollers, and signal processors.
- Real Time Interface (RTI) is add-on software of dSPACE which provides block libraries for I/O hardware integration of DS1104 R&D controller and generates optimized code for master and slave processors of the board.
- dSPACE's control desk is a software tool interfacing with real-time experimental setup and provides easy and flexible analysis, visualization, data acquisition and automation of the experimental setup. The major feature of real-time simulation is that the simulation has to be carried out as quickly as the real system would actually run, thus allowing to combine the simulation and the inverter (real plant).

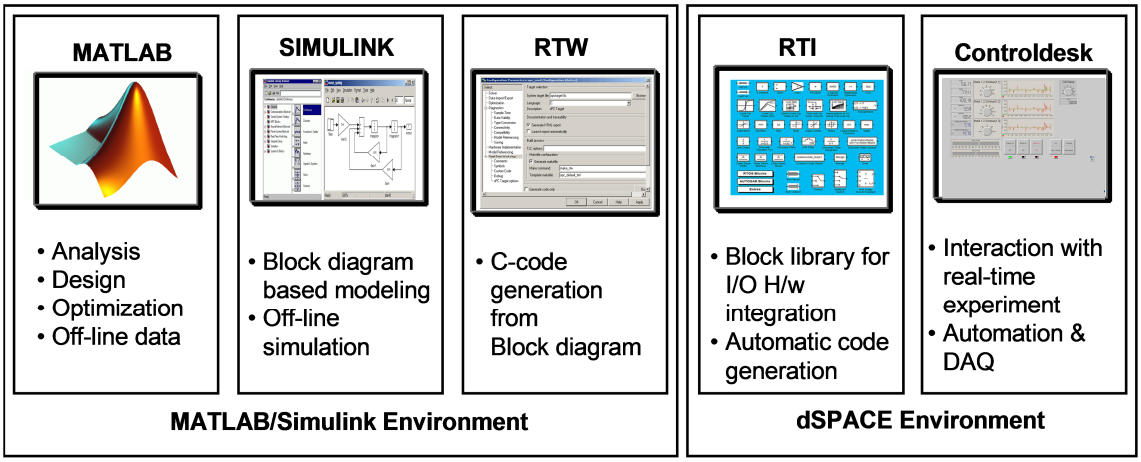

Fig.5.6: Total Development Environment of dSPACE with MATLAB.

The DSP DS1104 R&D controller board of dSPACE is a standard board that can be plugged into Peripheral Component Interconnect (PCI) slot of a desktop computer. The DS1104 is specially designed for the development of high-speed multivariable digital controllers and real-time simulations for various applications. It is a complete real-time control system based on an AMD Opteron™ processor running at 2.6 GHz. It has 256 MB DDR-400 SDRAM local memory for the application and dynamic application data and 128 MB SDR SDRAM global memory for host data exchange. DS1104 R&D controller is a very good platform for the development of dSPACE prototype system for cost-sensitive RCP applications. It is used for the real-time simulation and implementation of the control algorithm in real-time.

The sensed AC and DC voltages are fed to the dSPACE Multi-I/O Board (DS2201) of DS1006 via the available ADC channels on its connector panel. In order to add an I/O block (such as ADCs and master bit I/Os in this case) to the Simulink model, the required block is dragged from the dSPACE I/O library and dropped into the Simulink model of the CHBMLI based PVDG system. In fact, adding a dSPACE I/O block to a Simulink model is almost like adding any Simulink block to the model. The master bit I/Os configured in the output mode, are connected to the model for issuing a gate pulse signal to the MOSFETs. In addition to that ADCs are connected to the model for giving different sensed parameter as input to the DSP hardware. The number of master bit I/Os and ADCs required for the three above mentioned topologies of PVDG system are given in Table.5.1

Table 5.1: Number of I/Os and ADCs required for each PVDG topology

Topology	No. of Master bit I/Os		No. of ADCs	
2-Stage 2-level Inverter 2 -PV Module 2-boost converter 1-H bridge Inverter	4	**2:** For giving gate pulses to two DC-DC converter for MPPT **2:** For giving gate pulses to two level inverter	8	PV module output current (2), voltage(2), grid voltage(1), load current(1), inverter output current(1), DC-link voltage(1)
2-Stage 5-level CHBMLI 2 -PV Module 2-boost converter 2-H bridge Inverter	6	**2:** For giving gate pulses to two DC-DC converter for MPPT **4:** For giving gate pulses to 5-level CHBMLI	9	PV module output current(2),voltage(2), grid voltage(1), load current(1), inverter output current(1), DC-link voltage(2)
1-Stage 5-level CHBMLI 2 -PV Module 2-H bridge Inverter	4	For giving gate pulses to 5-level CHBMLI	7	PV module output current(2),voltage(2), grid voltage(1),load current(1), inverter output current(1)

The sensed signals of each topology are used for the processing in the designed control algorithm. The vital aspect for real-time implementation is the generation of real-time code of the controller to link the host computer with the hardware. For dSPACE systems, Real-Time Interface (RTI) carries out this linking function. Together with RTW from the Mathworks®, it automatically generates the real-time code from Simulink models and implements this code on the dSPACE real-time hardware. This saves the time and effort considerably as there is no need to manually convert the Simulink model into another language such as 'C'. RTI carries out the necessary steps needing only addition of the required dSPACE blocks (I/O interfaces) to the Simulink model. In other words, RTI is the interface between Simulink and various dSPACE platforms. It is basically the implementation software for single-board hardware and connects the Simulink control models to the I/O of

the board. In the present case, the optimized C-code of the Simulink model of the control algorithm is automatically generated by the RTW of MATLAB in conjunction with RTI of dSPACE.

The generated code is then automatically downloaded into the dSPACE hardware where it is implemented in real-time and the gating signals are generated. The gating pulses for the power switches of the converter are issued via the Master-bit I/Os available on the dSPACE board. The DS2201 Connector/LED combo panel provides easy-to-use connections between DS1006 board and the devices to be connected to it. The panel also provides an array of LEDs indicating the states of digital signals (gating pulses). The gating pulses are fed to various power devices driver circuits via dead-band and isolation circuits. Fig.5.7 shows the schematic diagram of dSPACE-DS1104 board interfaced with the host computer and the real-world plant (power circuit of PVDG system). Sensed signals are fed to the ADCs and generated gating pulses are given at Master bit I/Os.

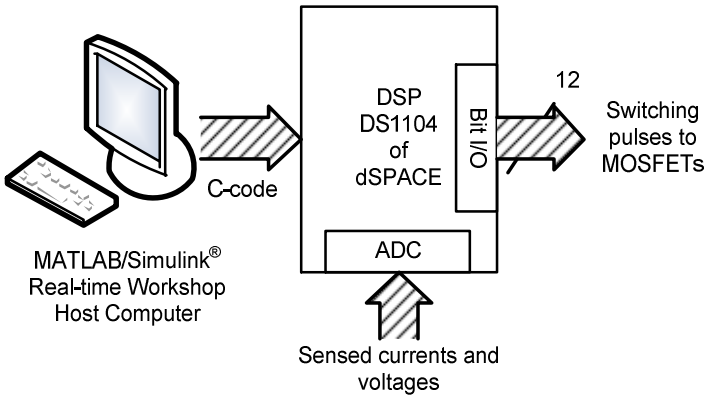

Fig.5.7: DSP (dSPACE-DS1104) circuit board interfacing.

5.2.4 Development of Control Hardware

The control algorithm is designed and built into the MATLAB/Simulink software and the control pulses for the power switches of each topology of PVDG system are generated by real-time simulation using the DSP of dSPACE. The optimized C-code of the Simulink model of control algorithm is generated with the help of Real-Time Workshop (RTW) of MATLAB. The RTW of MATLAB and the Real-Time Interface (RTI) of dSPACE result in the real-time simulation of the model. The control pulses are generated at the various Master-bit I/Os of the dSPACE which are interfaced with the MOSFET driver circuits through isolation and dead-band circuits. This ensures the necessary isolation of the dSPACE hardware from the power circuit that is required for its protection. Fig.5.8 shows the basic schematic diagram of interfacing firing pulses from the dSPACE board to switching devices of PV inverter and DC-DC converters. From Fig.5.8, it can be observed that the following hardware circuits are required for interfacing of DC-DC converters and CHBMLI with dSPACE board.

1. Dead-band circuit
2. MOSFET driver circuits for isolation and amplification

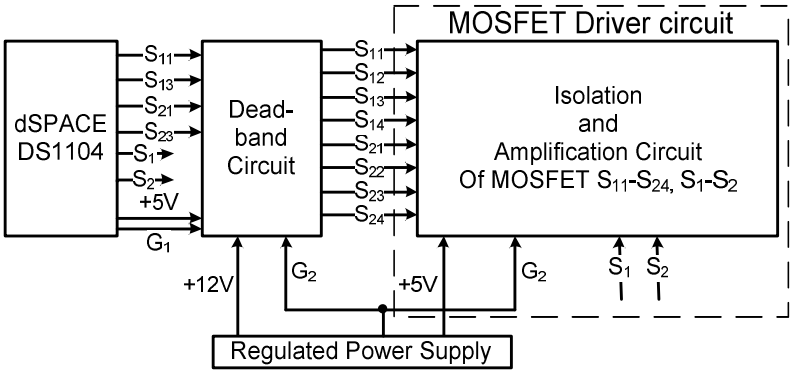

Fig.5.8: Schematic diagram of interfacing firing pulses from dSPACE controller board to switching devices

5.2.4.1 Dead-band Circuit

A dead-band (dead-time or delay) circuit is employed to provide a delay time (of about 1 μs) between the switching pulses to two complementary devices connected in the same leg of an H-bridge cell. This is required to avoid the short circuit of devices in the same leg due to simultaneous conduction. The delay time between switches of the same leg of the H-bridge cell is introduced by an *RC* integrator circuit as shown in Fig.5.9.

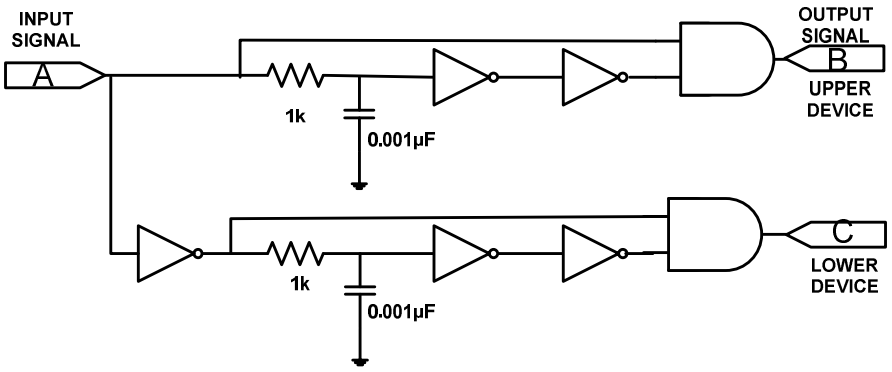

Fig.5.9: Dead-band circuit for single-leg of an H-bridge cell.

An identical dead-band circuit has been used for each leg of all H-bridge cells. The different switching signals obtained experimentally for semiconductor devices in the same leg of an H-bridge cell are shown in Fig.5.10(a) with a 1 μs delay. The switching delay for the upper and lower switch in same leg are shown in a clearer way in Fig.5.10 (b) and Fig.5.10 (c) respectively.

5.2.4.2 MOSFET Driver Circuits

The MOSFET driver circuits are used for pulse amplification and isolation purposes. The control pulses generated from dSPACE unit are not efficient to drive the switching devices. Thus, these signals are further amplified by using proper amplifier circuit. Fig.5.11(a) shows a circuit diagram of pulse isolation and amplifier circuit for MOSFET driver circuit. For isolation between power circuit and a control circuit, an optocoupler(MCT2E) is

used. Although common + 5V, regulated DC power supply is used at the input side of the optocoupler, but individual regulated DC power supplies of +12V are used to connect the output side of optocoupler. In order to test the MOSFET driver, a PWM signal is applied at point ‘a’ of Fig.5.11(a) and waveforms at different points (a, b, c and d) are recorded as shown in Fig.5.11(b). It is observed that the waveform at point ‘d’ is similar to the PWM signal applied at point ‘a’, but its amplitude is increased to 12 V which is used to drive the MOSFET.

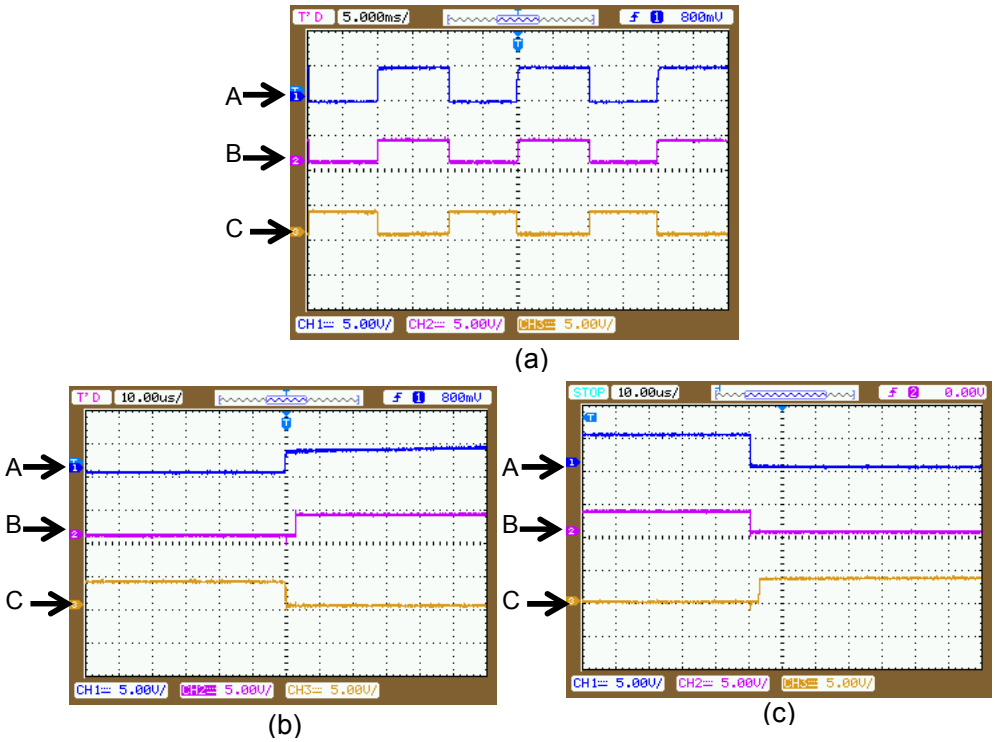

Fig.5.10: Firing signals for the switches S_{11} and S_{12} with dead-band circuit.

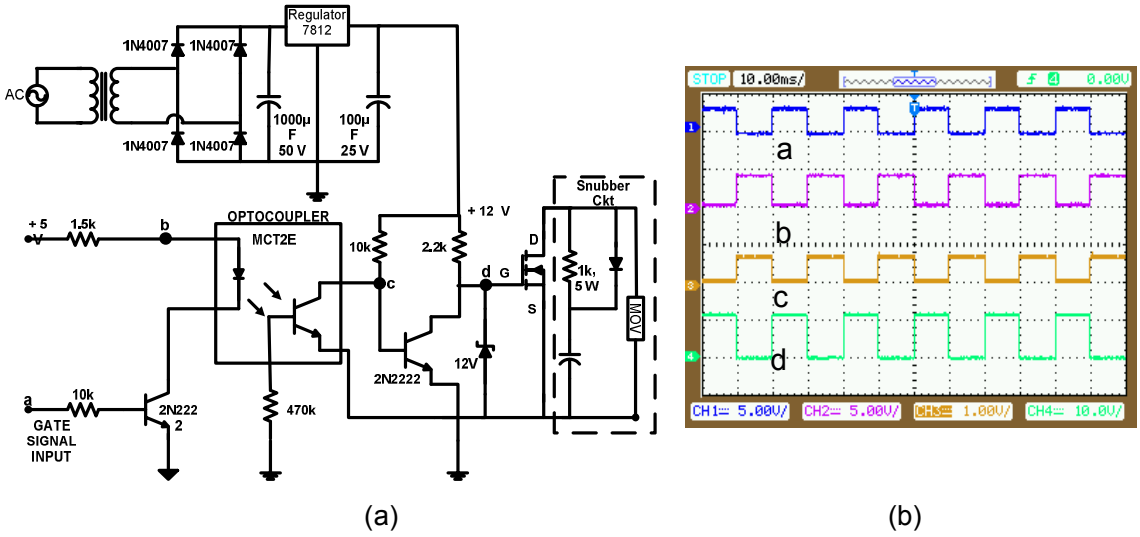

Fig.5.11: (a) MOSFET driver circuit for isolation and amplification (b) waveform at different points

5.3 Experimental Validation of single phase PVDG system

The prototype models of the 1-ϕ two-stage 2-level, two-stage and single-stage CHBMLI based PVDG system with an enhanced PQ feature have been developed by integrating the power circuit, the control hardware and the dSPACE controller. The general view of of the experimental test bench is shown in Fig.5.12. The prototype models have been tested in the laboratory to experimentally validate the simulation results. The experimental analysis consists of the following sections:

1. Determination of $P-V$ and $I-V$ curves of PV Module using experimental data under different irradiation and temperature conditions.
2. Testing of two-stage 2-level PVDG system
3. Testing of two-stage CHBMLI based PVDG system
4. Testing of single-stage CHBMLI based PVDG system using SVM scheme

Finally, the developed inverter prototype has been used to verify the simulation studies of the proposed PVDG topologies. The experimental results for each prototype are presented in the following sections. The PV inverter current, load current, grid current, grid voltage and DC-link voltage waveforms are captured by digital storage oscilloscope (DSO) whereas the active and reactive powers are captured in real time using the control desk developer environment of dSPACE DS-1104.

5.3.1 Characteristic curves of PV module from experimental data

To plot the $P-V$ and $I-V$ curves of the PV module a series of output voltage and current readings of the PV module at different irradiation and temperature conditions are recorded and for the corresponding values of PV current and voltage, the characteristic curves are plotted and are presented in Fig.5.13 and Fig.5.14 respectively. The voltage and current reading are obtained by connecting a rheostat across the PV module and for four different sets of irradiation and temperature conditions, a series of voltage and current readings are recorded by varying the resistance value. Finally, a comparative analysis is made between the obtained experimental maximum power and simulated maximum power which is modelled by using the manufacturer's datasheet which is given in Table.5.2. It is observed from the characteristic curve that the power which is generated experimentally is slightly less than that claimed by the manufacturer. This is due to the power loss associated across the connecting wire, slight deviation in the tilt angle or may be because of some other atmospheric conditions.

(a) PV Modules

(b) Pyranometer

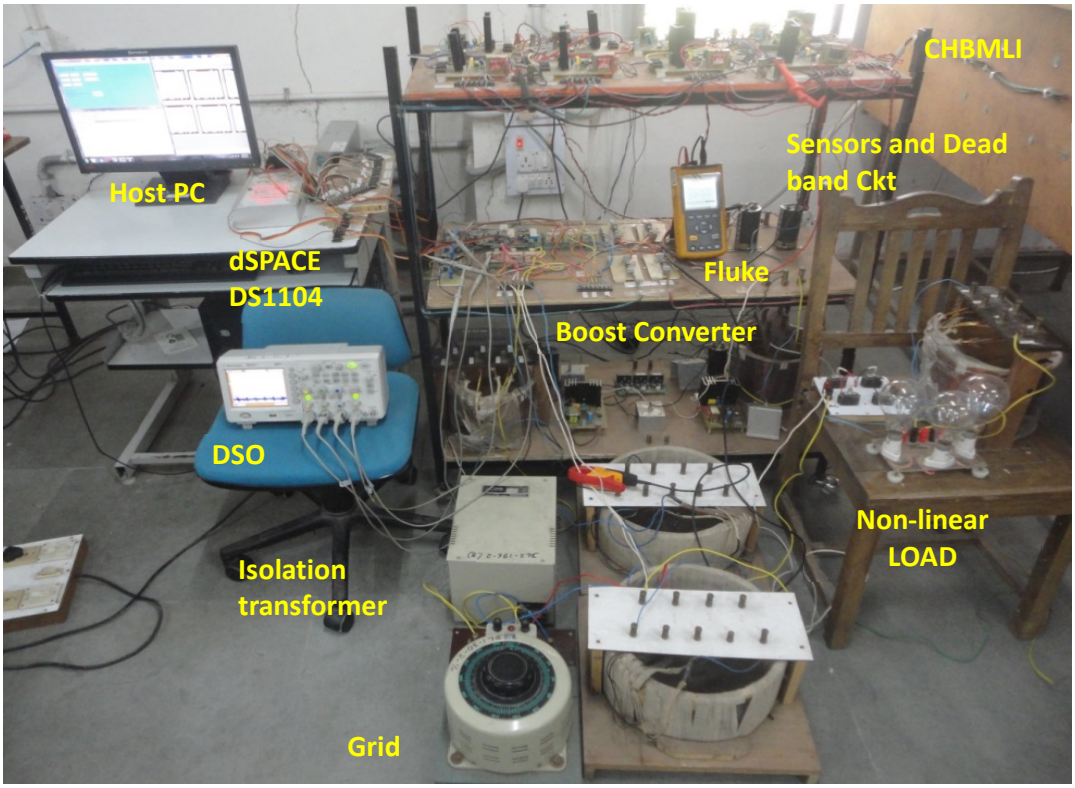

(c) Experimental Setup

Fig. 5.12: General view of the experimental test bench

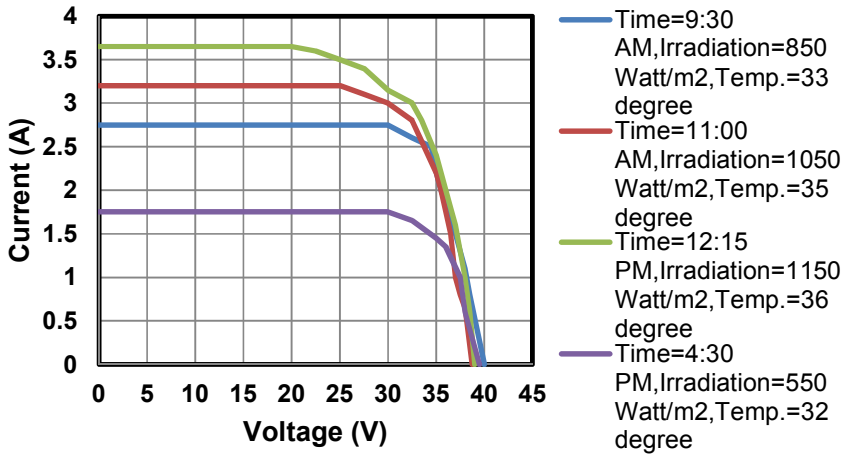

Fig.5.13: $I-V$ curves of PV module from experimental data

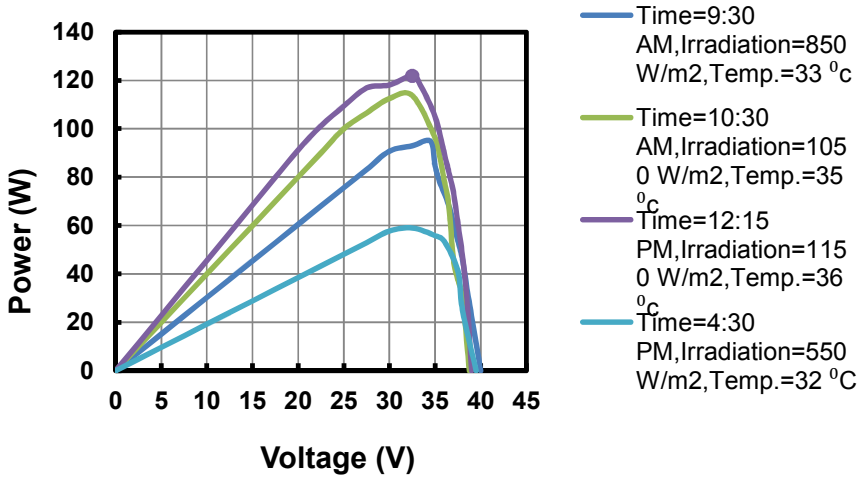

Fig.5.14: $P-V$ curves of PV module from experimental data

Table 5.2: Experimental and simulated Maximum power output of each module under different atmospheric conditions

Irradiation	**850 W/m^2**	**1050 W/m^2**	**1150 W/m^2**	**550 W/m^2**
Temperature	33^{0}C	35^{0}C	36^{0}C	36^{0}C
Experimental	96 W	117.25 W	121.87 W	58 W
Simulation	104 W	129 W	142 W	64 W

5.3.2 Two-stage 2-level inverter and 5-level CHBMLI based PVDG System with PQE Scheme

In this experimental study, the developed prototypes of two stage 2-level inverter and two stage 5-level CHBMLI based PVDG system are tested with different modes of the controller actions, varying load conditions to verify their viability and effectiveness of power transfer, harmonic elimination and reactive power compensation in the 1-ϕ PVDG system. In the first

step of prototype development, two PV modules of 128.1 W each are installed on the rooftop of the laboratory. The manufacturer's data sheet of the PV module is given in Table 2.1 of chapter.2. To extract maximum power from each PV module, two individual DC-DC boost converters are used. In case of 2-level topology, the outputs of two DC-DC converters are connected in a cascaded manner to have a single DC-link for the 2-level PV inverter. However, in case of 5-level CHBMLI, each DC-DC converter output is directly connected across two individual H-bridge cells. Finally, the developed PV inverter output is connected to the PCC with a series connected filter inductor. A 35.8V (50 V peak), 50 Hz grid is developed in the laboratory by using a step down transformer and is interfaced with the PV inverter through an isolation transformer.

All the passive elements used for the development of the above mentioned system such as electrolytic capacitor which is connected across the PV module, the inductor and capacitor for boost converter, filter inductor connected between PV inverter and PCC is designed as per the procedure discussed in earlier chapters and are chosen as per the market availability. All these parameters used for hardware development are tabulated in Table 5.3. The MPPT and PQEC are implemented in dSPACE. To verify the viability and effectiveness of the enhanced PQ based PVDG system for power flow operation, harmonic elimination and reactive compensation, experimental investigations have been conducted with non-linear loads. Uncontrolled rectifier with RL element on their DC side have been used as a nonlinear load. For this purpose, a 1-ϕ uncontrolled diode bridge rectifier is developed in the laboratory. Each device has been mounted on suitably designed heat sink to ensure proper heat dissipation. The schematic diagrams of uncontrolled rectifiers with RL elements on the DC side are shown in Fig.5.15. For the analysis purpose, two different non-linear loads has been considered (load-1 and load -2) for all the topologies. Fig.5.16 (a) and Fig.5.16 (b) shows the currents drawn by these non-linear loads and their harmonic spectrum respectively. The currents drawn by these load are found to be non-sinusoidal. The harmonic spectrum of the load current for load-1 and load-2 contains significant amounts of 5^{th}, 7^{th}, 11^{th} and 13^{th} order harmonics with resulting THD of 22 % and 26.5 % respectively.

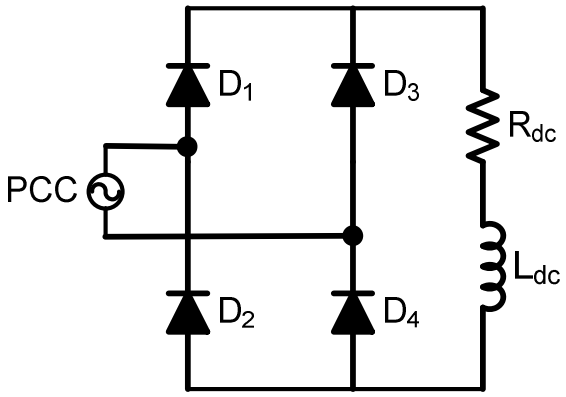

Fig.5.15: 1-ϕ nonlinear load consisting of uncontrolled rectifier with RL elements

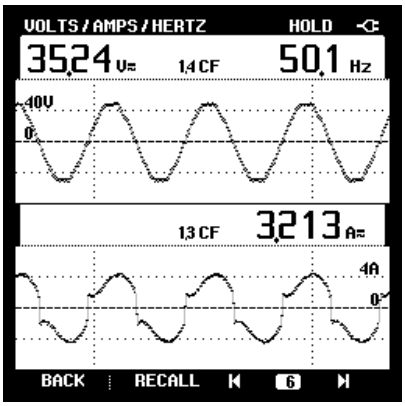

(i)

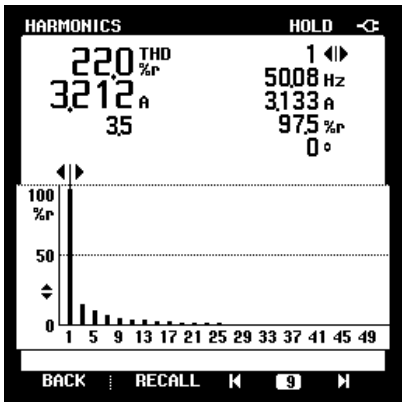

(ii)

(a)

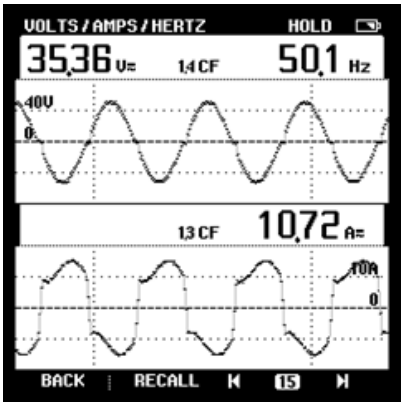

(i)

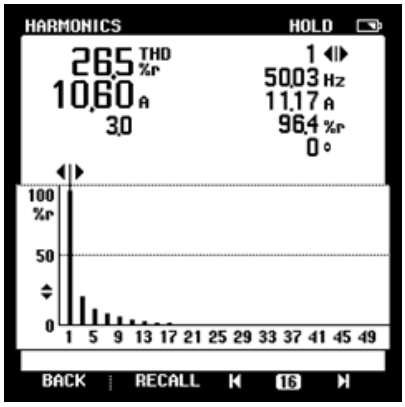

(II)

(b)

Fig.5.16: (i) PCC voltage, load current waveform (ii) harmonic spectrum of load current for (a) load-1 (b) load-2

In this section an extensive experimental studies have been carried out to investigate the performance of above mentioned 1-ϕ two stage PVDG systems for following modes of operation:

(i) Under different modes of PQEC

(ii) Under different modes of MPPT Controller

(iii) Under Varying load conditions

As the experimental studies have been conducted at reduced system voltage, for validating the experimental results, the simulation studies have also been carried out with reduced system voltage. The parameters used in the actual simulation studies (given in Chapter 3 and Chapter.4) and downscaled simulation studies are given in Table 5.4. The downscaled simulation parameters are kept as same as possible to the experimental parameters given in Table 5.3. The relevant discussions based on experimental and simulation results for all the above mentioned conditions are given below in the following sub-sections.

Table 5.3:Parameters used for the experimental validation of 1P2W PVDG System

Parameter	**Value**
AC line parameters	Single Phase, 50 V(Peak), 50 Hz
PV module (2 no.)	128 W each
DC bus voltage of PV inverter	50 V (for each capacitor in the H-bridge cell of 5-level CHBMLI) 100 V(For 2-level PV inverter)
DC –link capacitance	1000 µF
PV inverter side coupling inductor	$L_{inv}: 0.937mH$ for 2-level PV inverter $L_{inv}: 0.38mH$ for 5-level PV CHBMLI
Grid side inductor	$L_g: 0.12\,mH$
PWM switching frequency	3 kHz
PI controller parameters	For 2-level PV inverter: K_p= 0.4, K_i= 1.6 For 5-level CHBMLI: K_p= 0.1, K_i= 1.2.
Load	1-ϕ uncontrolled rectifier with *RL* loads Load-1: $R_{dc}: 10\Omega, L_{dc}: 18.5\,mH$ (light load for the PV system) Load-2: $R_{dc}: 3\Omega, L_{dc}: 9.25mH$ (Over load for the PV system)
Sampling time	T_s = 50 µs.

Table 5.4: The parameters used in the simulation studies.

Parameters	**For the actual PVDG System**	**For the downscaled PVDG System**
Grid	Single-phase, 230 , 50 Hz	Single-phase, 35.8 V(50V Peak) , 50 Hz
DC bus voltage of PV Inverter	250 V (for each capacitor in the H-bridge cell of CHBMLI 500 V (for 2-level PV inverter)	50 V (for each capacitor in the H-bridge cell of CHBMLI) 100 V (for 2-level PV inverter)
DC bus capacitance of PV inverter	1000µF (for each capacitor in the H-bridge cell)	1000 µF (for each capacitor in the H-bridge cell)
Coupling inductor(L_{inv})	1.2 mH (For 2-level PVDG System) 0.5 mH (For 5-level PVDG System)	0.937 mH (For 2-level PVDG System) 0.38 mH (For 5-level PVDG System)
Grid side inductance(L_g)	0.02 mH	0.12 mH
PWM switching frequency	3 kHz	3 kHz
PI controller parameters	DC-link Voltage Controller K_p= 1.1, K_i= 1.5.	DC-link voltage controller: K_p= 0.3, K_i= 1.3.
Single-phase uncontrolled rectifier with *RL* load	Load-1: $R_{dc}: 10\Omega, L_{dc}: 21mH$ (light load for the PV system) Load-2: $R_{dc}: 3.306\Omega, L_{dc}: 10.5mH$ (Over load for the PV system)	Load-1: $R_{dc}: 10\Omega, L_{dc}: 18.5\,mH$ (light load for the PV system) Load-2: $R_{dc}: 3\Omega, L_{dc}: 9.25mH$ (Over load for the PV system)
Sampling time	T_s = 10 µs.	T_s = 50 µs.

5.3.2.1 Two stage PVDG system under different modes of PQEC

This section presents the experimental results of two-stage 2-level and 5-level CHBMLI based PVDG system with different modes of PQEC. The experiment is conducted with the MPPT controller is enabled throughout the test. The irradiation and temperature level during the test condition are measured as 1050 W/m^2 and 35 ^{0}C respectively, with a non-linear load (load-2) connected across the PCC. To study the steady and dynamic performance of the PVDG system, the PQEC is initially operated in disabled mode and a few second later it is enabled to show its effectiveness for harmonics and reactive power compensation. The experimental results of two-stage 2-level and two-stage 5-level CHBMLI based PVDG system under this mode of operation are given in Fig.5.17 and Fig.5.19 respectively. Based on these experimental results the observations which are common for both these topologies are listed out as follows:

1. During disabled mode of PQEC, the PV inverter generates a sinusoidal current as per the PWM scheme. However, as the nonlinear load draws non-sinusoidal current from PV inverter, the grid current $(i_g = i_{inv} - i_L)$ becomes non-sinusoidal and of lagging nature w.r.t. grid voltage.

2. At the instant when PQEC is turned on, the PV inverter injects a non-sinusoidal current which contains harmonics and reactive components as per the load demand and thereby makes the grid current (i_g) sinusoidal and also in phase with the grid voltage.

3. It can also be observed from these experimental results that, in both modes of operation of PQEC, i_{inv}, i_L and i_g are in the same phase, which means the local load demand is shared by both PV inverter and the grid.

Finally, based on the experimental results the discussions of both the topologies under this mode of operation are given separately in the following sections:

A. Two-stage two-level inverter based PVDG system

The experimental results of 1-ϕ two-stage 2-level inverter based PVDG system with different modes of operation of PQEC is shown in Fig.5.17. The steady state plots of PV voltage at PCC (v_{pcc}) inverter output current (i_{inv}), non-linear load current (i_L) and grid current (i_g) under disabled and enabled modes of PQEC are depicted in Fig.5.17(a) and Fig.5.17(b) respectively. In disabled mode the rms value of i_{inv}, i_L and i_g are found out to be 6.09 A, 10.9 A and 6.35 A respectively. After enabling the PQEC, the rms values of i_{inv}, i_L and i_g are recorded as, 7.51 A, 10.9 A and 4.87 A respectively.

The transient response of the system under this condition is shown in Fig.5.17 (c). It can be observed that during transient operation, the DC-link capacitor voltage (V_{dc}) is changed from its reference value to accommodate the load harmonics and reactive power

demand. This variation in capacitor voltage is restored in 3–4 cycles. Overall, a smooth control of the DC capacitor voltage is achieved when the controller is turned on from off state. The harmonic spectrum of grid current before and after compensation is given in Fig. Fig.5.17(d). The load current harmonic spectrum is already given in Fig.5.13 (a) whose % THD is 26.5%. It can be observed that after compensation, the grid current % THD is found to be improved from 48.4% to 4.9%.

Finally, the experimental results of active and reactive power curves which are captured in real time using the control desk developer environment of dSPACE 1104 are given in Fig.5.17(e) and Fig.5.17(f) respectively. It can be observed from the active power curves that, the PV inverter power, load power and grid power before and after compensation are found to be remaining same and the values are recorded as 207 W, 350 W and 143 W respectively. Under both modes of operation of PQEC, the load power requirement is found to be more than PV generation; therefore the load demand is shared by both PV inverter and the grid. Similarly, from the experimental reactive curves it is observed that, during the disabled mode of PQEC, the load reactive power demand is completely supplied by the grid. However, at the instant when PQEC is enabled, the PV inverter starts feeding the load reactive power, thereby making the grid reactive power to zero.

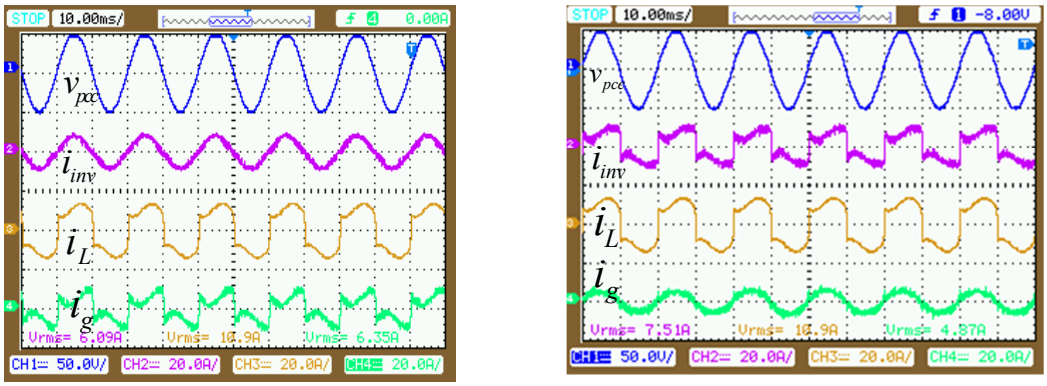

Fig.5.17 (a) Steady state response of voltage at PCC, PV inverter current, load current and grid current without PQEC (b) with PQEC

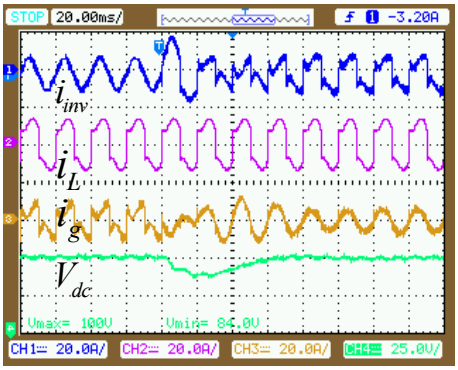

Fig.5.17 (c)Transient Response of PVDG system when PQEC is enabled from disabled mode

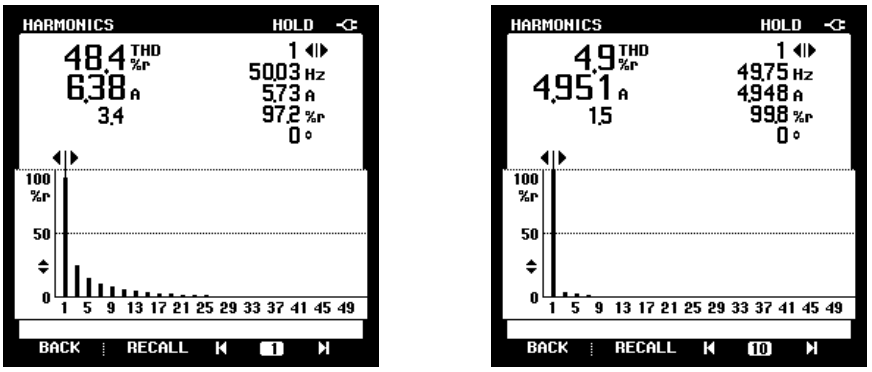

(i) (d) (ii)

Fig.5.17 (d) Harmonic Spectrum of grid current (i) without PQEC (ii) with PQEC

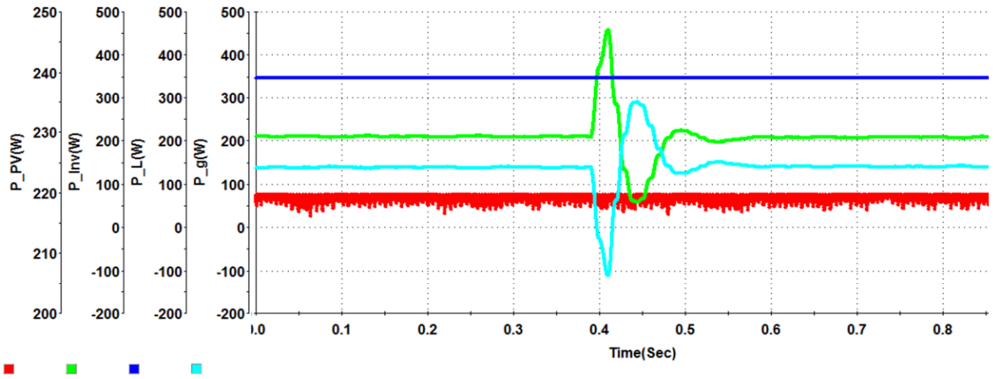

Fig.5.17 (e) Active power curves under different modes of PQEC

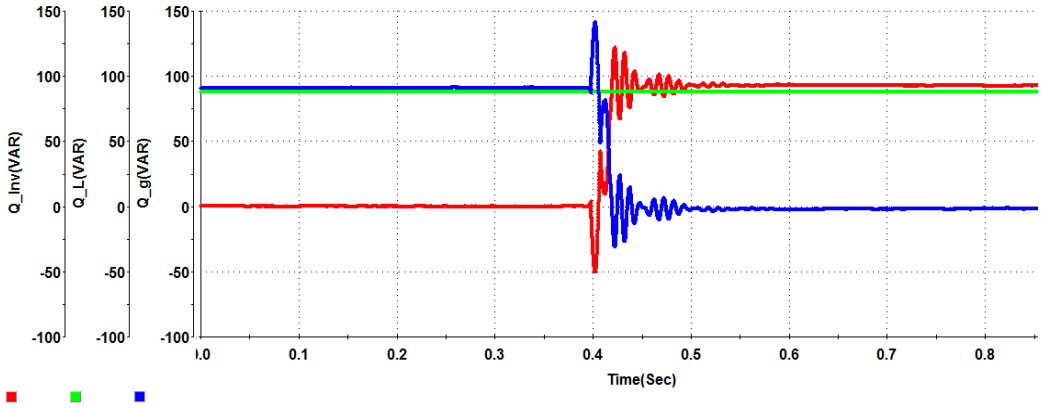

Fig.5.17 (f) Reactive power curves under different modes of PQEC

Fig.5.17: Experimental results of 2-stage 2-level inverter based PVDG system under different modes of PQEC.

In order to validate the experimental results of two-stage 2-level inverter based PVDG system under different modes of PQEC, the simulation studies have also been carried out with the experimental parameters. The simulated waveforms of voltage at PCC, inverter current, load current, grid current, active and reactive power curves are given in Fig.5.18. From these figures, it can be seen that the simulation results are in good agreement with experimental results. Based on the experimental and simulation results a comparative analysis is made which includes rms values of PV inverter current, load current, grid current,

% THD of grid current and active powers. These are tabulated in Table 5.5. It is observed that, the simulated PV inverter power output is more compared to that generated experimentally. This due to the poor efficiency of the practical PV module and the losses associated with the wires used for the interconnection of PV module from the rooftop to the associated PV inverter module.

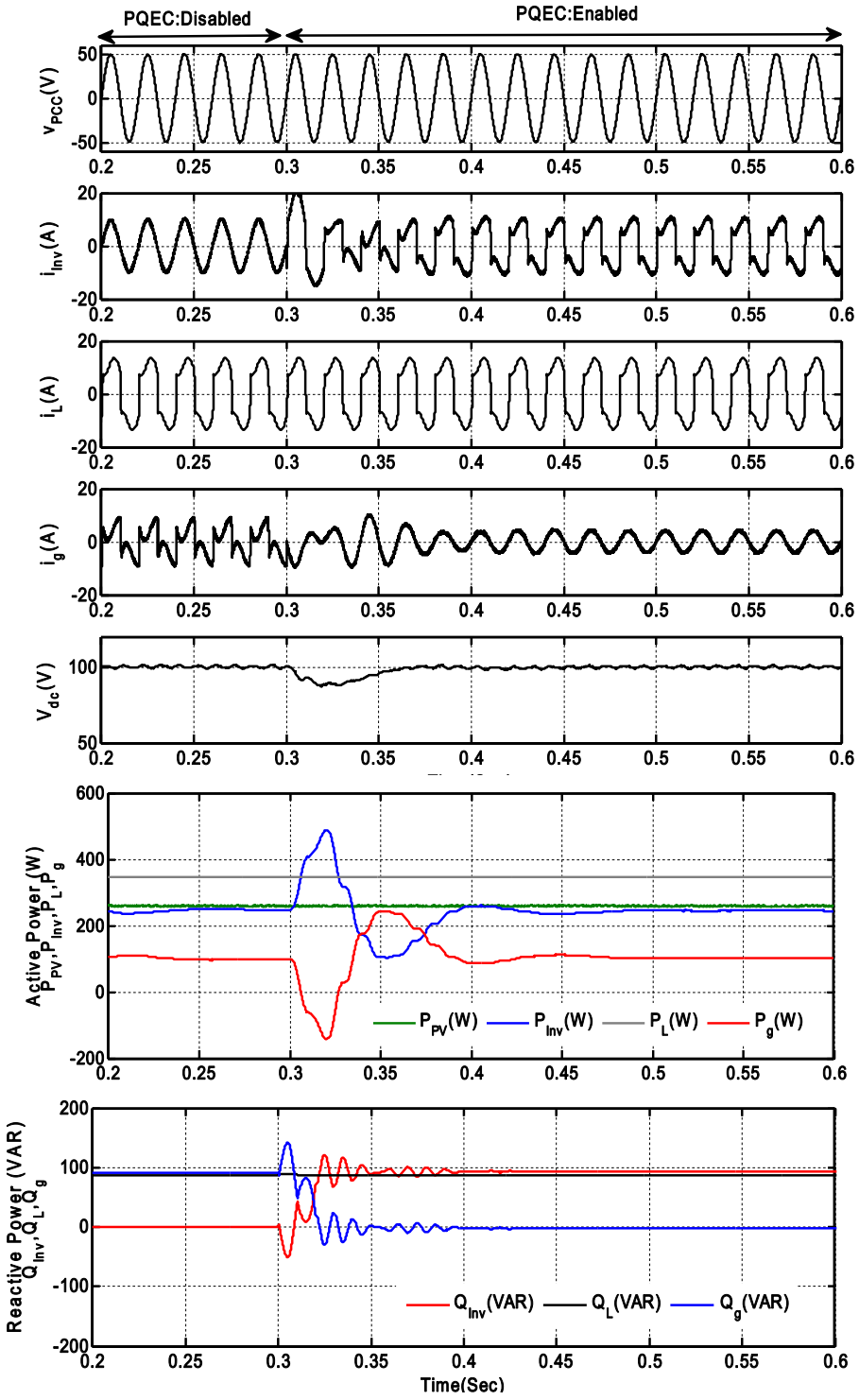

Fig. 5.18: : Simulation results of two-stage 2-level inverter based on experimental parameters under different modes of PQEC

B. Two-stage Five-level CHBMLI based PVDG system

The experimental results of 1-ϕ two-stage 5-level CHBMLI based PVDG system with different modes of operation of PQEC is presented here. The steady state plot of voltage at PCC (v_{pcc}), PV CHBMLI output current (i_{CHBMLI}), non-linear load current (i_L) and grid current (i_g) under disabled and enabled modes of PQEC are depicted in Fig.5.19 (a) and Fig.5.19 (b) respectively. Under disabled mode the rms values of PV CHBMLI current, load current and grid current are found out to be 6.25 A, 10.9 A and 6.55 A respectively. Similarly, after enabling the PQEC, the corresponding rms values of current are recorded as, 7.33 A, 10.9 A and 4.67 A respectively. The transient response of the PVDG system under this mode of operation is shown in Fig.5.19 (c) and Fig.5.19(d). It is observed that during transient conditions, both the DC-link capacitor voltages (V_{dc1}, V_{dc2}) changes from its reference value to accommodate the load harmonics and reactive power demand. This variation in capacitor voltage is restored in 1–2 cycles. Overall, a smooth control of the DC-link capacitor voltages are achieved when the controller is turned on from off state. The harmonic spectrum of grid current before and after compensation is given in Fig.5.19(e). Before compensation, as the grid was responsible for supplying harmonic components of load current, the % THD of grid current is found as 46.4%. However, after compensation, as the PV inverter compensates the load current harmonics, the grid current THD is reduced to 4.1%.

Finally, the experimental results of active and reactive power curves are presented in Fig.5.19 (f) and Fig.5.19(g) respectively. It can be observed from the active power curves that, CHBMLI output power, load power and grid power before and after compensation are found to be 210 W, 350 W and 140 W respectively. Under both modes of operation of PQEC, the load power requirement is found to be more than PV generation; therefore the load demand is shared by both PV CHBMLI and the grid. Likewise, from the experimental reactive curves it is observed that, under the disabled mode of PQEC, all the load reactive power demand is supplied by the grid and the instant when PQEC is enabled, the PV CHBMLI start feeding the load reactive power, thereby making the grid reactive power to be zero. This validates the reactive power compensation capability of the controller.

In order to validate the experimental results of two-stage 5-level CHBMLI based PVDG system under different modes of PQEC, the simulation studies have also been carried out with the experimental parameters. The simulated waveforms of voltage at PCC, inverter current, load current, grid current, active and reactive power curves are given in Fig. 5.20. From these figures, it can be seen that the simulation results are in good agreement with experimental results. Finally, a comparative analysis based on simulation and experimental results are given in Table 5.5.

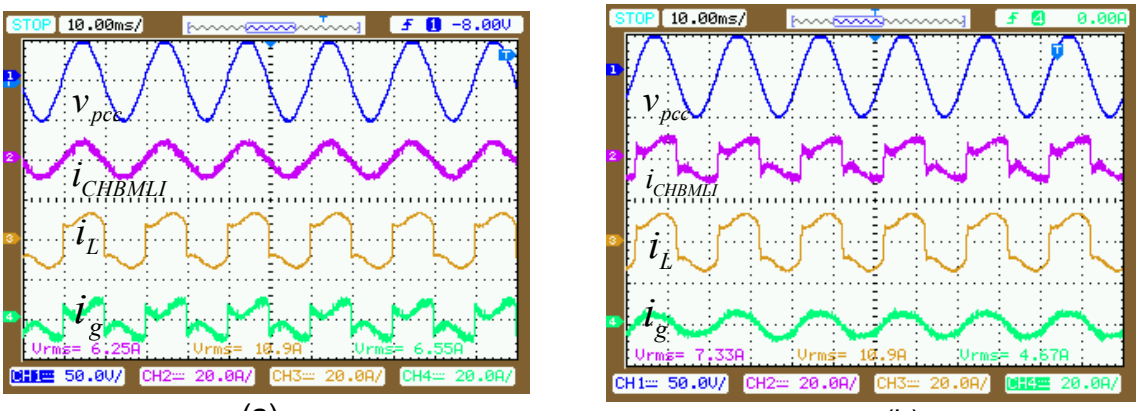

(a) (b)

Fig.5.19 Steady state response of voltage at PCC, PV CHBMLI current, load current and grid current (a) without PQEC (b) with PQEC

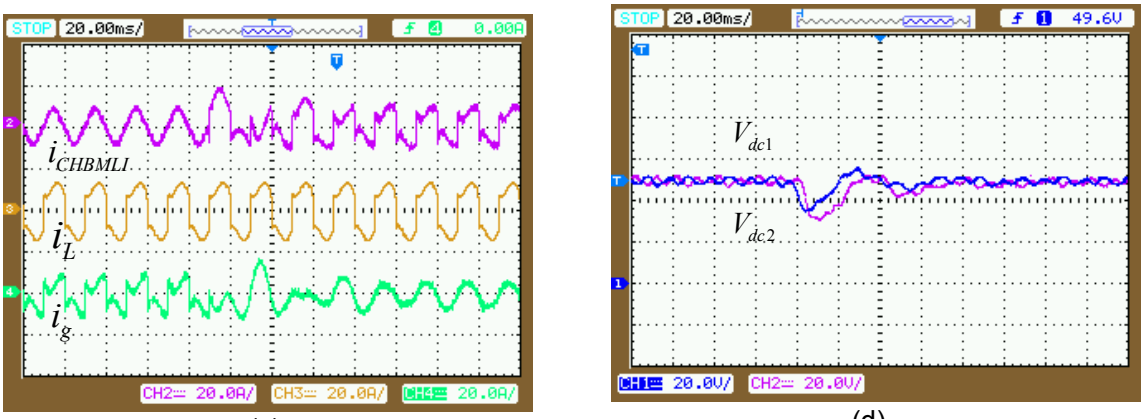

(c) (d)

Fig.5.19 (c) Transient Response of PVDG System when PQEC is enabled from disabled mode (d) DC-link voltages

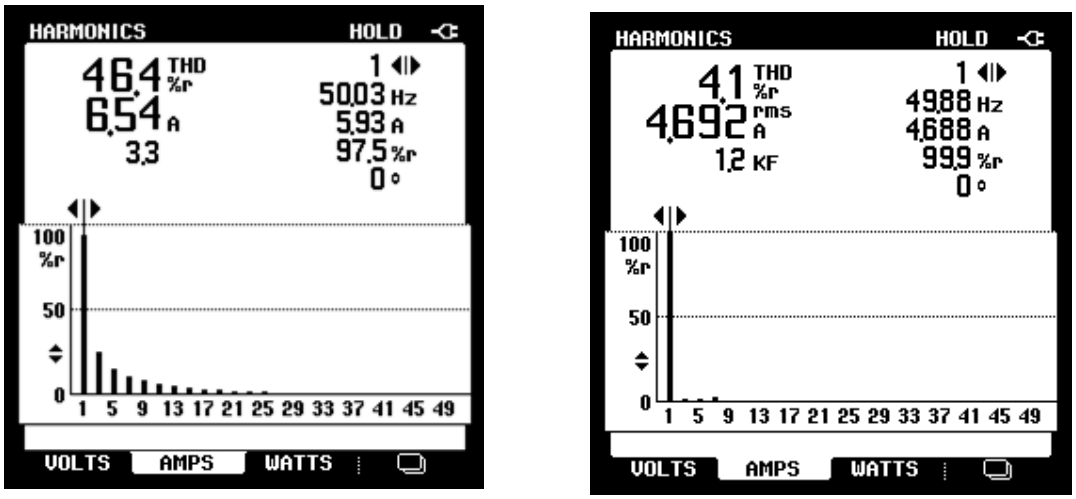

(i) (ii)

(e)

Fig.5.19 (e) Harmonic Spectrum of grid current (i) without PQEC (ii) with PQEC

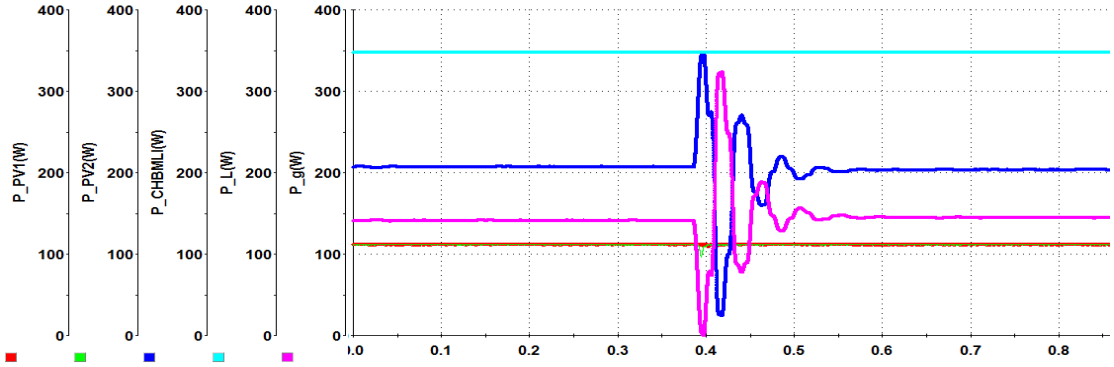

Fig.5.19 (f) Active power curves of PVDG system under different modes of PQEC

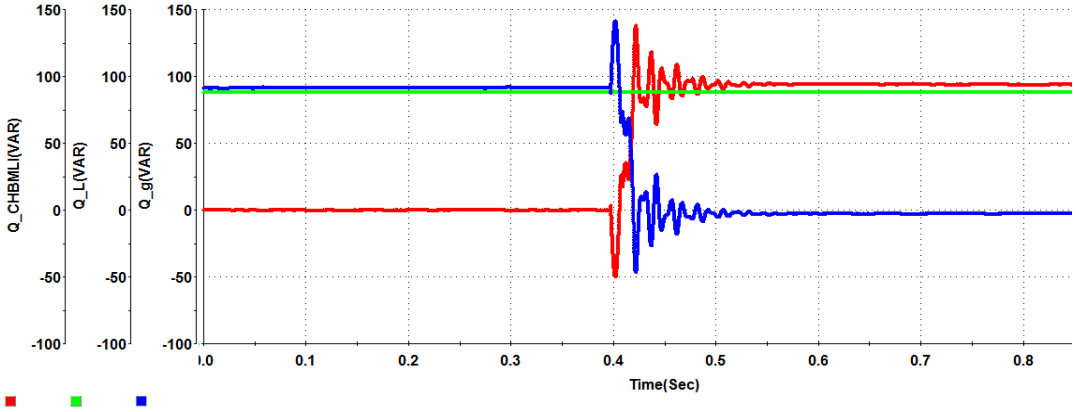

Fig.5.19 (g) Reactive power curves of PVDG system under different modes of PQEC

Fig.5.19: Experimental results of 2-stage 5-level CHBMLI based PVDG system under different modes of PQEC.

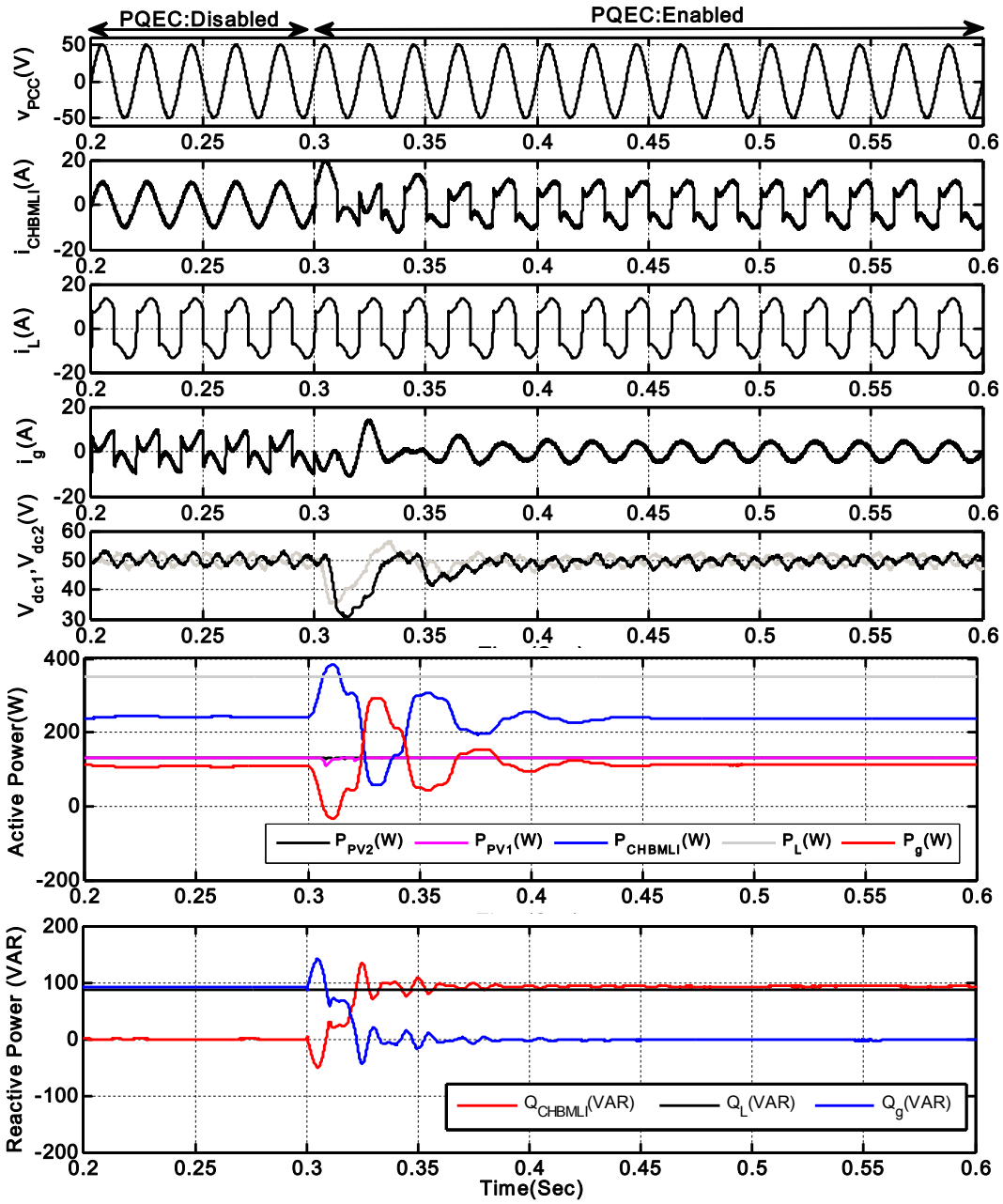

Fig.5.20 : Simulation results of 2-stage 5-level CHBMLI based PVDG system based on experimental parameters under different modes of PQEC

5.3.2.2 Different Modes of MPPT Controller

The experimental results of the PVDG system with disabled and enabled modes of MPPT controller with two-stage 2-level inverter and two-stage CHBMLI based topologies are shown in Fig.5.21 and Fig.5.23 respectively. The test is performed while employing the PQEC is enabled with a non-linear local (load-2) is connected at PCC. To study the steady and dynamic performances of these topologies, the MPPT controller is initially operated in disabled mode and a few second later, it is enabled to show its effectiveness for maximum power extraction. In two-stage topologies, MPPT is accomplished with the help of DC-DC

converter. During test condition, the irradiation and temperature level are recorded as 1055 W/m^2 and 35 ^{0}C respectively. Finally, based on the experimental results the observations which are common for both topologies are listed out as follows:

1. During disabled mode of MPPT control, the load current demand is more than that generated by the PV inverter and hence, the grid fulfills the rest of the load current requirement. With PQEC is enabled throughout the test, the PV inverter generates a non-sinusoidal current to compensate the load harmonics as well as supply the reactive component of current demanded by the load.

2. When the MPPT controller is turned on, the generated PV inverter current is found to be increased. As load current demand is still found to be more than generated PV inverter current, grid continues to supply the rest of the load current. However, it is observed that, with MPPT controller, current drawn from the grid is less compared to without MPPT controller mode.

3. With the implementation of PQE scheme, under both disabled and enabled modes of MPPT controller, the grid current is found to be in phase with the grid voltage.

Finally, based on the experimental results the discussion on each topology under different modes of operation of MPPT controller are given below:

A. Two-stage 2-level inverter based PVDG system

The steady state waveform of voltage at PCC (v_{pcc}), PV inverter output current (i_{inv}), non-linear load current (i_L) and grid current (i_g) under disabled and enabled modes of MPPT controller are shown in Fig.5.21 (a) and Fig.5.21(b) respectively. Under disabled mode of MPPT controller the rms values of PV inverter current, load current and grid current are found to be 4.93 A, 10.9 A and 8.54 A respectively. However, after enabling the MPPT controller, the corresponding rms values of current are recorded as, 7.59 A, 10.9 A and 4.67 A respectively. It clearly shows that, with MPPT controller the PV inverter output current increases from 4.93 A to 7.59 A and thereby a reduced amount of grid current is extracted from the grid to fulfill the load demand. The transient response of the system under different modes of MPPT controller is given in Fig.5.21(c). At the instant when the MPPT controller is turned on, the generated PV power increases. Hence, the DC-link capacitor voltage (V_{dc}) increases from its reference value to accommodate the increase in generation. This increase in capacitor voltage is restored in 2–3 cycles. The harmonic spectrum of grid current without and with MPPT controller is given in Fig. 5.20(d). It can be observed from these results that even though the load current % THD is 26.5 % (Fig. 5.13(b)) but the grid current %THD under disabled and enabled modes of MPPT are found out to be 4.4% and 5.4% respectively.

Finally, for the analysis of power under this mode, the active and reactive powers are captured in real time and are given in Fig.5.21(e) and Fig.5.21(f) respectively. It can be observed from this power curves that, without an MPPT controller, the PV inverter output

power, load power and grid power are recorded as 65 W, 350W and 284 W, which indicates that, the bulk amount of demanded load active power is extracted from the grid under this mode of MPPT controller. However, when the MPPT controller is enabled, the PV module gradually increases its generation to reach the MPP. During this mode, the PV inverter output power, load power and grid power are recorded as 203 W, 350W and 146 W respectively. In this mode, as the PV generation is increased, less amount of power is extracted from the grid. Similarly, from the experimental reactive power curves, it can be observed that, under both modes of MPPT controller, the reactive power demanded by the load is supplied by the PV inverter thereby relieving grid from feeding any reactive power towards PCC. To validate the experimental results of 2-stage 2-level inverter based PVDG system under different modes of MPPT controller, the simulation studies have also been carried out with the experimental parameters and the corresponding simulated waveforms of voltage at PCC, inverter current, load current, grid current, active and reactive power curves are given in Fig.5.22. From these figures, it can be seen that the simulation results are in good agreement with experimental results.

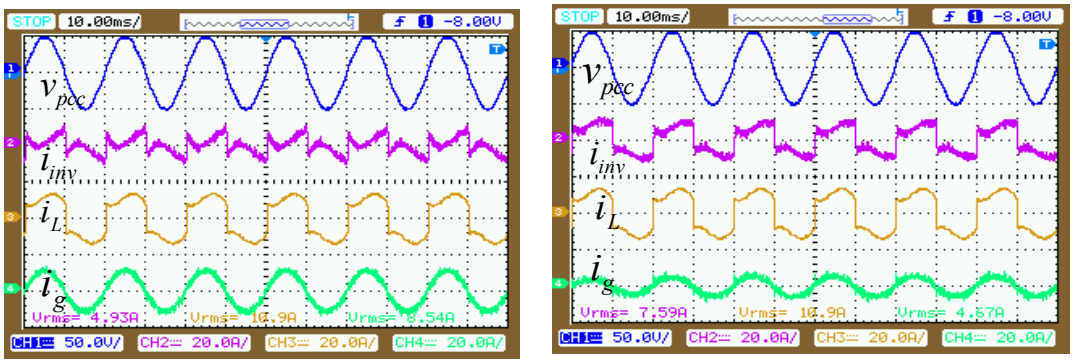

(a) (b)

Fig.5.21: Steady state response of voltage at PCC, PV inverter current, load current and grid current (a) without MPPT Controller (b) with MPPT controller

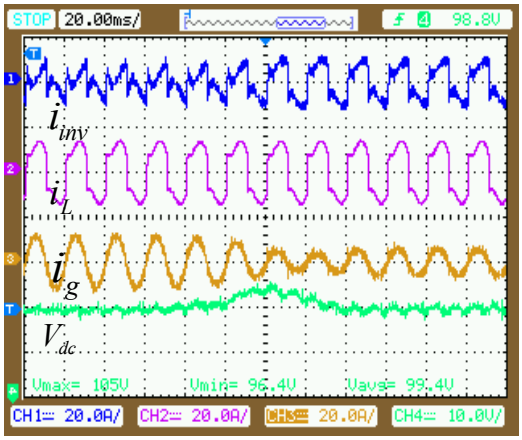

Fig.5.21 (c)Transient Response of the system when theMPPT controller is enabled from disabled mode

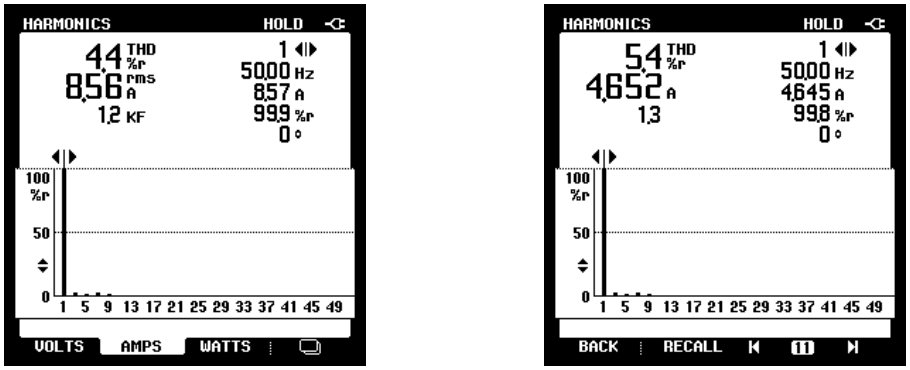

(i) (d) (ii)

Fig.5.21 (d) THD of grid current (i) without MPPT Controller (ii) with MPPT controller

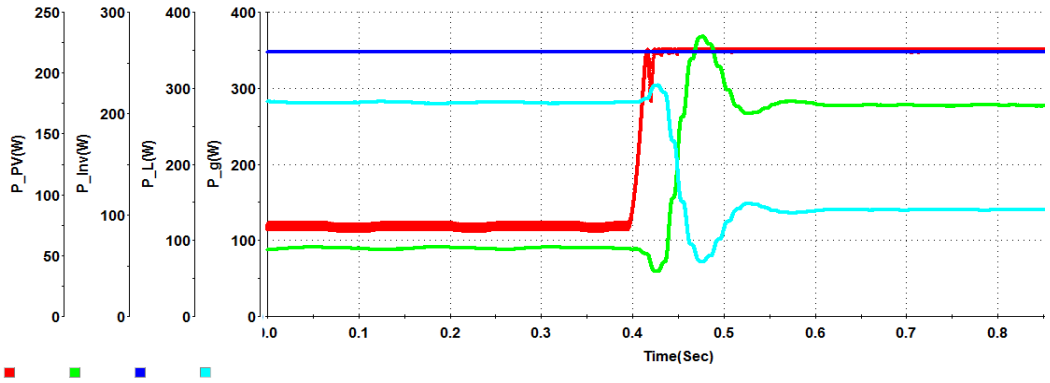

Fig.5.21 (e) Active Power curves of PVDG system under different modes of MPPT controller

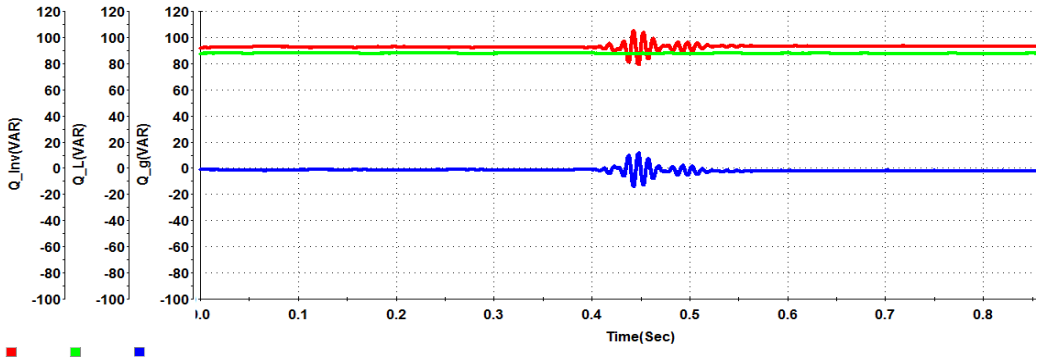

Fig.5.21 (f) Reactive Power curves of PVDG system under different modes of MPPT controller

Fig.5.21: Experimental results of enhanced power quality based PVDG system without and with MPPT controller.

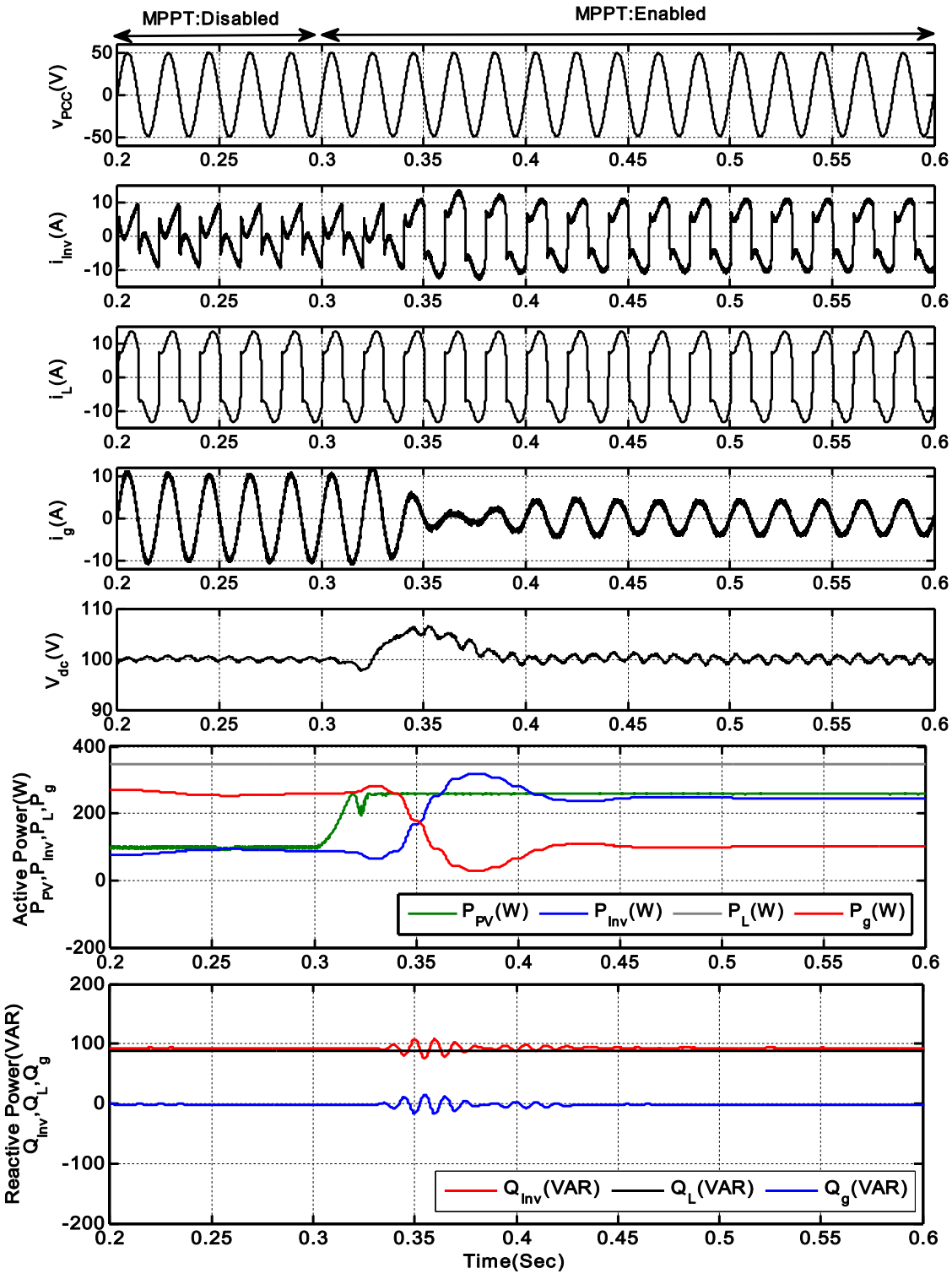

Fig.5.22: Simulation results based on experimental parameters under different modes of MPPT controller

B. Two-stage 5-level CHBMLI based PVDG system

The steady state waveform of PV CHBMLI output current (i_{CHBMLI}), non-linear load current (i_L) and grid current (i_g) under disabled and enabled modes of MPPT controller are shown in Fig.5.23(a) and Fig.5.23(b) respectively. Under disabled mode of MPPT control the rms value of PV CHBMLI current, load current and grid current are found to be 5A, 10.8A and 8.31 A respectively. Similarly, after enabling the MPPT control, the corresponding rms values of current are recorded as, 7.29 A, 10.8 A and 4.60 A respectively. At the instant when the MPPT controller is turned on, the generated PV power of each PV module is increasing. Hence, the DC-link capacitor voltage of each H-bridge cell (V_{dc1}, V_{dc2}) increases from its reference values to accommodate the increase in generation. This enhancement in capacitor voltages are restored in few cycles. Overall, a smooth control of the DC capacitor voltages has been achieved when the MPPT controller is turned on from off state. These transient responses of the system are shown in Fig.5.23 (c) and Fig.5.23 (d) respectively. The harmonic spectrum of grid current without and with MPPT controller is given in Fig.5.22(e). It can be observed from these results that even though the load current % THD is 30.5% but the grid current %THD under disabled and enabled modes of MPPT is found to be 4.1% and 4.2% respectively, which well within the limits of IEEE-519-1992 recommended value of 5%.For the analysis of power under this this mode, the experimental results of active and reactive power which is captured in real time using the control desk developer environment of dSPACE 1104 is given in Fig.5.23(e) and Fig.5.23(f) respectively. It can be observed from Fig.5.23(e) that without an MPPT controller, the PV module unable to generate the maximum power as per the PV module datasheet (Table. I). Without MPPT control, the CHBMLI, load and grid active power are noted as 68 W, 350 W and 282 W respectively. This implies that without MPPT controller, the bulk amount of demanded load active power is extracted from the grid. The instant when MPPT controller is enabled, the PV module gradually increases its generation and CHBMLI output is found to be 220 W. During this mode, as the PV generation is still not sufficient to fulfil the load demand, the rest of the required load power demand is met by the grid. However, it can be observed that, the power extracted from the grid is only 130 W. The positive value of the active power supplied by the PV inverter implies that power flows from PV inverter towards PCC, whereas a negative value of grid active power implies that power is absorbed by the grid. To validate the experimental results of 2-stage 5-level CHBMLI based PVDG system under different modes of MPPT controller action, a simulation study has also been carried out with experimental parameters. The simulated waveforms of voltage at PCC, inverter current, load current, grid current, active and reactive power curves are given in Fig.5.24. From these figures, it can be seen that the simulation results are in good agreement with experimental results for this mode of operation.

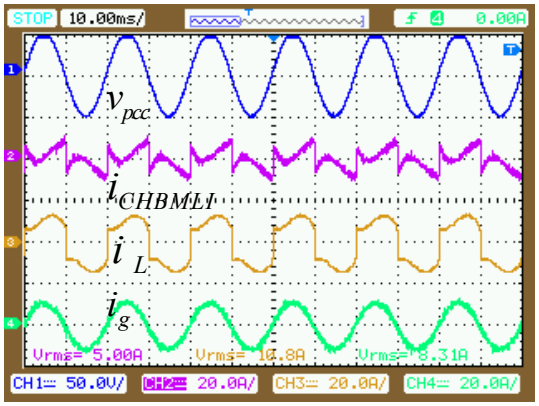

(a)

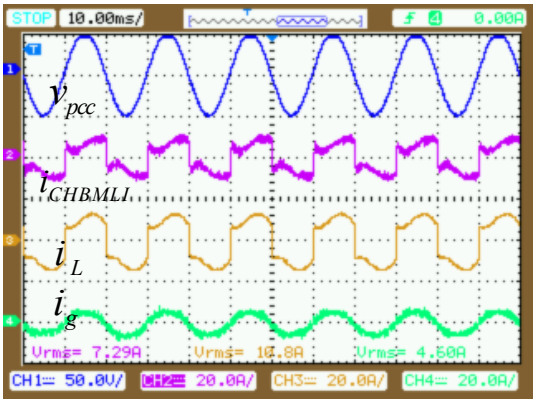

(b)

Fig.5.23 Steady state response of voltage at PCC, PV inverter current, load current and grid current (a) without MPPT controller (b) with MPPT controller

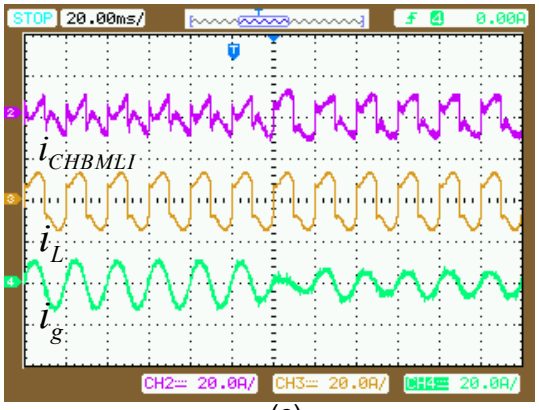

(c)

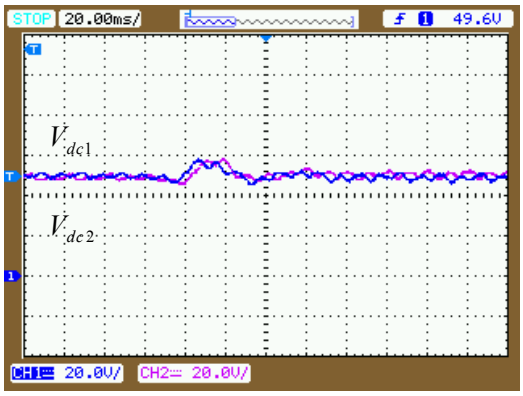

(d)

Fig. 5.23 Transient Response of PVDG System under different modes of MPPT controller (c) current waveforms (d) DC-link voltage waveforms

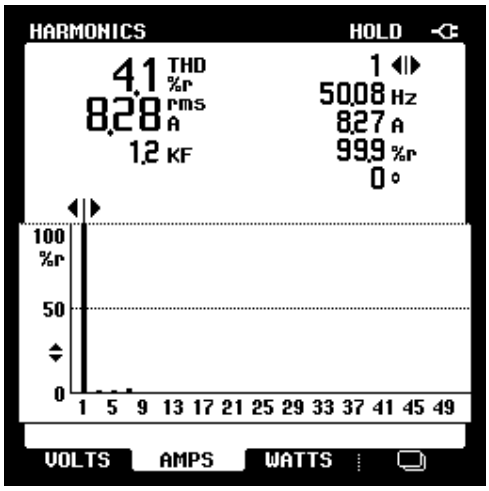

(i)

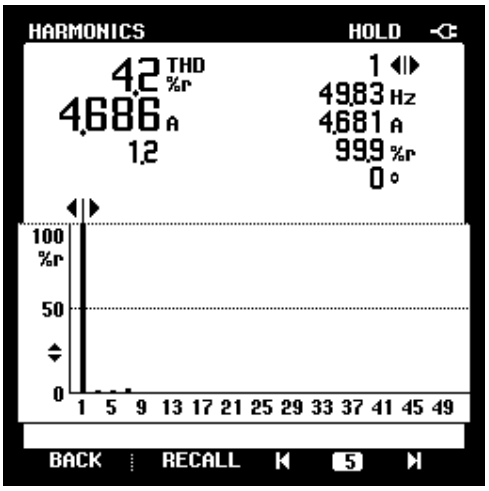

(ii)

(e)

Fig.5.23(e) Harmonic Spectrum of grid current (i) without MPPT (ii) with MPPT

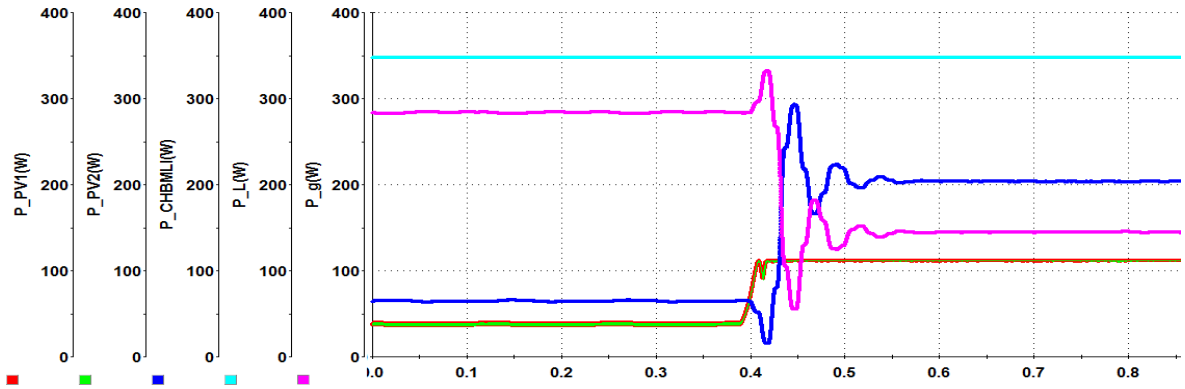

Fig.5.23(f) Active power curves of PVDG system under different modes of MPPT controller

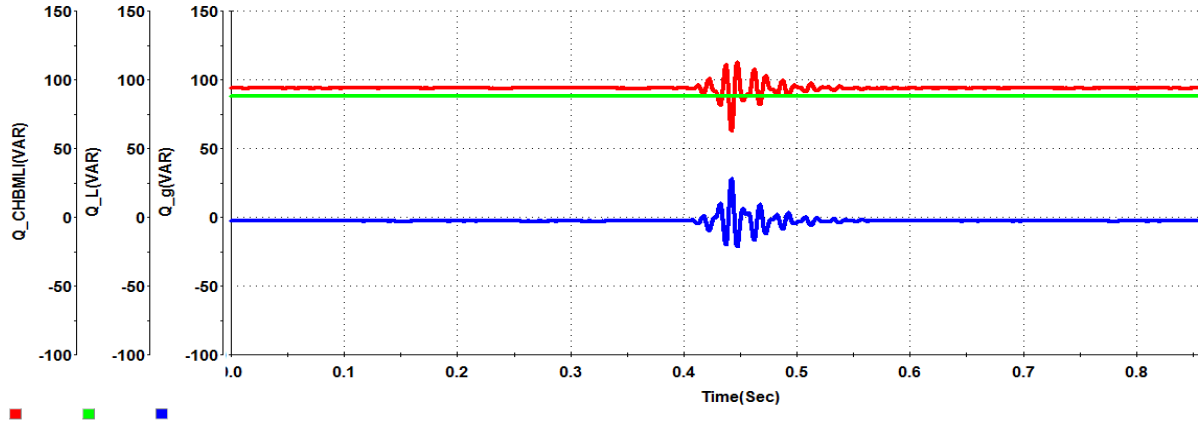

Fig.5.23(f) Reactive power curves of PVDG system under different modes of MPPT controller

Fig.5.23: Experimental results of 2-stage 5-level CHBMLI based PVDG system under different modes of MPPT Controller.

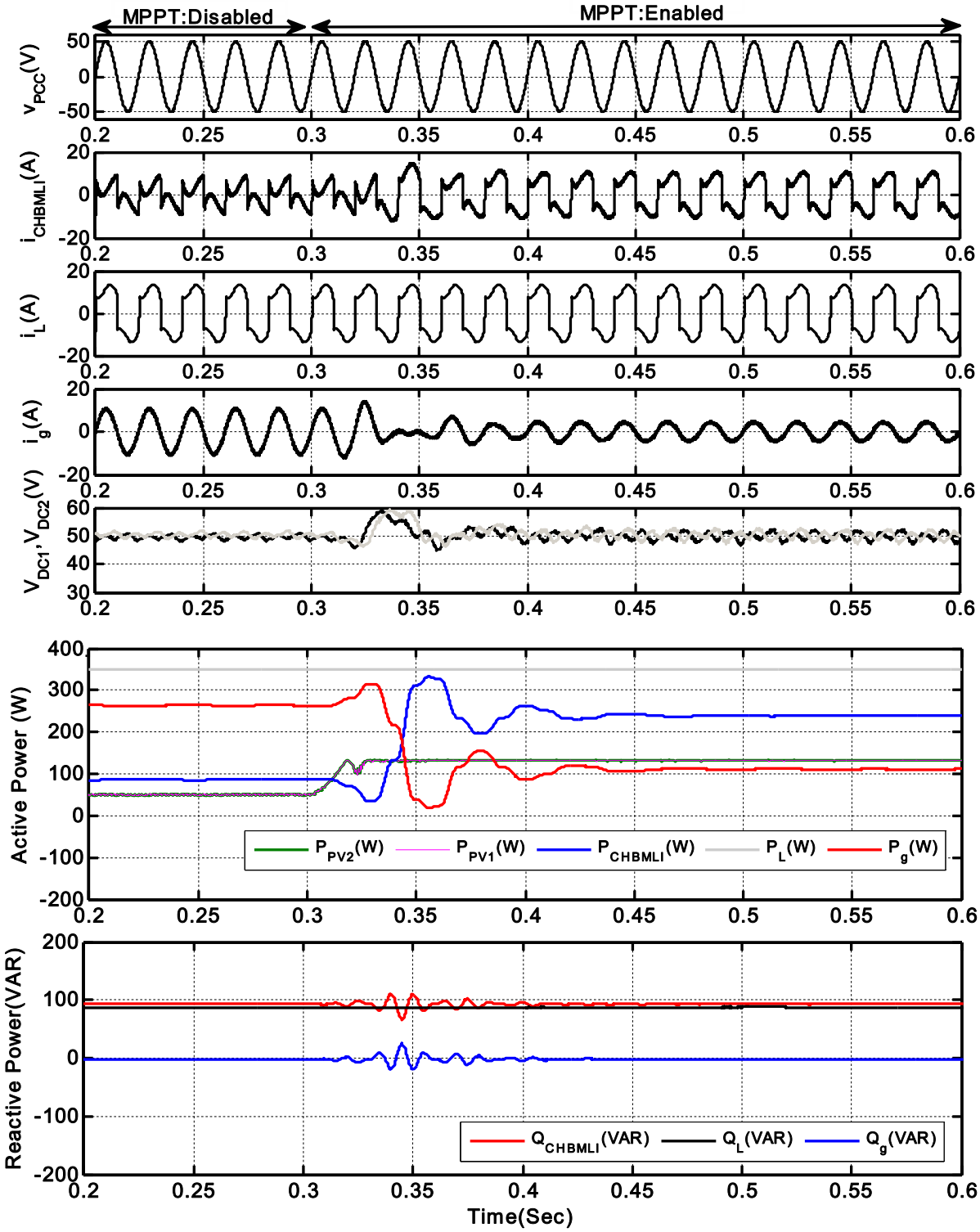

Fig.5.24: Simulation results of 5-level CHBMLI based PVDG system under different modes of MPPT controller based on experimental parameters

5.3.2.3 Under varying load condition

The experimental results of enhanced PQ based PVDG system under varying load conditions with two-stage 2-level inverter and two-stage CHBMLI based topologies are shown in Fig.5.25 and Fig.5.27 respectively. The test is performed while employing the PQEC and MPPT controllers in enabled mode. To study the steady and dynamic performance of the above mentioned topologies of PVDG system, under varying load condition, load-1 is initially connected across the PV inverter and a few second later load-1 is disconnected and load-2 is connected across the PV inverter. Based on the experimental results the observations which are common to these two topologies are listed out as follows,

- With load-1 is connected across the PV inverter, the load current demand is found to be less than that generated by the PV inverter and hence, the surplus current is fed to the grid. With the PQEC is in enabled mode, the PV inverter generates a non-sinusoidal current to compensate the load harmonics as well as supply the reactive component of current demanded by the load.
- Similarly, when the load is increased to create an overload condition, the load current demand is found to be more than that generated by PV inverter and hence, the rest of the load current demand is met from the grid. Similar to a previous condition, the harmonic components of the load current still continue to be supplied by the PV inverter thereby making the grid current sinusoidal.

Finally, based on the experimental results, the discussions on each topology under this mode of operation are given one by one in the following sections.

A. Two-stage 2-level inverter based PVDG system

The steady state waveform of PV inverter output current (i_{inv}), non-linear load current (i_L) and grid current (i_g) during light load and overload condition are shown in Fig.5.25(a) and Fig.5.25(b) respectively. It can be observed from Fig.5.25(a) that under light load condition (i_g) is out of phase from (i_{inv}), which means that the surplus generated PV inverter current is fed to the grid. However, with overload condition, all three currents are found to be in the same phase. This is because; the PV generation is not sufficient to fulfill the local load demand. Hence the rest of the load current demand is supplied by the grid. Under light load condition, the rms value of PV inverter current, load current and grid current are found out to be 6.15 A, 3.49 A and 3.30 A respectively. Similarly, under an overload condition, the corresponding rms values of current are recorded as, 7.46 A, 10.8 A and 4.23 A respectively. The transient response of the PVDG system under varying load conditions is shown in Fig.5.25(c). At the instant when load current increases, the DC capacitor voltage drops from its reference value to accommodate the enhancement in the load current. This drop in

capacitor voltage is restored in 2–3 cycles which demonstrates its good dynamic response. Finally the harmonic spectrum of grid current is given in Fig.5.25(d). It can be observed from these results that the grid current %THD under light and overload conditions are found out to be 5.2 % and 4.6 % respectively.

For the analysis of power under varying load condition, the active power is captured in real time using the control desk developer environment of dSPACE 1104 which is given in Fig.5.25(e). It is observed from this power curve that under both light load and overload conditions the power generated by the PV inverter is the same which is 206 W. However, in light load condition the load power demand is less which is 111 W. Therefore, the surplus power is fed to the grid, which is recorded as 96 W. Similarly, under overload conditions as the local load demand 350 W, the grid supplied 143 W powers to fulfill the load demand. The grid feeding condition and load sharing condition can be observed by the negative and positive value of grid active power respectively. Similarly, the experimental results of reactive power curves under varying load conditions are shown in Fig.5.25(f). From these results it can be observed that, under both types of loading conditions, the reactive power demanded by the load is completely supplied by the PV inverter and hence the grid reactive power is found to be zero.

To validate the experimental results of two-stage two-level inverter based PVDG system under varying load conditions, the simulation studies have also been carried out with the experimental parameters and the corresponding simulated waveforms of voltage at PCC, inverter current, load current, grid current, active and reactive power curves are given in Fig.5.26. From these figures, it can be seen that the simulation results are in good agreement with experimental results.

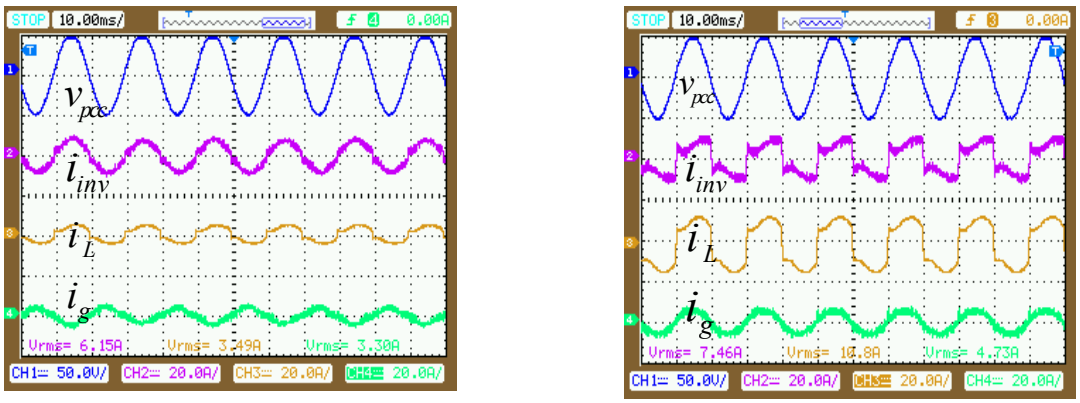

(a) (b)

Fig.5.25. Steady state response of voltage at PCC, PV inverter current, load current and grid current (a) under light load condition (b) under overload condition

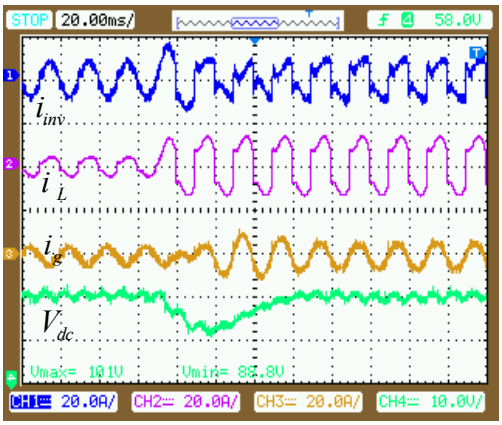

Fig.5.25 (c)Transient Response of PVDG system under varying load condition

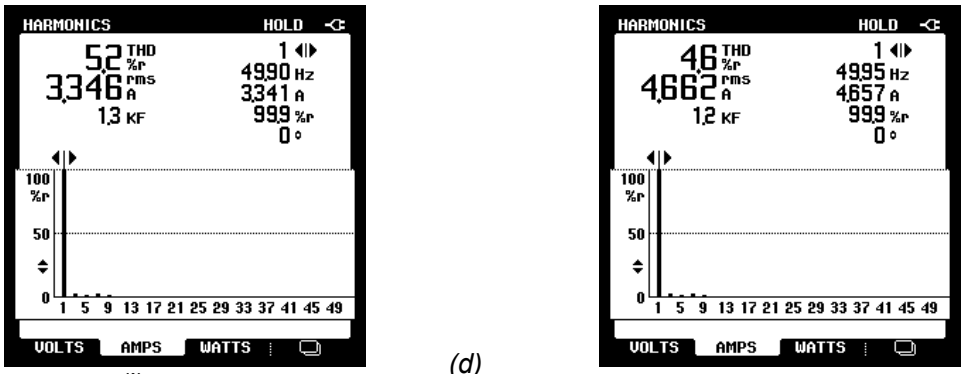

(i) *(d)* (ii)

Fig.5.25 (d) Harmonic Spectrum of grid current (i) under light load (ii) under overload condition

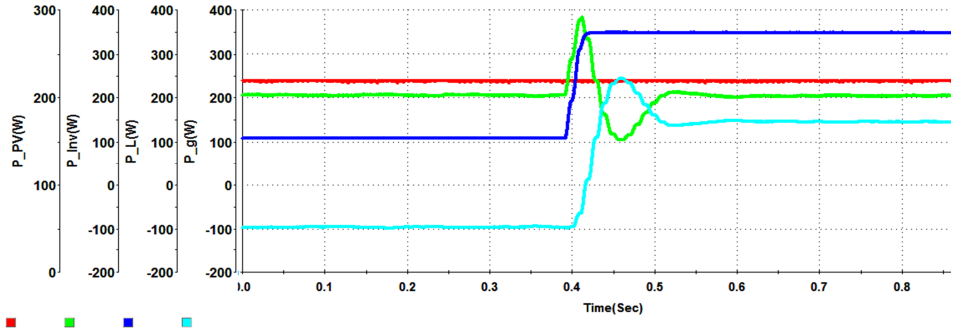

Fig.5.25.(e) Active power curves of the PVDG system under varying load condition

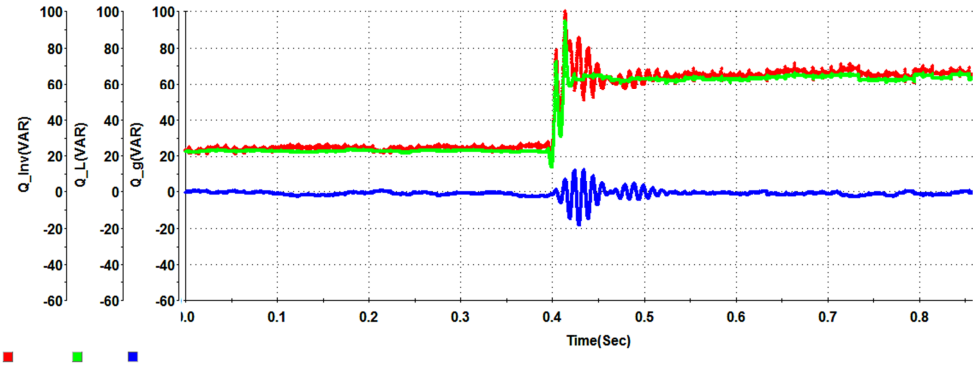

Fig.5.25(f) Reactive power curves of the PVDG system under varying load condition

Fig.5.25: Experimental results of 2-stage 2-level inverter based PVDG system with varying load condition.

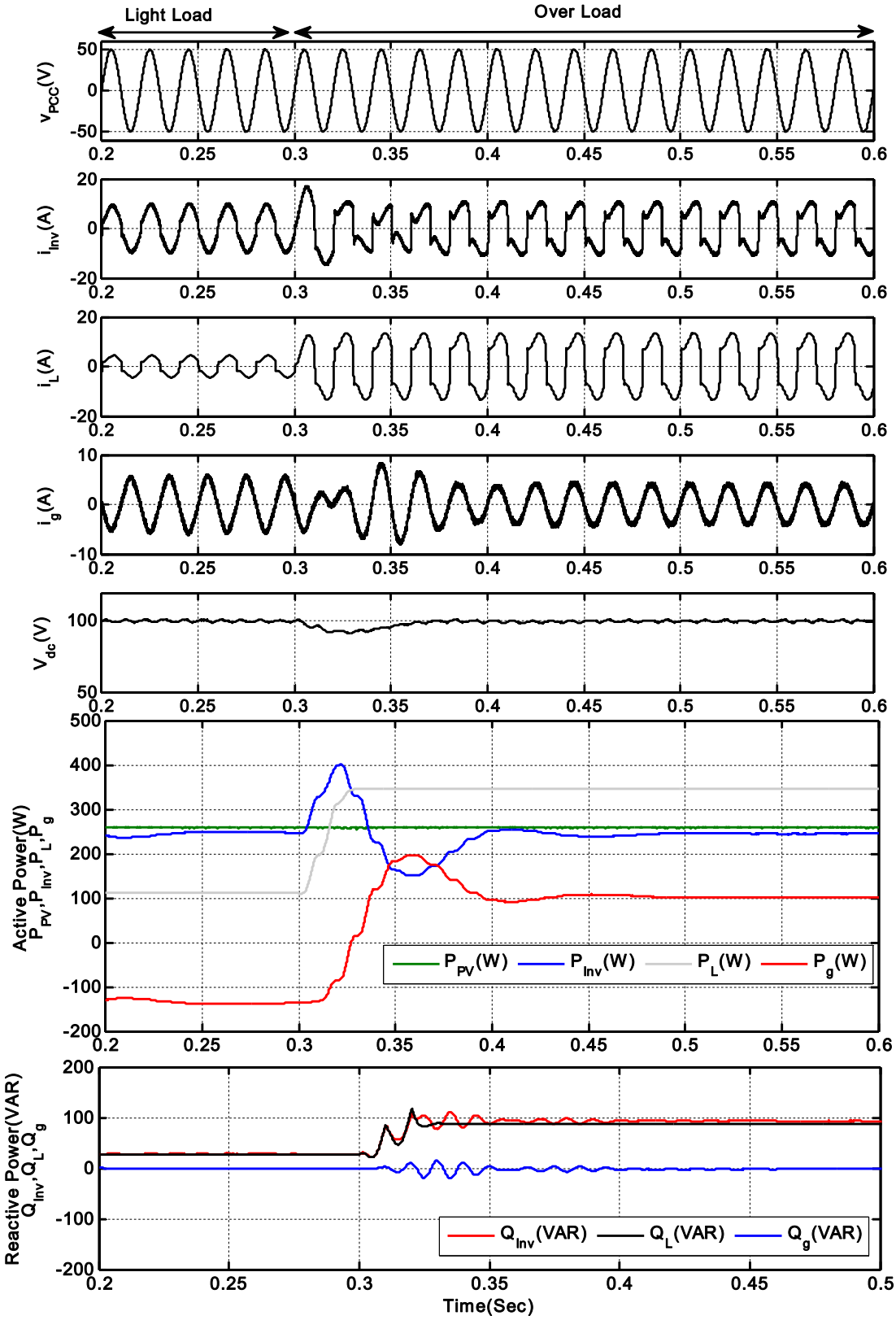

Fig.5.26: Simulation Results based on experimental parameters

B. Two-stage CHBMLI based PVDG system

The steady state waveform of PV CHBMLI output current (i_{inv}), non-linear load current (i_L) and grid current (i_g) during light load and overload condition are shown in Fig.5.27(a) and Fig.5.27(b) respectively. Under light load condition, the rms value of PV inverter current, load current and grid current are found out to be 6.15A, 3.49A and 3.30A respectively. Similarly, under an overload condition, the corresponding rms values of current are recorded as, 7.46 A, 10.8 A and 4.23 A respectively. The transient response of the PVDG system under varying load conditions is shown in Fig.5.27(c) and Fig.5.27(d). At the instant when load current increases, the DC capacitor voltage drops from its reference value to accommodate the enhancement in the load current. This drop in capacitor voltages is restored in 2–3 cycles which demonstrates its good dynamic response. Finally the harmonic spectrum of grid current is given in Fig.5.27(e). It can be observed from these results that the grid current %THD under light and overload conditions are found out to be 5.2 % and 4.6 % respectively.

For the analysis of power under varying load condition, the active power is captured in real time using the control desk developer environment of dSPACE 1104 which is given in Fig.5.27 (f). It is observed from this power curve that under both light load and overload conditions the power generated by the PV inverter is the same which is 210 W. However, in light load condition the load power demand is less which is 110 W. Therefore, the surplus power is fed to the grid, which is recorded as 110 W. Similarly, under overload conditions as the local load demand 350 W, the grid supplied 240 W powers to fulfill the load demand. The grid feeding condition and load sharing condition can be observed by the negative and positive value of grid active power respectively. Similarly, the experimental results of reactive power curves under varying load conditions are shown in Fig.5.27(g). From these results it can be observed that, under both types of loading conditions, the reactive power demanded by the load is completely supplied by the PV CHBMLI and hence the grid reactive power is found to be zero.

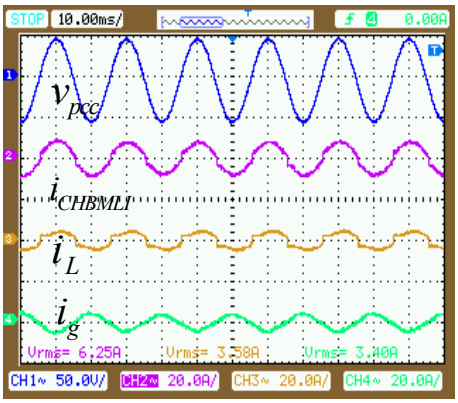

(a)

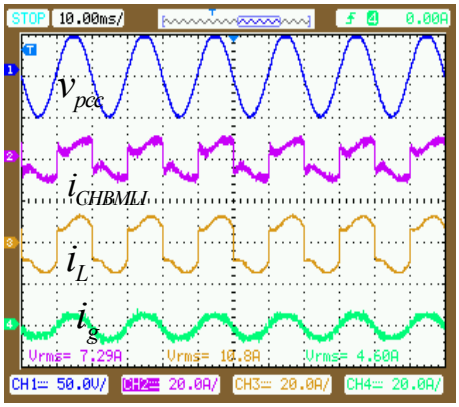

(b)

Fig. 5.27. Steady state response of voltage at PCC, PV CHBMLI current, load current and grid current (a) under light load condition (b) under overload condition

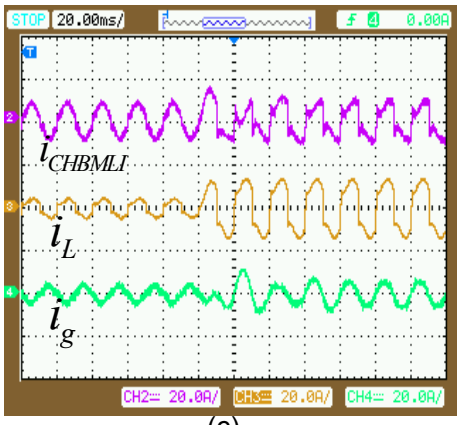

(c)

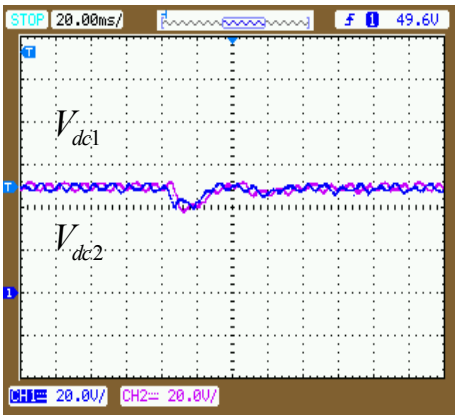

(d)

Fig.5.27 (c) Transient Response of PVDG System during varying load condition (d) DC-link voltages

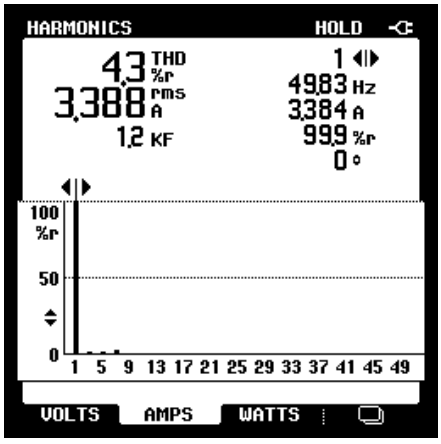

(i)

(e)

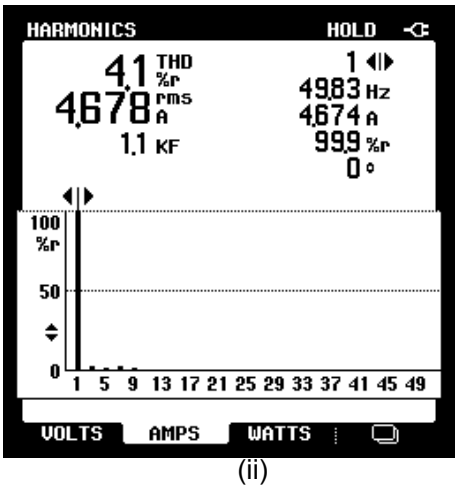

(ii)

Fig.5.27 (e) Harmonic Spectrum of grid current (i) under light load (ii) overload condition

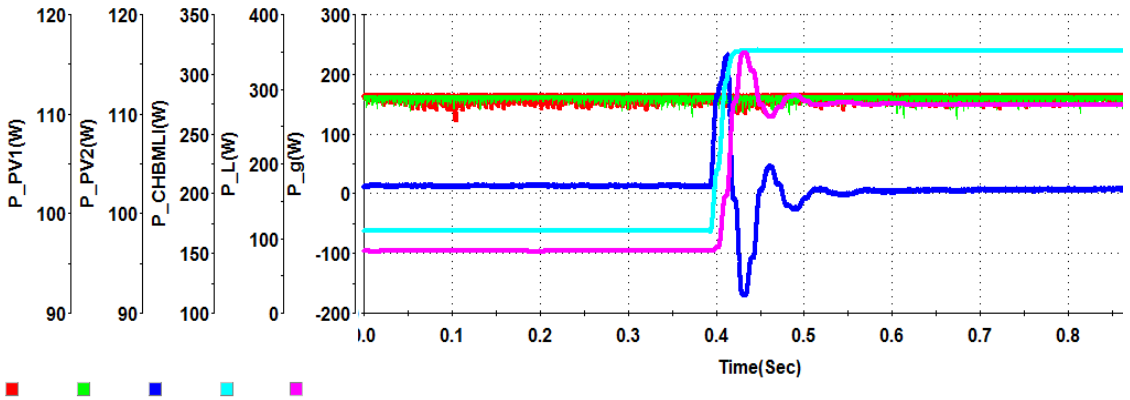

Fig.5.27 (f) Active power curves of PVDG system under varying load conditions

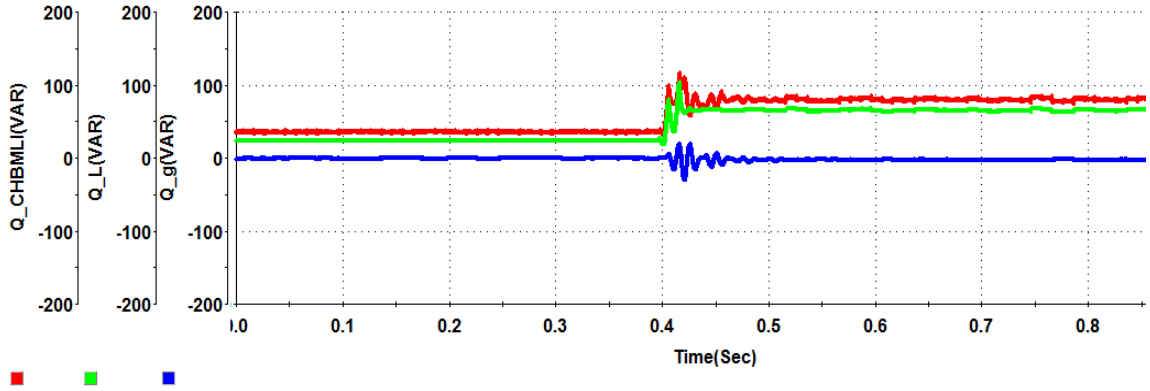

Fig.5.27 (g) Reactive power curves of PVDG system under varying load conditions

Fig.5.27: Experimental results of two-stage CHBMLI based PVDG system under varying load conditions

Finally, to validate the experimental results of two-stage five-level CHBMLI based PVDG system under varying load conditions, the simulation studies have also been carried by using the experimental parameters. The simulated waveforms of voltage at PCC, inverter current, load current, grid current, active and reactive power curves are given in Fig.5.28. From these figures, it can be seen that the simulation results are in good agreement with experimental results for the load varying condition.

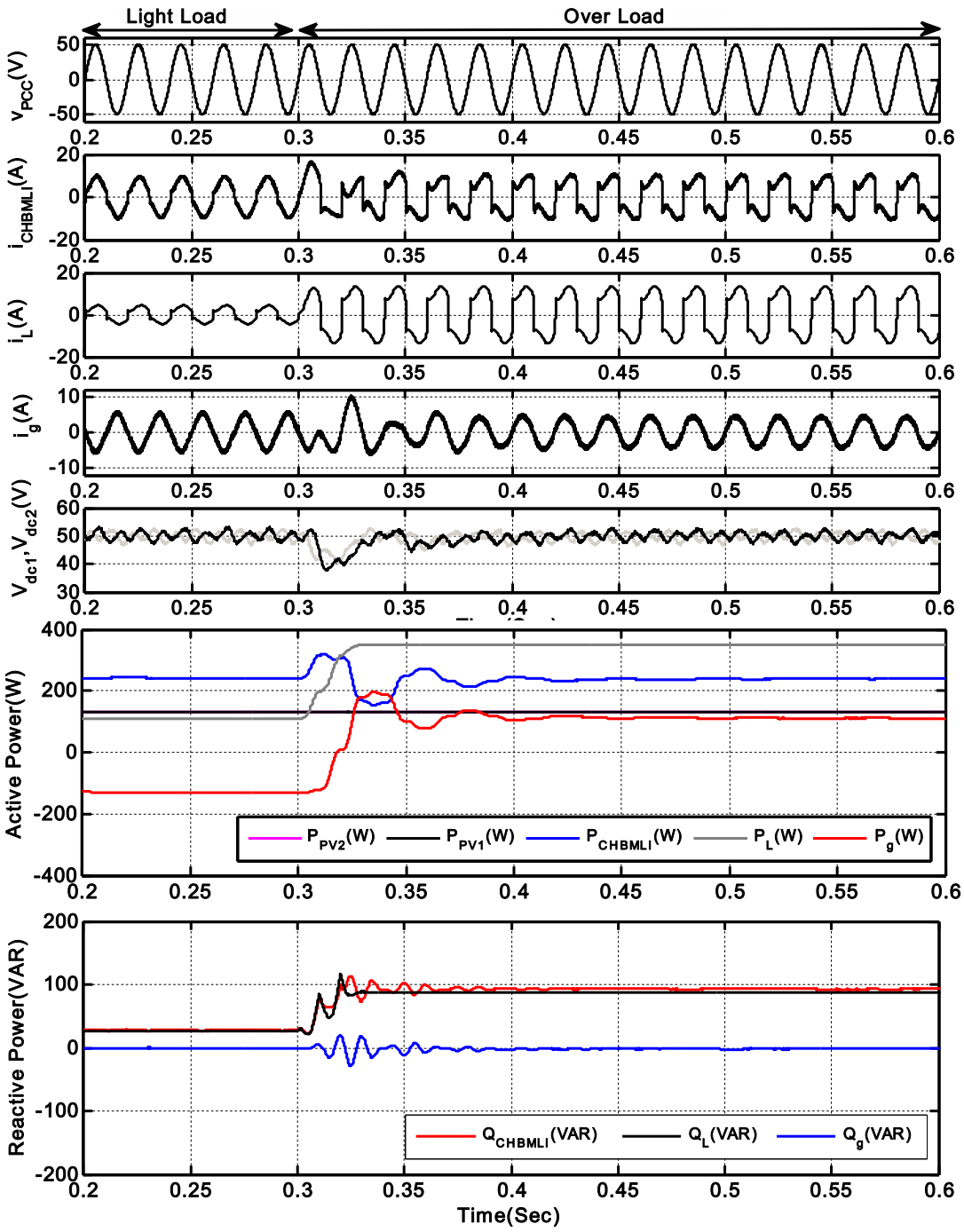

Fig.5.28: Simulation results of CHBMLI based PVDG system under varying load conditions

Table 5.5: Comparison of experimental and simulation results for 2-stage 2-level and 5-level inverter based PVDG system under different modes of operation

Mode of Operation		2-stage 2-level Inverter based PVDG System							2-stage 5-level CHBMLI based PVDG System						
		i_{inv} (A)	i_L (A)	i_g (A)	%THD Of i_g	P_{inv} (W)	P_L (W)	P_g (W)	i_{CHBMLI} (A)	i_L (A)	i_g (A)	%THD Of i_g	P_{CHBMLI} (W)	P_L (W)	P_g (W)
PQEC disabled	Experimental Results	6.09	10.9	6.35	48.40%	207	350	143	6.25	10.9	6.55	46.40%	210	350	140
	Simulation Results	6.98	10.72	5.1	42.58%	241.9	249.9	108	6.85	10.72	5.25	41.67%	246.8	349.6	102.8
PQEC enabled	Experimental Results	7.51	10.9	4.87	4.90%	204	350	146	6.54	10.9	4.67	4.10%	208	350	142
	Simulation Results	7.88	10.72	3.18	4.57%	238.1	349.9	111.8	8.07	10.72	2.97	4.02%	245.6	349.9	104.4
MPPT disabled	Experimental Results	4.93	10.9	8.54	4.40%	65	350	284	5	10.8	8.31	4.10%	68	350	282
	Simulation Results	4.833	10.72	7.42	4.18%	87.82	349.9	262.1	4.83	10.72	7.37	3.98%	89.91	349.9	260
MPPT enabled	Experimental Results	7.59	10.9	4.67	5.40%	203	350	146	7.29	10.8	4.6	4.20%	208	350	142
	Simulation Results	7.88	10.72	3.17	4.68%	238.6	349.9	111.4	8.04	10.72	2.99	4.17%	244.7	349.9	105.3
Light Load	Experimental Results	6.15	3.49	3.3	5.20%	206	111	96 Grid Feeding	6.35	3.67	3.57	4.30%	209	111	98 Grid Feeding
	Simulation Results	6.98	3.72	3.32	4.55%	241.6	110.8	130.8 Grid Feeding	7.06	3.32	3.85	3.95%	246.8	110.8	136 Grid Feeding
Over Load	Experimental Results	7.46	10.8	4.73	4.60%	203	350	147	7.29	10.8	4.6	4.10%	208	350	142
	Simulation Results	7.89	10.72	3.17	4.62%	238.5	349.9	111.5	8.06	10.72	2.96	4.01%	246.6	349.9	104.4

5.3.3 Performance of 1-ϕ single-stage CHBMLI based PVDG System with PQE Scheme

In this part of experimental work, the developed prototypes of single-stage CHBMLI based PVDG system with an enhanced PQ feature is tested under varying load conditions to verify its viability and effectiveness for power transfer, harmonic elimination and reactive power compensation in 1-ϕ DG system. As explained in Chapter.4, in the single stage PVDG system, maximum power extraction from each PV module is accomplished by PV CHBMLI itself. In 5-level CHBMLI topology, two individual PV module output is directly connected across two individual H-bridge cells. Finally, the developed PV CHBMLI output is connected to the PCC with a series connected filter inductor. Similar to two-stage topologies, a 35.8V (50 V peak), 50 Hz grid is developed in the laboratory by using a step down transformer and is interfaced with the PV CHBMLI through an isolation transformer.

All the passive elements used for the development of the above mentioned system such as electrolytic capacitor which is connected across the PV module, the inductor and capacitor for boost converter, coupling inductor connected between PV CHBMLI and PCC are designed as per the procedure discussed in earlier chapters and are chosen as per the market availability. All these parameters used for hardware development are tabulated in Table 5.2. The MPPT and PQE controller are implemented in dSPACE.

To verify the viability and effectiveness of the enhanced PQ based single stage PVDG system for power flow operation, harmonic elimination and reactive compensation, experimental investigations have been conducted with non-linear loads. For the analysis purpose, similar to two-stage topologies which are discussed in the earlier part of this chapter, two different non-linear loads has been considered (load-1 and load -2) which are given in Table.5.1. Fig.5.14 (a) and Fig.5.14 (b) shows the currents drawn by these non-linear loads as well as their harmonic spectrum.

As in case of single-stage CHBMLI based PVDG system, with the PV module is directly connected across the H-bridge cell, there is always a possibility of an input DC-link unbalancing in CHBMLI. The main causes of voltage unbalance in PV application are the partial shading, dust collection and PV ageing. This voltage unbalance in CHBMLI, leads to distortion in the output voltages and currents of the CHBMLI. Therefore, to obtain an optimal output from CHBMLI fed from PV module, the single stage PVDG system is operated with SVM controller which is already discussed in detail in Chapter.4. The experimental validation of single stage CHBMLI based PVDG system is divided into two sections. In section-1, the 1-ϕ SVM scheme for the CHBMLI under both balanced and unbalanced DC-link voltage conditions are experimentally validated and in section-2, the experimental results of enhanced PQ based single stage CHBMLI based PVDG system under varying load conditions is presented.

5.3.3.1 Validation of 1-ϕ space vector modulation scheme

In order to validate the 1-ϕ SVM scheme under both balanced and unbalanced DC voltages, experimental results have been obtained using the developed CHBMLI prototype. The detailed description of the control algorithm has already been presented in Chapter.4. For the experimental validation of SVM, a reference voltage of 28.28 V (40 V (peak)) is chosen and a lamp load is connected at the output terminal of CHBMLI. The switching frequency is selected as 3 kHz. The test is carried out in three different cases of DC-link voltage ratio $(V_{dc1} : V_{dc2})$ of two H-bridge cells, such as 1:1, 2:1 and 3:1. In these three cases, the DC-link voltages are chosen as $V_{dc1} = V_{dc2} = V_{dc} = 30V$, $V_{dc1} = 30V, V_{dc2} = 15V$ and $V_{dc1} = 30V$, $V_{dc2} = 10V$ respectively. The output voltage levels of CHBMLI for the different combinations of voltage vectors of each H-bridge cell are tabulated in Table.5.6. As discussed in chapter.4, the generalized SVM scheme for any DC-voltage ratio is based on the calculation of the control region of the CHBMLI by accounting the instantaneous value of each DC-link capacitor voltages. The evaluation of the switching sequence and the duty cycle is made by using the control region which was determined online. The complete algorithm of SVM is developed in the embedded Matlab function block of MATLAB Simulink software. For the real time implementation, this Simulink model of the SVM schemes of the CHBMLI has been implemented using dSPACE-DS1104 controller. The generated firing pulses have been given to the corresponding semiconductor devices of each H-bridge of the CHBMLI through isolation, delay and pulse amplification circuits. The experimental results of duty cycle for H-bridge-1, H-bridge-2 and the switching pulses generated by the SVM controller is given in Fig. 5.29(a). The output voltage and its harmonic spectrum of CHBMLI for the three above mentioned cases of voltage ratio are shown in Fig. 5.30. For the DC voltage ratio of 1:1, with, the output modulated voltage and its harmonic spectrum are shown in sub-figure (i) and (ii) of Fig. 5.30(a) respectively. Under this condition, the number of levels in the output voltage is found to be 5. The rms value of output voltage and its THD are found to be 28.27 V and 8.2% respectively. The harmonic spectrum of the output voltage is captured by Fluke 43 B power quality analyzer. One of the limitations of this power analyzer is that, it calculates the THD of a signal by considering up to 2500 Hz frequency. Therefore, in this case the THD of the output voltage up to 2500 Hz frequency is presented even though the switching frequency is considered as 3 kHz.

Table.5.6: Output voltage of two cells CHBMLI with 1:1, 2:1 and 3:1 DC-link Voltage ratio

State of upper H-bridge (H-1)	State of lower H-bridge (H-2)	Output Voltage		
		Case-1 DC-link voltage ratio 1:1	Case-2 DC-link voltage ratio 1:2	Case-3 DC-link voltage ratio 1:3
0	0	-60	-45	40
0	1	-30	-30	-30
1	0		-15	-10
0	2	0	-15	-20
1	1		0	0
2	0		15	20
1	2	30	15	10
2	1		30	30
2	2	60	45	40

Similarly, for the unbalanced condition, with $V_{dc1} = 30V, V_{dc2} = 15V$ (i.e. the DC-link voltage ratio of 2:1), the output modulated voltage and its harmonic spectrum are shown in sub-figure (i) and (ii) of Fig.5.30 (b) respectively. In this case the number of levels of the output voltage waveform has increased from 5 (in case of 1:1) to 7. With the increment in number of levels, the THD of out voltage waveform is reduced from 8.2% (in case of 1:1) to 5%. Similar to the previous case, the rms value of output voltage found to be 28.27 V which is follow the reference voltage.

Finally, the experimental results of output voltage and its harmonic spectrum for the DC voltage ratio of 3:1, with $V_{dc1} = 30, V_{dc2} = 10V$ is presented in a sub-figure (i) and (ii) of Fig.5.30 (c) respectively. In this case the number of levels of the output voltage waveform is increased to 9 and with this increase in number of levels; the THD of out voltage waveform is found to be 3.2%. Therefore, using this modulation scheme, any DC voltage ratio in the CHBMLI input can be accommodated in the modulation process to generate the reference voltage. The SVM controller determines the best output voltage of the CHBMLI and this voltage is generated by the controller even under extreme DC-link voltage unbalance situations.

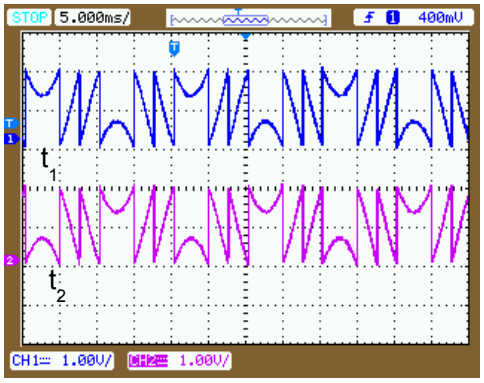

(a)

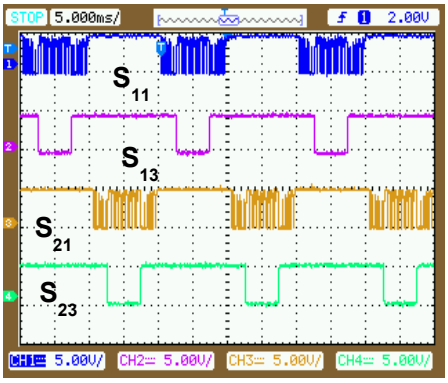

(b)

Fig.5.30(a) Duty cycle for upper and lower H-bridge switching vector(b) switching pulses

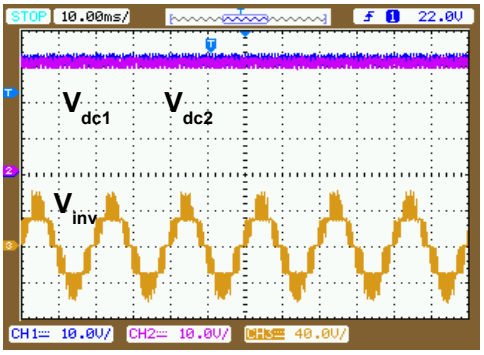

(a)

(i)

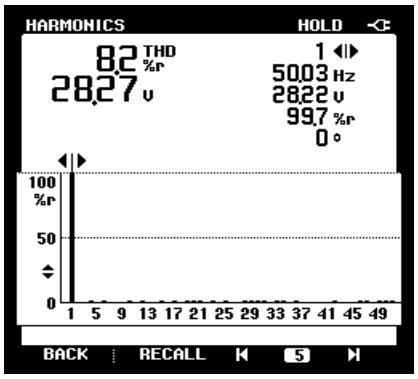

(b)

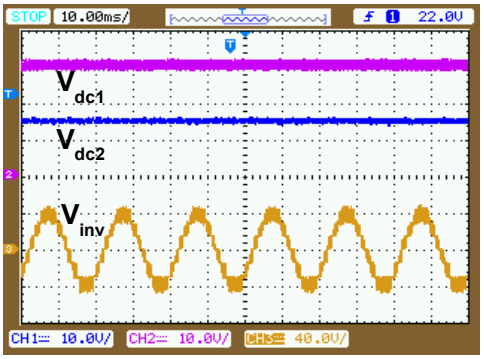

(a)

(ii)

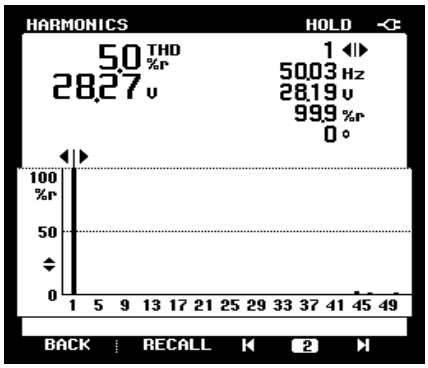

(b)

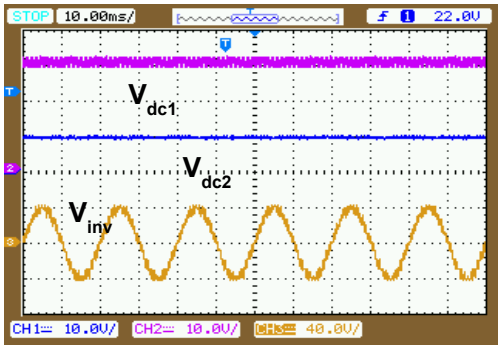

(a)

(iii)

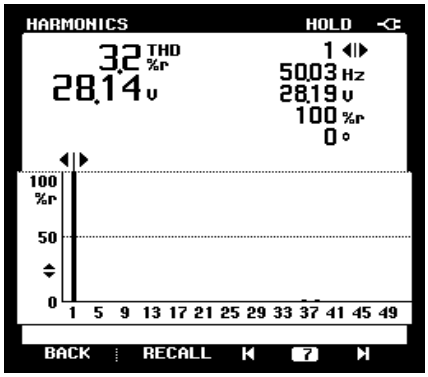

(b)

Fig.5.31: Output voltage and its harmonic spectrum of CHBMLI when the DC-link voltage ratio is (i) 1:1 (ii) 2:1 (iii) 3: 1

5.3.3.2 Experimental Validation of single stage CHBMLI based PVDG system under load varying condition

The experimental results of enhanced PQ based single stage PVDG system under varying load condition is shown in Fig.5.32. The test is performed while employing the PQEC and MPPT controller in enabled mode. To study the steady and dynamic performance of the above mentioned topologies of PVDG system, under varying load condition, load-1 is initially connected across the PV inverter and a few second later load-1 is disconnected and load-2 is connected across the PCC and based on the experimental results following observations are made,

1. With load-1 is connected across the PCC, the load current demand is found to be less than that generated by the PV CHBMLI and hence, the surplus current is fed to the grid. With the PQEC is in enabled mode, the PV CHBMLI generates a non-sinusoidal current to compensate the load harmonics as well as supply the reactive component of current demanded by the load.
2. Similarly, when the load is increased to create an overload condition, the load current demand is found to be more than that generated by PV CHBMLI and hence, the rest of the load current demand is met by the grid. Similar to a previous condition, the harmonic components of the load current still continue to be supplied by the PV CHBMLI thereby making the grid current purely sinusoidal.

The steady state waveform of PV CHBMLI output current (i_{CHBMLI}), non-linear load current (i_L) and grid current (i_g) during light load and overload condition is shown in Fig.5.32(a) and Fig.5.32(b) respectively. It can be observed from Fig.5.32(a) that under light load condition, i_g is out of phase from i_{CHBMLI}, which means that the surplus generated PV CHBMLI current is fed to the grid. However, with overload condition, all three currents are found to be in the same phase. This is because; the PV generation is less than the local load demand. Hence the load demand is fulfilled by both PV CHBMLI and the grid. Under light load condition, the rms values of PV CHBMLI current, load current and grid current are found out to be 6.35A, 3.67A and 3.67A respectively. Similarly, under an overload condition, the corresponding rms values of current are recorded as, 7.25A, 10.9A and 4.23 A respectively. The transient response of the PVDG system under varying load condition is shown in Fig.5.32(c) and Fig.5.32(d). At the instant when load current increases, the DC capacitor voltage drops from its reference value to accommodate the enhancement in the load current. This drop in capacitor voltages are restored in 5–6 cycles. Finally the harmonic spectrum of grid current under light and overload condition is given in Fig.5.32(e). It can be observed from these results that the grid current %THD under light and overload conditions are found out to be 4.3 % and 4.2 % respectively. For the analysis of power under varying load condition, the active power is captured in real time using the control desk developer environment of

dSPACE 1104 which is given in Fig.5.32(f). It is observed from this power curve that under both light load and overload conditions the power generated by the PV CHBMLI is the same which is 216 W. However, in light load condition the load power demand is less which is 110 W. Therefore, the surplus power is fed to the grid, which is recorded as 116 W. Similarly, under overload conditions as the local load demand 350 W, the grid supplied 234 W powers to fulfill the load demand. The grid feeding condition and load sharing condition can be observed by the negative and positive value of grid active power respectively. If we compare the generated PV CHBMLI power output of a single-stage system with that of a two-stage system, it can be observed that there is a significant increase in power generation in the single stage system. This is due to the absence of power losses associated across the DC-DC converter in case of two-stage system. Similarly, the experimental results of reactive power curves under varying load conditions are shown in Fig.5.32(g). From these results it is observed that, under both types of loading conditions, the reactive power demanded by the load is completely supplied by the PV CHBMLI and hence the grid reactive power is found to be zero.

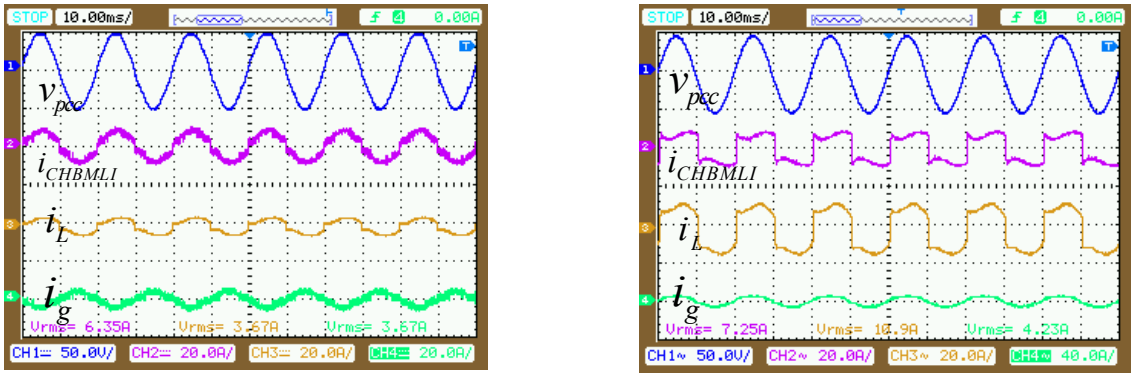

(a) (b)

Fig.5.32. Steady state waveform of voltage at pcc, PV CHBMLI current, load current and grid current (a)under light load condition (b) under overload condition

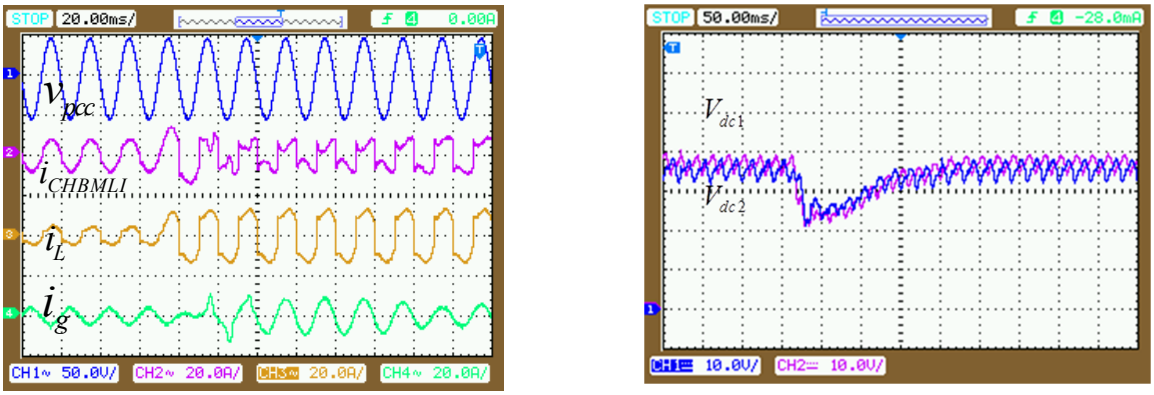

(c) (d)

Fig.5.32. Transient Response of PVDG System during varying load condition (c) current waveforms (d) DC-link voltage waveforms

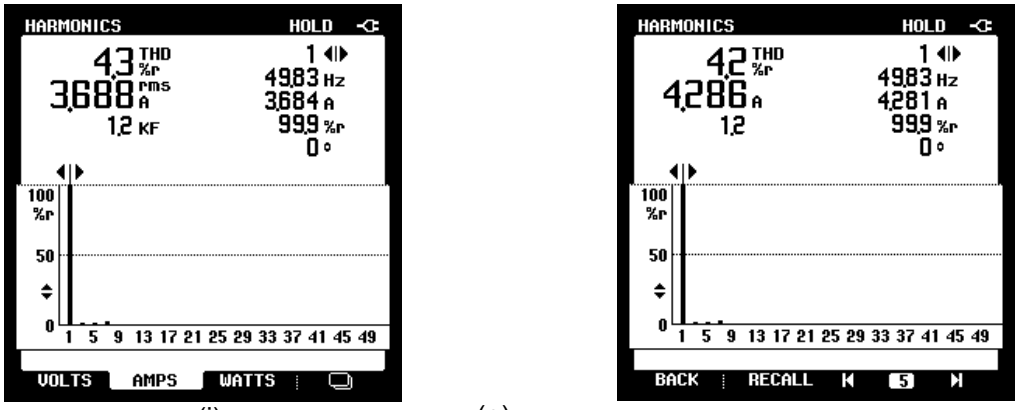

(i) (e) (ii)

Fig.5.32(e) Harmonic Spectrum of grid current (i) Before compensation (ii) after compensation

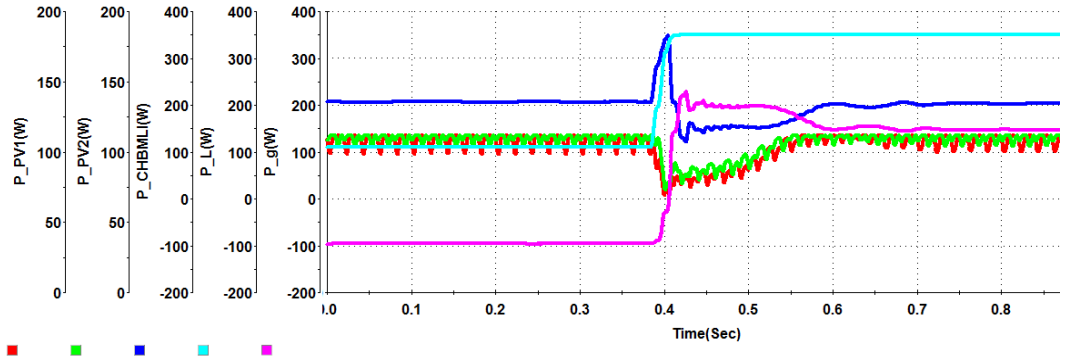

Fig.5.32(f) Active power curves under varying load conditions

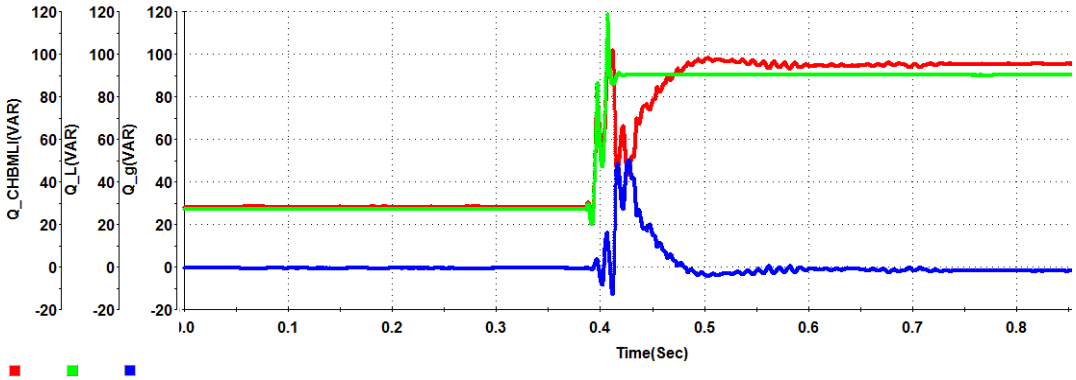

Fig.5.32(g) Reactive power curves under varying load conditions

Fig.5.32: Experimental results of single stage CHBMLI based PVDG system under varying load condition

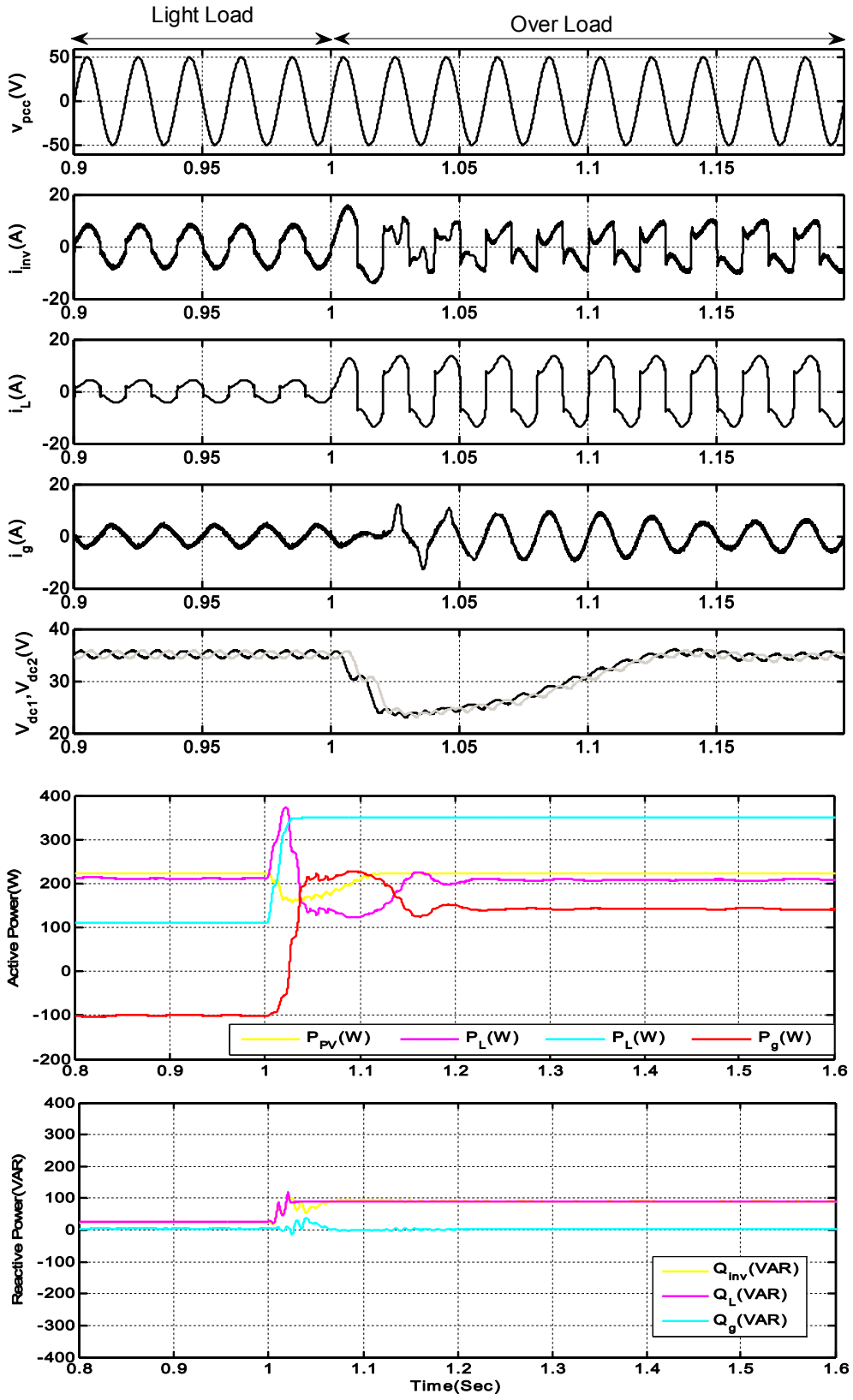

Fig.5.33:Simulation results of single stage CHBMLI based PVDG system under varying load conditions

5.4 Conclusion

In this chapter, the detailed descriptions of the design and development of laboratory prototype of two-stage 2-level inverter, two-stage and single stage CHBMLI based PVDG system have been given.

In the first part of the experimental work, the developed power circuits of two-stage 2-level inverter and 5-level CHBMLI based PVDG system has been tested for optimal power transfer, reactive power compensation and harmonic elimination under different loading and controller action. The steady-state and transient performances of the PVDG system have been found to be satisfactory with both 2-level and multi-level topologies. A smooth control of DC voltages of H-bridge cells ensured the effectiveness of the DC voltage controller in both 2-level and multilevel topologies. It is also observed that with the CHBMLI based PVDG system, the active power injection at PCC is more compared to 2-level inverter topology. Further, the experimental results of both the topologies under different modes of operation are validated with simulation results by using the experimental parameters. Finally a comparative analysis is made between two-stage 2-level and CHBMLI based PVDG system and from this it is observed that the power generation in the CHBMLI based PVDG system is slightly more compared to two-level topology. Similarly, the % THD of grid current is found to be more improved in case of CHBMLI topology compared to 2-level topology.

In the second part of the experimental work, a single stage CHBMLI based PVDG system is tested for MPPT, reactive power compensation and harmonic elimination under varying load conditions. In this topology, each H-bridge cell of CHBMLI is directly connected across the PV module. Because of the absence of intermediate DC-DC converter between the PV module and the CHBMLI, there is always a chance of DC-link unbalance in the CHBMLI. This is due to the partial shadow condition or dust collection on the PV module. This DC-link unbalance leads to distorted output voltage and current in the CHBMLI output. In order to overcome from such type of unbalancing problem in CHBMLI system, a single phase SVM is implemented. The developed single-stage CHBMLI power circuit has been tested initially as a DC-AC inverter to experimentally validate the efficacy of the SVM scheme under balanced and unbalanced DC-link voltage conditions. Three different cases of DC-link voltage ratio has been chosen and the output voltages and their corresponding harmonic spectrum of the CHBMLI have been observed to be improved even under highly unbalanced input condition. Finally, the single-stage PVDG system with the PQE features and MPPT capability is tested under varying load condition. The steady-state and transient performance of the single-stage PVDG system is found to be satisfactory with single phase space vector modulation scheme. Further, the experimental results are validated with simulation results by using the experimental parameters. In the absence of DC-DC converter the single stage system is still found to be operating at MPP of the PV modules. The PV inverter output power in case of single stage system is found to be more than two stage topology.

[The main conclusions of the presented work and possible future research have been summarized in this chapter]

6.1 Conclusion

In this work, a 1-ϕ improved PQ based PVDG system has been proposed. The major conclusions starting from modeling of PV module to interconnection with a grid with improved PQ features derived from this work are summarized one by one as follows:

1. In the first step of the research work, a simplified approach of PV modeling under varying atmospheric conditions is presented. All the required parameters for the modeling purpose are not provided by the manufacturer, and for this, a step by step approach for parameter determination of the unknown parameters is presented. Here Gauss-Seidel based iterative method is used to determine the equivalent model parameters of the PV array. In order to validate the effectiveness of the aforementioned modeling scheme of PV module, a simulation program is developed in Matlab Simulink. The $P-V$ and $I-V$ characteristics of PV module for different temperatures, irradiations and circuit resistances were plotted and validated with the manufacturer's datasheet.
2. The output power produced by the PV module is depends on atmospheric conditions. Therefore, to maximize the efficiency of the PV module, it is necessary to track the MPP of the PV module. A fuzzy based MPPT controller is presented to improve the power extraction process. A simulation is carried out to make a comparative analysis between the conventional P&O method and fuzzy based MPPT.
3. For this MPPT control boost converter is used. The performance of the MPPT control is vastly depends on the DC-DC converter control and its ability to regulate the operating point of the PV module. The converter transfer function for the input voltage control of the boost converter with duty cycle control is developed. This transfer function revealed important dynamic characteristics of the input controlled boost converter when it is fed from a PV module. Finally, with the help of this converter transfer function, a controller for the PV module is designed.
4. In a PVDG system, the quality of the grid current is decided by the load. A PQE scheme for the control of reactive power as well as harmonic current elimination in a 1-ϕ PVDG system is presented. The 2-level PV inverter with the proposed control scheme is utilized to inject the generated PV power to the grid with an integrated shunt APF capability to eliminate the need of an extra converter for the power quality improvement at PCC. The idle state of PV inverter at night time leads to the underutilization of such an expensive system. This issue of PVDG system has also been considered and hence, the concept of the utilization of the PV inverter as a shunt APF during night time has also been presented. Rigorous simulation study under different conditions such as with and without

PQEC, light and overload condition, low and high solar irradiation level, and night mode operation are presented to demonstrate the effectiveness of this system.

5. The CHBMLI based topology features several advantages such as generation of high quality currents, the capacity to operate at a lower switching frequency than two-level topology and the modularity. A 1-ϕ two-stage and single-stage CHBMLI based PVDG system with an improved PQ features is presented. The current control scheme of PV CHBMLI includes a compensating current generator based on IRP theory to obtain the aforementioned objective. Both two-stage and single-stage PVDG system is control in such a way to inject the maximum PV power to the grid while compensating the load reactive power and harmonic components. Exhaustive simulation results are presented to investigate the performance of the PVDG system during varying atmospheric as well as varying load conditions. With single-stage topology, the need of DC-DC converter for MPPT is eliminated. This leads to more power injection to the grid as compared to two-stage system. The performance of both two-stage and single-stage PVDG system along with harmonic and reactive power compensation has been found satisfactory and meeting IEEE standards for PVDG system.
6. In the last part of the work, a detailed description for the design and development of laboratory prototype of two-stage 2-level inverter, two-stage and single stage CHBMLI based PVDG system have been presented. A DSP DS1104 of dSPACE has been used for the real-time implementation of various control algorithms in the PVDG system in MATLAB/Simulink software. In the first part of the experimental work, the developed power circuits of two-stage 2-level inverter and 5-level CHBMLI based PVDG system has been tested for optimal power transfer, reactive power compensation and harmonic elimination under different loading and controller actions. The steady-state and transient performances of the PVDG system have been found to be satisfactory with both 2-level and multi-level topologies. It is observed that with CHBMLI based PVDG system, the active power injection at PCC is slightly more compared to 2-level inverter topology. Further, the experimental results of both the topologies under different modes of operation are validated with simulation results by using the experimental parameters.
7. In the second part of the experimental work, the single stage CHBMLI based PVDG system is tested for maximum power point tracking, reactive power compensation and harmonic elimination under varying load conditions. In this topology, each H-bridge cell of CHBMLI is directly connected across the PV module. Because of the absence of intermediate DC-DC converter between the PV module and the CHBMLI, there is always a chance of DC-link unbalance in the CHBMLI which leads to distorted output voltage and current in the CHBMLI output. In order to overcome from such type of unbalancing problem in CHBMLI system, a single phase SVM is implemented. The developed single-stage CHBMLI power circuit has been tested initially as a DC-AC inverter to

experimentally validate the efficacy of the SVM scheme under balanced and unbalanced DC-link voltage conditions. Finally, the whole single-stage PVDG system with the PQE features and MPPT capability is tested under varying load condition. The steady-state and transient performance of the single-stage PVDG system is found to be satisfactory with single phase SVM scheme.

6.2 Future Scope

The research work presented in this thesis discloses a number of issues that could be further investigated.

1. Practical implementation of multilevel inverters for high power applications is still an active area of research. The development of high power inverters involves a higher number of levels, large number of devices, complex control, large size and higher cost. Intensive research needs to be done on developing new multilevel inverter topologies with reduced number of components, low THD and high reliability.
2. Development of new modulation techniques for high power inverters with reduced power losses and natural balance of capacitor voltages is a potential area of research.
3. The conventional PI controller of the PVDG control system can be replaced by soft computing techniques such as fuzzy logic, neural network, and genetic algorithms to further improve the transient response of the system.
4. Design of the controller of the PVDG using advanced control techniques such as model predictive control is an active area of research.
5. Another interesting topic could be the research on the combination of APF and passive harmonic filters. This research could include the selection of topology, inspection of compensating characteristics, losses, cost and rating of the individual and overall compensator.
6. The integration of the PQ features has the drawback that the PV inverter will also deliver the harmonic compensation current with the direct consequences of increase the PV inverter overall current and cost. A current limitation strategy has to be implemented and if the PV inverter output current exceeds the switch rating, then the supplied harmonic current must be reduced. The analysis of inverter design that takes into account the current required for reactive power and harmonic compensation can be a subject of future study.

Journals

1. Aurobinda Panda, M.K. Pathak, S.P. Srivastava, “Enhanced Power Quality Based Single Phase Photovoltaic Distributed Generation System”, International Journal of Electronics, Taylor and Francis. (Accepted for publication).
2. Aurobinda Panda, M.K. Pathak, S.P. Srivastava, “A Single Phase Photovoltaic Inverter Control for Grid Connected System”, SADHANA, Springer. (Submitted after 2nd minor revision).
3. Aurobinda Panda, M.K. Pathak, S.P. Srivastava, “Fuzzy Intelligent Controller for the Maximum Power Point Tracking of a Photovoltaic Module at Varying Atmospheric Conditions,” Journal of Energy Technologies and policy, vol.1,no.2,pp.18-27,2011.
4. Aurobinda Panda, M.K. Pathak, S.P. Srivastava, “Feed-forward SVM Scheme for a 1-ϕ CHBMLI based PVDG system with an Integrated Power Quality Features”, Electrical Power components and systems, Taylor and Francis. (Minor revision).
5. Aurobinda Panda, M.K. Pathak, S.P. Srivastava, “An Integrated Power Quality Enhancement Scheme For a 1-ϕ 5-level CHBMLI Based Photovoltaic Distributed Generation System”, SADHANA, Springer. (Under Review).
6. Aurobinda Panda, M.K. Pathak, S.P. Srivastava, “Interval Type-2 Fuzzy Based Photovoltaic Distributed Generation System with Enhanced Power Quality”, IETE Journal of research, Taylor and Francis. (Under Review).
7. Aurobinda Panda, M.K. Pathak, S.P. Srivastava, “Power Quality Enhancement schemes in CHBMLI Based 1-ϕ Photovoltaic Distributed Generation System”, Electrical Power components and systems, Taylor and Francis (Under Review).

International conferences

8. Panda, A.; Pathak, M.K.; Srivastava, S.P., "An improved power converter for standalone Photovoltaic system," Annual IEEE India Conference (INDICON), pp.1-6, 13-15 Dec. 2013.

9. Panda, A.; Pathak, M.K.; Srivastava, S.P., "Grid tie inverter control for rooftop photovoltaic system," IEEE Fifth Power India Conference, pp.1-6, 19-22 Dec. 2012.

[1] I. Statistics, "CO2 Emissions From Fuel Combustion Highlights 2013," *IEA, Paris Cited July,* 2014.

[2] I. PVPS, "Trends in photovoltaic applications. Survey report of selected IEA countries between 1992 and 2011," *Report IEA-PVPS T1–21,* 2012.

[3] C. S. Solanki, *Renewable energy technologies: A practical guide for beginners*: PHI Learning Pvt. Ltd., 2008.

[4] M. Singh, K. Thirugnanam, P. Kumar, and I. Kar, "Real-Time Coordination of Electric Vehicles to Support the Grid at the Distribution Substation Level," *IEEE Systems Journal,* vol. PP, no. 99, pp. 1-11, 2013.

[5] H. Gil and G. Joos, "Models for quantifying the economic benefits of distributed generation," *IEEE Transactions on Power Systems,* vol. 23, no. 2, pp. 327-335, 2008.

[6] P. Kumar, S. Suryateja, G. Naveen, M. Singh, and P. Kumar, "Smart home energy management with integration of PV and storage facilities providing grid support," in *IEEE Power and Energy Society General Meeting (PES)*, 2013, pp. 1-5.

[7] T. Ackermann, G. Andersson, and L. Söder, "Distributed generation: a definition," *Electric power systems research,* vol. 57, no. 3, pp. 195-204, 2001.

[8] A. Poullikkas, "Implementation of distributed generation technologies in isolated power systems," *Renewable and Sustainable Energy Reviews,* vol. 11, no. 1, pp. 30-56, 2007.

[9] W. El-Khattam and M. Salama, "Distributed generation technologies, definitions and benefits," *Electric power systems research,* vol. 71, no. 2, pp. 119-128, 2004.

[10] G. Pepermans, J. Driesen, D. Haeseldonckx, R. Belmans, and W. D'haeseleer, "Distributed generation: definition, benefits and issues," *Energy policy,* vol. 33, no. 6, pp. 787-798, 2005.

[11] W. Kramer, S. Chakraborty, B. Kroposki, and H. Thomas, "Advanced power electronic interfaces for distributed energy systems," *National Renewable Energy Laboratory, Cambridge, MA Rep. NREL/Tp–581–42672,* vol. 1, 2008.

[12] J. V. Paatero and P. D. Lund, "Effects of large-scale photovoltaic power integration on electricity distribution networks," *Renewable Energy,* vol. 32, no. 2, pp. 216-234, 2007.

[13] R. Teodorescu, M. Liserre, and P. Rodriguez, *Grid converters for photovoltaic and wind power systems* vol. 29: John Wiley & Sons, 2011.

[14] J. J. Bzura, "Photovoltaic research and demonstration activities at New England Electric," *IEEE Transactions on Energy Conversion,* vol. 10, no. 1, pp. 169-174, 1995.

[15] B. H. Chowdhury and A. W. Sawab, "Evaluating the value of distributed photovoltaic generations in radial distribution systems," *IEEE Transactions on Energy Conversion,* vol. 11, no. 3, pp. 595-600, 1996.

[16] M. Dai, M. N. Marwali, J.-W. Jung, and A. Keyhani, "Power flow control of a single distributed generation unit," *IEEE Transactions on Power Electronics,* vol. 23, no. 1, pp. 343-352, 2008.

[17] S. Jain and V. Agarwal, "An integrated hybrid power supply for distributed generation applications fed by nonconventional energy sources," *IEEE Transactions on Energy Conversion,* vol. 23, no. 2, pp. 622-631, 2008.

[18] A. Canova, L. Giaccone, F. Spertino, and M. Tartaglia, "Electrical impact of photovoltaic plant in distributed network," *IEEE Transactions on Industry Applications,* vol. 45, no. 1, pp. 341-347, 2009.

[19] D. S. Chan and J. C. Phang, "Analytical methods for the extraction of solar-cell single- and double-diode model parameters from IV characteristics," *IEEE Transactions on Electron Devices,* vol. 34, no. 2, pp. 286-293, 1987.

[20] J. Gow and C. Manning, "Development of a photovoltaic array model for use in power-electronics simulation studies," in *IEE Proceedings Electric Power Applications*, 1999, pp. 193-200.

[21] E. Dallago, D. Finarelli, and P. Merhej, "Method based on single variable to evaluate all parameters of solar cells," *Electronics letters,* vol. 46, no. 14, pp. 1022-1024, 2010.

[22] Y. J. Wang and P. C. Hsu, "Analytical modelling of partial shading and different orientation of photovoltaic modules," *IET Renewable Power Generation* vol. 4, no. 3, pp. 272-282, 2010.

[23] D. Sera, R. Teodorescu, and P. Rodriguez, "PV panel model based on datasheet values," in *IEEE International Symposium on Industrial Electronics*, 2007, pp. 2392-2396.

[24] K. Zweibel, J. Mason, and V. Fthenakis, "A solar grand plan," *Scientific American,* vol. 298, no. 1, pp. 64-73, 2008.

[25] M. G. Villalva and J. R. Gazoli, "Comprehensive approach to modeling and simulation of photovoltaic arrays," *IEEE Transactions on Power Electronics,* vol. 24, no. 5, pp. 1198-1208, 2009.

[26] N. D. Benavides and P. L. Chapman, "Modeling the effect of voltage ripple on the power output of photovoltaic modules," *IEEE Transactions on Industrial Electronics,* vol. 55, no. 7, pp. 2638-2643, 2008.

[27] R. C. Campbell, "A circuit-based photovoltaic array model for power system studies," in *39th North American Power Symposium*, 2007, pp. 97-101.

[28] A. Al Amoudi and L. Zhang, "Application of radial basis function networks for solar-array modelling and maximum power-point prediction," in *IEE Proceedings on Generation, Transmission and Distribution*, 2000, pp. 310-316.

[29] H. Patel and V. Agarwal, "MATLAB-based modeling to study the effects of partial shading on PV array characteristics," *IEEE Transactions on Energy Conversion,* vol. 23, no. 1, pp. 302-310, 2008.

[30] Y. J. Wang and P. C. Hsu, "Analysis of partially shaded PV modules using piecewise linear parallel branches model," *World Academy of Science, Engineering and Technology,* vol. 60, pp. 783-789, 2009.

[31] T. Esram and P. L. Chapman, "Comparison of photovoltaic array maximum power point tracking techniques," *IEEE TRANSACTIONS ON ENERGY CONVERSION* vol. 22, no. 2, p. 439, 2007.

[32] M. Veerachary, T. Senjyu, and K. Uezato, "Neural-network-based maximum-power-point tracking of coupled-inductor interleaved-boost-converter-supplied PV system using fuzzy controller," *IEEE Transactions on Industrial Electronics,* vol. 50, no. 4, pp. 749-758, 2003.

[33] N. Femia, G. Petrone, G. Spagnuolo, and M. Vitelli, "Optimization of perturb and observe maximum power point tracking method," *IEEE Transactions on Power Electronics,* vol. 20, no. 4, pp. 963-973, 2005.

[34] D. Casadei, G. Grandi, and C. Rossi, "Single-phase single-stage photovoltaic generation system based on a ripple correlation control maximum power point tracking," *IEEE Transactions on Energy Conversion,* vol. 21, no. 2, pp. 562-568, 2006.

[35] T. Esram, J. W. Kimball, P. T. Krein, P. L. Chapman, and P. Midya, "Dynamic maximum power point tracking of photovoltaic arrays using ripple correlation control," *IEEE Transactions on Power Electronics,* vol. 21, no. 5, pp. 1282-1291, 2006.

[36] I.-S. Kim, M.-B. Kim, and M.-J. Youn, "New maximum power point tracker using sliding-mode observer for estimation of solar array current in the grid-connected photovoltaic system," *IEEE Transactions on Industrial Electronics,* vol. 53, no. 4, pp. 1027-1035, 2006.

[37] L.-R. Chen, C.-H. Tsai, Y.-L. Lin, and Y.-S. Lai, "A biological swarm chasing algorithm for tracking the PV maximum power point," *IEEE Transactions on Energy Conversion,* vol. 25, no. 2, pp. 484-493, 2010.

[38] T. L. Kottas, Y. S. Boutalis, and A. D. Karlis, "New maximum power point tracker for PV arrays using fuzzy controller in close cooperation with fuzzy cognitive networks," *IEEE Transactions on Energy Conversion,* vol. 21, no. 3, pp. 793-803, 2006.

[39] L. Piegari and R. Rizzo, "Adaptive perturb and observe algorithm for photovoltaic maximum power point tracking," *IET Renewable Power Generation,* vol. 4, no. 4, pp. 317-328, 2010.

[40] T. Senjyu and K. Uezato, "Feedforward maximum power point tracking of PV systems using fuzzy controller," *IEEE Transactions on Aerospace and Electronic Systems,* vol. 38, no. 3, pp. 969-981, 2002.

[41] K. Kobayashi, I. Takano, and Y. Sawada, "A study of a two stage maximum power point tracking control of a photovoltaic system under partially shaded insolation conditions," *Solar energy materials and solar cells,* vol. 90, no. 18, pp. 2975-2988, 2006.

[42] H. Patel and V. Agarwal, "Maximum power point tracking scheme for PV systems operating under partially shaded conditions," *IEEE Transactions on Industrial Electronics,* vol. 55, no. 4, pp. 1689-1698, 2008.

[43] O. Wasynczuk, "Modeling and dynamic performance of a line-commutated photovoltaic inverter system," *IEEE Transactions on Energy Conversion,* vol. 4, no. 3, pp. 337-343, 1989.

[44] O. Wasynczuk and N. Anwah, "Modeling and dynamic performance of a self-commutated photovoltaic inverter system," *IEEE Transactions on Energy Conversion,* vol. 4, no. 3, pp. 322-328, 1989.

[45] H. Asano, K. Yajima, and Y. Kaya, "Influence of photovoltaic power generation on required capacity for load frequency control," *IEEE Transactions on Energy Conversion,* vol. 11, no. 1, pp. 188-193, 1996.

[46] Y. T. Tan, D. S. Kirschen, and N. Jenkins, "A model of PV generation suitable for stability analysis," *IEEE Transactions on Energy Conversion,* vol. 19, no. 4, pp. 748-755, 2004.

[47] J. T. Bialasiewicz, "Renewable energy systems with photovoltaic power generators: Operation and modeling," *IEEE Transactions on Industrial Electronics,* vol. 55, no. 7, pp. 2752-2758, 2008.

[48] M. E. Ropp and S. Gonzalez, "Development of a MATLAB/simulink model of a single-phase grid-connected photovoltaic system," *IEEE Transactions on Energy Conversion,* vol. 24, no. 1, pp. 195-202, 2009.

[49] K. El-Arroudi, G. Joós, I. Kamwa, and D. T. McGillis, "Intelligent-based approach to islanding detection in distributed generation," *IEEE Transactions on Power Delivery,* vol. 22, no. 2, pp. 828-835, 2007.

[50] S. Samantaray, K. El-Arroudi, G. Joós, and I. Kamwa, "A fuzzy rule-based approach for islanding detection in distributed generation," *IEEE Transactions on Power Delivery,* vol. 25, no. 3, pp. 1427-1433, 2010.

[51] B. H. Chowdhury, "Optimizing the integration of photovoltaic systems with electric utilities," *IEEE Transactions on Energy Conversion,* vol. 7, no. 1, pp. 72-78, 1992.

[52] B. Yang, W. Li, Y. Zhao, and X. He, "Design and analysis of a grid-connected photovoltaic power system," *IEEE Transactions on Power Electronics,* vol. 25, no. 4, pp. 992-1000, 2010.

[53] S. Jain and V. Agarwal, "A single-stage grid connected inverter topology for solar PV systems with maximum power point tracking," *IEEE Transactions on Power Electronics,* vol. 22, no. 5, pp. 1928-1940, 2007.

[54] S. Jain and V. Agarwal, "Comparison of the performance of maximum power point tracking schemes applied to single-stage grid-connected photovoltaic systems," *IET Electric Power Applications,* vol. 1, no. 5, pp. 753-762, 2007.

[55] D. Garrett and S. Jeter, "A photovoltaic voltage regulation impact investigation technique. I. Model development," *IEEE Transactions on Energy Conversion,* vol. 4, no. 1, pp. 47-53, 1989.

[56] Y.-K. Lo, H.-J. Chiu, T.-P. Lee, I. Purnama, and J.-M. Wang, "Analysis and design of a photovoltaic system DC connected to the utility with a power factor corrector," *IEEE Transactions on Industrial Electronics,* vol. 56, no. 11, pp. 4354-4362, 2009.

[57] R. A. Mastromauro, M. Liserre, T. Kerekes, and A. Dell'Aquila, "A single-phase voltage-controlled grid-connected photovoltaic system with power quality conditioner functionality," *IEEE Transactions on Industrial Electronics,* vol. 56, no. 11, pp. 4436-4444, 2009.

[58] J. M. Carrasco, L. G. Franquelo, J. T. Bialasiewicz, E. Galván, R. P. Guisado, M. A. Prats, J. I. León, and N. Moreno-Alfonso, "Power-electronic systems for the grid integration of renewable energy sources: A survey," *IEEE Transactions on Industrial Electronics,* vol. 53, no. 4, pp. 1002-1016, 2006.

[59] I. Patrao, E. Figueres, F. González-Espín, and G. Garcerá, "Transformerless topologies for grid-connected single-phase photovoltaic inverters," *Renewable and Sustainable Energy Reviews,* vol. 15, no. 7, pp. 3423-3431, 2011.

[60] S. Dasgupta, S. K. Sahoo, and S. K. Panda, "Single-Phase Inverter Control Techniques for Interfacing Renewable Energy Sources With Microgrid;Part I: Parallel-Connected Inverter Topology With Active and Reactive Power Flow Control Along With Grid Current Shaping," *IEEE Transactions on Power Electronics,* vol. 26, no. 3, pp. 717-731, 2011.

[61] S. Dasgupta, S. K. Sahoo, S. K. Panda, and G. Amaratunga, "Single-Phase Inverter-Control Techniques for Interfacing Renewable Energy Sources With Microgrid;Part II: Series-Connected Inverter Topology to Mitigate Voltage-Related Problems Along With Active Power Flow Control," *IEEE Transactions on Power Electronics,* vol. 26, no. 3, pp. 732-746, 2011.

[62] S. B. Kjaer, J. K. Pedersen, and F. Blaabjerg, "A review of single-phase grid-connected inverters for photovoltaic modules," *IEEE Transactions on Industry Applications,* vol. 41, no. 5, pp. 1292-1306, 2005.

[63] Z. Chen and E. Spooner, "Voltage source inverters for high-power, variable-voltage DC power sources," in *IEE Proceedings- Generation, Transmission and Distribution*, 2001, pp. 439-447.

[64] D. Yadav and T. Bhatti, "Voltage control through reactive power support for WECS based hybrid power system," *International Journal of Electrical Power & Energy Systems,* vol. 62, pp. 507-518, 2014.

[65] M. N. Marwali, J.-W. Jung, and A. Keyhani, "Control of distributed generation systems-Part II: Load sharing control," *IEEE Transactions on Power Electronics,* vol. 19, no. 6, pp. 1551-1561, 2004.

[66] F. Blaabjerg, R. Teodorescu, M. Liserre, and A. V. Timbus, "Overview of control and grid synchronization for distributed power generation systems," *IEEE Transactions on Industrial Electronics,* vol. 53, no. 5, pp. 1398-1409, 2006.

[67] I. Standard, "61727,"Characteristic of the utility interface for photovoltaic (PV) systems,"" IEC, Tech. Rep2002.

[68] T. S. Basso and R. DeBlasio, "IEEE 1547 series of standards: interconnection issues," *IEEE Transactions on Power Electronics,* vol. 19, no. 5, pp. 1159-1162, 2004.

[69] J. Arrillaga and N. R. Watson, *Power system harmonics*: 2nd Edition, John Wiley & Sons Ltd., 2003.

[70] R. C. Dugan, M. F. McGranaghan, and H. W. Beaty, *Electrical power systems quality*: 2nd Edition, McGraw-Hill New York, 2003.

[71] A. B. Baggini, *Handbook of power quality*: John Wiley & Sons Ltd, England, 2008.

[72] J. S. Subjak Jr and J. S. McQuilkin, "Harmonics-causes, effects, measurements, and analysis: An update," *IEEE Transactions on Industry Applications,* vol. 26, no. 6, pp. 1034–1042, Nov./Dec. 1990.

[73] A. Ghosh and G. F. Ledwich, *Power quality enhancement using custom power devices*: Kluwer Academic Publishers, Boston, 2002.

[74] V. Kumar, K. K. Reddy, and D. Thukaram, "Coordination of reactive power in grid-connected wind farms for voltage stability enhancement," *IEEE Transactions on Power Systems,* vol. 29, no. 5, pp. 2381-2390, 2014.

[75] T. J. E. Miller, *Reactive power control in electric systems*: John Willey & Sons, 1982.

[76] N. G. Hingorani and L. Gyugyi, *Understanding FACTS: concepts and technology of flexible AC transmission systems*: IEEE Press, New York, 1999.

[77] C. Surapong, C. Yu, D. Thukaram, T. Nipon, and K. Damrong, "Minimization of the effects of harmonics and voltage dip caused by electric arc furnace," in *Power Engineering Society Winter Meeting, 2000. IEEE*, 2000, pp. 2568-2576.

[78] P. Sharma and D. Thukaram, "Reactive power and voltage control in grid connected wind farms," in *7th IEEE International Conference on Industrial and Information Systems (ICIIS)*, 2012, pp. 1-6.

[79] A. Moreno-Munoz, *Power quality: mitigation technologies in a distributed environment*: Springer-Verlag Limited, London, 2007.

[80] P. Sharma, T. Bhatti, and K. Ramakrishna, "Compensation of Reactive Power of Isolated Wind-Diesel Hybrid Power Systems," *Journal of The Institution of Engineers (India): Series B,* vol. 93, no. 1, pp. 1-6, 2012.

[81] C. Patel and R. Mahanty, "Unified power quality conditioner using a fuzzy controller," *International Journal of Emerging Electric Power Systems,* vol. 11, no. 4, 2010.

[82] R. Bansal, T. Bhatti, and D. Kothari, "Artificial intelligence techniques for reactive power/voltage control in power systems: a review," *International journal of power & energy systems,* vol. 23, no. 2, pp. 81-89, 2003.

[83] *IEEE Recommended Practices and Requirements for Harmonic Control in Electrical Power Systems, IEEE Standard 519–1992,* 1993.

[84] B. Singh, B. N. Singh, A. Chandra, K. Al-Haddad, A. Pandey, and D. P. Kothari, "A review of single-phase improved power quality AC-DC converters," *IEEE Transactions on Industrial Electronics,* vol. 50, no. 5, pp. 962–981, Oct. 2003.

[85] B. Singh, B. N. Singh, A. Chandra, K. Al-Haddad, A. Pandey, and D. P. Kothari, "A review of three-phase improved power quality AC-DC converters," *IEEE Transactions on Industrial Electronics,* vol. 51, no. 3, pp. 641–660, Jun. 2004.

[86] H. Akagi, "New trends in active filters for power conditioning," *IEEE Transactions on Industry Applications,* vol. 32, no. 6, pp. 1312–1322, Nov./Dec. 1996.

[87] N. Mohan, H. A. Peterson, W. F. Long, G. R. Dreifuerst, and J. J. Vithayathil, "Active filters for AC harmonic suppression," in *IEEE/PES Winter Meeting*, 1977.

[88] H. Akagi, "Trends in active power line conditioners," *IEEE Transactions on Power Electronics,* vol. 9, no. 3, pp. 263–268, May 1994.

[89] F. Z. Peng, "Harmonic sources and filtering approaches," *IEEE Industry Applications Magazine,* vol. 7, no. 4, pp. 18–25, Jul./Aug. 2001.

[90] R. Mahanty, "Large value AC capacitor for harmonic filtering and reactive power compensation," *IET Generation, Transmission & Distribution,* vol. 2, no. 6, pp. 876-891, 2008.

[91] M. Rastogi, N. Mohan, and A.-A. Edris, "Hybrid-active filtering of harmonic currents in power systems," *Power Delivery, IEEE Transactions on,* vol. 10, no. 4, pp. 1994-2000, 1995.

[92] J. C. Das, "Passive filters-potentialities and limitations," *IEEE Transactions on Industry Applications,* vol. 40, no. 1, pp. 232–241, Jan./Feb. 2003.

[93] W. Chi-Jui, C. Jung-Chen, Y. Shih-Song, L. Ching-Jung, Y. Jin-Shyr, and G. Tzong-Yih, "Investigation and mitigation of harmonic amplification problems caused by single-tuned filters," *IEEE Transactions on Power Delivery,* vol. 13, no. 3, pp. 800–806, Jul. 1998.

[94] H. Sasaki and T. Machida, "A new method to eliminate ac harmonic currents by magnetic flux compensation-considerations on basic design," *IEEE Transactions on Power Apparatus and Systems,* vol. 90, no. 5, pp. 2009–2019, Sept. 1971.

[95] L. Gyugyi and E. C. Strycula, "Active ac power filters," in *Proc. IEEE Ind. Appl. Ann. Meeting*, 1976, pp. 529–535.

[96] B. Singh, K. Al-Haddad, and A. Chandra, "A review of active filters for power quality improvement," *IEEE Transactions on Industrial Electronics,* vol. 46, no. 5, pp. 960–971, Oct. 1999.

[97] W. M. Grady, M. J. Samotyj, and A. H. Noyola, "Survey of active power line conditioning methodologies," *IEEE Transactions on Power Delivery,* vol. 5, no. 3, pp. 1536–1542, Jul. 1990.

[98] C. Quinn and N. Mohan, "Active filtering of harmonic currents in three-phase, four-wire systems with three-phase and single-phase nonlinear loads," in *Applied Power Electronics Conference and Exposition, 1992. APEC'92. Conference Proceedings 1992., Seventh Annual*, 1992, pp. 829-836.

[99] H. Fujita and H. Akagi, "A practical approach to harmonic compensation in power systems-series connection of passive and active filters," *IEEE Transactions on Industry Applications,* vol. 27, no. 6, pp. 1020–1025, Nov./Dec. 1991.

[100] R. Mahanty, "Indirect current controlled shunt active power filter for power quality improvement," *International Journal of Electrical Power & Energy Systems,* vol. 62, pp. 441-449, 2014.

[101] C. S. Solanki, *Solar photovoltaics: fundamentals, technologies and applications*: PHI Learning Pvt. Ltd., 2011.

[102] R. Dubey, S. Chattopadhyay, V. Kuthanazhi, J. J. John, J. Vasi, A. Kottantharayil, B. M. Arora, K. Narsimhan, V. Kuber, and C. S. Solanki, "Performance degradation in field-aged crystalline silicon PV modules in different indian climatic conditions," in *40th IEEE Photovoltaic Specialist Conference (PVSC)*, 2014, pp. 3182-3187.

[103] http://www.maharishisolar.com/.

[104] N. Mohan and T. M. Undeland, *Power electronics: converters, applications, and design*: John Wiley & Sons, 2007.

[105] IEC Standard, "61727,"" *Characteristic of the utility interface for photovoltaic (PV) systems,* 2002.

[106] V. Khadkikar, R. K. Varma, R. Seethapathy, A. Chandra, and H. Zeineldin, "Impact of distributed generation penetration on grid current harmonics considering non-linear loads," in *3rd IEEE International Symposium on Power Electronics for Distributed Generation Systems (PEDG)*, 2012, pp. 608-614.

[107] B. Singh, K. Al-Haddad, and A. Chandra, "A review of active filters for power quality improvement," *IEEE Transactions on Industrial Electronics,* vol. 46, no. 5, pp. 960-971, 1999.

[108] A. Chandra, B. Singh, B. Singh, and K. Al-Haddad, "An improved control algorithm of shunt active filter for voltage regulation, harmonic elimination, power-factor correction, and balancing of nonlinear loads," *IEEE Transactions on Power Electronics,* vol. 15, no. 3, pp. 495-507, 2000.

[109] M. Singh, V. Khadkikar, A. Chandra, and R. K. Varma, "Grid interconnection of renewable energy sources at the distribution level with power-quality improvement features," *IEEE Transactions on Power Delivery,* vol. 26, no. 1, pp. 307-315, 2011.

[110] R. K. Varma, V. Khadkikar, and R. Seethapathy, "Nighttime application of PV solar farm as STATCOM to regulate grid voltage," *IEEE Transactions on Energy Conversion,* vol. 24, no. 4, pp. 983-985, 2009.

[111] R. K. Varma, S. A. Rahman, and T. Vanderheide, "New Control of PV Solar Farm as STATCOM (PV-STATCOM) for Increasing Grid Power Transmission Limits During Night and Day," *IEEE Transactions on Power Delivery,* vol. 30, no. 2, pp. 755-763, 2015.

[112] S. Mishra and P. Sekhar, "Real and Reactive Power Control of Voltage Source Converter-Based Photovoltaic Generating Systems," *Solar Cell Nanotechnology,* pp. 475-503, 2013.

[113] G. F. Franklin, J. D. Powell, and A. Emami-Naeini, "Feedback control of dynamics systems," *Pretince Hall Inc,* 2006.

[114] V. Khadkikar, A. Chandra, and B. Singh, "Generalised single-phase pq theory for active power filtering: simulation and DSP-based experimental investigation," *IET Power Electronics,* vol. 2, no. 1, pp. 67-78, 2009.

[115] H. Akagi, S. Inoue, and T. Yoshii, "Control and performance of a transformerless cascade PWM STATCOM with star configuration," *IEEE Transactions on Industry Applications,* vol. 43, no. 4, pp. 1041–1049, Jul./Aug. 2007.

[116] H. Akagi, M. Hagiwara, and R. Maeda, "Negative-sequence reactive-power control by a PWM STATCOM based on a Modular Multilevel Cascade Converter (MMCC-SDBC)," *IEEE Transactions on Industry Applications,* vol. 48, no. 2, pp. 720–729, Mar./Apr. 2012.

[117] X. Wu, S. K. Panda, and J. Xu, "Effect of pulse-width modulation schemes on the performance of three-phase voltage source converter," in *33rd Annual Conference of the IEEE Industrial Electronics Society*, 2007, pp. 2026-2031.

[118] B. Wu, *High-power converters and AC drives*: Piscataway, NJ: IEEE Press, 2006.

[119] S. Kouro, M. Malinowski, K. Gopakumar, J. Pou, L. G. Franquelo, B. Wu, J. Rodriguez, M. A. Perez, and J. I. Leon, "Recent advances and industrial applications of multilevel

converters," *IEEE Transactions on Industrial Electronics,* vol. 57, no. 8, pp. 2553–2580, Aug. 2010.

[120] B. P. McGrath and D. G. Holmes, "Multicarrier PWM strategies for multilevel inverters," *IEEE Transactions on Industrial Electronics,* vol. 49, no. 4, pp. 858–867, Aug. 2002.

[121] L. Li, D. Czarkowski, Y. Liu, and P. Pillay, "Multilevel selective harmonic elimination PWM technique in series-connected voltage inverters," *IEEE Transactions on Industry Applications,* vol. 36, no. 1, pp. 160–170, Jan. 2000.

[122] L. G. Franquelo, J. Napoles, R. C. P. Guisado, J. I. Leon, and M. A. Aguirre, "A flexible selective harmonic mitigation technique to meet grid codes in three-level PWM converters," *IEEE Transactions on Industrial Electronics,* vol. 54, no. 6, pp. 3022–3029, Dec. 2007.

[123] B. Yin, R. Oruganti, S. K. Panda, and A. K. Bhat, "An output-power-control strategy for a three-phase PWM rectifier under unbalanced supply conditions," *IEEE Transactions on Industrial Electronics,* vol. 55, no. 5, pp. 2140-2151, 2008.

[124] V. Khadkikar, A. Chandra, and B. Singh, "Digital signal processor implementation and performance evaluation of split capacitor, four-leg and three H-bridge-based three-phase four-wire shunt active filters," *IET Power Electronics,* vol. 4, no. 4, pp. 463–470, Apr. 2011.

[125] S. K. Jain, P. Agarwal, and H. O. Gupta, "Fuzzy logic controlled shunt active power filter for power quality improvement," *IEE Proceedings on Electric Power Applications,* vol. 149, no. 5, pp. 317–328, Sept. 2002.

[126] B. Singh, P. Jayaprakash, S. Kumar, and D. P. Kothari, "Implementation of neural network-controlled three-leg VSC and a transformer as three-phase four-wire DSTATCOM," *IEEE Transactions on Industry Applications,* vol. 47, no. 4, pp. 1892–1901, Jul./Aug. 2011.

[127] B. Singh, P. Jayaprakash, T. R. Somayajulu, and D. P. Kothari, "Reduced rating VSC with a zig-zag transformer for current compensation in a three-phase four-wire distribution system," *IEEE Transactions on Power Delivery,* vol. 24, no. 1, pp. 249–259, Jan. 2009.

[128] B. Singh, P. Jayaprakash, and D. P. Kothari, "A T-connected transformer and three-leg VSC based DSTATCOM for power quality improvement," *IEEE Transactions on Power Electronics,* vol. 23, no. 6, pp. 2710–2718, Nov. 2008.